Switching kinetics of valence change memory devices on a sub-100 ps timescale

Von der Fakultät für Elektrotechnik und Informationstechnik der Rheinisch-Westfälischen Technischen Hochschule Aachen zur Erlangung des akademischen Grades eines Doktors der Naturwissenschaften genehmigte Dissertation

vorgelegt von

Moritz von Witzleben

M. Sc.

aus Trier

Berichter: Univ.-Prof. Dr.-Ing. Rainer Waser
Univ.-Prof. Dr. sc. techn. Renato Negra

Tag der mündlichen Prüfung: 17.09.2021

Abstract

The further development of today's memory technologies faces several technological barriers, which yields the demand for new approaches. One emerging memory type that has the potential to overcome these barriers is the valence change memory (VCM), which may also be usable for neuromorphic applications or in-memory computations. In VCM devices, the information is stored within different resistive states, namely a high resistive state (HRS) and a low resistive state (LRS), which can be programmed with electrical stimuli. The transition from the HRS to the LRS is referred to as SET and the opposite transition as RESET.

In this thesis, the SET and RESET times of TaO_x-, ZrO_x-, and HfO_x/TiO_x-based VCM devices were studied in the time regime from 50 ps to 100 ns. Signals in this time regime contain high frequency components in the gigahertz regime. The signals require proper impedance matching up to the VCM device, which are, therefore, integrated into coplanar waveguide (CPW) structures. Nevertheless, an integrated VCM device constitutes a parallel plate capacitor with a considerable electrical charging time, which delays the measured SET and RESET times.

To estimate the electrical charging time, an experimental approach was used, with which the time-dependent effective voltage at the VCM device could be determined. This approach used the Fourier transformation of the applied voltage pulse and the VCM device's scattering parameters. From the resulting effective voltage at the VCM device, the electrical charging time of all tested VCM devices was determined. The results indicate that conducted optimizations of the CPW structure decreased the electrical charging time significantly and allowed fast measurements on a sub-100 ps time scale.

By employing dedicated hardware and integrating this hardware into a software, the measurements could be automated. This allowed collecting comprehensive data sets on the SET and RESET kinetics of the tested VCM devices and, thereby, allowed resolving their transient resistance on a picosecond time scale.

The measured SET kinetics revealed that all studied devices can switch within 50 ps from the HRS to the LRS. To the author's knowledge, this is the fastest switching time reported for VCM devices. By comparing the SET kinetics of differently sized TaO_x-based VCM devices and using the determined electrical charging times, it could be shown that the SET kinetics of VCM devices in the subnanosecond regime are mainly limited by the electrical charging time. The migration of mobile donors (e.g. oxygen vacancies), which limits the SET kinetics on slower time scales, and the heating time of the VCM device have only a minor influence.

Achieving similar fast RESET times proved to be more difficult. In all studied VCM devices, the coexistence of a unipolar switching mode could be shown. This unipolar switching mode is triggered at higher voltages, which would be required for faster RESET times. Nevertheless, on some HfO_x/TiO_x-based VCM devices 50 ps fast RESET times could be measured repeatedly. From these kinetics measurements, RESET programming windows could be determined and, finally, approaches were derived to achieve faster RESET times.

Kurzfassung

Die Weiterentwicklung heutiger Speichertechnologien sieht sich mehreren technologischen Hürden konfrontiert, wodurch die Nachfrage nach neuen Ansätzen wächst. Ein neuer Speichertyp, der das Potenzial hat, diese Hürden zu überwinden, ist der Valenzwechselspeicher (VCM), welcher auch für neuromorphe Anwendungen oder In-Memory-Berechnungen verwendet werden kann. Bei VCM-Zellen ist die Information in verschiedenen resistiven Zuständen gespeichert, namentlich einem hochohmigen Zustand (HRS) und einem niederohmigen Zustand (LRS), der mit elektrischen Stimuli programmiert werden kann. Der Übergang vom HRS zum LRS wird als SET und der umgekehrte Übergang als RESET bezeichnet.

In dieser Arbeit wurden die SET- und RESET-Zeiten von TaO_x-, ZrO_x- und HfO_x/TiO_x-basierten VCM-Zellen im Zeitbereich von 50 ps bis 100 ns untersucht. Signale in diesem Zeitbereich enthalten Komponenten mit hohen Frequenzen im GHz-Bereich. Die Signale erfordern eine korrekte Impedanzanpassung bis zur VCM-Zelle, welche daher in koplanare Wellenleiterstrukturen (CPW) integriert werden. Dennoch stellt eine integrierte VCM-Zelle einen Plattenkondensator mit einer erheblichen elektrische Aufladezeit dar, welche die gemessenen SET- und RESET-Zeiten verzögert.

Zur Abschätzung dieser elektrischen Ladezeit wurde ein experimenteller Ansatz verwendet, mit dem die zeitabhängige effektive Spannung an der VCM-Zelle bestimmt werden konnte. Dieser Ansatz nutzt die Fourier-Transformation des angelegten Spannungspulses und die Streuparameter der VCM-Zelle. Aus der resultierenden effektiven Spannung an der Zelle wurde die elektrische Aufladezeit aller getesteten VCM-Zellen bestimmt. Die Ergebnisse zeigen, dass durchgeführte Optimierungen der CPW-Strukturen die elektrische Aufladezeit deutlich verkürzten und damit schnellere Messungen auf einer sub-100 ps Zeitskala ermöglichten.

Durch den Einsatz dedizierter Hardware und deren Einbindung in eine Software konnte der experimentelle Aufbau so erweitert werden, dass Messungen automatisiert durchgeführt werden konnten. Dies ermöglichte die Erfassung umfangreicher Datensätze zur SET- und RESET-Kinetik der getesteten VCM-Zellen und es wurde dadurch möglich, deren transienten Widerstand auf einer Zeitskala im Pikosekundenbereich aufzulösen.

Die gemessene SET-Kinetik ergab, dass alle untersuchten Zellen innerhalb von 50 ps vom HRS in den LRS schalten können. Nach Kenntnis des Autors ist dies die schnellste Schaltzeit, die für VCM-Zellen berichtet wurde. Durch den Vergleich der SET-Kinetik von unterschiedlich großen TaO_x-basierten VCM-Zellen und der Verwendung der berechneten elektrischen Aufladezeiten konnte gezeigt werden, dass die SET-Kinetik von VCM-Zellen im Sub-Nanosekundenbereich hauptsächlich durch die elektrische Aufladezeit limitiert wird. Die Migration von mobilen Donatoren (z.B. Sauerstoffleerstellen), welche die SET-Kinetik auf langsameren Zeitskalen limitiert, und die Aufheizzeit der VCM-Zellen haben nur einen geringen Einfluss.

Die Realisierung ähnlich schneller RESET-Zeiten erwies sich als schwierig. Bei allen untersuchten VCM-Zellen konnte die Koexistenz eines unipolaren Schaltmodus gezeigt werden. Dieser unipolare Schaltmodus tritt bei höheren Spannungen auf, welche für schnellere

RESET-Zeiten erforderlich wären. Dennoch konnte mit einigen HfO_x/TiO_x-basierten VCM-Zellen, 50 ps schnelle RESET-Zeiten reproduzierbar gemessen werden. Aus diesen Kinetikmessungen konnten RESET-Programmierfenster erstellt und Ansätze entwickelt werden, um schnellere RESET-Zeiten zu realisieren.

Acknowledgments

The work at hand was only possible with the support of many people, to whom I would like to say: **Thank you!**

Firstly, I would like to thank **Prof. Rainer Waser** for allowing me to pursue my Ph.D. at his institute and for creating a constructive, multi-disciplinary, and international working atmosphere.

Secondly, I would like to thank **Prof. Negra** for agreeing to be the co-examiner of my thesis.

I thank my first supervisor **Dr. Ulrich Böttger** for the excellent supervision, constructive discussions and also for giving me the freedom to realize new ideas. I also acknowledge his contributions to the joint publications and advices in LT Spice.

I also thank my second supervisor **Dr. Stephan Menzel** for the excellent supervision, especially for teaching me much about ReRAM devices and assisting me with interpretation of the experimental results and also for his contributions in the joint publications.

To my predecessors **Dr. Viktor Havel** and **Dr. Karsten Fleck** I am thankful for providing me operational and state-to-the-art setups, for the excellent knowledge transfer, and for their contributions to the joint publications.

I thank **Tyler Hennen** for programming *py-ivtools*, assisting me with the measurements of the unipolar SET voltage, teaching me much about programming in python, and giving me advices for fast measurements.

I thank **Sebastian Walfort** for supporting me with the analysis of the scattering parameters.

I thank **Dr. Andreas Kindsmüller** for fabracting many TaO_x- and ZrO_x-based devices and his suggestions on how to realize faster RESET times.

I am grateful to **Carsten Funck** for helping me with the simulations in Comsol.

Many people were involved in the fabrication of the devices which were used in this thesis. Therefore, I would like to thank **Erdoglija Daliborka**, **Petra Grewe**, **René Borowksi**, and **Alfred Steffen** for fabricating the TaO_x- and ZrO_x-based devices.

Also, I would like to thank **Alexander Hardtdegen**, **Felix Cüppers**, and **Stephan Aussen** for fabricating the HfO_x-based devices.

I thank **Dr. Xuan Thang Vu** for fabricating PCM devices and instructing me how to measure them.

I thank **Dr. Susanne Hoffmann-Eifert**, **Dr. Vikas Rana**, and **Prof. Martin Salinga** for granting the resources, with which the devices could be fabricated.

I thank **Jan Lübben** for giving me advices on measurements of scattering parameters and capacitances.

I am thankful to **Fenja Berg** and **Dr. Michael Lübben** for the joint fast measurements on FeRAM and ECM devices.

I am thankful to **Stefan Wiefels**, **Christopher Bengel**, and **Sebastian Siegel** for giving me the opportunity to contribute to their works.

I am grateful for the support of the student research assistants **Erik Wichmann**, **Alexander Idt**, **Lena Hellmich**, **Brigitte Baumkötter**, **Sergej Liberda**, **Cornelia Höhl**, **Milena Zuric**, and **Georg Wendorf**.

More explicitely I want to thank **Artem Zaidman** and **Stefan Leisten** for fabricating the crossbar ZrO_x-based devices and for conducting kinetic and endurance measurements on them.
I thank **Udo Evertz**, **Marcel Gerst**, **Giesela Wasse**, **Jochen Heiss**, **Hartmut Pütz**, **Dagmar Leisten** and **Peter Röggels** for technical support.
For helping me with my figures and teaching me how to use the Adobe Illustrator, I thank **Thomas Pössinger**.
Furthermore, I would like to thank **Martina Heins** and **Maria Garcia** for the great administrative help and support.
I thank **Dr. Alvaro M. Mártir** and **Dr. Florian Merget** from the Integrated Photonics institute (RWTH) for providing the Agilent Technologies N5245A VNA and consulting me with regard to frequency domain measurements.
I thank the teachers **Dr. Carole Veldman-Genz**, **Reinhard Oechtering**, and **Pal Dosanj** of the CDS courses I attended, for helping me to improve my soft skills. I also want to thank **Prof. Joachim Mayer**, **Dr. Oana Cojocaru-Mirédin** and **Thomas Czirnich** for organizing the CDS courses.
More explicitly I want to thank **Leyla Haferkamp** for teaching me in scientific writing and for proof reading the introduction of my thesis.
I thank **Dr. Bernd Brinkmeier**, **Ingo Brinkmeier** and **Jan Willmann** from the SYMPULS GmbH for fabricating a customized pulse generator, with which the fast and automated kinetic measurements became possible.
I would like to thank my office mates **Johannes Mohr**, **Dr. Alexander Schönhals**, **Dr. Jonathan Rupp**, **Dr. Daniel Bick**, and **all other colleagues** at the IWE 2 and the PGI 7 for contributing to a good working atmosphere.
I thank **Tiziana von Witzleben** for proof reading my thesis.
Finally, I thank **Jenny**, my **family**, my **friends** and my soccer team **Bierunion West** for the life besides work.

Contents

Introduction

One of the skills that made humans the most dominant life form on earth is our ability to pass on information to future generations. Passing on information requires both a medium, in which the information can be stored, and a code or language, which can be decoded and understood by future generations. More than 35,000 years ago, the first information were passed on in the form of cave paintings, which still help us today to understand how humans used to live at that time [1]. The information was coded as image, which is the most accessible form of coding an information. It is, however, challenging to describe more sophisticated topics, theories or methods only in images. Therefore, around 5,300 BC first fonts were developed and engraved in walls or stone plates [2]. A prominent example are the Egyptian hieroglyphs, which were used from 3,200 BC [3]. After 2,000 BC first alphabets were developed and resulted, among others, in the Latin and the Greek alphabet [4]. Descendants of both alphabets are still used worldwide today [5]. So approaching Year Zero, languages and fonts allowing precise coding of information existed, however, they were still engraved in stone plates. This was disadvantageous because the *writing time* of the information was slow and the information density (or *storage density*) on the stone plates was low. A better medium is paper, which was invented around 105 BC in China [6, 7]. As it is easier and faster to write with ink and as paper weighs less than stone plates, this invention accelerated the writing times and increased the storage density. The invention of the modern letterpress by Gutenberg in 1,450 AD accelerated the writing times even further [8]. Newspapers and books were printed in larger quantity and became available to a broader spectrum of the population. In the 18th century, information was for the first time stored digitally in form of punched cards [9]. It took, however, up to the early 1970s until information were stored digitally on a larger scale.

At that time, magnetic (floppy drive disks) and electrical memories (Dynamic random access memory – DRAM) improved writing times and storage density by orders of magnitudes [10, 11]. Modern floppy drive disks had a storage capacity of 1.44 megabyte, which corresponds to more than 700 written pages. The information in today's memory technologies is still stored digitally. Developments in the device fabrication have made it possible to store information in nanometer-sized memory cells and thereby improved writing times and storage density even further [12, 13]. Today's long-term memory technologies like Flash have writing times down to tens of nanoseconds and can store more than one terabyte on a small device, corresponding to millions of books [14, 15]. This progress has extended the

field of application of these memories. Only a small fraction is used to store information in text-form. More storage capacity is used for images, videos, computer games, and other applications. Also science and industry require large storage capacities because their acquired data and calculations have become more and more complex [16].

In view of the impressive progress made during the last century, the question arises as to why do we need to further improve memory technologies – especially regarding writing times. This development is necessary for both science and industry, as illustrated by the following examples. The first is the Large Hadron Collider in Geneva, which allows physicists to address many fundamental questions about the universe and the matter of which everything is built. Their experiment comprises 150 million sensors, which detect particles 40 million times per second [17]. No technology can store this amount of data; 99.9 % of the sensor's detections are, therefore, immediately discarded [18]. Nevertheless, the collected data amount to more than 200 petabytes annually [19] and are evaluated by more than 170 computing centers around the world [20]. The second example is the realization of robotic systems, such as autonomously driving vehicles. To participate in traffic, an autonomously driving vehicle needs to perceive information about its environment from all angles. For this purpose, various sensors and cameras are installed [21]. For fast reactions of the vehicle, these sensors and cameras collect data several times per seconds. As these data also include high definition images, they can amount to up to one gigabyte per second [22]. Thus, developing faster memories is not only about improving private computers, smartphones and other electronic devices, but also about supporting scientific and technological projects.

Faster devices already exist: the most prominent example is the dynamic random access memory (DRAM), which has writing times down to 50 nanoseconds [14, 15]. However, the *retention time* of today's fastest memories is very short and the stored information is lost within fractions of seconds. To preserve the information, it is read and rewritten in short intervals, *i.e.* for DRAM every 64 milliseconds [15, 23]. For this purpose, the device requires a power supply. As soon as the power supply is turned off, all information is lost. Today's computers are mostly based on the von Neumann architecture, which means that the central processing unit (CPU) and the main memory are spatially separated [24]. This decelerates the data transfer between CPU and memory significantly and is referenced to as memory bottleneck [25]. Transistor-based memories (*cache*) are integrated into the CPU to bypass this issue. As these memories have large feature sizes, their fabrication costs are high and their storage density is low. Even the cache of state-of-the-art processors can store less than 100 megabytes [26, 27]. In-memory-computing or on-chip memory would remove this limitation.

Among other emerging non-volatile memory technologies, redox-based random access memory (ReRAM) [28–31] fulfils all requirements of long-term memories. Its information is saved as different resistive states, which are programmed using electrical stimuli. The transition from a high to a low resistive state (HRS and LRS) is referred to as *SET* process

and the opposite transition as *RESET* process. In contrast to today's long-term memories, the writing times of ReRAMs are significantly faster [32–39]. Also, the storage of more than one bit per device is possible [40, 41]. This not only enables a higher storage density, but it also makes ReRAM compatible with neuromorphic applications [25, 42, 43]. These applications aim to adopt calculation processes of the human brain [44] and have the potential to considerably decrease the power consumption of processing units as well as to improve artificial intelligence. ReRAM has also the potential for in-memory computations, which would eliminate the memory bottleneck [25, 43]. Evidence for writing times of less than 100 picoseconds in ReRAM devices has already been presented [34]. The determination of the absolute writing speed limit, however, remains an experimental challenge.

This thesis investigates the limits of writing times of valence change memory (VCM) and is structured in six chapters. The active switching materials of the devices are TaO_x, ZrO_x and HfO_x. The first chapter, gives an overview of emerging memory technologies and then summarizes the theory and models of VCM devices with emphasis on their writing times. Additionally, intrinsic mechanisms and technological issues that could limit writing times are explained. Fast electrical measurements comprise frequencies in the gigahertz regime, which increases the requirements on the experiment. For this purpose, the theory of transmission lines and waveguides is also elucidated.

The second chapter describes the experimental setup for kinetic measurements in the regime between 100 nanoseconds and 50 picoseconds. The setup could be automated, which made it possible to collect comprehensive statistics on the switching kinetics. Signals in the subnanosecond regime require proper impedance matching, which has to be provided from the signal source to the VCM device, which therefore needs to be implemented in a coplanar waveguide (CPW) structure. Also, an approach was developed which allows determining the effective electrical stimulus on the VCM device by using its scattering parameters.

The investigated VCM devices are presented in chapter 3. To improve the electrical charging time, which delays the measured writing times, a mask for the optical lithography process has been designed, in which the overall size of the CPW structure and the size of the integrated VCM device has been decreased, compared to previous masks. The devices were characterized with regard to their IV-characteristics, capacitance, scattering parameters and finally their electrical charging time. Comparing the electrical charging times revealed that the devices fabricated with this mask can be charged faster by one order of magnitude.

The results of the SET kinetics are shown in the fourth chapter. Here, the SET kinetics of devices with different capacitances are compared. The SET kinetics of all devices bend to slower writing times in the regime below 10 ns. It could be proven that this bending is due to the electrical charging of the devices. SET times of 50 ps were measured with all devices. By collecting a large data set with the automated setup, the transient change in the devices' resistance could also be resolved on a picosecond timescale.

Achieving comparable fast RESET times proved to be more difficult, as shown in chapter 5. The coexistence of a unipolar switching mode hindered faster RESET times in many devices, and constitutes an intrinsic RESET speed limitation of VCM devices. This results in RESET programming windows, which are compared to the SET programming window of *phase change memories* (PCMs). Nevertheless, some HfO_x/TiO_x-based devices could be switched repeatedly from the LRS to the HRS within 50 ps. This observation could be linked to the unipolar SET voltage, which is highest for the HfO_x/TiO_x-based devices.

In chapter 6, possible future experiments in the fast regime are suggested. They are needed in parts to achieve a better understanding of the unipolar switching mode and to determine the intrinsic speed limit of VCM devices more precisely. Also, neuromorphic applications could be realized on a subnanosecond timescale. Finally, it is shown that other emerging memory technologies have the potential for similar fast writing times as VCM devices.

1. Fundamentals

This chapter starts with an overview of the state-of-the-art memory technologies. Also, the necessity for new technologies and their requirements to become marketable is elucidated. Afterwards, this chapter focuses on ReRAM devices (especially on the VCM type) as they are relevant for this thesis. The underlying physical mechanisms, responsible for the switching process, are explained. Chapter 1.2.3 focuses on the kinetics of ReRAM devices, *i.e.* the dependence of the writing time on the applied voltage, and lists their possible speed limits. Studying the switching speed in the sub-nanosecond regime increases the requirements on the experiment. The involved electrical signals comprise frequencies in the GHz regime. Their preservation requires high frequency components and proper impedance matching at all interconnects. Chapter 1.3, therefore, treats the theory of microwave transmission-lines and elucidates experimental techniques.

1.1. Memory types

Most of today's computer are based on the von Neumann architecture, in which the CPU is separated from the main memory [24, 25]. To perform calculations, the CPU stores data in the main memory, for which usually DRAM is used. The information is stored in capacitors, which can be charged in two different directions, corresponding to the logical '0' and '1'. Although DRAM has fast writing times down to 10 ns [14, 15], the capacitors start discharging as soon as the applied voltage is turned off. Therefore, the information needs to be rewritten every 64 ms [15, 23]. Accordingly, DRAM is classified as *volatile* memory.

To store data permanently today's computers are equipped with additional long term memory type, which has a *retention times* of ten years or more. Thus, it is classified as *non-volatile* memory. Most prominent examples of non-volatile memories are the hard disk drive (HDD) and the solid state drive (SSD). The information in HDDs is stored in magnetic in-plane domains on the disk. To access these domains, the disk is rotating and a movable arm brings the read-write head to the targeted domain. As the rotation speed of the disk only amounts to several thousand rounds per minute, the read and writing times of HDDs are above 1 ms [14]. Due to the power consumed by the rotator and the movements of the arm, HDDs require the most energy for read and write operations compared to other broadly used memories [14].

The memory technology used in SSDs and USB (Universal Serial Bus) drives is Flash. The information is stored as electrical charge in a metal-oxide-semiconductor (MOS) structure. Similar to MOS-field effect transistors the electrical charge induces an electrically conducting channel in the semiconductor. The presence of the electrical charge, therefore, corresponds to the logical '1' and its absence to the logical '0'. Although flash-based memories have a good retention over more than 10 years, their writing time of down to 50 ns cannot compete with DRAM [15]. Storing or removing the electrical charge in the MOS structure requires a voltage of over 10 V. Consequently, the energy consumed per write operation is the second highest among state-of-the-art memories and the endurance is comparable low [15].

The difference in the writing time of Flash and DRAM is about a factor of 1000 [45], which is also illustrated in fig. 1.1. The gap between these two memory types is referred to as *memory gap*, as the fastest non-volatile memory is significantly slower than state-of-the-art volatile memories. Also, the production costs of volatile memories are higher. This is due to their larger feature sizes compared to the ones of non-volatile memories, which have a higher information density [14]. A memory that would fill this gap is referred to as *storage class memory*. Several emerging non-volatile memories are likely to overcome this gap [46]. Among them are ReRAMs, which are relevant for this thesis and explained in section 1.2. Other prominent candidates are *ferroelectric random access memory* (FeRAM), *spin-transfer-torque random access memory* (STTRAM), and phase change memory (PCM) which are briefly summarized in the following.

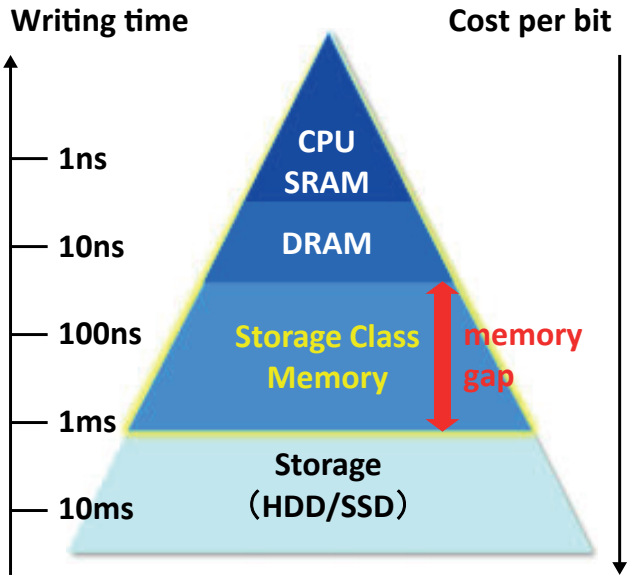

Figure 1.1.: Illustration of memory gap. Adapted with permission from [45] © Copyright (2016) The Japan Society of Applied Physics.

Ferroelectric random-access-memory

The functionality of ferroelectric random access memory (FeRAM) is similar to Flash, which uses an electric charge to modulate the conductivity of a semiconductor [46]. FeRAM, on the other hand, employs the ferroelectric polarization to change the conductivity of the semiconductor. For this purpose, a ferroelectric layer (usually $PbZr_xTi_{1-x}O_3$ [47]) is placed between the gate electrode and the semiconductor. The direction of the polarization can be programmed by electrical stimuli to the gate electrode. FeRAM has a very low switching power due to its low leakage current [46]. Additionally, it has an endurance of up to $4 \cdot 10^{10}$ cycles [48] and fast writing times down to 20 ns [49]. The scalability is so far limited to 22 nm [50] and the ferroelectric film thickness can be thinner than 5 nm for HfO_x- or ZrO_x-based devices [51].

Spin-transfer-torque random-access-memory

Similar to ReRAM and PCM devices, the information in spin-transfer-torque random-access-memory (STTRAM) is stored in an HRS (logical '0') and in an LRS (logical '1') [52]. A typical device has three vertically stacked layers in which the upper and lower layers are ferromagnetic (*e.g.* Co, Ni or Fe). The layer in the middle constitutes a magnetic tunnel junction (*e.g.* AlO_x or MgO_x). The magnetization's direction of the lower ferromagnetic layer is pinned and the one of the upper ferromagnetic layer is free. An antiparallel orientation of the ferromagnetic layer results in the HRS and a parallel orientation in the LRS. The information is driven by inducing spin-polarized currents, which can flip the magnetization of the upper free ferroelectric layer. STTRAM has the potential to achieve an endurance of up to 10^{15} cycles [53] and writing times down to 120 ps [54]. A scalability down to 22 nm has been demonstrated [55].

Phase change memory

Phase change memory (PCM) can also be programmed in an HRS and an LRS by applying electrical stimuli [56, 57]. It is usually operated in a unipolar switching mode, which means that the device's SET occurs at the same voltage polarity as its RESET. It is realized by placing a chalcogenide glass (acting as active material) between two metallic electrodes either in a vertical stack [58] or in a lateral structure [59]. In the HRS, the active material is usually in an amorphous state. During the SET operation a current is induced, which heats up the active material by Joule heating, which allows it to crystallize, driving the device in the LRS. To RESET the device a higher voltage is applied, which increases the Joule heating further and the chalcogenide glass starts to melt. By abruptly reducing the applied voltage, the active material is melt-quenched into an amorphous state again. The fastest observed RESET times amounts to 200 ps [60] and the fastest electrically measured SET time to 550 ps [61]. By preheating, SET times down to 500 ps were observed [62], and

optical measurements suggest SET times down to 1 ps [63]. The highest reported endurance amounts to 10^{12} cycles [64] and the smallest scaled device amounts to 7.5 nm [65].

1.2. Redox-based resistive random access memory

1.2.1. Types

In redox-based resistive random access memories (ReRAM) the information is also stored in an HRS and an LRS, which can be programmed by applying electrical stimuli. Electrochemical reactions and the migration of mobile ions are responsible for a change in the devices resistance [28, 66]. Three types can be distinguished: *electrochemical metallization memory* (ECM), *thermochemical memory* (TCM) and *valence change memory* (VCM). All types consist of a metal-insulator-metal stack, in which the insulator is an ionic conductor. All of the three ReRAM types usually require an initial electroforming step in which typically a relatively high voltage amplitude is applied to the device, during which an electronically conducting filament is formed within the insulator. To prevent the devices from taking damage during this electroforming step, the current is limited either by an active current compliance or a resistor in series.

In ECM devices, one of the electrodes consists of an electrochemically active electrode (*e.g.* Ag or Cu) and the other electrode is inert (*e.g.* Pt) [67, 68]. ECM devices are usually operated in a bipolar switching mode, which means that the SET and RESET operations are conducted with different voltage polarities. During the SET, a negative voltage is applied to the active electrode, which initiates redox reactions, forming positively charged metallic ions. These ions drift, subsequently, towards the inert electrode at which they are electrically reduced and, consequently, form a metallic bridge. The device is now in the LRS. During the RESET, a positive voltage is applied to the active electrode and attracts the metallic ions (after they were reoxidized). The metallic bridge is thereby destroyed and the device is back in the HRS.

TCM devices usually consists of two symmetrical electrodes (*e.g.* Pt) and an ion conducting insulator (*e.g.* NiO_x) [69]. The switching mode is unipolar. Opposite to the unipolar switching mode of PCM devices, higher voltage amplitudes are applied during the SET than during the RESET. During the SET, a current is induced, which increases the device's temperature and thereby increases its electrical conductivity, leading to a thermal runaway. The significant increase in temperature within the conducting path facilitates redox reactions, leading to a thermodiffusion of oxygen anions into the surroundings of the conductive path. The remaining oxygen vacancies remain in the conductive path and act as n-type donors, which permanently decreases the device's resistance and, consequently, brings the device to the LRS. Relatively high currents are required to achieve successful unipolar SET operations and, therefore, relatively high current compliances around 1 mA are used [70]. The RESET

is achieved by applying a lower voltage than during the SET without current compliance, which attracts the oxygen vacancies towards the negatively charged electrode. This results in a rupture in the conductive path, bringing the device back to the HRS.

In this thesis, only VCM devices were investigated, which are therefore explained more explicitly in the following section.

1.2.2. Valance change memory

Valance Change Memory (VCM) devices usually consist of two asymmetric metallic electrodes sandwiching a transition metal oxide layer (*e.g.* TaO_x, ZrO_x, or HfO_x), which constitutes the active switching layer [66]. One of the two metallic electrodes is oxygen affine (*e.g.* Ta) and referred to as ohmic electrode and the other one is inert (*e.g.* Pt) and referred to as active electrode (AE). The devices' resistance is modulated by rearranging mobile donors, which form a conductive filament within the active switching layer [28]. Several spectroscopic studies could detect a movement of oxygen vacancies [71–73]. Also, the movement of other metallic ions has been observed [74–76]. The conductive filament is assumed to be very narrow, having a diameter of only 1 nm to 4 nm [77, 78]. This is close to the smallest realized sized VCM devices of $2 \times 2\,\mathrm{nm}^2$ [79].

If the device is in the LRS, this conductive filament ranges from the ohmic electrode to the active electrode, which decreases the device's resistance. The RESET is realized by applying a positive voltage to the active electrode. The positively charged oxygen vacancies are, consequently, repelled from the active electrode and drift towards the ohmic electrode. The resulting rupture in the conductive filament brings the device to the HRS. The SET is realized by applying a negative voltage to the active electrode. The oxygen vacancies are, thus, attracted towards the active electrode, which closes the rupture in the conductive filament. Finally, the device is again in the LRS. In simulation models, the part of the conductive filament close to the active electrode is referred to as *disc*, having a varying concentration of oxygen vacancies, and the remaining part as *plug*, having a constant concentration of oxygen vacancies [80, 81].

Another operation mode of VCM devices is the so-called "eightwise" switching mode, which has been demonstrated in several devices [82–84], including TaO_x-based devices [85]. The LRS of the eightwise switching mode corresponds to the HRS of the "counter-eightwise" switching mode. Different to the counter-eightwise switching mode, the SET occurs at positive voltages and the RESET at negative voltages (applied to the active Pt electrodes). In case of the eightwise RESET operation, the applied voltage is lower than the counter-eightwise SET voltage and drives the device to a higher HRS. The eightwise switching mode originates from an oxygen exchange between the active Pt electrode and the oxide, which could be resolved with spectroscopic measurements [82]. This oxygen exchange, and consequently also the eigthwise switching mode, could be suppressed by introducing oxygen

blocking layers, such as C [85] or Al_2O_3 [83], between the Pt electrode and the oxide. Another switching mode is the area-depend mode (or non-filamentary) switching mode [86], which has for example been observed in $Pr_{0.5}Ca_{0.5}MnO_3$-based devices [87].

In this thesis, TaO_x-, ZrO_x-, and HfO_x/TiO_x-based VCM devices were studied. For TaO_x- and HfO_x-based devices an endurance of 10^{12} and 10^9 cycles has been proven, respectively [88,89]. For ZrO_x-based devices, the highest measured endurance amounts to 10^7 cycles [90]. The fastest reported SET and RESET times amount to 85 ps [34]. It could be shown that both the SET (see chapter 4) and the RESET (see chapter 5) operation can be conducted within 50 ps. Achieving reproducible results for the RESET was, however, difficult due to the presence of a unipolar switching mode, which is attributed to the presence of two switching modes, VCM and TCM, within the tested TaO_x-, ZrO_x-, and HfO_x/TiO_x-based devices. Kärkkaenen *et al.* have shown for ZrO_x-based devices that the LRS of the unipolar switching mode is metallic, while the LRS of the bipolar switching mode is semiconducting [91]. A list of unipolar and bipolar devices with metal oxides as active switching layer is given in [92].

1.2.3. Nonlinear switching kinetics of VCM devices

The voltages applied during the readout of the device's resistance are significantly lower, than the voltages applied during the SET and the RESET operations. This results in a need for a long data retention at low voltages and fast switching times at high voltages [93] (also referred to as *voltage-time-dilemma* [28]). Overcoming the voltage-time-dilemma can be realized with devices, which have a strong nonlinear dependence of the SET and RESET times on the applied voltage. It was shown that the SET time depends indeed strongly nonlinearly on the applied voltage in the broad range from 250 ps to 10^4 s [37]. A strong nonlinearity was also observed for the RESET kinetics [35, 94]. Consequently, it is possible to address the voltage-time-dilemma with VCM devices.

This strong nonlinearity in the SET and RESET kinetics results from the thermally accelerated drift of oxygen vacancies. This drift is facilitated by Joule heating occurring within the conductive filament during the SET and the RESET operation [80, 94, 95], which could also be observed experimentally [96–99]. An overview of the involved processes limiting the SET and RESET kinetics is given in [36, 56].

Two exemplary studies are shown in fig. 1.2. In the first study (see fig. 1.2a), a 2D *finite element model* (FEM) of a $SrTiO_3$-based VCM device was built. The results show that the strong nonlinearity of the SET kinetics origins mainly from the thermally accelerated drift of oxygen vacancies [80]. In the second study [95], a nanometer-sized heater was used to heat a TaO_x-based VCM device within 40 ns to temperatures up to 787 K. The SET kinetics were measured at different temperatures showing a strong acceleration of the SET time with increasing temperatures by almost 6 orders of magnitude, which supports the simulation results from [80].

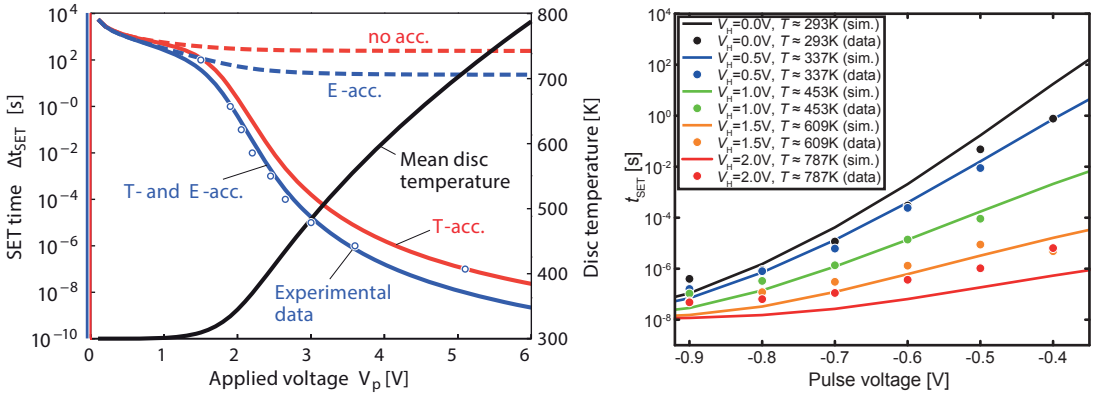

(a) Taken with permission from [80] © 2011 WILEY-VCH Verlag GmbH & Co. KGaA, Weinheim.

(b) Taken with permission from [95] © 2017 WILEY-VCH Verlag GmbH & Co. KGaA, Weinheim.

Figure 1.2.: Two studies of the thermal influence on the SET kinetics of VCM-based devices. In (a), a 2D FEM simulation model showed that the acceleration of the SET kinetics can only be explained by a temperature increase within the conductive filament. In (b), this temperature dependency could be proven experimentally.

At slow timescales (above 10 ns), both SET and RESET kinetics are limited by the temperature accelerated drift velocity of oxygen vacancies [80,94]. At faster timescales the capacitive charging (see section 1.4.2) and the heating of the filamentary region of the VCM devices become relevant [36] for the SET kinetics. It is shown in chapter 4.3 that for filamentary VCM devices the main limitation down to 50 ps origins from the capacitive charging [100].

1.3. High frequency domain

Measuring fast writing times requires fast signals, which comprise high frequencies (referred to as radio frequencies (RF)). High frequencies imply short electrical wavelengths, which becomes an issue, if the wavelength becomes shorter than the length of the considered transmission-line [101]. In this case, the voltage varies over the length of the transmission-line and is treated with the transmission-line theory, which is presented below. The phase velocity and the skin depth are also elucidated, as they are relevant for the thesis at hand. Later in this section, the relevance of this theory for experiments on VCM devices in the RF frequency range is elucidated and the definition of the scattering parameters is given at the end. The argumentation in this section is based on [101].

The Maxwell's equations are of crucial importance for applications in the RF regime, as they yield the solution for the propagation of electromagnetic waves in different media. Consequently, RF signals can also be described by waves. The Maxwell's equations also yield the solution of the phase velocity and the skin depth. The phase velocity, v_p, is defined as the speed, with which an electric field propagates through a medium:

$$v_\mathrm{p} = \frac{c}{\sqrt{\epsilon_r \mu_r}}. \tag{1.1}$$

Here, c is the speed of light, ϵ_r the relative permittivity and μ_r the relative magnetic permeability of the considered medium. As the inner conductor of a cable is surrounded by a nonmagnetic dielectric, the relative permeability can be approximated as one $\mu_r \approx 1$. The relative permittivity of the cables' dielectric amounts to $\epsilon_r = 1.7$ [102]. According to eq. 1.1 this results in a phase velocity of $v_\mathrm{p} = 2.30 \cdot 10^8\,\mathrm{m/s}$, which corresponds to about 3/4 of the speed of light c.

The skin depth, δ_s, is defined as the depth, at which the amplitude of a signal is attenuated by a factor of e^{-1}. It is described by

$$\delta_\mathrm{s} = \sqrt{\frac{2}{\omega \mu \sigma}}, \tag{1.2}$$

in which ω is the angular frequency, $\mu = \mu_r \mu_0$ the permeability of the conductor, μ_r its relative permeability, μ_0 the vacuum permeability, and σ the electrical conductivity of the conductor.

In this thesis, the conductors consist of Pt, which is not magnetic ($\mu_r = 1$) and has a high electric conductivity of $\sigma = 9.52 \cdot 10^6\,\mathrm{S/m}$ at 20 °C [103]. According to eq. 1.2, this results in a skin depth of $\delta_\mathrm{s} = 816\,\mathrm{nm}$ at a frequency of 40 GHz.

1.3.1. Transmission-line theory

A transmission-line can be separated in infinitesimal pieces Δz with a series resistance per unit length R, a series inductance per unit length L, a shunt conductance per unit length G, and a shunt capacitance per unit length C. All these quantities are illustrated in fig. 1.3. The incoming signal is characterized by its voltage $v(z,t)$ and its current $i(z,t)$, which depend on the location in the transmission-line z and on the time t. By means of the Kirchhoff's laws, two differential equations can be derived:

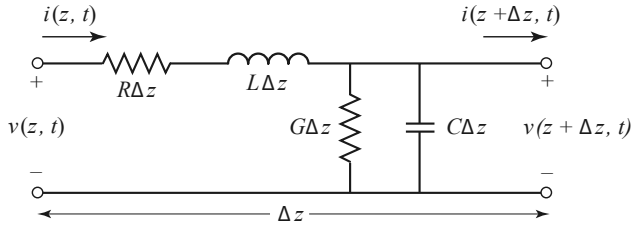

Figure 1.3.: Infinitesimal piece Δz of a transmission-line. The quantities are described in the main text. Taken with permission from [101] © 2012, 2005, 1998 by John Wiley & Sons, Inc. All rights reserved.

$$v(z,t) - R\Delta z i(z,t) - L\Delta z \frac{\partial i(z,t)}{\partial t} - v(z+\Delta z, t) = 0, \tag{1.3}$$

$$i(z,t) - G\Delta z v(z+\Delta z,t) - C\Delta z \frac{\partial v(z+\Delta z,t)}{\partial t} - i(z+\Delta z,t) = 0. \tag{1.4}$$

By dividing these equations by Δz and approaching Δz as close to zero, the *telegrapher's equations* can be derived:

$$\frac{\partial v(z,t)}{\partial z} = -Ri(z,t) - L\frac{\partial i(z,t)}{\partial t} \tag{1.5}$$

$$\frac{\partial i(z,t)}{\partial z} = -Gv(z,t) - C\frac{\partial v(z,t)}{\partial t} \tag{1.6}$$

These equations are solved explicitly in [101] by using sinus-shaped signals for $v(z,t)$ and $i(z,t)$ with an angular frequency ω and an amplitude of V and I, respectively. Only relevant solutions for the thesis at hand are shown. This is for once the equation of the *characteristic impedance*, Z_0, of a transmission-line:

$$Z_0 = \sqrt{\frac{R + j\omega L}{G + j\omega C}}, \tag{1.7}$$

and if the transmission-line is terminated by a load impedance of Z_L, the equation for the *reflection coefficient*, Γ:

$$\Gamma = \frac{v^-(t)}{v^+(t)} = \frac{Z_\mathrm{L} - Z_0}{Z_\mathrm{L} + Z_0}, \tag{1.8}$$

in which $v^+(t)$ represents the incoming voltage and $v^-(t)$ the reflected voltage. This solution shows the importance of proper impedance matching of $Z_0 = 50\Omega$ at every connection in the experimental setup, as improper impedance matching would yield reflections of the incoming signal.

These two equations are of high importance, as they help to estimate the voltage that is effectively applied to the device under test (DUT), which is in this thesis always a VCM device. The voltage at the device V_DUT is given by the sum of the incoming and reflected voltage. By inserting eq. 1.8 for $v^-(t)$, it can be shown that $V_\mathrm{DUT}(t)$ also depends strongly on Z_L and Z_0:

$$V_\mathrm{DUT}(t) = v^+(t) + v^-(t) = 2v^+(t)\frac{Z_\mathrm{L}}{Z_\mathrm{L} + Z_0}. \tag{1.9}$$

This solution will be used in the following sections to estimate V_DUT.

1.3.2. Experimental approaches

Most studies on the kinetics of VCM devices use pulse generators and cables with an impedance of $Z_0 = 50\Omega$. VCM devices, however, have higher resistances, even in the LRS ($Z_\mathrm{L} > 1\mathrm{k}\Omega$). In this case ($Z_\mathrm{L} \gg Z_0$), eq. 1.8 simplifies to $\Gamma = 1$, meaning that the entire

signal at the device is reflected. According to eq. 1.9 the voltage at the device is twice the voltage of the incoming voltage $V_{\mathrm{DUT}}(t) = 2v^{+}(t)$.

After the pulse reaches the DUT, its reflection propagates from the DUT back to the pulse generator. The time it takes, for the pulse to propagate from the pulse generator to the DUT is referred to as t_{Setup}:

$$t_{\mathrm{Setup}} = \frac{l_{\mathrm{Cable}}}{v_{\mathrm{p}}}. \tag{1.10}$$

Here, l_{Cable} is the cable length. If the pulse width is twice as long as t_{Setup}, the incoming and reflected pulse superimpose at every point in the cables and the voltage, consequently, amounts to twice the adjusted voltage.

By assuming a cable length of $l_{\mathrm{Cable}} = 1\,\mathrm{m}$ and using the permittivity of the used cables $\epsilon_r = 1.7$ [102], eq. 1.1, and eq. 1.10, t_{Setup} amounts to 4.35 ns. Kinetic measurements on VCM devices can, therefore, be separated into two time regimes: A slow regime, in which the kinetics above 10 ns ($2t_{\mathrm{Setup}} \approx 10\,\mathrm{ns}$) are investigated and a fast regime, in which the kinetics below 10 ns are investigated.

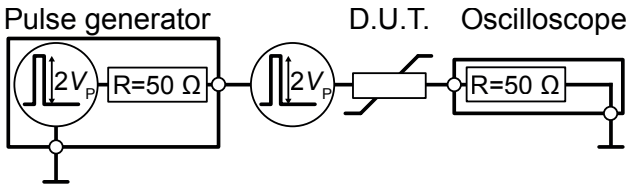

(a) Only DUT connected.

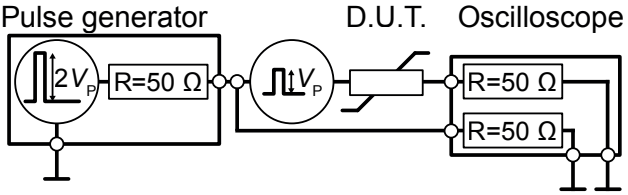

(b) DUT and 50Ω input of the oscilloscope connected.

Figure 1.4.: Setups used in the slow regime.

In case of the slow regime, it is possible to calculate voltages and currents at the device with direct current (DC) rules. As most pulse generators and oscilloscopes have 50Ω connectors, one can assume their internal resistance to 50Ω (see fig. 1.4a). Internally, the generated voltage corresponds to twice the adjusted voltage by the user (V_{P}). In case of a load resistor with 50Ω connected to the pulse generator, this would constitute a voltage divider with two 50Ω-resistors. Consequently, half of the internally generated voltage ($2V_{\mathrm{P}}$) would drop over the device ($V_{\mathrm{DUT}} = V_{\mathrm{P}}$). The DUT, however, has a much higher resistance ($R_{\mathrm{DUT}} \gg 50\Omega$) and, therefore, the internally generated voltage ($2V_{\mathrm{P}}$) drops entirely over the device ($V_{\mathrm{DUT}} = 2V_{\mathrm{P}}$). Kinetic studies using this approach are taking this factor of two into account [104, 105].

Other studies investigating the switching kinetics of VCM devices in the slow regime, split the signal after the 50Ω output of their pulse generator in two (see fig. 1.4b) [40, 80, 106, 107]. This approach is also used for studies on PCM devices [107]. One end is connected directly to a 50Ω input of the oscilloscope. Thereby, the external resistance amounts to 50Ω and only half of the internally generated voltage ($2V_P$) drops over the device ($V_{DUT} = V_P$). The measured voltage at the oscilloscope ($V_{Osc.}$) corresponds to the voltage at the DUT ($V_{Osc} = V_P$). The other end is connected to the device, which is connected to another 50Ω input of the oscilloscope. Both approaches of the slow regime are summarized in table 1.1. In the fast regime, the DC rules do not apply anymore. Here, the equations of section 1.3.1 are applicable. Similar to above, the impedance of the pulse generators and oscilloscopes is 50Ω. Also, all components (cables, connectors, etc.) have a characteristic impedance of 50Ω and, therefore, provide proper impedance matching. As the DUT has a high resistance, almost the entire signal is reflected, and the voltage of the signal doubles at the DUT.

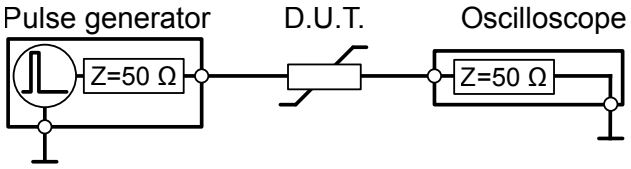

(a) Only DUT connected.

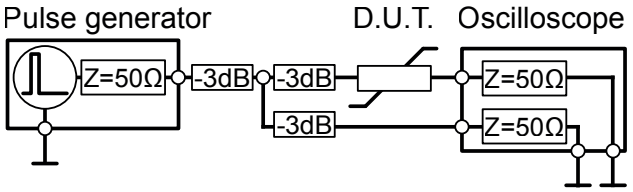

(b) DUT and 50Ω input of oscilloscope connected.

Figure 1.5.: Setups used in the fast regime.

If the DUT is connected directly to the pulse generator (see 1.5a), the voltage at the DUT is, consequently, twice the voltage emitted by the pulse generator ($V_{DUT} = 2V_P$). Studies using this approach, therefore, indicate twice the pulse voltage of their pulse generators in their results [32, 37, 108, 109].

Another approach is again, to split the signal after the output of the pulse generator and to connect one end to the oscilloscope (see 1.5b) [32–34, 37, 39, 110, 111]. The pulses emitted at the two outputs of the power splitter have only half of the amplitude as the incident pulse. This corresponds to an attenuation of approx. -6 dB. The other end is connected to the DUT, which is also connected to the oscilloscope. Again, the voltage of the pulse doubles at the DUT. As this signal was halved at the splitter, the voltage at the DUT corresponds to the voltage of the emitted pulse ($V_{DUT} = V_P$). Different to the slow regime, the voltage sampled at the oscilloscope after the splitter corresponds only to $V_{Sample} = {}^{V_P}/_2$. Both approaches of the slow regime are summarized in table 1.1.

Table 1.1.: Summary of V_{DUT} and $V_{\mathrm{Osc.}}$.

	slow regime		fast regime	
Channels	1	2	1	2
V_{DUT}	$2V_{\mathrm{P}}$	V_{P}	$2V_{\mathrm{P}}$	V_{P}
$V_{\mathrm{Osc.}}$	-	V_{P}	-	$V_{\mathrm{P}}/2$

Capacitances and inductances in cables also influence the pulses emitted from the pulse generator. Consequently, the applied signal to the device varies from the emitted one. At every connection a part of the signal is reflected and does not reach the device. Consequently, every component used in the RF circuit should be chosen carefully. *E. g.* a 2.92 mm adapter causes already a loss of about -0.5 dB at a frequency of 40 GHz [112], which corresponds to a loss of 5.6 %. Also, cables usually have a loss between 2 dB/m and 3 dB/m at a frequency of 40 GHz [102], which corresponds to a loss between 20.6 %/m and 29.6%/m. The number of interconnects should, therefore, be minimized and short cables should be used. All RF components used in this thesis are optimized for 40 GHz.

Coplanar waveguides (CPWs)

To minimize the impedance mismatch between the contact pads of the samples and the probes, CPW structures are used, in which the device is incorporated [32, 38, 108]. They consist of three parallel metallic stripes (see fig. 1.6a). The inner stripe (S) conducts the signal and the two outer stripes (G) are grounded. The advantages of CPWs are their CMOS (Complementary metal-oxide-semiconductor) compatibility [113] and their broad bandwidth from DC to more than 100 GHz [114]. Their characteristic impedance, Z_0, depends on the relative permittivity, ϵ_{r}, of the substrate and on the geometry of the CPW structure, such as the width, w, of the inner conductor, the spacing, s, between the inner and the outer conductors and the thickness, h, of the substrate [115].

If the three metallic stripes were completely in air, the solution of the Laplace equation would yield transversal electromagnetic modes (TEM) [101, 116]. This means that the components of the electric and magnetic field parallel to the magnetic stripes are zero. The derivation is shown in detail in [101]. If the substrate is considered, the solution changes as the modes in the air (above the stripes) have a different relative permittivity than the ones in the substrate (below the stripes) and they are, therefore, referred to as quasi-TEMs (see fig. 1.6b).

1.3.3. Scattering parameters

Scattering parameters, S_{ij}, describe the transmission and the reflection of an incoming signal $v_i^+(t)$ at port i of a network [101]. The emitted signal at port i is referenced to as $v_i^-(t)$. The case $i \neq j$ describes the transmission from port j to i and the case $i = j$ the reflection

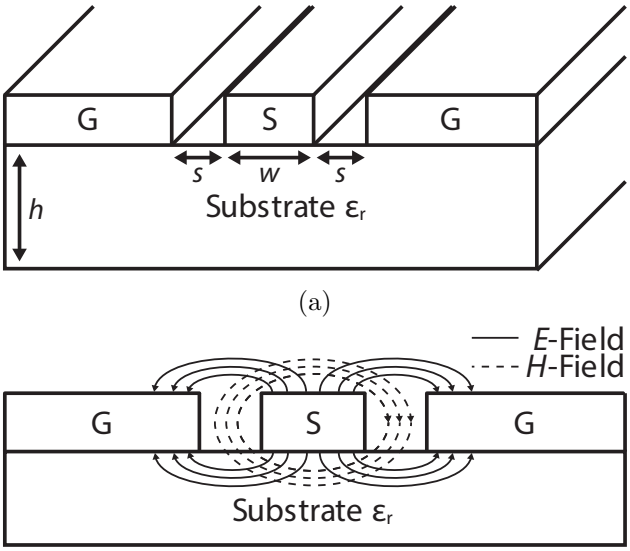

(a)

(b) Electric (solid lines) and magnetic fields (dashed lines) in the CPW structure.

Figure 1.6.: (a) Sketch of a CPW structure. (b) Electric (solid lines) and magnetic fields (dashed lines) within the CPW structure.

at port i. The scattering parameters $S_{ij}(f)$ are frequency dependent and indicate in case of $S_{ij}(f) > 1$ the gain or in case of $S_{ij}(f) < 1$ the attenuation of the signal's components at a frequency, f.

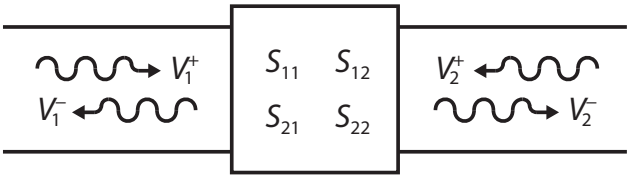

Figure 1.7.: Conventions of the scattering parameters.

The scattering parameters, $S_{ij}(f)$, the inputs, $V_i^+(f)$, and the outputs, $V_i^-(f)$, of the network are defined in the frequency-domain and are complex. $V_i^+(f)$ and $V_i^-(f)$ can be derived by building the Fourier transformations of the incoming signals, $V_i^+(f) = \mathcal{F}(v_i^+(t))$, or of the transmitted or reflected signals, $V_i^-(f) = \mathcal{F}(v_i^-(t))$, which are defined in the time-domain.

The scattering matrix of an n-port network is defined as:

$$\begin{pmatrix} V_1^- \\ \vdots \\ V_n^- \end{pmatrix} = \begin{pmatrix} S_{11} & \dots & S_{1n} \\ \vdots & \ddots & \vdots \\ S_{n1} & \dots & S_{nn} \end{pmatrix} \cdot \begin{pmatrix} V_1^+ \\ \vdots \\ V_n^+ \end{pmatrix}. \tag{1.11}$$

For a two port network (which is a ReRAM device with two contacts) the scattering matrix simplifies to:

$$\begin{pmatrix} V_1^- \\ V_2^- \end{pmatrix} = \begin{pmatrix} S_{11} & S_{12} \\ S_{21} & S_{22} \end{pmatrix} \cdot \begin{pmatrix} V_1^+ \\ V_2^+ \end{pmatrix}. \tag{1.12}$$

During kinetic measurements the pulses are only applied to one contact of a DUT and, therefore, the second component of the incoming signal can be neglected ($V_2^+ = 0$). Consequently, only two components of the scattering matrix in eq. 1.12 are relevant, which are the forward reflection S_{11}

$$S_{11} = \left.\frac{V_1^-}{V_1^+}\right|_{V_2^+=0} \tag{1.13}$$

and the forward transmission S_{21}

$$S_{21} = \left.\frac{V_2^-}{V_1^+}\right|_{V_2^+=0}. \tag{1.14}$$

If these two scattering parameters are known, it is possible to calculate the reflection $v_1^-(t)$ and the transmission $v_2^-(t)$ of the incoming signal $v_1^+(t)$, by using the inverse Fourier transformation of $V_1^-(f)$ and $V_2^-(f)$:

$$v_1^-(t) = \mathcal{F}^{-1}(V_1^-(f)) \tag{1.15}$$

$$v_2^-(t) = \mathcal{F}^{-1}(V_2^-(f)) \tag{1.16}$$

This approach is used in chapter 2.2.2 to derive the time-dependent-voltage at the device $V_{\mathrm{DUT}}(t)$, which is the sum of the incoming $v_1^+(t)$ and the reflected signal $v_1^-(t)$, as stated by eq. 1.9. The measurement technique to determine the scattering parameters is explained in chapter 2.1.3.

1.3.4. Fourier transformation of a square pulse

During measurements of the switching kinetics of VCM devices, usually square pulses are applied to the device. Calculating the effective voltage at the device requires the Fourier transformation of the applied pulse, as explained in chapters 1.3.3 and 2.2.2. The analytic deviation of a square pulse is, therefore, shown in the following. The argumentation is based on [117].

An ideal square pulse, $x(t)$, with a width, T, can be defined as

$$x(t) = \begin{cases} 1 & |t| \leq T/2 \\ 0 & |t| > T/2 \end{cases}. \tag{1.17}$$

The Fourier transformation of $x(t)$ results in

$$\begin{aligned}\mathcal{F}(x(t))(f) &= \frac{1}{\sqrt{2\pi}} \int_{-\infty}^{\infty} x(t) e^{-\mathrm{i}ft}\,\mathrm{d}t \\ &= \frac{1}{\sqrt{2\pi}} \int_{-T/2}^{T/2} e^{-\mathrm{i}ft}\,\mathrm{d}t \\ &= \frac{1}{\sqrt{2\pi}} \left.\frac{e^{-\mathrm{i}ft}}{-\mathrm{i}f}\right|_{-T/2}^{T/2} \\ &= \frac{1}{\sqrt{2\pi}} \frac{e^{\frac{-\mathrm{i}fT}{2}} - e^{\frac{\mathrm{i}fT}{2}}}{-\mathrm{i}f} \\ &= \sqrt{\frac{2}{\pi}} \frac{\sin\left(\frac{fT}{2}\right)}{f}. \end{aligned} \tag{1.18}$$

The sinus shaped form of $\mathcal{F}(x(t))(f)$ can be seen in fig. 2.15b in chapter 2.2.2, in which the discrete Fourier transformation of a 10 ns square pulse is shown.

1.4. Electrical charging time of VCM devices

The voltage at the VCM device is not only influenced by cables, probes and connectors and other components of the RF circuit. It is mainly influenced by the CPW structure and the VCM device's stack. VCM devices are usually fabricated on an oxidized Si wafer. This results in an fringing capacitance with the metallic stripes of the CPW structure as top electrode, SiO_2 as dielectric and Si as bottom electrode (see fig. 1.6b). To minimize the capacitive currents, the employed Si wafers have a high resistivity of up to $\rho > 10\,\mathrm{k\Omega cm}$ [37]. Increasing the thickness of the SiO_2 and shortening the length of the CPW structure also reduces the capacitance, which is shown in chapter 3.

For VCM devices also the vertical layer stack constitutes a capacitor. Both top and bottom electrode are metallic and the transition metal oxide in the center has dielectric properties. As shown in chapter 3.2.4, it can take several nanoseconds to fully charge a VCM device. Optimizing the integration of the VCM device into a CPW structure is, consequently, equally important for the experiment as choosing a pulse generator with fast rise times. This optimization was addressed in the framework of this thesis and the resulting recommendations are summarized in chapter 3.3.

1.4.1. Other works

That the charging of capacitances limits the measurable switching time was already shown in previous studies, which are summarized in the following. Lu *et al.* have developed a complex circuit-based simulation model, which compromises several capacitances, resistances and also the leads' inductances of a HfO_x-based VCM device [118]. From their simulation,

they could estimate the effectively applied voltage to the VCM device. They also conducted experiments in which they compared the SET and RESET kinetics of differently sized VCM devices. As the VCM devices size scales with its capacitance, they could study the influence of the capacitance on the SET and RESET kinetics. Their results indicate that the SET and RESET times are mainly limited by the capacitance of the VCM device's stack. In chapter 4.1, the SET times of differently sized VCM devices are compared, but on a much faster timescale. The shortest SET and RESET times observed in [118] amount to 100 ns, while in this thesis, they amount to 50 ps (see chapter 4 and 5). In chapter 3.2.4, the electrical charging time is estimated by using the scattering parameters to determine the rise time of VCM devices. A similar approach was used in the model of Torrezan *et al.*, to reproduce the VCM device's current response. They measured its scattering parameters up to a frequency of 20 GHz and developed a circuit-based simulation model [32]. The simulated scattering parameters matched the experimental ones well. With this model, they also calculated the effective voltage at the device. However, they did not draw any conclusion on the electrical charging time.

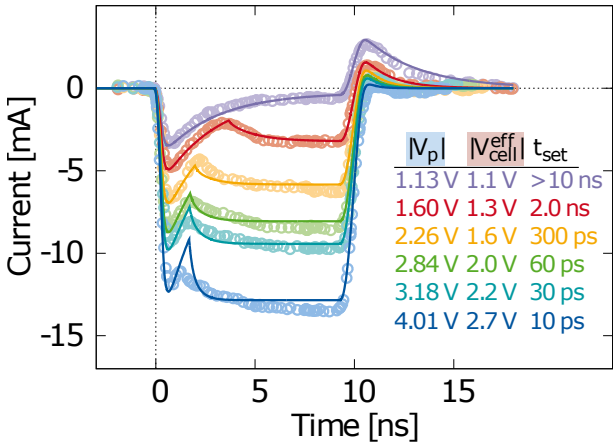

Figure 1.8.: Resulting current response of the LT Spice model used in [119] and the derived effective voltages. Taken from [119].

In the framework of this thesis an LT spice-based simulation model of a TaO_x-based VCM device was built and the results are published in [119]. The simulated current responses matched the experimental ones well and also the effective voltage at the device could be extracted. The results showed that it takes more than 2 ns to fully charge the device (see fig. 1.8). Later in this thesis, the effective voltage was determined purely experimentally with the scattering parameters of the VCM devices. This method provides several advantages, as explained in chapter 2.2.2.

1.4.2. Measures for electrical charging time

Several measures for the electrical charging time exist. A simple measure is the RC time τ_{RC}. Here, a circuit with a resistance, R, and a capacitance, C, in series is assumed. Both, R and

C can be measured, as it has been done in [37,38] or estimated, *e.g.* by calculating C using the formula of a parallel plate capacitor. It is defined as the time until the voltage reaches $1 - \exp(-1)$ or 63.2 % of its maximum. Other measures for the electrical charging time are the rise time (20 %-80 %) t_{80} and the rise time (10 %-90 %) t_{90}. The rise time t_{90} (t_{80}) is defined as the time, the voltage requires to reach 90 % (80 %) of the maximum voltage, starting from 10 % (20 %). Further measures for the rise time exist and are summarized in [120].

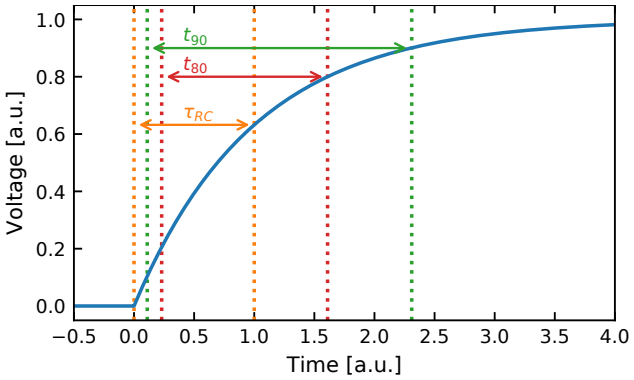

Figure 1.9.: Illustration of the electrical charging of a VCM device using eq. 1.19. The different measures of the electrical charging time are indicated with different colors: the RC time τ_{RC} in orange, the rise time (20 %-80 %) t_{80} in red, and the rise time (10 %-90 %) t_{90} in green.

To illustrate these measures, a simplified exponential function for the effective voltage at the VCM device $V_{\mathrm{DUT}}(t)$ is assumed, which is similar to the observed electrical charging:

$$V_{\mathrm{DUT}}(t) = 1 - \exp\left(-\frac{t}{\tau_{RC}}\right), \tag{1.19}$$

in which t is the time and $\tau_{RC} = 1$ the normalized RC time. $V_{\mathrm{DUT}}(t)$ is plotted in fig. 1.9, along with the definitions of τ_{RC}, t_{80}, and t_{90}.

The RC time τ_{RC} is clearly the fastest measure for the electrical charging time. The rise time (20 %-80 %) t_{80} amounts to $1.38\tau_{RC}$ and t_{90} amounts to $2.20\tau_{RC}$. As it takes forever for eq. 1.19 to reach 100 %, t_{90} seems to be the most reasonable measure. τ_{RC} and t_{80} are far shorter and, therefore, suggest short charging times. Therefore, t_{90} is used throughout this thesis.

2. Experimental Methods

This chapter summarizes all experimental procedures and evaluation methods, which will be used in the following chapters. It also presents improvements of the experimental setup, which were implemented in the framework of this thesis. This is mainly the automation of the kinetic measurements and their evaluation, which has become possible with a broadband bias tee. It could be shown that this bias tee only decreases the amplitude of the transmitted voltage pulse by less than 0.35 % and also its impact on the measured resistance is low. Finally, an approach is presented in detail with which the effective voltage at the device can be determined by using the scattering parameters.

2.1. Experimental setup

The state of the setup at the beginning of this thesis is described in [121]. It consists basically of an oscilloscope, a pulse generator, and a DUT, which was usually a VCM device. In this thesis, the pulse generator is always connected directly to the device as depicted in fig. 1.4a. A picture of the setup along with a simplified equivalent circuit is shown in fig. 2.1. The labels are listed below:

1. Tektronix DPO73304D oscilloscope [122]
2. Picosecond Pulse labs 2600C pulse generator [123]
3. Sympuls PG5 pulse generator
4. HP 8722ES VNA [124]
5. Cascade Microtech EPS150RF probe station
6. Cascade Microtech RPP210-S/100TPI probe positioners
7. Motic PSM 1000 Microscope
8. Cascade Microtech Z40-X-GSG-150 probes [125]
9. Newport vibration isolation platform VIP600
10. Computer controlling pulse generator and the oscilloscope
11. Operating components of the computer

The Tektronix DPO73304D oscilloscope (violet 1 in fig. 2.1) has a bandwidth of $F_{\mathrm{Osc}} = 33\,\mathrm{GHz}$ and a sampling rate of $f_{\mathrm{S}} = 100\,{}^{\mathrm{GS}}/_{\mathrm{s}}$ [122]. Its rise time (10 % to 90 %) T_{Osc} can be calculated from its bandwidth by $T_{\mathrm{Osc}} = {}^{0.339}/_{F_{\mathrm{Osc}}}$ and amounts to 10.3 ps [120]. The sampling time T_{S} of the oscilloscope can be calculated by $T_{\mathrm{S}} = {}^{1}/_{f_{\mathrm{S}}}$ and amounts to 10.0 ps

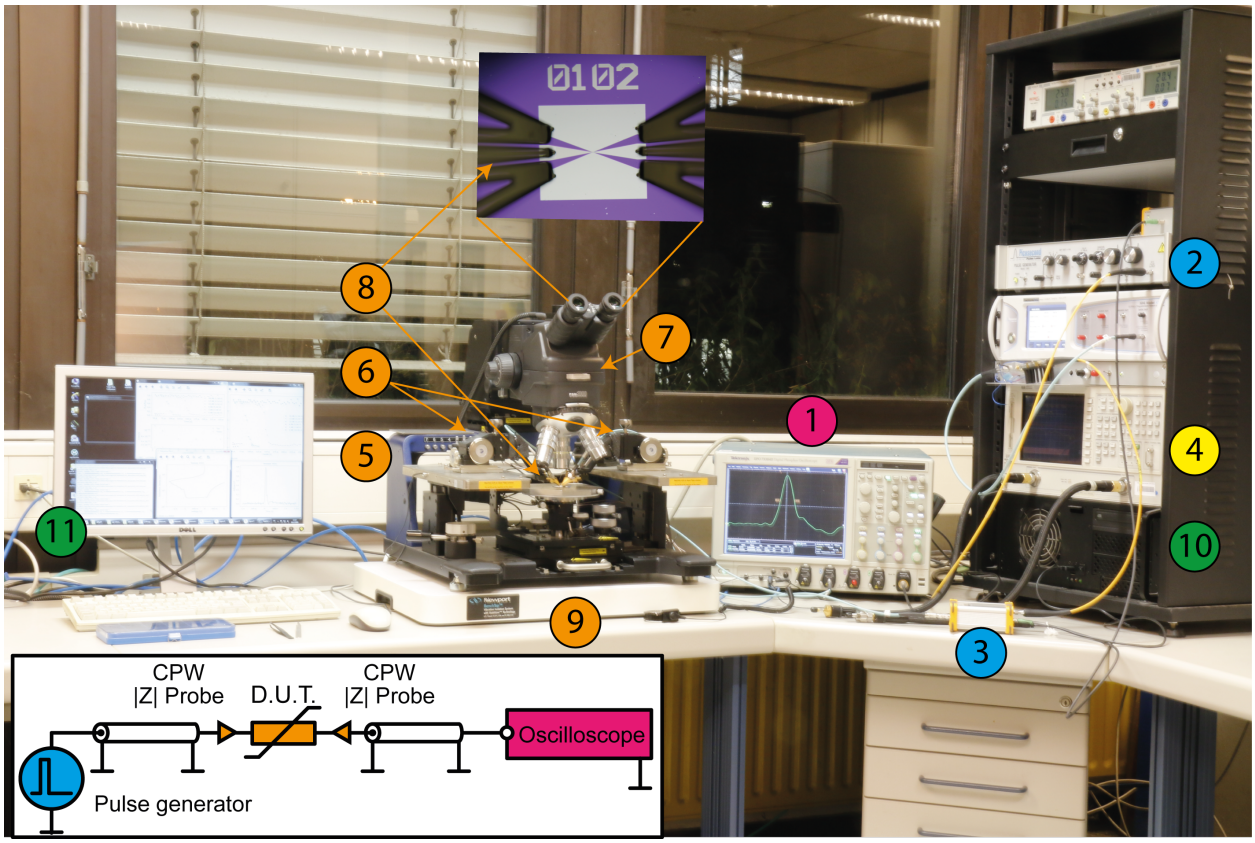

Figure 2.1.: Picture of the experimental setup. The labels are listed in the main text. The inset on the lower left is a simplified equivalent circuit of the experimental setup. The inset above the microscope shows the view through the microscope on a CPW structure. The picture of the setup was taken with the help of T. Pössinger. The picture of the CPW structure has been taken from [38], with the permission of AIP Publishing.

and is, therefore, suited to capture T_{Osc}. Calculating the rise times of the employed pulse generators requires T_{Osc}, as shown below. The higher sampling rate can also be seen as a result of the Nyquist–Shannon sampling theorem: to detect a signal with a frequency f, it needs to be measured at a sample rate, f_{S}, which is at least twice the signal's frequency ($f_{\mathrm{S}} \geq 2 \cdot f$) [126, 127].

All other passive components (cables, attenuators, probes, and adapters) have a bandwidth of 40 GHz. The HP 8722ES VNA (yellow 4) is used to measure the scattering parameters in the range between 50 MHz and 40 GHz (see section 2.1.3) [124]. The devices are connected via GPIB and USB to a computer (green 10 and 11) and are controlled with the software *py-ivtools*[1]. The oscilloscope and the pulse generator PG5 were integrated into this software in the framework of this thesis.

Probing system

The sample is connected with a Cascade Microtech EPS150RF probe station (orange 5 in fig. 2.1). All other components of the probing system are labeled in orange in fig. 2.1. The

[1]Source code at `https://git.rwth-aachen.de/hennen/py-ivtools/-/tree/Witzleben`

probe station is placed on a vibration isolation platform (Newport VIP600, orange 9) to avoid disturbances resulting from vibrations in the laboratory. The RF cables are connected to the device with RF probes (Cascade Microtech Z40-X-GSG-150 probes, orange 8), which also have a bandwidth of 40 GHz [125]. They are controlled with two Cascade Microtech RPP210-S/100TPI probe positioners (orange 6). The microscope Motic PSM 1000 (orange 7) has lenses with a magnification of 5x, 10x, and 20x. The view through the microscope onto a sample with connected RF probes is shown in the inset of fig. 2.1. On the platform four additionally Süss Microtech micromanipulators with DC probes are placed, to which a source measure unit (SMU) can be connected. This allows for precise resistance measurements of the DUT.

Pulse generators

Two different pulse generators are used in this thesis (blue 2 and 3 in fig. 2.1). The pulse generator PSPL2600C (blue 2) can emit single electrical pulses with an amplitude of up to 50 V [123]. The polarity can be chosen and the amplitude is adjusted with a manual discrete attenuator. The pulse width can also be adjusted between 550 ps and 100 ns. The rise time (10 % - 90 %) amounts to 359 ps. Two exemplary pulses are shown in fig. 2.2: (a) One with the shortest possible pulse width of 550 ps and an amplitude of 1.00 V and (b) one with the longest possible pulse width of 100 ns and an amplitude of 0.67 V.

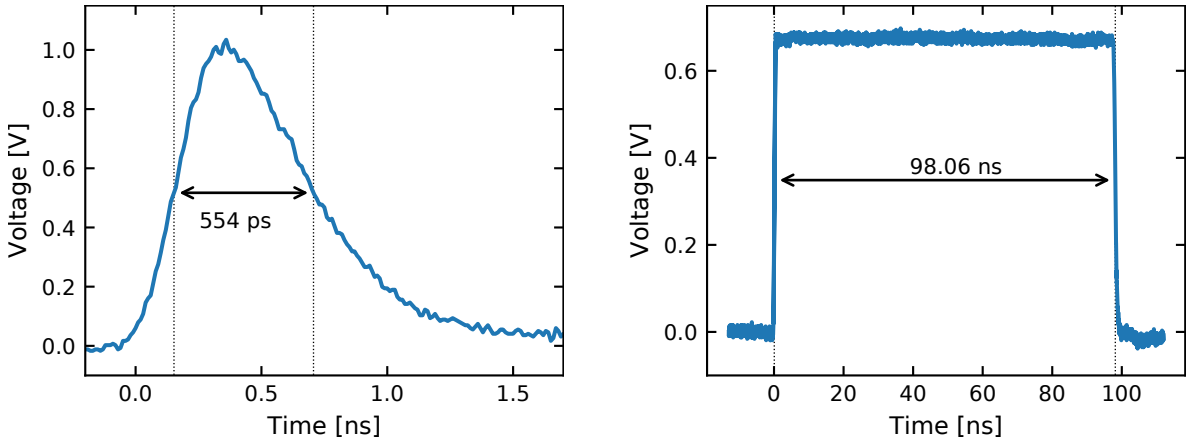

(a) 550 ps pulse.

(b) 100 ns pulse.

Figure 2.2.: Exemplary pulses emitted by the pulse generator PSPL 2600C with a pulse width of (a) 550 ps and (b) 100 ns.

The pulse generator PG5 (blue 3 in fig 2.1) was purchased in the framework of this thesis. It was fabricated by the SYMPULS GmbH and has been optimized for kinetic measurements. It can generate pulses with a fixed amplitude of 5.0 V and has an adjustable pulse width between 50 and 250 ps. Its rise time amounts to 34.5 ps. Exemplary pulses with a width of 50 ps and 250 ps are shown in fig. 2.3. The measurement was conducted by the SYMPULS

GmbH with an Agilent 86100B oscilloscope, equipped with a remote sampling head 86118A, providing a bandwidth of 70 GHz.

To control the pulse amplitude, fixed attenuators from Api technologies with a bandwidth of 40 GHz are placed at the output of the PG5 pulse generator [128]. The pulse voltage after the attenuator V_P is defined as

$$V_P = 5\,V \cdot 10^{-\frac{A[\mathrm{dB}]}{20\,\mathrm{dB}}}, \tag{2.1}$$

in which A is the attenuation in dB. The available attenuators along with the resulting V_P are summarized in tab. 2.1. As explained in chapter1.3.1 and 1.3.2, the voltage of the pulse doubles at the DUT and is referred to as effective pulse voltage, $V_{P,\mathrm{eff.}}$, which is also listed in tab. 2.1.

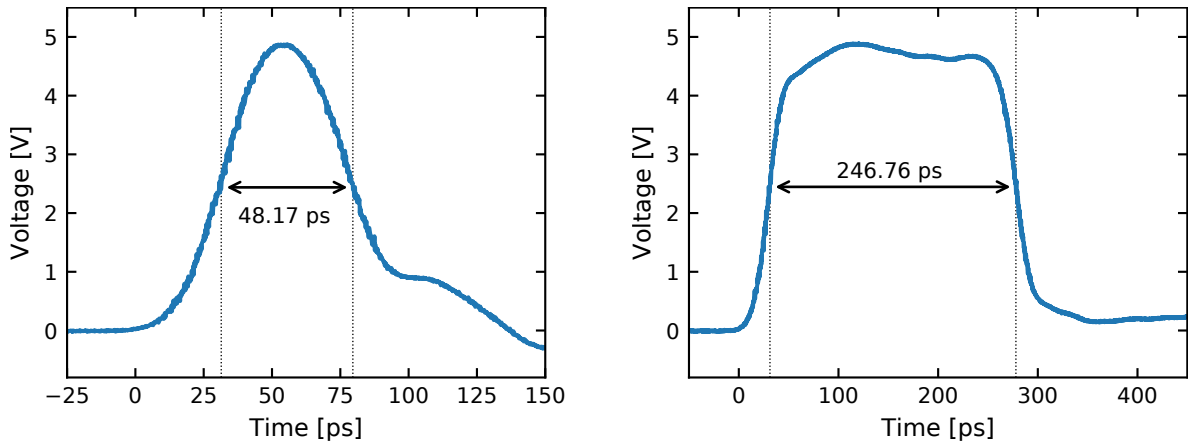

(a) 50 ps pulse.

(b) 250 ps pulse.

Figure 2.3.: Exemplary pulses emitted by the pulse generator Sympuls PG5 with a pulse width of (a) 50 ps and (b) 250 ps. Measurement conducted by Sympuls Aachen GmbH.

Table 2.1.: List of the attenuators connected to the pulse generator PG5 and corresponding voltages.

Attenuation [dB]	V_P [V]	$V_{P,\mathrm{eff.}}$ [V]
0	5.00	10.00
3	3.54	7.07
6	2.51	5.01
9	1.77	3.54
10	1.58	3.16
13	1.12	2.24
16	0.79	1.58
19	0.56	1.12
20	0.50	1.00

Rise times of the pulse generators

The rise times of the pulse generators are determined from the measured pulses shown above. In case of the PSPL 2600C the 100 ns pulse (see fig. 2.2b) and in case of the PG5, the 250 ps pulse (see fig. 2.3b) is used. As the sampling time of the oscilloscope amounts to 10.0 ps, the time and voltage arrays were interpolated with a spline function to a 0.1 ps timescale to achieve more precise results of the rise time. Subsequently, the time the voltage requires to reach 90 % of the maximum voltage (starting from 10 %) is determined and referred to as T_{maes}. It is defined as the square sum of all occurring rise times T_n in the system [120]:

$$T_{\mathrm{maes}} = \sqrt{\sum_{n=0}^{N} T_n^2}. \tag{2.2}$$

In case of a pulse generator directly connected to the oscilloscope, only the rise time of the pulse generator T_{PG} and the rise time of the oscilloscope, T_{Osc}, are relevant. Only short cables with 2.92 mm connectors (having a bandwidth of 40 GHz) were used and are, therefore, neglected in the calculation of the pulse generator's rise time, T_{PG}. The oscilloscope's rise time was already derived above and amounts to $T_{\mathrm{Osc}} = 10.3\,\mathrm{ps}$ (10 % - 90 %). In case of the PG5 pulse generator, T_{Osc} amounts to 4.84 ps, because its signal was measured with a 70 GHz oscilloscope. Consequently, T_{PG} can be calculated by

$$T_{\mathrm{PG}} = \sqrt{T_{\mathrm{maes}}^2 - T_{\mathrm{Osc}}^2}. \tag{2.3}$$

The resulting rise time, T_{PG}, of all three pulse generators is summarized in tab. 2.2. As expected, the PG5 pulse generator achieves the fastest rise time, which amounts to 34.5 ps. Additionally, the rise time[2] (20 % - 80 %) is shown. The pulse generator PSPL 2600C has a slower rise times of 359 ps. The rise time (20 % - 80 %) definition reaches significantly faster results for both pulse generators.

Table 2.2.: Rise times of the used pulse generators.

Pulse generator	Pulse width	T_{P} (10 % - 90 %)	T_{P} (20 % - 80 %)
PSPL 2600C	100 ns	359 ps	234.4 ps
PG5	250 ps	34.5 ps	17.8 ps

2.1.1. Kinetic measurements

In preliminary works, the SET kinetics of VCM devices were investigated in the time regime from 250 ps to 100 ns [37, 121, 129] and in the time regime from 10 ns to 10^5 s [81, 130–132]. Overall, the SET kinetics of a $15 \times 20\,\mu\mathrm{m}^2$ Ta\$\mathrm{TaO_x}$\Pt VCM device (which is later referred

[2]The rise time (20 % - 80 %) of the oscilloscope is $^{0.223}/_{F_{\mathrm{Osc}}} = 6.76\,\mathrm{ps}$ [120].

to as Ta1, see tab. 3.1) was measured from 250 ps to 10^5 s (see fig. 2.4) [37, 121, 129]. This corresponds to almost 15 orders of magnitude and proved that the VCM devices can overcome the voltage-time dilemma (see chapter 1.2.3). This measurement serves as example for the following explanation of kinetic measurements on VCM devices. The derivation of the SET time, t_{SET}, is explained in section 2.2.1.

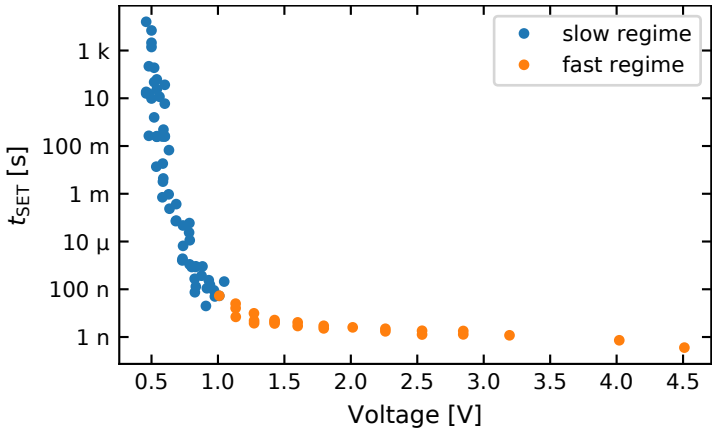

Figure 2.4.: SET kinetics of a Ta\TaO_x\Pt device. The blue points mark the slow regime and the orange points the fast regime. Data from [37].

The regime from 10 ns to 10^5 s is referred to as slow regime (blue points in fig. 2.4) [130]. In range from 10 ns to 10^5 s the kinetics are strongly nonlinear and follow an exponential function [37]. The regime from 250 ps to 10 ns is referred to as fast regime (orange points in fig. 2.4) [121]. Additional points in the fast regime were measured in the framework of this thesis to achieve a more continuous line at the intersection of both regimes. At about 20 ns, the curve flattens due to the presence of capacitances, which originate from the Ta\TaO_x\Pt stack and from the CPW structure. The origin of these capacitances is explained in chapter 1.4 and the influence of the capacitances on the SET kinetics is demonstrated in chapter 4 .

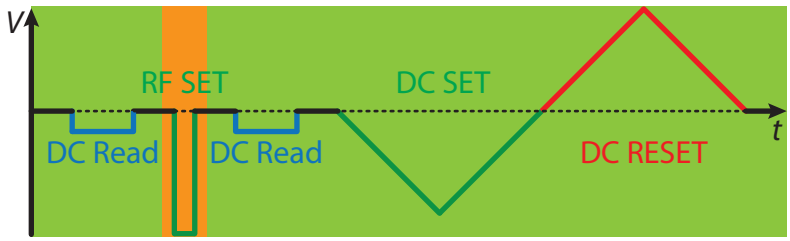

Figure 2.5.: Measurement cycle used in the fast regime. During the green shaded area the device is connected to the DC probes and during the orange shaded area to the RF probes.

The measurement cycle used in the fast regime is shown in fig. 2.5. All voltages are applied to the active Pt electrode of the Ta1 device, which is at the beginning in the HRS. Its resistance is measured with a Keithley 2636A SMU at a low voltage (in this thesis always at 0.2 V). During this read-out (labeled as blue DC Read in fig. 2.5) the Ta1 device is connected with the DC probes.

To apply a short pulse with the pulse generator PSPL 2600C, the Ta1 device is manually connected to the RF probes. The corresponding pulse is marked in green as RF SET. The width of the pulse is varied from 250 ps to 100 ns and its effective amplitude from -0.80 V to -4.5 V. The transmitted voltage was measured with the Tektronix DPO73304D oscilloscope.

Subsequently, the Ta1 device is again manually connected to the DC probes to repeat the resistance measurement. If the pulses amplitude was sufficiently high and its width sufficiently long, the device is now in the LRS. Also, intermediate states can occur [37, 121]. At low pulse amplitudes and short pulse widths, the Ta1 device is still in the HRS. Lastly, a DC sweep is conducted with the Keithley 2636A SMU. The sweep starts with a negative voltage (green DC SET), which brings the Ta1 device to the LRS. Afterwards, the Ta1 device is brought back to the initial HRS with a positive voltage (red DC RESET). The DC sweep also serves to test the functionality of the Ta1 device.

Two different probes had to be used during one measurement cycle. The part measured with the DC probes in the measurement cycle is shaded in green in fig 2.5 and the part measured with the RF probes is shaded in orange. Manually switching from the DC to the RF probes is time consuming and requires the presence of an operator. In the following section 2.1.2 an approach is presented, with which all parts of the measurement cycle can be conducted with the RF probes in an automated fashion.

2.1.2. Automation of kinetic measurements

Manually conducting the kinetic measurements is time-consuming and, consequently, prohibits the collection of comprehensive data sets. To automate the setup, all signals applied to the DUT during the measurement cycle (see fig. 2.5) need to be conducted with the RF probes, which provide the necessary bandwidth for measurements in the gigahertz regime. The measurements with the SMU were so far conducted with the DC probes. To connect both, the SMU and the pulse generator, to the RF probes, an RF switch could be used. This is, however, a hazardous operation, because an active element can also induce undesired electrical pulses. As VCM devices are very sensitive, these pulses could also switch or even destroy them.

An approach to connect an SMU and a pulse generator simultaneously to the RF probes by using a passive component was published in the framework of this thesis [38]. The setup of this approach is sketched in fig. 2.6. The passive component is a 40 GHz broad band bias tee (API 8810KFM3-40 [133]), which has three ports:

1. A direct current (DC) port, serving as low pass filter and blocking high frequency components. In the simplified equivalent circuit of fig. 2.6a a coil is placed at the DC port, having a high inductive reactance at high frequencies ($Z_\mathrm{L} \sim \omega L$).
2. An alternating current (AC) port, providing a low insertion loss below 3 dB in the frequency range from 50 kHz to 40 GHz [133]. Frequencies below 50 kHz are strongly

attenuated [133]. This is sufficient for the transmission of a 100 ns pulse, as its frequency content does not include frequencies below 1 MHz (as shown in fig. 2.15b). In the simplified equivalent circuit of fig. 2.6a, a capacitor is placed at the AC port, having a low capacitive reactance at high frequencies ($Z_C \sim {}^1/_{\omega C}$).

3. An AC + DC port, having a broad bandwidth from DC to 40 GHz, through which both, low and high frequencies, can be transmitted.

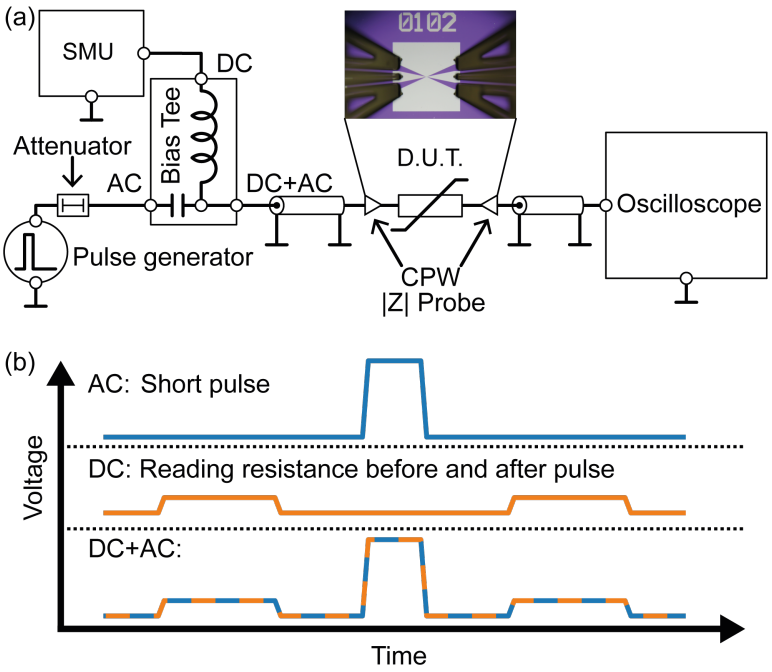

Figure 2.6.: (a) Sketch of the automatized setup. The inset is a picture of the RF probes connecting a VCM device. (b) Pulse sequence at the AC port (upper blue line), at the DC port (middle orange line), and at the combined DC + AC port. Adapted from [38], with the permission of AIP Publishing.

A typical measurement cycle is depicted in fig. 2.6b: the DUT is connected to the AC + DC port of the bias tee (see fig. 2.6a), the pulse generator to the AC port (upper blue line), and the SMU to the DC port (middle orange line). Consequently, the bias tee allows the application of short electrical pulses with a pulse generator and the precise determination of the DUT's resistance using the SMU. The combined signal at the AC + DC port is depicted as lower blue-orange dashed line.

The insertion loss of up to 3 dB at 40 GHz has an influence on the transmitted pulses. To determine this influence, pulses with a width of 50 ps and 250 ps, emitted by the PG5 pulse generator, were once directly measured with the oscilloscope and once transmitted through the bias tee, before they were measured with the oscilloscope. Each pulse was repeated 10,000 times to achieve a profound statistic. Subsequently, the full-width-half-maximum (FWHM) and the maximum voltage of each pulse is determined. For the FWHM's determination the measured voltage was interpolated to achieve more precise results. Otherwise, the precision

of the FWHM's result would be limited by the sampling time of the oscilloscope, which amounts to 10.0 ps as shown in section 2.1.

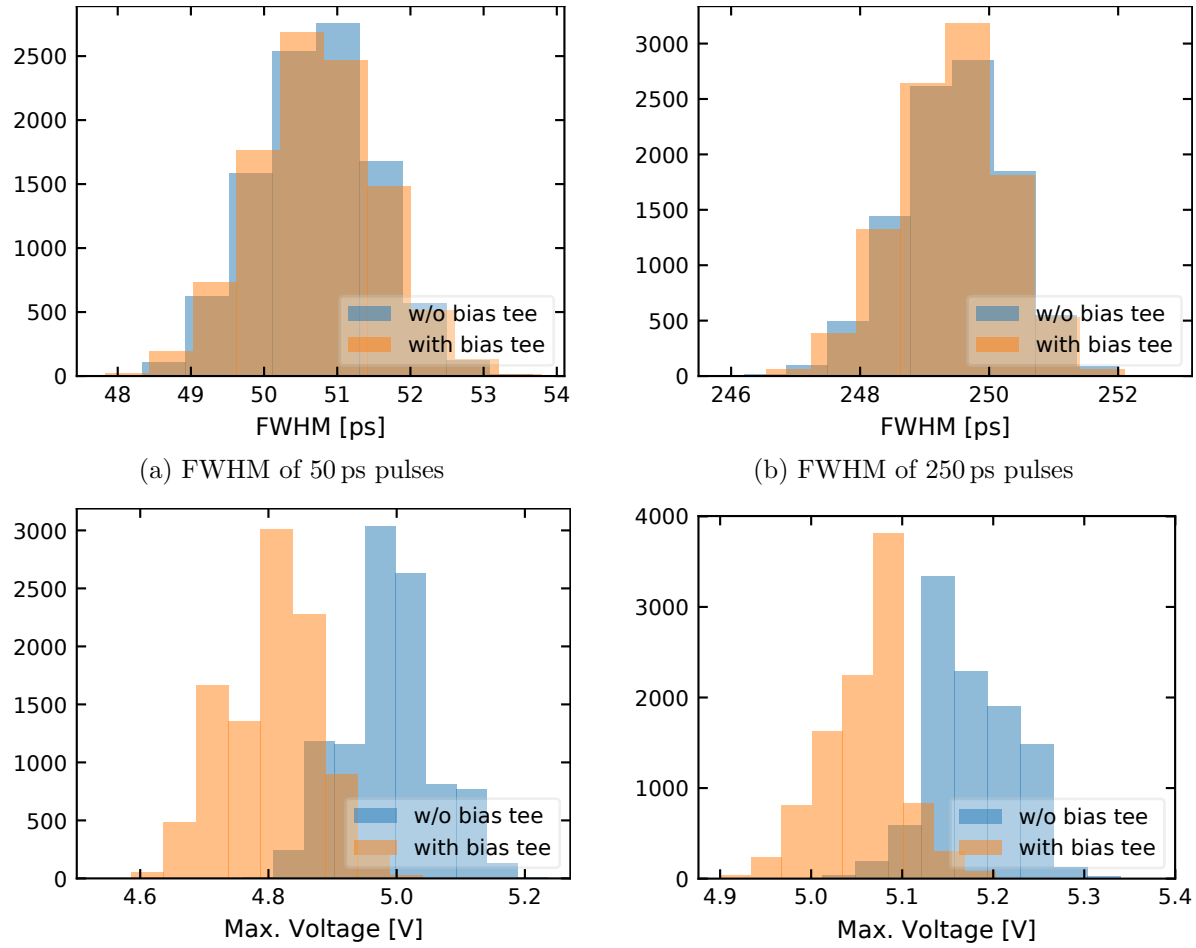

(a) FWHM of 50 ps pulses

(b) FWHM of 250 ps pulses

(c) Max. voltage of 50 ps pulses

(d) Max. voltage of 250 ps pulses

Figure 2.7.: (a) Measured FWHMs of 50 ps and (b) 250 ps pulses. (c) Measured maximum voltages of 50 ps and (d) 250 ps pulses. Blue curves correspond to the measurements without bias tee and orange curves to measurements with bias tee.

The resulting histograms are presented in fig. 2.7. The means and standard deviations of the FWHMs and maximum voltages are summarized in tab. 2.3. The distributions of the FWHMs of the 50 ps and 250 ps pulses are shown in fig. 2.7a and fig. 2.7b, respectively. In case of the 50 ps and the 250 ps pulses, the measured FWHM with and without bias tee is almost identical and is within one standard deviation. The bias tee has, consequently, no measurable influence on the FWHM.

The distributions of the measured maximum voltages of the 50 ps and 250 ps pulses are shown in fig. 2.7c and fig. 2.7d, respectively. In both cases, the bias tee shifts the distribution to lower voltages, which results from the insertion loss. The insertion loss is, however, low and amounts to 3.81 % in case of the 50 ps pulses and to 2.32 % in case of the 250 ps pulses. This corresponds to an attenuation of less than 0.35 dB in both cases, which is negligible compared to other losses. For example, the insertion loss of the cables amounts to 2.52 $^{\mathrm{dB}}/_{\mathrm{m}}$

at 40 GHz [102]. The low dependency of the FWHM results from the flat dependency of the insertion loss on the frequency, which is depicted in the data sheet of the bias tee [133]. For the kinetic measurements the preservation of the FWHM is more important than the loss in pulse amplitude.

Table 2.3.: Calculated means and standard deviations of the FWHM and maximum voltage values from fig. 2.7.

	Adj. pulse width	Mean(FWHM)	Mean(Max. voltage)
w/o bias tee	50 ps	50.7 ± 0.9 ps	4.99 ± 0.07 V
w/o bias tee	250 ps	249.5 ± 0.9 ps	5.18 ± 0.05 V
with bias tee	50 ps	50.7 ± 0.9 ps	4.80 ± 0.08 V
with bias tee	250 ps	249.4 ± 0.9 ps	5.06 ± 0.05 V

For resistance measurements with an SMU, the leakage current between the AC and the DC port of the bias tee is an issue. It was measured with a Keithley 2634B at different sweep rates (see fig. 2.8). The leakage current depends linearly on the sweep rate. At a sweep rate of 14.8 $^{V}/_{s}$ the leakage current reaches 21.9 µA. Supposing a DUT had a resistance of 100 kΩ and its resistance was read at a read voltage of 0.2 V, this would result in a current of 2.0 µA. Consequently, the leakage current would be larger than the current through the device by more than one order of magnitude and, thereby, falsify the derived resistance values of the DUT.

To contain this issue all sweeps are conducted at a low sweep rate of 0.5 $^{V}/_{s}$, which results in a lower leakage current of 468 nA. The VCM devices used in this thesis have always HRS values below 100 kΩ and, consequently, the leakage current is less significant. To achieve precise results for the DUTs resistances, the measurements are conducted with a DC voltage of 0.2 V (see measurement cycle in fig. 2.5). Here, the leakage current is below 10 nA and not crucial for detecting the VCM device's resistance. At 100 kΩ and 0.2 V the current through the device would amount to 2 µA. Consequently, the error due to leakage current would be below 1 %. This approach is also transferable to other memory types. Bias tees were *e.g.* already used in studies on PCM devices [134, 135].

Automatic measurements require a software, which sends commands to measurement devices and stores the measured data. For this purpose, the oscilloscope (Tektronix DPO73304D) and the pulse generator PG5 were implemented in the software *py-ivtools* in the framework of this thesis. The pulse generator PSPL 2600C has no programming interface and, therefore, cannot be implemented.

2.1.3. Frequency-domain measurements

As shown in section 2.2.2, the time-dependent effective voltage at the device can be determined with the frequency-dependent scattering parameters (explained in chapter 1.3.3). They are determined with a vector network analyzer (VNA), which applies signals with

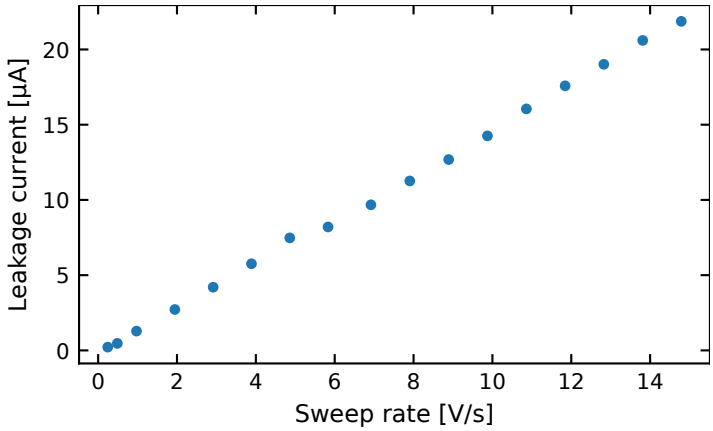

Figure 2.8.: Leakage current between the DC and the AC port of the bias tee in dependence of the sweep rate.

different frequencies to DUTs and measures their reflected and transmitted signals. More information on their functionality can be found in [101]. The scattering parameters are used in chapter 3.2.4 to determine the charging times of the investigated VCM devices. The VNAs used in this thesis, are listed in tab. 2.4.

Table 2.4.: List of used VNAs.

VNA	Frequency range
Rohde & Schwarz ZVL3[3]	9 kHz - 3 GHz [136]
HP 8722ES	50 MHz - 40 GHz [124]

Prior to the measurement of the scattering parameters of a device, the used VNA needs to be calibrated. In this thesis, the SOLT method is used, which stands for short open load through. For this purpose, a calibration substrate (Cascade Microtech CSR-8 100-250 GSG) is used, which has short, open, load and through structures and is compatible with the used RF probes (Cascade Microtech Z40-X-GSG-150) [125]. The calibration serves to detect the losses and reflections occurring in the used cables, probes and connectors. The losses and reflections are later considered in the measurements and only the losses and reflections occurring at the VCM device are measured and recorded.

A microscope picture of a load structure is shown in fig. 2.9. The load structure has a 50Ω load resistance between the Au contact pads for ground (G) and the signal (S). In case of the short structure the ground and signal pads are short-circuited and in case of the open structure they are isolated. The through structure consists of an almost ideal CPW with Au stripes.

The power of the signal in all measurements is set to -3.0 dBm, which corresponds to a power of 0.5 mW or to a voltage amplitude of 0.16 V at a characteristic impedance of 50 Ω. At the DUT this voltages doubles as explained in chapter 1.3.2. As the switching voltages of VCM devices are higher than 0.5 V, the devices cannot switch during the VNA

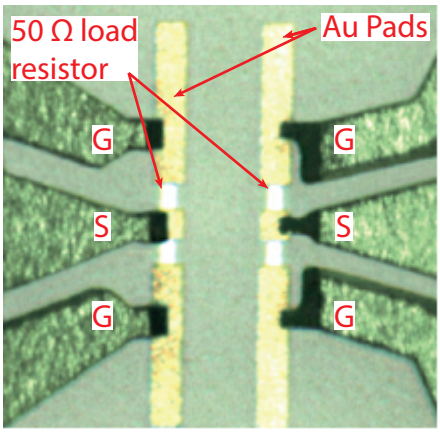

Figure 2.9.: Calibration substrate CSR-8 100-250 GSG with a load resistor of 50 Ω. Reprinted from [125] © 2018 FormFactor, Inc. All rights reserved.

measurements. To avoid leakage currents, the VCM devices were driven to the HRS prior to the frequency-domain measurements.

Two exemplary frequency-domain measurements conducted with the VNA HP 8722ES are shown in fig. 2.10. The first has been conducted on a 590 µm long CPW structure, consisting of a 5 nm thick Ti adhesion layer and a 30 nm thick Pt layer. The width of the inner conductor amounts to 100 µm and the spacing between the inner and outer conductors amounts to 60 µm. As shown in fig. 2.10a, the transmission is higher than -3.0 dB at all frequencies. At low frequencies, the signal is only slightly attenuated. The attenuation becomes more significant at frequencies above 5 GHz and reaches -2.6 dB at 40 GHz . The bandwidth of a circuit component or oscilloscope is defined as the frequency, below which all frequencies are attenuated by less than -3.0 dB. Therefore, the used CPW structures also have a bandwidth of at least 40 GHz.

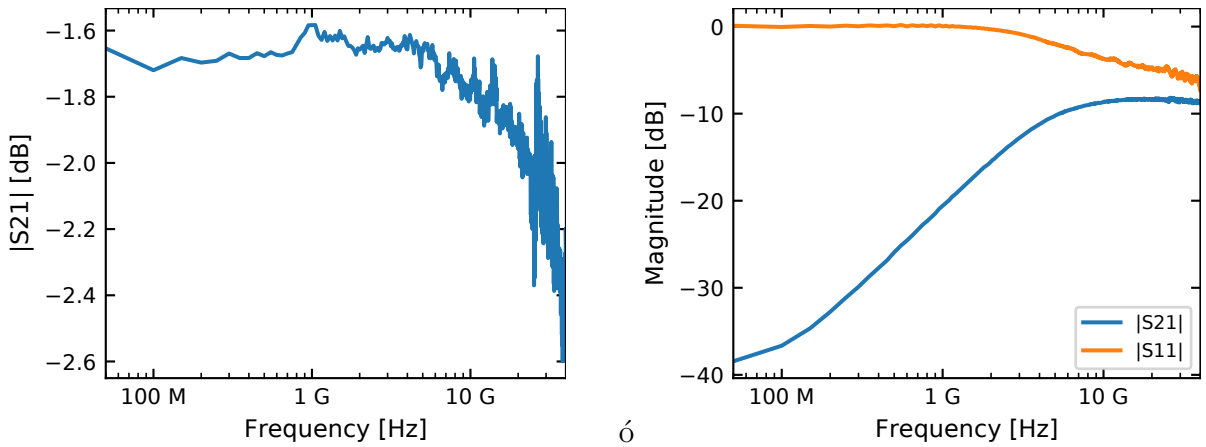

(a) CPW

(b) 2 x 2 μm^2 TaO_x device

Figure 2.10.: (a) Forward transmission of a CPW structure, and (b) forward transmission (blue) and forward reflection (orange) of a 2 x 2 μm^2 TaO_x device. Adapted from [38], with the permission of AIP Publishing.

A similar CPW structure has been used in [32], consisting of a 200 nm thick Pt layer. The forward transmission of this structure was measured over a distance of 930 µm. Although, their CPW structure is longer than the one used in this thesis (590 µm), it has a lower attenuation. At a frequency of 20 GHz the attenuation amounted to -1.6 dB. At this frequency, the CPW structure used in this thesis, has an attenuation of -1.9 dB. The better forward transmission in [32] is attributed to the thicker Pt layer. As shown in chapter 1.3, Pt has a skin depth of 815 nm at 40 GHz and, therefore, the forward transmission of both CPW structures would benefit from thicker Pt layers. However, if thicker Pt layers were used, short circuits occurred in the devices used in this thesis.

In fig. 2.10b, a frequency-domain measurement on a TaO_x device (Ta3 device, see table 3.1) with a feature size of $2 \times 2\,\mu m^2$ is shown. The SET kinetic measurements presented in chapter 4.2 were conducted on this device. At low frequencies the forward reflection is close to 0 dB and the forward transmission is very low, which implies that most of the signal is reflected. This is expected, as the TaO_x device has a much higher resistance than 50 Ω, even in the LRS ($R_{LRS} > 550\,\Omega$). As explained in chapter 1.3.2, this represents the case $Z_L \gg Z_0$, in which almost the entire signal is reflected and the voltage at the device corresponds to twice the pulse's voltage ($V_{DUT} = 2V_p$).

At higher frequencies, the forward reflection decreases down to -6.2 dB at 40 GHz and the forward transmission increases up to -8.5 dB. This is a result of the capacitance of the TaO_x device, which forms a highpass filter. As only approximately half of the incoming signal is reflected at high frequencies, the reflected signal differs from the incoming signal. This also influences the voltage at the device, which is the superposition of the incoming and the reflected signal (see eq. 1.9). This effect is taken into account in chapter 2.2.2, in which the time-dependent voltage at the device $V_{DUT}(t)$ is derived by using the device's scattering parameters.

2.2. Evaluation methods

This section, firstly, summarizes the evaluation methods, with which the SET and RESET time can be determined. The importance of the automation of the setup (see chapter 2.1.2) is highlighted. Secondly, this section presents an approach, with which it is possible to determine the transient voltage at the VCM device.

2.2.1. Determination of switching time

Two evaluation methods exist, with which the SET and RESET time of VCM devices can be determined, and are explained in the following subsections.

Determination from current responses

With the first evaluation method, the switching time is determined by analyzing the current response of the device. The SET event of VCM devices occurs abruptly, which results in a sudden current increase in their current response [37, 81, 137, 138]. The time at which the current increase starts is usually defined as SET time. The RESET of VCM devices occurs gradually [94,132] and, consequently, a different definition for the RESET time is required. In this case, usually the half-value time of the current decrease is used as RESET time [94,132].

This method is well suited at timescales above 100 ns. Its application for the SET time is illustrated in fig. 2.11, in which a 10 µs pulse (blue) with an amplitude of -0.8 V and its current response (red) of a Zr\ZrO$_x$\Pt VCM device is shown[4]. The voltage is applied to the active Pt electrode. At the beginning of the pulse, the absolute current is below 50 µA, indicating that the device is still in the HRS, and after 6.14 µs the absolute current increases abruptly to more than 250 µA, which corresponds to the SET event. These 6.14 µs are used as SET time.

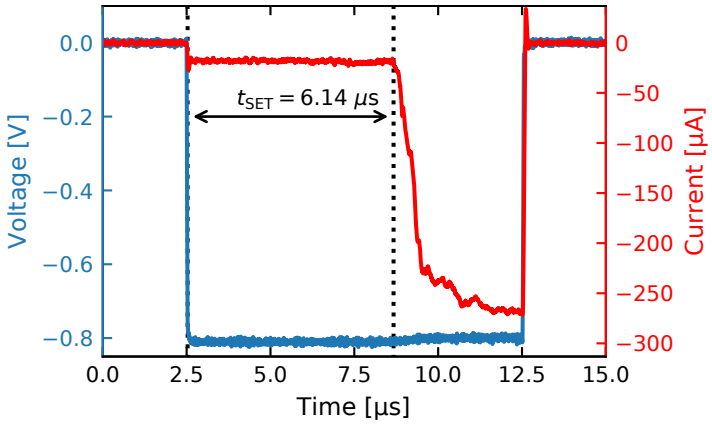

Figure 2.11.: Exemplary determination of the SET time from the current response of a 5 × 5 µm^2 Zr\ZrO$_x$\Pt VCM device. The blue curve is the applied voltage and the red curve is the current response of the device.

At faster timescales, in the range of the capacitive charging time of the DUT, this method becomes imprecise. This is illustrated with an exemplary measurement on the Ta1 device (15 × 20 µm^2 Ta\TaO$_x$\Pt, see tab. 3.1). Two 10 ns pulses[5] were applied to the active Pt electrode of the device, one with an amplitude of $V_P = -4.50$ V and one with an amplitude of $V_P = -1.13$ V [37, 121, 129]. The device was driven to the HRS prior to the application of the pulses. Fig. 2.12 shows the measured current I_{Meas} of the $V_P = -4.50$ V pulse (blue) and of the $V_P = -1.13$ V pulse (orange) .

During the $V_P = -4.50$ V pulse (blue curve in fig. 2.12), the Ta1 device switched to the LRS. The blue dashed line marks the SET time determined at 1.7 ns. It is less obvious

[4]The VCM device is incorporated into a 5 × 5 µm^2 crossbar structure [139, 140].
[5]Emitted by the pulse generator PSPL 2600C. Both pulses were measured by V. Havel. The following analysis resulted in the framework of the thesis at hand.

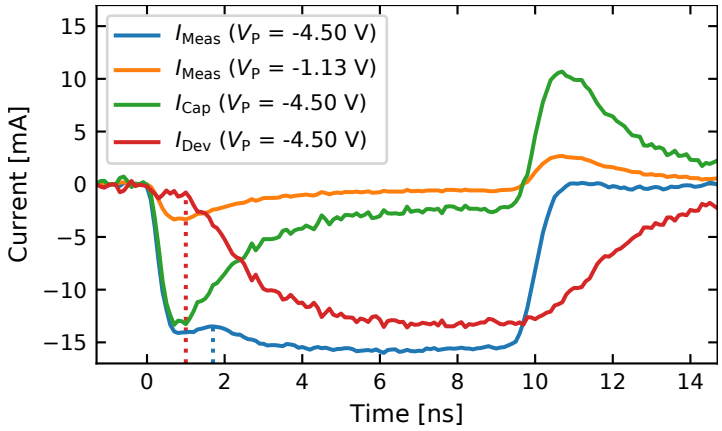

Figure 2.12.: Measured current response I_{Meas} of the Ta1 device ($15 \times 20\,\mu m^2$, Ta\TaO$_x$\Pt, see tab. 3.1) during a 10 ns pulse with an amplitude of $V_P = -4.50\,V$ (blue) and $V_P = -1.13\,V$ (orange). Capacitive current I_{Cap} (green) determined with eq. 2.5 and current through the device I_{Dev} (red) determined with eq. 2.6. The left red dashed line marks the SET time, determined from I_{Dev} and the right blue dashed line marks the SET time, determined from I_{Meas}.

than the SET event observed in fig 2.11, which is due to the superposition of the increasing current through the device, I_{Dev}, and the capacitive current, I_{Cap}. Their sum results in the measured current I_{Meas}:

$$I_{Meas} = I_{Cap} + I_{Dev}. \tag{2.4}$$

To determine $I_{Dev}(-4.50\,V)$, the capacitive current, $I_{Cap}(-4.50\,V)$, needs to be determined first. During the $V_P = -1.13\,V$ pulse (orange curve in fig. 2.12) the Ta1 device did not switch and remained in the HRS. Consequently, the current through the device, $I_{Dev}(-1.13\,V)$, is negligible compared to the capacitive current, $I_{Cap}(-1.13\,V)$, and the measured current at $V_P = -1.13\,V$ corresponds only to the capacitive current $I_{Meas}(-1.13\,V) = I_{Cap}(-1.13\,V)$.

The capacitive current is in general proportional to the change of the applied voltage $I_{Cap} \sim {}^{\partial V}/_{\partial t}$. As the rise times of the PSPL 2600C pulse generator, T_P, barely depend on the applied voltage, I_{Cap} scales with the pulse amplitude ${}^{\partial V}/_{\partial t} \sim {}^{V_P}/_{T_P}$. As a result, the capacitive current also scales proportionally with the pulse amplitude $I_{Cap} \sim V_P$. Consequently, the capacitive current at $V_P = -4.50\,V$ can be calculated by

$$I_{Cap}(-4.50\,V) = I_{Cap}(-1.13\,V) \cdot \frac{-4.50\,V}{-1.13\,V}. \tag{2.5}$$

The resulting $I_{Cap}(-4.50\,V)$ is shown in green in fig. 2.12. According to eq. 2.5 the current through the device $I_{Dev}(-4.50\,V)$ can be calculated by

$$I_{Dev}(-4.50\,V) = I_{Meas}(-4.50\,V) - I_{Cap}(-4.50\,V). \tag{2.6}$$

The resulting $I_{Dev}(-4.50\,V)$ is shown as red line in fig. 2.12. The SET event after 1.0 ns (marked with the red dashed line) is more obvious compared to the SET event observed in

$I_{\mathrm{Meas}}(-4.50\,\mathrm{V})$. More importantly, however, is the fact that the SET time determined from $I_{\mathrm{Dev}}(-4.50\,\mathrm{V})$ is 700 ps faster than the SET time determined from $I_{\mathrm{Meas}}(-4.50\,\mathrm{V})$. This proves that at timescales in the range of the device's capacitive charging time, it is necessary to determine the SET time from I_{Dev} and not from I_{Meas}. In this example, the SET time determined from I_{Meas} deviates by 70 % from the SET time determined from I_{Dev}. At slower timescales, the determination from I_{Meas} is also valid.

Determining the starting time of the pulse is also necessary to derive the SET time. Unfortunately, no convention applies at timescales in the fast regime below 10 ns, in which the SET time is in the range of the electrical charging time of the VCM device. At slower timescales usually the point at which the voltage of the applied pulse reaches 90 % of the maximum voltage is used [81,95,130–132] or after the capacitive peak of the current response has passed [106, 141–143]. Both definitions cannot be applied in the fast regime, because the VCM devices can switch within the electrical charging time, which would result in a negative SET time. This would also be the case for the example in fig. 2.12. As shown below in section 2.2.2, it can take up to 2.54 ns to fully charge a VCM device. Instead, the starting time has been chosen as the time, at which 20 % of the capacitive current's maximum is reached. This definition yields slower SET times as the previous mentioned conventions, which makes the claimed SET times less attackable.

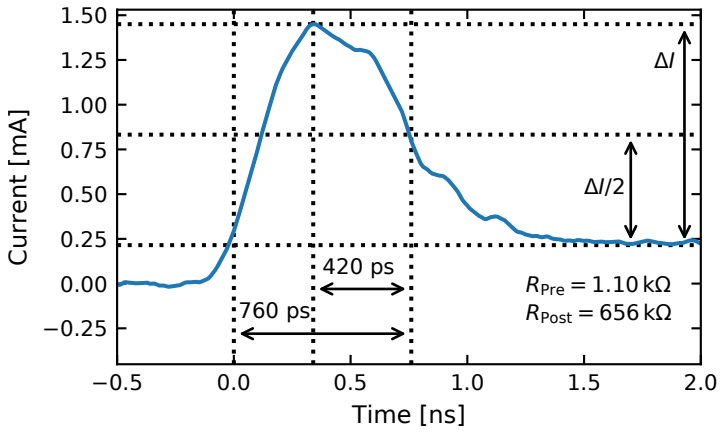

Figure 2.13.: Zoom into the beginning of the Zr1 device's ($2 \times 2\,\mu\mathrm{m}^2$ Ta\ZrO$_x$\Pt, see table 3.1) current response to a 100 ns pulse with an amplitude of $V_{\mathrm{P}} = 0.8\,\mathrm{V}$. The data were smoothened with a Savitzky Golay filter. The upper horizontal dotted line marks I_{Max}, the lower one I_{Min} and the central one $I_{\mathrm{Min}} + \Delta I/2$, which corresponds to the threshold of the RESET time. The vertical lines mark the time at which the current begins, reaches its maximum and, falls below the threshold of the RESET time.

In the following, the determination of the RESET time is explained. A zoom into an exemplary current response of a Ta\ZrO$_x$\Pt device onto a 100 ns pulse with an amplitude of $V_{\mathrm{P}} = 0.8\,\mathrm{V}$ is shown in fig. 2.13. During the application of this pulse the device switched from 1.10 kΩ to 656 kΩ. As shown in chapter 5.1.1, the current peak at the beginning does not correspond to the capacitive current, but to the current through the device (see fig. 5.3). After its maximum at about $I_{\mathrm{Max}} = 1.5\,\mathrm{mA}$ (upper horizontal line), it decreases

gradually to $I_{\mathrm{Min}} = 215\,\mu\mathrm{A}$ (lower horizontal line). The difference is referred to as $\Delta I = I_{\mathrm{Max}} - I_{\mathrm{Min}}$ and amounts to about 1.3 mA in this example. In previous studies on the RESET kinetics, the time from the occurrence of the maximum current to the half-value current (being $I_{\mathrm{Min}} + {}^{\Delta I}/_{2}$, central horizontal line) is referred to as the RESET time [94,132]. According to this definition, the RESET time would amount to 420 ps in this example. The maximum current, however, occurred during the rise time of the pulse (approx. 359 ps) and, therefore, shorter rise times than the pulse generator's rise time would be possible. To circumvent this issue, similar to the definition of the SET time, the time at which the current reaches 20 % of I_{Max} is used as the start of the RESET time. According to this definition, the RESET time amounts to 760 ps. As this definition yields less attackable results, it is used in chapter 5.1.1.

Determination using FWHM

Evaluation the SET or RESET time from the measured current has two disadvantages: he determination of SET and RESET times is elaborate and at even faster timescales I_{Cap} increases due to the shorter rise times of the applied pulses. Therefore, at timescales below 1 ns, the SET time is usually derived from the FWHM of I_{Meas} [32–34, 37, 121, 129]. As the measured FWHM can be longer than the effective SET time, this method rather determines an upper limit of the SET time.

The SET and the RESET kinetics on a timescale below 250 ps of VCM devices (see chapter 4 and 5) were, therefore, evaluated with a different method, which also determines the SET and RESET times from the FWHM of I_{Meas}. Different to previous studies in the subnanosecond regime [32–34,37,121,129], however, this method achieves more precise results for the SET and RESET time by using a larger set of statistics. Instead of just applying one pulse, multiple pulses are applied and their width is varied in small steps. The resistance is read before (R_{LRS}) and after (R_{HRS}) the application of each pulse. With this method the change in resistance can, consequently, be determined as a function of the FWHM [38].

An exemplary measurement on the Ta3 device with this method is shown in fig. 2.14. Pulses[6] with an amplitude of -1.58 V were applied to the active Pt electrode. The pulse width was varied from 50 ps to 250 ps in steps of 5 ps. Each cycle has been repeated 10 times. The current response was interpolated and its FWHM determined and plotted on the abscissa. The ratio of the measured resistance before (R_{HRS}) and after (R_{LRS}) the pulse's application is plotted on the ordinate as boxplot (each comprises 10 values). The red line connects the median values of the boxplots.

The ratio ${}^{R_{\mathrm{LRS}}}/_{R_{\mathrm{HRS}}}$ scatters around unity for short FWHMs, indicating that the device remains in the HRS. At 100 ps, the device switched randomly to the LRS and at 175 ps, the device switched always to the LRS. The occurrence of values above unity of the ratio

[6] Emitted by the PG5 pulse generator.

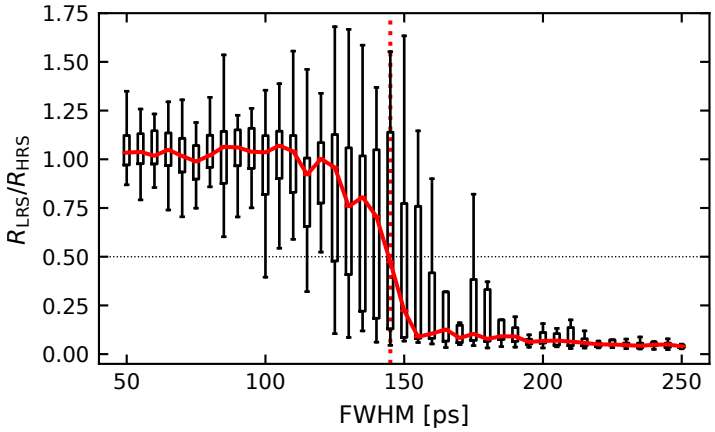

Figure 2.14.: SET kinetic measurement on the Ta3 device ($2 \times 2\,\mu m^2$ Ta\TaO$_x$\Pt, see table 3.1), with the boxplot representation of the ratio R_{LRS}/R_{HRS} at different FWHMs. The solid red line connects the median values and the vertical red dotted line marks the SET event at 145 ps. The pulse amplitude was -1.58 V. Adapted from [38], with the permission of AIP Publishing.

R_{LRS}/R_{HRS} is explained in chapter 4.2. The SET time is defined as the time at which the median value of the ratio R_{LRS}/R_{HRS} reaches values below 0.5 (marked as horizontal dotted line). In this example, the SET occurs at 145 ps (marked as red vertical dotted line), which corresponds to the SET time.

The procedure to determine the RESET time is in analogy to determination of the SET time (see chapter 5). Again, the ratio R_{LRS}/R_{HRS} is built for various FWHMs in the range from 50 ps to 250 ps. Differently to the SET kinetics, the time at which R_{LRS}/R_{HRS} surpasses the threshold of 2, is taken as RESET time.

This method has two requirements: Firstly, a large set of statistics needs to be collected, which requires an automated setup and, also, the evaluation needs to be conducted in an automated fashion. The automated setup presented in chapter 2.1.2 can cover the range between 50 ps and 250 ps and the evaluation is also automated. This method also works on slower timescales, if an automated setup is available [80, 144]. Secondly, the devices need to remain in their resistive state after the application of the pulse, which is the case for VCM devices.

2.2.2. Determination of effective voltage at the DUT

The bandwidth of the CPW structure is limited by the parasitic capacitances, inductances, and the thin conducting Pt layers, which are thinner than the skin depth as explained in section 2.1.3. In this section, an approach is presented, with which it is possible to reconstruct the voltage that is effectively applied to the device. This approach takes the rise and fall times of the pulse generator, the capacitances, inductances, and resistances of the CPW structure and the integrated VCM device into account. The capacitance of the device influences the SET kinetics significantly [37, 118], which is also shown in chapter 4.1. As

a capacitor has a characteristic charging time, the voltage of the pulse is not immediately applied to the device and delayed on the timescale of the charging time. Consequently, the voltage at the device is also time-dependent $V_{\mathrm{DUT}}(t)$. In addition, the rise and fall times of the pulse generator influence $V_{\mathrm{DUT}}(t)$. Parts of this section were published in [100]. Several studies determined $V_{\mathrm{DUT}}(t)$ by using circuit-based models [32, 118, 119]. These studies are more elaborately summarized in chapter 1.4.1. The experimental method presented in the following uses the scattering parameters and the frequency content of the applied voltage pulse. By transferring the product from the frequency-domain to the time-domain, $V_{\mathrm{DUT}}(t)$ can be obtained. Scattering parameters are explained in chapter 1.3.3 and their experimental determination in section 2.1.3. This method has two advantages:

1. No circuit-based model needs to be developed. It takes less time to conduct a frequency-domain measurement with a VNA than to develop a circuit-based model of a VCM device.

2. Opposite to circuit-based models, this method does not rely on assumptions made about the circuit. All inductances, capacitances and resistances are considered, as well as their frequency dependence. If thin films are considered, their properties may differ from their bulk values, which makes simulations or analytic calculations difficult.

Later in this chapter, the rise time of $V_{\mathrm{DUT}}(t)$ is extracted, which is a measure of the electrical charging time, as explained in chapter 1.4.2. So far, no study investigating the subnanosecond regime of VCM devices included the rise time of $V_{\mathrm{DUT}}(t)$ in their evaluation. This method to determine $V_{\mathrm{DUT}}(t)$ is used in chapter 3.2.4 to derive the devices' electrical charging times. It is also used in chapter 4.3 to derive the experimental limitation of the SET and RESET kinetics of the investigated VCM devices. Finally, this method helps designing future experiments with CPW structures. For example, the heating time of VCM devices could be studied and its implementation in neuromorphic applications could be tested (see chapter 6.2.1). The effective voltage at the device can now be calculated before the experiment is conducted, if the device's scattering parameters are available.

This method is also transferable to other memory technologies such as PCM or FeRAM. Utilizing this method requires solely the scattering parameters of the DUT in a sufficiently broad frequency regime. This might be the only disadvantage of the presented method, because VNAs with a broad frequency range are expensive and, therefore, not available for many scientific groups.

The explanation in the section is illustrated with an exemplary 10 ns pulse[7], applied to the Ta1 device[8] [37]. Prior to the frequency-domain measurements, the Ta1 device was driven to the HRS, which is at 3.0 kΩ. Its scattering parameters are shown in fig. 3.6. This method also works on faster timescales, as demonstrated in chapter 3.2.4 with a 250 ps pulse.

[7] Emitted by the PSPL 2600C pulse generator.
[8] Ta\TaO_x\Pt, see table 3.1.

As shown in chapter 1.3.1, $V_{\mathrm{DUT}}(t)$ is the superposition of the incoming $v_1^+(t)$ and the reflected pulse $v_1^-(t)$, which is expressed by eq. 1.9. However, a part of the signal is also transmitted $v_2^-(t)$ to the other electrode of the VCM device. This reduces the effective voltage drop over the device and needs to be considered. The overall voltage at the device is consequently:

$$V_{\mathrm{DUT}}(t) = v_1^+(t) + v_1^-(t) - v_2^-(t). \tag{2.7}$$

This approach has also been used in [32,145]. The incoming voltage pulse $v_1^+(t)$ is measured with the oscilloscope Tektronix DPO73304D. The determination of the reflected $v_1^-(t)$ and transmitted pulse $v_2^-(t)$ is more elaborate. In the following, the determination of $v_1^-(t)$ is explained in detail. The determination of $v_2^-(t)$ is in analogy to the one of $v_1^-(t)$. Firstly, the discrete Fourier transformation of the incoming signal is built:

$$V_1^+(f) = \mathcal{F}(v_1^+(t)), \tag{2.8}$$

which corresponds to the frequency content of the signal. An exemplary 10 ns pulse[9] is shown in fig. 2.15a, which is used as $v_1^+(t)$. A low voltage amplitude of -0.52 V, below the switching voltage of VCM devices, has been chosen to prevent the device from switching during the pulse's application.

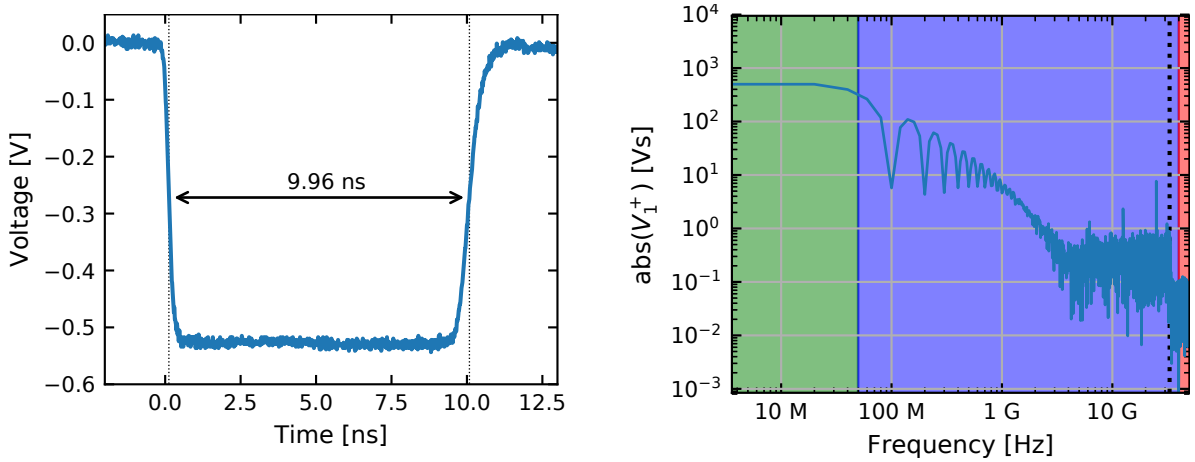

(a) $v_1^+(t)$ (b) abs($V_1^+(f)$)

Figure 2.15.: (a) 10 ns pulse $v_1^+(t)$ with an amplitude of -0.52 V emitted by the PSPL 2600C pulse generator and (b) the absolute value of its frequency content $V_1^+(f)$. The vertical dotted line marks the bandwidth limit of the Tektronix DPO73304D oscilloscope. The green, blue and red shaded area are explained in the caption of fig. 2.16. Adapted from [100].

The corresponding absolute values of $V_1^+(f)$ are shown in fig. 2.15b. As the sample rate of the oscilloscope is $f_S = 100\,\mathrm{GS/s}$, the highest frequency of $V_1^+(f)$ is 50 GHz. The solution of the Fourier transformation yields results at positive and negative values of f, which is

[9]Emitted by the PSPL 2600C pulse generator.

referred to as double-sided spectrum, covering the values from -50 GHz to 50 GHz. As the scattering parameters are only defined for positive values of f, the single-sided spectrum is used, which has only positive values of f ranging from 0 to 50 GHz. This also reflects the Nyquist-Shannon sampling theorem, according to which, only frequencies f can be detected, which are smaller than half the sampling rate $f \leq f_S/2$. The bandwidth of the oscilloscope is limited at 33 GHz, which is marked as vertical dotted line in fig. 2.15b. The frequency content above the bandwidth limit was not captured by the oscilloscope. The periodicity in the low frequency regime below 1 GHz is expected, because the Fourier transformation of an ideal square pulse yields a sinc function [117] as shown in chapter 1.3.4.

Secondly, $V_1^+(f)$ is multiplied with the forward reflection $S_{11}(f)$, which results in the frequency content of the reflected signal $V_1^-(f)$:

$$V_1^-(f) = V_1^+(f) \cdot S_{11}(f). \tag{2.9}$$

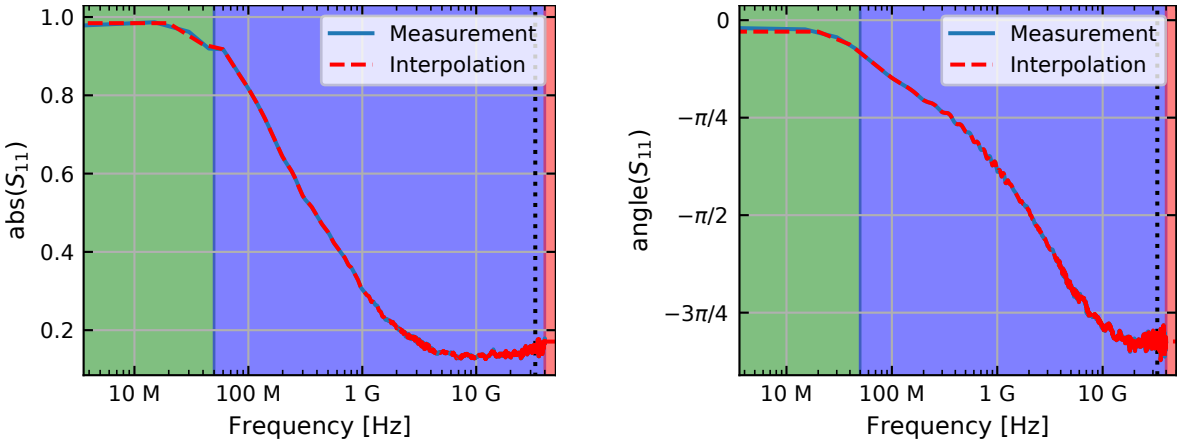

(a) abs(S_{11}) (b) angle(S_{11})

Figure 2.16.: Measurement (blue line) and interpolation (red dashed line) of the (a) absolute value and (b) the angle of the forward reflection S_{11} of the Ta1 device (see table 3.1). The green shaded area marks the regime, which was measured with the VNA Rohde & Schwarz ZVL3 and the blue shaded area the regime, which was measured with the VNA HP 8722ES. The red shaded area was not measured by any VNA in this example. The vertical dotted line marks the bandwidth limit of the oscilloscope.

As $S_{11}(f)$ is complex, it can be separated into an absolute value and an angle. The measurement of the absolute value of $S_{11}(f)$ and the angle are shown as blue lines in fig. 2.16a and fig. 2.16b, respectively. The measurement procedure is described in chapter 2.1.3.

The sampled frequencies of $V_1^+(f)$ cover a range from 20 MHz to 50 GHz (see fig. 2.15b). None of the available VNAs covers this frequency range (see table 2.4). Therefore, the frequency regime from 20 MHz to 50 MHz was measured with the VNA Rohde & Schwarz ZVL3 (marked as green shaded area) and the regime from 50 MHz to 40 GHz was measured with the VNA HP 8722ES (marked as blue shaded area). The frequency regime above 40 GHz is marked as red shaded area and was not measured. This regime is, however, above

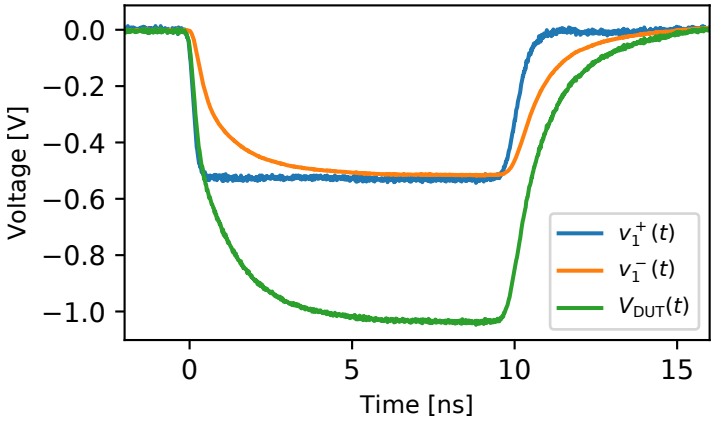

Figure 2.17.: Original signal $v_1^+(t)$ (blue), calculated reflection $v_1^-(t)$ using eq. 2.11 (orange) and the calculated voltage at the Ta1 device $V_{\mathrm{DUT}}(t)$ using eq. 2.7 (green). Adapted from [100].

the bandwidth limit of the oscilloscope, which is at 33 GHz (shown as dotted line in fig. 2.16a and fig. 2.16b). The values of $V_1^+(f)$ are, therefore, also strongly attenuated and not critical for the evaluation. This is also shown in fig. 2.15b, in which the presented frequency regimes are also marked accordingly.

As $V_1^+(f)$ is sampled at different frequencies than $S_{11}(f)$, one of those two quantities needs to be interpolated to the sampled frequencies of the other quantity. The interpolation of a Fourier transformation would require the use of sinc functions [146]. Interpolating $S_{11}(f)$ is less elaborate and is, therefore, interpolated using a spline function (see red dashed line in fig. 2.16a and fig. 2.16b). As $S_{11}(f)$ was not measured in the frequency regime above 40 GHz (see red shaded area in fig. 2.16a and fig. 2.16b), the interpolated value at 40 GHz is used in this regime.

Finally, the inverse discrete Fourier transformation of $V_1^-(f)$ corresponds to the reflected signal $v_1^-(t)$:

$$v_1^-(t) = \mathcal{F}^{-1}(V_1^-(f)). \tag{2.10}$$

Inserting eq. 2.8 and eq. 2.9 into eq. 2.10 results in:

$$v_1^-(t) = \mathcal{F}^{-1}\left(\mathcal{F}(v_1^+(t)) \cdot S_{11}(f)\right). \tag{2.11}$$

In fig. 2.17 $v_1^+(t)$ (corresponding to the original pulse) and its reflection $v_1^-(t)$ (calculated with eq. 2.7) are shown in blue and orange, respectively. The amplitude of $v_1^-(t)$ is almost identical to the one of $v_1^+(t)$. This is expected, because the resistance of the Ta1 device ($Z_{\mathrm{L}} = 1.5\,\mathrm{k}\Omega$) is much larger than the impedance of the cables and probes ($Z_0 = 50\,\Omega$). This corresponds to the case $Z_{\mathrm{L}} \gg Z_0$, in which, according to eq. 1.8, the entire signal $v_1^+(t)$ is reflected. This case is explained more elaborately in chapter 1.3.1.

The transmitted part of the incoming pulse $v_2^-(t)$ can be calculated in analogy to $v_1^-(t)$ by using the forward transmission S_{21} (shown in fig. 3.6b), instead of S_{11}:

$$v_2^-(t) = \mathcal{F}^{-1}\left(\mathcal{F}(v_1^+(t)) \cdot S_{21}(f)\right). \tag{2.12}$$

As the transmitted voltage $v_2^-(t)$ can also be measured, the calculated one is referred to as $v_{2,\mathrm{calc}}^-(t)$ and the measured one as $v_{2,\mathrm{meas}}^-(t)$ in the following. To validate the calculation of $V_{\mathrm{DUT}}(t)$, it is necessary to compare $v_{2,\mathrm{calc}}^-(t)$ with $v_{2,\mathrm{meas}}^-(t)$. If the calculation is correct, they should be identical.

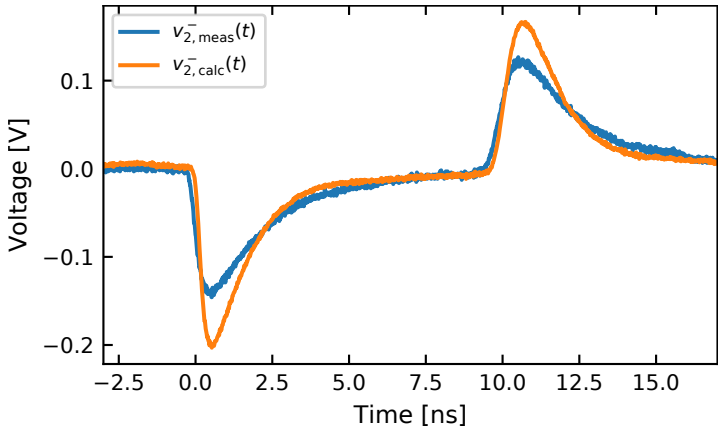

Figure 2.18.: Measured transmission $v_{2,\mathrm{meas}}^-(t)$ (blue) and calculated transmission $v_{2,\mathrm{calc}}^-(t)$ (orange) through the Ta1 device using eq. 2.12. Adapted from [100].

In fig. 2.18 both $v_{2,\mathrm{meas}}^-(t)$ and $v_{2,\mathrm{calc}}^-(t)$ are shown. The applied pulse $v_1^+(t)$ is shown in fig. 2.15a. They both have a capacitive peak at the beginning and at the end of the pulse, which occurs during the charging and discharging of the Ta1 device. As both $v_{2,\mathrm{meas}}^-(t)$ and $v_{2,\mathrm{calc}}^-(t)$ are similar, the approach presented in this chapter is valid. However, the amplitude of the capacitive peaks differs, which results from the losses occurring in the cables, probes and connector. This is illustrated at the end of this section.

The voltage at the device $V_{\mathrm{DUT}}(t)$ is finally derived using eq. 2.7 and is shown as green line in fig. 2.17. Its amplitude is almost twice the amplitude of $v_1^+(t)$, which is expected, as almost the entire signal is reflected. It takes, however, some time until $V_{\mathrm{DUT}}(t)$ reaches its maximum. This corresponds to the electrical charging time, which is analyzed in the following.

The rise time, T_{Rise}, (10 % to 90 %) of $v_1^+(t)$, $v_1^-(t)$, and $V_{\mathrm{DUT}}(t)$ are determined as explained in section 2.1 for the pulse generators and are summarized in tab 2.5. For $v_1^-(t)$ and $V_{\mathrm{DUT}}(t)$, the rise time of the pulse generator $T_{\mathrm{PG}} = 359\,\mathrm{ps}$ is quadratically subtracted:

$$T_{\mathrm{Rise}} = \sqrt{T_{\mathrm{Calc}}^2 - T_{\mathrm{PG}}^2}. \tag{2.13}$$

Also, the rise times of the capacitive peaks of $v_{2,\mathrm{Calc}}^{-}(t)$ and $v_{2,\mathrm{Meas}}^{-}(t)$ are determined and summarized in tab 2.5. As these peaks include the high frequency part of $v_1^{+}(t)$, they have even shorter rise times and, consequently, T_{PG} cannot be considered anymore.

Table 2.5.: Calculated rise times T_{Calc} for $v_1^{+}(t)$, $v_1^{-}(t)$, and V_{DUT}. Measured rise times for $v_1^{+}(t)$ and $v_{2,\mathrm{Meas}}^{-}(t)$. T_{Rise} is determined using eq. 2.13.

Voltage	T_{Meas}	T_{Calc}	T_{Rise}
$v_1^{+}(t)$	359 ps	-	-
$v_1^{-}(t)$	-	2.35 ns	2.33 ns
$V_{\mathrm{DUT}}(t)$	-	2.57 ns	2.54 ns
$v_{2,\mathrm{Calc}}^{-}(t)$	-	333 ps	-
$v_{2,\mathrm{Meas}}^{-}(t)$	459 ps	-	-

The rise times of $v_1^{-}(t)$ and $V_{\mathrm{DUT}}(t)$ are significantly slower than the one of $v_1^{+}(t)$. This is due to the stronger attenuation and higher transmission of higher frequencies at the VCM device a(see fig. 2.16a). As the Ta1 device in this example is relatively large ($15 \times 20\mu\mathrm{m}^2$), its capacity amounts to 4.6 pF (measured at 1 MHz with a HP 4284A LCR meter). This capacitance acts as highpass filter and, consequently, higher frequencies are transmitted through the Ta1 device. These frequencies are, therefore, not present in the reflection. As T_{Rise} depends strongly on the presence of high frequencies, T_{Rise} of $v_1^{-}(t)$ is longer (2.33 ns) than the one of $v_1^{+}(t)$ (359 ps).

The rise time of $V_{\mathrm{DUT}}(t)$ is even longer (2.54 ns). This is a result of the transmitted signal. As shown later in fig. 3.6, the forward transmission S_{21} is larger than the forward reflection S_{11} at higher frequencies. This means that $v_2^{-}(t)$ contains higher frequencies than the reflected voltage $v_1^{-}(t)$ at port 1. Consequently, the calculated transmitted voltage $v_{2,\mathrm{Calc}}^{-}(t)$ rises within 333 ps, which is much faster than the rise time of $v_1^{-}(t)$ (2.33 ns). The faster rising at port 2 reduces the voltage drop over the VCM device. The assumption that the voltage at the device is twice the pulses amplitude ($V_{\mathrm{DUT}}(t) = 2V_{\mathrm{P}}$), consequently, no longer holds at timescales in the range of the rise time of $V_{\mathrm{DUT}}(t)$.

The divergence in the capacitive peak's rise time of the calculated $v_{2,\mathrm{Calc}}^{-}(t)$ (333 ps) and measured transmission $v_{2,\mathrm{Meas}}^{-}(t)$ (459 ps) indicates the presences of unaccounted losses, which is addressed at the end of this chapter.

This example shows that the design of the VCM device and the CPW structure is more important for the measurement of short switching times than choosing a pulse generator with short rise times. As shown in chapter 4.1, smaller devices have lower capacitances and, therefore, the rise time of $V_{\mathrm{DUT}}(t)$ also shortens, which allows more precise measurements in the subnanosecond regime.

Consideration of cables

In fig. 2.19 the forward transmission S_{21} of the used 1.2 m long cables is shown. Cable 1 connects the pulse generator to the VCM device and cable 2 connects the VCM device to the oscilloscope. The forward transmission of cable 1 and 2 is referred to as $S_{21,\mathrm{I}}$ and $S_{21,\mathrm{II}}$, respectively. The measurement was conducted with an Agilent Technologies N5245A VNA in the frequency range from 10 MHz to 50 GHz. The VNA was borrowed from the Institute of Integrated Photonics (IPH) of the RWTH Aachen University. Both cables have a high transmission at low frequencies. At frequencies above 1 GHz their attenuation increases, which also impacts the transmitted signals. This impact is considered with the following approach.

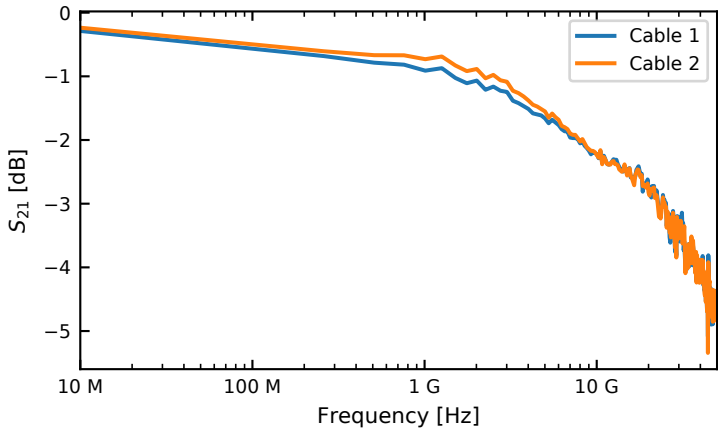

Figure 2.19.: Forward transmission S_{21} of the used 1.2 m long cables. Adapted from [100].

The transmission through cable 1 $v_{2,\mathrm{I}}^{-}(t)$ is calculated in analogy to the transmission through the VCM device. Instead of using the VCM device's forward transmission $S_{21,\mathrm{DUT}}$, as done in eq. 2.11, $S_{21,\mathrm{I}}$ is used:

$$v_{2,\mathrm{I}}^{-}(t) = \mathcal{F}^{-1}\left(\mathcal{F}(v_1^{+}(t)) \cdot S_{21,\mathrm{I}}(f)\right). \tag{2.14}$$

In the next step, the transmission of $v_{2,\mathrm{I}}^{-}(t)$ through the VCM device is derived, which is now referred to as $v_{2,\mathrm{DUT}}^{-}(t)$. To consider the impact of cable 1, $v_{2,\mathrm{I}}^{-}(t)$ (result of eq. 2.14) is used, instead of the original signal $v_1^{+}(t)$. Similar to the previous approach (see eq. 2.12) the forward transmission of the VCM device $S_{21,\mathrm{DUT}}$ is now used:

$$v_{2,\mathrm{DUT}}^{-}(t) = \mathcal{F}^{-1}\left(\mathcal{F}(v_{2,\mathrm{I}}^{-}(t)) \cdot S_{21,\mathrm{DUT}}(f)\right). \tag{2.15}$$

In the last step, the impact of cable 2 $S_{21,\mathrm{II}}$ on the transmitted signal is calculated analogously (using $v_{2,\mathrm{DUT}}^{-}(t)$, result of eq. 2.15) to obtain the transmitted signal through the device $v_{2,\mathrm{II}}^{-}$:

$$v_{2,\mathrm{II}}^{-}(t) = \mathcal{F}^{-1}\left(\mathcal{F}(v_{2,\mathrm{DUT}}^{-}(t)) \cdot S_{21,\mathrm{II}}(f)\right). \tag{2.16}$$

The result for $v_{2,\mathrm{II}}^{-}(t)$ is shown in green in fig. 2.20. Also, the results from fig. 2.18 are repeated for convenience: the measured results of the transmitted voltage $v_{2,\mathrm{meas}}^{-}(t)$ in blue and the calculated transmission without the consideration $v_{2,\mathrm{calc}}^{-}(t)$ (see eq. 2.12) of the cables in orange.

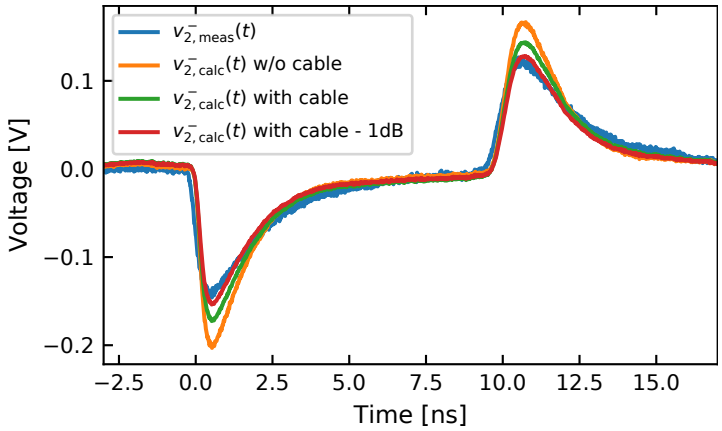

Figure 2.20.: Measured transmission $v_{2,\mathrm{meas}}^{-}(t)$ (blue) and calculated transmission $v_{2,\mathrm{calc}}^{-}(t)$ (orange) using eq. 2.12 without the consideration of the cables' influence from fig. 2.18. The green line indicates the calculated transmission with the cables' influence taken into account using eq. 2.14 to 2.16. The red line is identical to the green line but attenuated by 1 dB, which is an estimate of the insertion loss of the RF probes and other components of the experimental setup. Adapted from [100].

The capacitive peak's amplitude of $v_{2,\mathrm{II}}^{-}(t)$ is lower than the one of $v_{2,\mathrm{calc}}^{-}(t)$, which brings $v_{2,\mathrm{II}}^{-}(t)$ closer to the measured transmission $v_{2,\mathrm{meas}}^{-}(t)$. Nevertheless, the capacitive peak's amplitude of $v_{2,\mathrm{II}}^{-}(t)$ is still higher than the one of $v_{2,\mathrm{meas}}^{-}(t)$. Also, the rise time of $v_{2,\mathrm{II}}^{-}(t)$ is with 345 ps only a little higher than the one of $v_{2,\mathrm{calc}}^{-}(t)$ (333 ps) and still significantly lower than the rise time of $v_{2,\mathrm{meas}}^{-}(t)$ (459 ps). These observations indicate that not all losses occurring in the RF setup could be accounted for. These losses might origin from adapters or the RF probes, which are not considered in the presented approach. As indicated in [147], the used FormFactor Z-Probes have an insertion loss of up to 0.8 dB. Subtracting 1 dB from $v_{2,\mathrm{II}}^{-}(t)$ (see red line in fig. 2.20) results in a good fit to $v_{2,\mathrm{meas}}^{-}(t)$, which suggests that the other losses in the RF setup are on the order of 1 dB.

3. Devices

This chapter firstly lists all VCM devices, which were used in this thesis (see table 3.1). Their fabrication process is explained subsequently in chapter 3.1. The first devices were fabricated using an optical lithography process with an existing mask, which is referred to as mask A. In the framework of this thesis a new mask has been designed, which is referred to as mask B. To decrease the device's electrical charging times, the devices size (which is the VCM stack) was reduced to $2 \times 2\,\mu m^2$ (from $5 \times 5\,\mu m^2$), the narrowed area's length shortened to $10\,\mu m$ (from $50\,\mu m$), and the CPW structure's overall length shortened to $590\,\mu m$ (from $930\,\mu m$).

The VCM devices are then characterized with regard to their IV characteristics, capacitances, scattering parameters and electrical charging times in chapter 3.2. The results indicate that the optimizations of mask B lead to significantly shorter electrical charging times. It could also be shown that the reduction of the device size (VCM stack) has the largest influence on the electrical charging times. Finally, suggestions for the optimal integration of VCM devices into CPW structures are given in section 3.3.

All devices were given identifiers, which are indicated in the first column of table 3.1. Also, the film thicknesses and device sizes are given. The SET kinetics were measured on the Ta1, Ta2, Ta3, Zr1, HfA2, and HfB1 devices and the RESET kinetics on the Ta3, Zr1, Ta-C, Zr-C, HfA1, HfA3, HfB2, and HfB3 devices. The results of the SET kinetics are shown in chapter 4 and the results of the RESET kinetics in chapter 5.

3.1. Fabrication

As the thesis at hand focuses on measurement techniques, the fabrication processes are described only briefly. Literature references with more details on the fabrication are given, as well as fabrication protocols in the appendix section A.

All devices were fabricated on an oxidized Si substrate with a high resistivity ($\rho > 10 k\Omega cm$). The oxidization is realized by thermal annealing and results in a 430-nm to 450-nm-thick SiO_2 layer on top of the Si substrate. The 5 nm thick Ti or Ta film of the bottom electrodes serves as adhesion layer. The Pt bottom electrode acts as active electrode and the Ta or Ti top electrode as ohmic electrode.

The fabrication of the Ta1 and Ta2 device is described in [37] and is similar to the one presented in [94, 155]. The protocol of the fabrication process can be found in the appendix

Table 3.1.: List of VCM devices used for the SET (Ta1, Ta2, Ta3, Zr1, HfA2, and HfB1 device, see chapter 4) and RESET kinetics (Ta3, Zr1, Ta-C, Zr-C, HfA1, HfA3, HfB2, and HfB3 device, see chapter 5).

Identifier	Mask	Bottom electrode	Active layer(s)	Top electrode	Size [μm^2]	Literature
Ta1	A	Ti (5 nm)\Pt (25 nm)	TaO_x (5 nm)	Ta (5 nm)\Pt (25 nm)	15×20	[37]
Ta2	A	Ti (5 nm)\Pt (25 nm)	TaO_x (5 nm)	Ta (5 nm)\Pt (25 nm)	5×5	[37]
Ta3	B	Ti (5 nm)\Pt (30 nm)	TaO_x (5 nm)	Ta (20 nm)\Pt (30 nm)	2×2	[148, 149]
Ta-C	B	Ti (5 nm)\Pt (30 nm)	C (1.5 nm)\TaO_x (5 nm)	Ta (20 nm)\Pt (30 nm)	3×2	[150]
Zr1	B	Ti (5 nm)\Pt (30 nm)	ZrO_x (5 nm)	Ta (20 nm)\Pt (30 nm)	2×2	[151, 152]
Zr-C	B	Ti (5 nm)\Pt (30 nm)	C (1.5 nm)\ZrO_x (5 nm)	Ta (20 nm)\Pt (30 nm)	2×2	[150–152]
HfA1	B	Ti (5 nm)\Pt (25 nm)	HfO_x (3 nm)\TiO_x (3 nm)	Ti (10 nm)\Pt (20 nm)	2×3	[153]
HfA2	B	Ti (5 nm)\Pt (25 nm)	HfO_x (3 nm)\TiO_x (3 nm)	Ti (10 nm)\Pt (20 nm)	3×3	[153]
HfA3	B	Ti (5 nm)\Pt (25 nm)	HfO_x (3 nm)\TiO_x (3 nm)	Ti (10 nm)\Pt (20 nm)	4×4	[153]
HfB1	B	Ta (5 nm)\Pt (25 nm)	HfO_x (3 nm)\TiO_x (3 nm)	Ti (10 nm)\Pt (20 nm)	3×3	[153, 154]
HfB2	B	Ta (5 nm)\Pt (25 nm)	HfO_x (3 nm)\TiO_x (3 nm)	Ti (10 nm)\Pt (20 nm)	2×2	[153, 154]
HfB3	B	Ti (5 nm)\Pt (25 nm)	HfO_x (3 nm)\TiO_x (3 nm)	Ti (10 nm)\Pt (20 nm)	10×10	[153, 154]

section A. The Ti and Pt layer of the bottom electrode and the active material (TaO_x) were deposited by RF magnetron sputtering. The Ta and Pt layers of the top electrode were deposited by physical vapor deposition.

The CPW structure was fabricated using optical lithography with mask A, which is depicted to scale in fig. 3.1a. The CPW structure consists of the bottom electrode's layers (Ti(5 nm)\Pt(25 nm)) and has a length of 930 µm. The central conductor has a width of $w = 100\,\mu m$ and a spacing of $s = 60\,\mu m$ to the outer conductors. At the center of the CPW structure of the Ta1 device, the width of the inner conductor narrows to $w = 20\,\mu m$ and the spacing to the outer conductor to $s = 10\,\mu m$. The length of the narrowed area amounts to 50 µm. In case of the Ta2 device, the width narrows to $w = 5\,\mu m$ and the spacing to $s = 4\,\mu m$. On the left side, the inner conductor consists of the bottom electrode's materials and on the right side, it consists of the top electrode's materials. In case of the Ta1 device, both electrodes overlap over a length of 15 µm and in case of the Ta2 device over a length of 5 µm. This results in a $15 \times 20\,\mu m^2$ (Ta1) and a $5 \times 5\,\mu m^2$ (Ta2) large VCM device. The TaO_x layer is sandwiched between the two electrodes. The overlapping area is referred to as A and is depicted in fig. 3.1b. The size of the VCM devices is indicated as $x \times y$, in which x represents the overlapping area's length parallel to the inner conductor and y the overlapping area's width perpendicular to the inner conductor. The dimension x and y are also illustrated in fig. 3.1b.

Both devices were formed by applying a 4 V sweep to the active Pt electrode. To prevent the devices from damage, a current compliance (CC) of 100 µA is used.

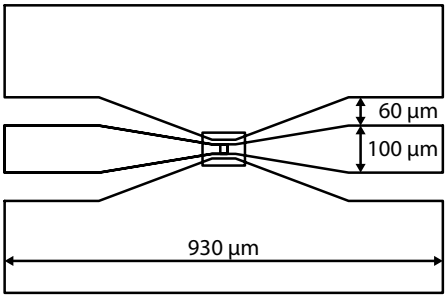

(a) Mask of CPW structure (to scale).

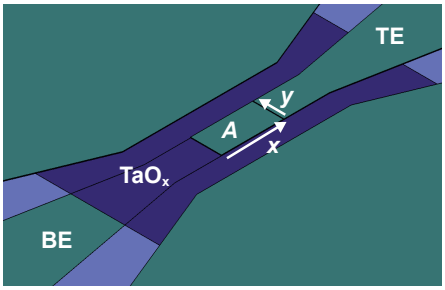

(b) Center of CPW structure.

Figure 3.1.: (a) CPW structure of the Ta1 device (to scale). (b) Zoom into the center of the CPW structure. The bottom and top electrode overlap in the area A. The length x and width y of the overlapping area are also indicated, corresponding to the definition of the device size ($x \times y$).

The stack of these VCM devices constitutes a parallel plate capacitor. Its capacitance has a significant influence on the devices' electrical charging times (see section 3.2.4) and consequently also on their switching kinetics, which is shown in chapter 4.3. To reduce the capacitive effects, mask B includes smaller devices, down to $2 \times 2\,\mu m^2$. In this case, the spacing to the outer conductors of the CPW structure amounts to $s = 2\,\mu m$. As shown at the end of section 3.2.4, smaller devices would have an even shorter electrical charging

time. Smaller devices can, however, not be produced with the available optical lithography, as its resolution is limited at 2 µm. Also, larger devices up to $30 \times 10\,\mu m^2$ were placed on the mask. The overall length of the device has also been reduced to 590 µm, which decreases the size of the contact pads and, thereby, reduces the capacitances between the inner and outer conductors as shown below in section 3.2.2. For smaller devices the narrowed area's length has been reduced from 50 µm to 10 µm. This is illustrated in fig. 3.2, which compares mask A with mask B. All devices listed in table 3.1, except the Ta1 and Ta2 device, were fabricated with mask B.

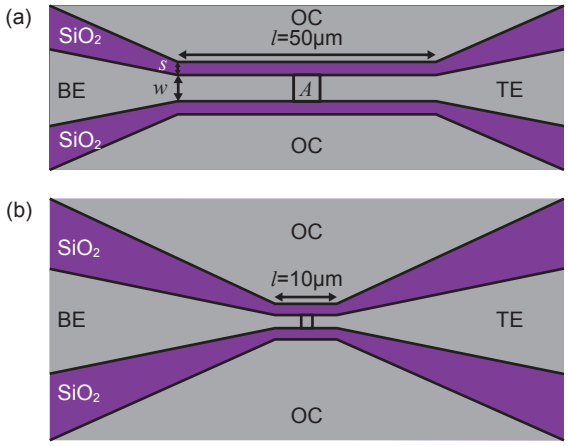

Figure 3.2.: Zoom into the mask's center of (a) mask A (Ta2) and (b) mask B (Ta3). Both figures are on the same length scale. The outer conductors of the CPW structure are labeled as OC. The inner conductor consists of the bottom (BE) and the top electrode (TE), which overlap in the area A. The narrowed width w of the inner conductor and its spacing to the outer conductor s are also indicated. The length of the narrowed area l has been shortened on mask B from 50 µm to 10 µm.

All materials of the Ta3, Zr1, Ta-C, and Zr-C devices were deposited by means of RF magnetron sputtering [148, 149, 151, 152]. The additional C layer in the Ta-C and Zr-C device serves as oxygen-blocking layer [150,156]. The devices were formed by applying a -4 V sweep to the active Pt electrode with a current compliance of 100 µA.

The endurance of the Ta3 device was already demonstrated in [157], showing an endurance of up to 10^6 cycles. The highest measured endurance for TaO_x-based devices amounts to 10^{12} cycles [88]. Until 2020, only an endurance of up to 10^4 cycles had been reported for the ZrO_x-based devices [73]. The endurance of a $5 \times 5\,\mu m^2$ crossbar ZrO_x-based device was, therefore, measured and published in the supplementary information of [38]. The SET and RESET voltages, were chosen to 0.9 V and -1.8 V, respectively, and the resistance was read at -0.2 V. No current compliance was used. The measurement is shown in fig. 3.3 and was aborted after 10^6 cycles, although the device was still operable. A higher endurance of up to 10^7 cycles was recently reported for ZrO_x-based devices [90]. As Zr is chemically similar to Hf [158], HfO_x-based and ZrO_x-based devices may also have a similar endurance. For HfO_x-based devices an endurance of up 10^9 cycles has been reported [89], which could also be possible for ZrO_x-based devices.

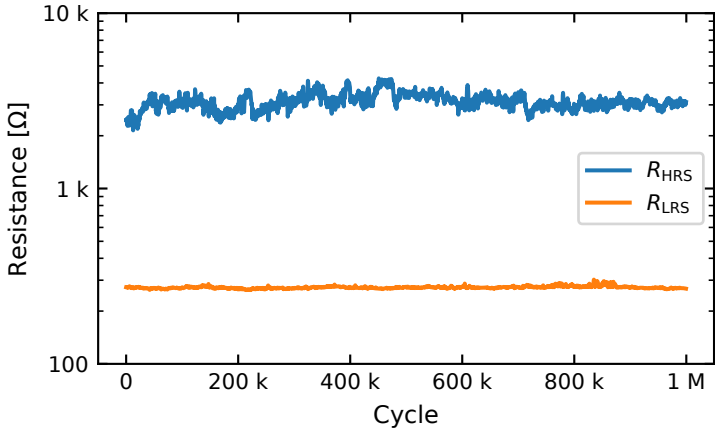

Figure 3.3.: Endurance measurement of a $5 \times 5\,\mu m^2$ ZrO_x-based crossbar device. The fabrication process is identical to the one of the Zr1 device. Only a different mask has been used. The measurement has been conducted with a Keithley 2636A SMU. Taken from the supplementary information of [38].

The HfA1, HfA2, and HfA3 devices are on the same wafer, which is referred to as HfAx and, in analogy, the devices HfB1, HfB2 and HfB3 are also on one wafer, which is referred to as HfBx. The HfAx and HfBx devices have an almost identical fabrication process. The flow chart of the fabrication process can be found in the appendix section A [153]. The only difference between both samples is the deposition of the bottom electrode. The Ti and Pt layers of the HfAx devices' bottom electrode were deposited by RF magnetron sputtering. An off-axis sputter tool was used for the deposition of the Ta and Pt layers of the HfBx devices' bottom electrode [154]. The Ta layer was deposited by RF magnetron sputtering and the Pt layer by DC sputtering. The TiO_x and HfO_x films were deposited by atomic layer deposition. The Ti and Pt layers of the top electrode were again deposited by means of RF magnetron sputtering. The devices were again formed by applying a -4 V sweep to the active Pt electrode with a current compliance of 100 µA.

The active layer of the HfAx and HfBx devices is the HfO_x layer, which is at the interface to the Pt bottom electrode. The additional TiO_x layer acts as serial resistance and reduces the VCM device's variability significantly with regard to SET and RESET voltages [42,159]. These VCM devices can also be operated in an analogous mode, which is beneficial for neuromorphic applications [160,161]. As mentioned above, HfO_x-based devices can achieve an endurance of up 10^9 cycles [89].

3.2. Characterization

All investigated devices (see table 3.1) were characterized with regard to their *IV* characteristics, capacitances, scattering parameters and electrical charging time.

3.2.1. IV characteristics

The *IV* characteristics of the Ta1, Ta2, Ta3, and Zr1 devices were conducted with a Keithley 2634B SMU and are shown in fig. 3.4. The sweep settings can be found in table 3.2. The *IV* characteristics of all four sample are typical for VCM devices, as they have a nonlinear HRS and a linear LRS. The Ta1 and Ta2 devices were operated in a different resistance window than the Ta3 and Zr1 devices, which originates from higher SET and RESET voltages used in the sweeps of the Ta1 and Ta2 devices. Also, no current compliance was used during their SET sweep. The HRS of the Ta1 and Ta2 is in the range of from 2 kΩ to 10 kΩ and their LRS in the range from 200 Ω to 400 Ω.

Table 3.2.: Settings of the *IV* characteristics shown in fig. 3.4.

Device	Sweep rate	SET Voltage	RESET Voltage	CC
Ta1	$0.1\,^{V}/_{s}$	−1.5 V	2.0 V	-
Ta2	$0.1\,^{V}/_{s}$	−1.5 V	2.0 V	-
Ta3	$0.5\,^{V}/_{s}$	−1.0 V	1.6 V	300 µA
Zr1	$0.5\,^{V}/_{s}$	−1.2 V	1.6 V	300 µA
Ta-C	$0.5\,^{V}/_{s}$	−1.2 V	1.6 V	300 µA
Zr-C	$0.5\,^{V}/_{s}$	−1.2 V	1.6 V	300 µA
HfA2	$0.5\,^{V}/_{s}$	−1.2 V	1.2 V	300 µA
HfB3	$0.5\,^{V}/_{s}$	−1.2 V	1.2 V	300 µA

The Ta3 and Zr1 devices were later used in the automated setup (see chapters 2.1.2 and 4.2), which requires the collection of a large data set and, consequently, a high endurance. To reduce the stress on the devices, lower SET and RESET voltages were chosen and a current compliance of 300 µA was used during the SET sweeps. The HRS of the Ta3 and Zr1 devices is in the range from 10 kΩ to 30 kΩ. The LRS of the Ta3 and Zr1 device is in the range from 1.0 kΩ to 3.0 kΩ.

The *IV* characteristics of the Ta-C, Zr-C, HfA2, and HfB3 (representing the devices on the HfAx and HfBx wafer, respectively) devices are shown in fig. 3.5. To achieve a comprehensive statistic, these devices were also protected with a current compliance of 300 µA during the SET sweep.

The additional C layer in the Ta-C and Zr-C devices has no significant impact on the *IV* characteristics. Both devices could be operated in a resistance window between 1.0 kΩ and 3.0 kΩ in the LRS and between 10 kΩ and 30 kΩ in the HRS, which is identical to the resistance window of the Ta3 and Zr1 devices. Also, the settings in the sweeps (see table 3.2) are identical. The Ta-C and Zr-C devices also have a nonlinear HRS and a linear LRS.

The HfAx and HfBx devices were operated in a different resistance window. The settings for the SET sweep were chosen identically as the ones of the previous devices (SET voltage: -1.2 V, current compliance: 300 µA) reaching the same LRS window (between 1.0 kΩ and 3.0 kΩ). The HfAx and HfBx devices, however, have a significant higher HRS and, therefore,

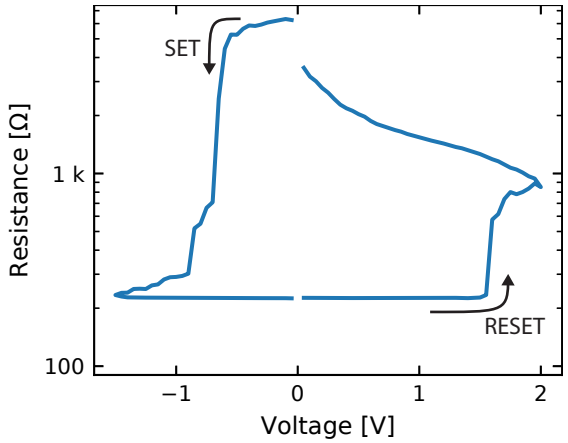

(a) Ta1 device. Redrawn from [119].

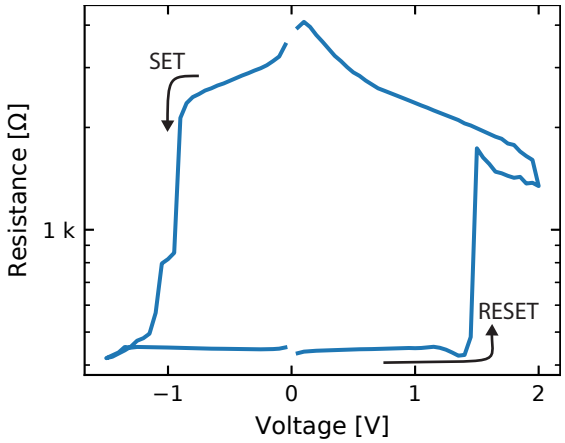

(b) Ta2 device.

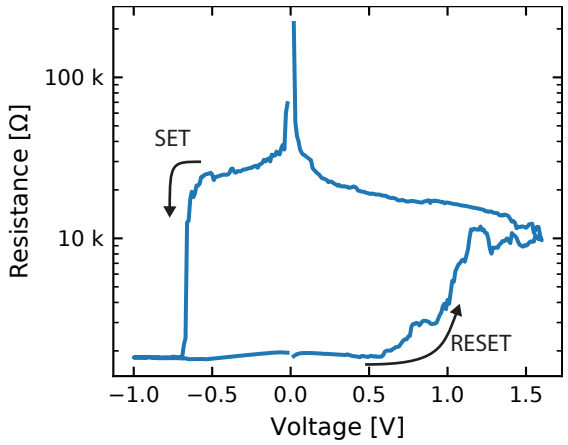

(c) Ta3 device. Redrawn from [38], with the permission of AIP Publishing.

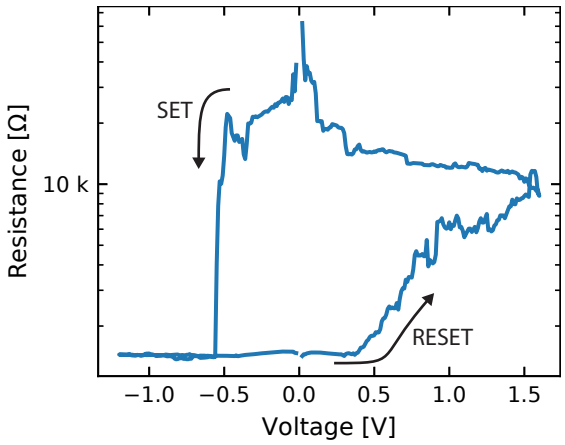

(d) Zr1 device. Redrawn from [38], with the permission of AIP Publishing.

Figure 3.4.: *IV* characteristics of the Ta1, Ta2, Ta3, and Zr1 devices (see table. 3.1). The settings of the sweeps are listed in table 3.2).

the RESET voltage was reduced from 1.6 V to 1.2 V, because otherwise the HRS would be shifted to resistances above 100 kΩ. The HRS is again nonlinear. After the initial elctroforming process, the devices have a linear LRS (see fig. 3.5c), which becomes slightly nonlinear with the number of driven cycles (see fig. 3.5d).

3.2.2. Capacitances

All capacitances were measured with an HP 4284A LCR meter at a frequency of 1 MHz and a stimulus of 50 mV.

Capacitances of the CPW structure

Firstly, the capacitances between the inner and outer conductors of the Ta2 and Ta3 device were measured. They amount to 1.27 pF for the Ta2 and to 0.82 pF for the Ta3 device. This results from the reduction of the contacting pad sizes on mask B, as explained above in chapter 3.2.1. These capacitances yield a low capacitive reactance for high frequencies

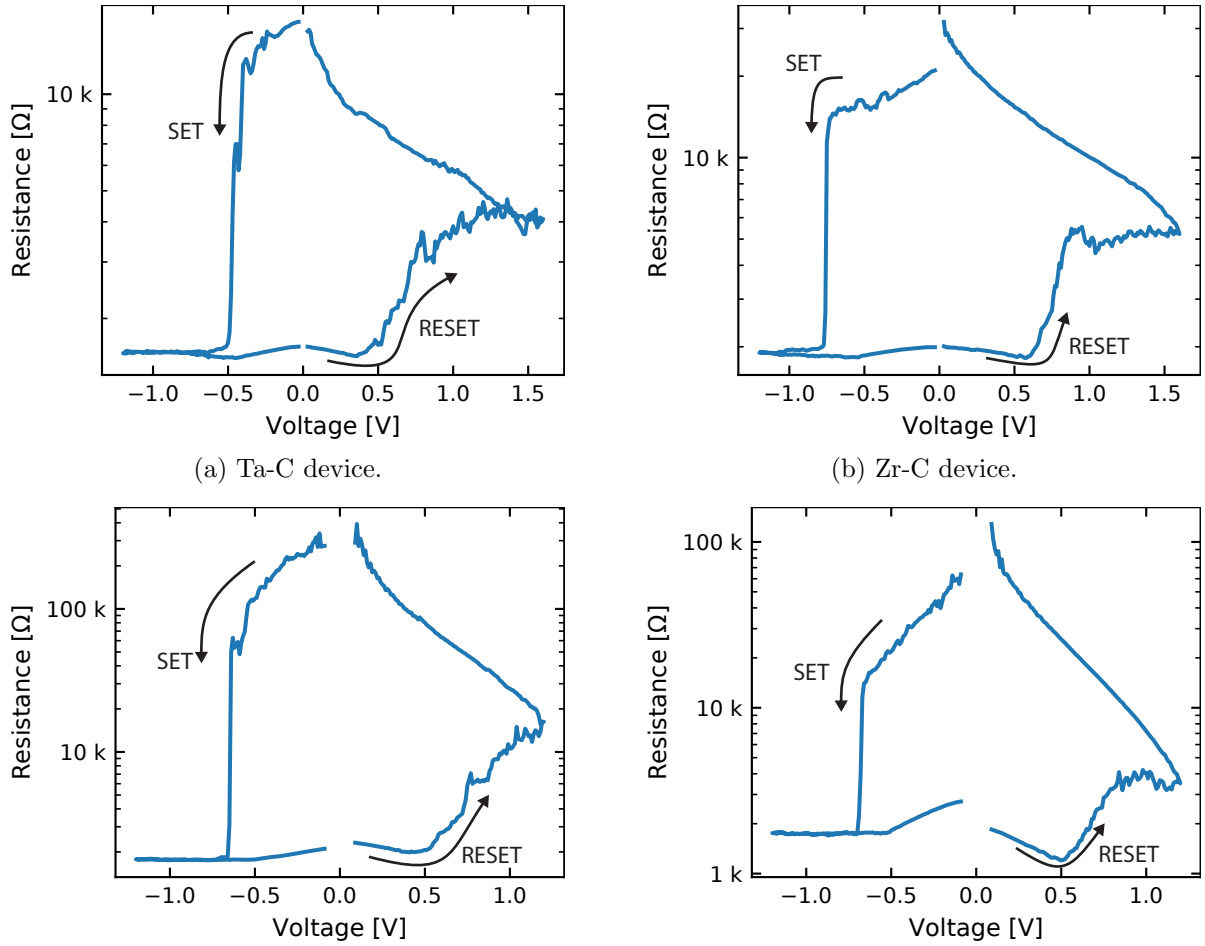

(a) Ta-C device.

(b) Zr-C device.

(c) HfA2 device.

(d) HfB3 device.

Figure 3.5.: *IV* characteristics of the Ta-C, Zr-C, HfA2, and HfB3 device (table 3.1. The settings of the sweeps are listed in table 3.2.

and, therefore, higher frequencies are more easily transmitted from the inner to the outer conductor, which increases the electrical charging time. The smaller contacting pads on mask B, consequently, contribute to faster electrical charging times.

Capacitances of VCM stack

Subsequently, the capacitances of the devices listed in table 3.1 were measured and are summarized in table 3.3, sorted by the device size.

The capacitance clearly scales with the device size. Although, the Ta3 and the Zr1 device have an identical device area, the Ta3 device has a higher capacitance. This cannot originate from the relative permittivity, which is higher for ZrO_x ($\epsilon_r = 28.5$ [91]) than for TaO_x ($\epsilon_r = 26$ [162]). The discrepancy in the capacitance most likely originates from alignment mismatches. Measuring the capacitance of a different $2 \times 2\,\mu m^2$ device on the Ta3 device's wafer resulted in a capacitance of 0.28 pF, indicating a relative strong device-to-device variability. This correlates with the optical lithographic resolution, which is around 2 µm and,

Table 3.3.: Capacitances of the measured devices' VCM stack (see table 3.1), sorted by device size. Measurements were conducted with an HP 4284A LCR meter.

Device	Device size	Capacitance
Ta3	$2 \times 2\,\mu m^2 \mathrel{\widehat{=}} 4\,\mu m^2$	0.38 pF
Zr1	$2 \times 2\,\mu m^2 \mathrel{\widehat{=}} 4\,\mu m^2$	0.29 pF
Zr-C	$2 \times 2\,\mu m^2 \mathrel{\widehat{=}} 4\,\mu m^2$	0.31 pF
Ta-C	$3 \times 2\,\mu m^2 \mathrel{\widehat{=}} 6\,\mu m^2$	0.41 pF
HfA1	$2 \times 3\,\mu m^2 \mathrel{\widehat{=}} 6\,\mu m^2$	0.32 pF
HfA2	$3 \times 3\,\mu m^2 \mathrel{\widehat{=}} 9\,\mu m^2$	0.42 pF
HfB1	$3 \times 3\,\mu m^2 \mathrel{\widehat{=}} 9\,\mu m^2$	0.44 pF
HfB2	$5 \times 3\,\mu m^2 \mathrel{\widehat{=}} 15\,\mu m^2$	0.71 pF
HfA3	$4 \times 4\,\mu m^2 \mathrel{\widehat{=}} 16\,\mu m^2$	0.80 pF
Ta2	$5 \times 5\,\mu m^2 \mathrel{\widehat{=}} 25\,\mu m^2$	1.11 pF
HfB3	$10 \times 10\,\mu m^2 \mathrel{\widehat{=}} 100\,\mu m^2$	1.96 pF
Ta1	$15 \times 20\,\mu m^2 \mathrel{\widehat{=}} 300\,\mu m^2$	4.60 pF

consequently, on the same length scale as the device size. Calculating the capacitance $C_{||}$ with the formula of a parallel plate capacitor:

$$C_{||} = \frac{\epsilon_0 \epsilon_r A}{d_{Ox}} \tag{3.1}$$

results in 0.18 pF for the Ta3 device and to 0.20 pF for the Zr1 device. As indicated in table 3.1, the oxide thickness d_{Ox} amounts to 5 nm and the device size A to $4\,\mu m^2$. The deviation between the calculated and measured capacitances originates from additional angular capacitances. This argumentation was also used in [38]. The capacitances of the Ta-C and the Zr-C devices are a little larger than the ones of the Ta and the Zr device.

An analogous estimation was conducted with the HfAx and HfBx device's stack. They have a 3 nm thick HfO_x and a 3 nm thick TiO_x in series, which changes the formula of the parallel plate capacitance $C_{||}$ to

$$C_{||} = \frac{\epsilon_0 A}{d_{Ox}} \cdot \frac{\epsilon_{r,HfOx}\epsilon_{r,TiOx}}{\epsilon_{r,HfOx} + \epsilon_{r,TiOx}}. \tag{3.2}$$

Using the values $A = 6\,\mu m^2$, $d_{Ox} = 3\,nm$, $\epsilon_{r,TiOx} = 12.3$ [163], and $\epsilon_{r,HfOx} = 14.0$ [164,165] for the HfA1 device results in $C_{||} = 0.12\,pF$. This capacitance is significantly below the measured value of 0.32 pF, which is again probably due to the negligence of angular capacitances and alignment mismatches. Calculating the capacitance for the much larger HfB3 device ($A = 100\,\mu m^2$) results in 1.93 pF, which is close to the measured capacitance of 1.96 pF.

As shown in chapter 3.2.4, the capacitances of the CPW structure and of the VCM device's stack have a significant impact on the scattering parameters and on the devices' electrical charging time. In consequence, they also delay the switching kinetics, as demonstrated in chapter 4.1.

3.2.3. Scattering parameters

The measurements of the scattering parameters were conducted in the range from 50 MHz to 40 GHz (see chapter 2.1.3). In general, a high reflection at the VCM device for all frequencies is desired. Frequencies, transmitted through the device, do not contribute to its electrical charging. Consequently, the charging time of the device increases, which is disadvantageous for fast measurements. As shown in chapter 2.2.2, it can take up to 2.54 ns to charge a VCM device.

Ta1, Ta2, Ta3, and Zr1 devices

The scattering parameters of the Ta1, Ta2, Ta3 and Zr1 device are shown in fig 3.6. The lowest forward reflection S_{11} is observed for the Ta1 device (see blue line in fig. 3.6a). Already at 1 GHz, the reflection is attenuated by 10 dB, meaning that only 10 % of the signal is reflected. Oppositely, the Ta1 device has the highest forward transmission S_{21} in the range below 3 GHz (see blue line in fig. 3.6b). This is due to the high capacitance of the Ta1 device, which amounts to 4.6 pF (see table 3.3). Higher frequencies are, therefore, transmitted through the VCM device and are missing in the reflection. The crossing with the Ta3 and Zr1 devices' forward transmission between 3 GHz and 10 GHz is explained below.

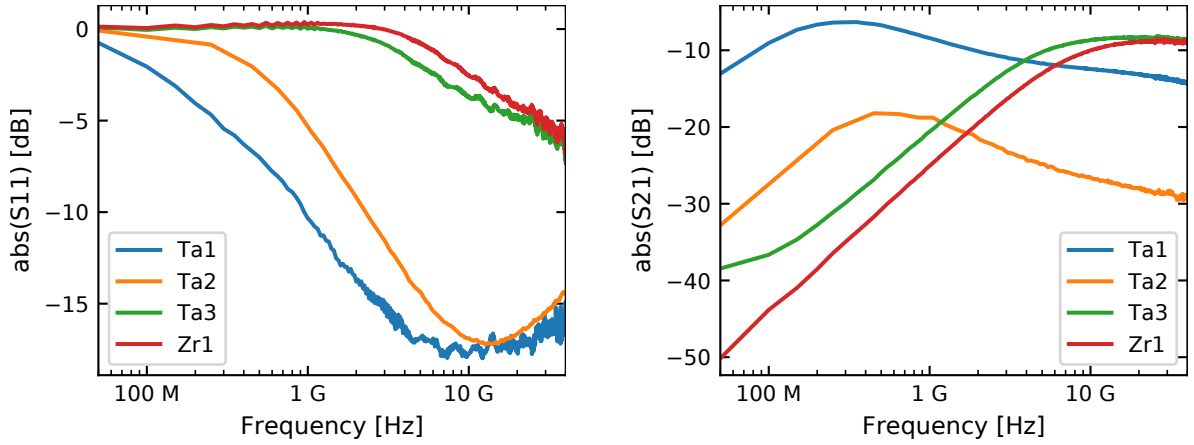

(a) S_{11} (b) S_{21}

Figure 3.6.: Absolute values of the (a) forward reflection S_{11} and (b) the forward transmission S_{21} of the Ta1, Ta2, Ta3 and Zr1 device (see table 3.1). The measurement was conducted with the VNA HP 8722ES.

The overlap of the bottom and top electrode of the Ta2 device is significantly smaller ($5 \times 5\,\mu m^2$), corresponding to an overlapping surface of $25\,\mu m^2$. For comparison, the Ta1 device's size amounts to $300\,\mu m^2$. Consequently, the Ta2 device has a significantly smaller capacitance, which amounts to 1.11 pF (see table 3.3). For that reason, the forward reflection S_{11} of the Ta2 device is higher (see orange line in fig. 3.6a) and its forward transmission S_{21} (see orange line in fig. 3.6b) is lower than S_{11} and S_{21} of the Ta1 device, respectively. The

crossing with the Ta3 and Zr1 devices' forward transmission between 1 GHz and 2 GHz is explained below.

The Ta3 and Zr1 device are smaller ($2 \times 2\,\mu m^2$) than the Ta1 and Ta2 device and, consequently, also have a smaller capacitance (0.38 pF and 0.29 pF, respectively). For that reason, the forward reflection S_{11} of the Ta3 and Zr1 device (see green and red line in fig. 3.6a) is higher than S_{11} of the Ta1 and Ta2 device. Analogously, the forward transmission S_{21} of the Ta3 and the Zr1 device (see green and red line in fig. 3.6b) is lower than S_{21} of the Ta1 and Ta2 device, up to a frequency of 1GHz. The Ta3 device has a little lower S_{11} and a little higher S_{21} than the Zr1 device, which is attributed to its higher capacitance (see table 3.3). Above 7 GHz, S_{21} of both, the Ta3 and the Zr1 device, is above S_{21} of the Ta1 and Ta2 device. This results from the lower bandwidth of the Ta1 and Ta2 devices' CPW structure, which is explained in the following.

The forward transmission S_{21} increases for all four devices in fig. 3.6b with the frequency, up to a certain point. The Ta1 and Ta2 devices' S_{21} reaches a maximum at about 300 MHz and at about 500 MHz, respectively, after which S_{21} decreases with increasing frequency. The Ta3 and Zr1 devices' S_{21} increases with the frequency up to about 10 GHz and 20 GHz, respectively. Up to this maximum, S_{21} is limited by the VCM device's capacitance, at which low frequencies are reflected, while high frequencies are transmitted through the device. After the maximum of S_{21} is reached, S_{21} is no longer limited by the VCM device's capacitance, but by the bandwidth of the CPW structure. This bandwidth prevents higher frequencies to reach the VCM device at the center of the CPW structure and also attenuates the part of the signal, which has been transmitted through the VCM device.

To demonstrate the influence of the CPW structure's bandwidth on the measured S_{21} in fig. 3.6b, the S_{21} of two CPW through structures without VCM device at the center was measured. The Ta1 device's CPW through structure is on the same wafer as the Ta1 device itself and, consequently, corresponds to the design of mask A and its material stack is identical to one of the Ta1 device's bottom electrode. The width of its inner conductor was reduced to $w = 20\,\mu m$ over a length of $w = 50\,\mu m$ (see also fig. 3.2(a)). Analogously, the Zr1 device's CPW through structure is one the same wafer as the Zr1 device itself and its design corresponds to the layout of mask B. Its inner conductor width was reduced to $w = 2\,\mu m$ over a length of $w = 10\,\mu m$ (see also fig. 3.2(b)). Consequently, the CPW through structures have the same attributes as their corresponding devices with regard to the CPW structure's geometry and the bottom electrode's material stack.

The forward transmission S_{21} of the CPW through structure are shown in fig. 3.7. The S_{21} of the Ta1 device's CPW through structure (solid blue line) starts at -5.5 dB and depends only slightly on the frequency up to about 300 MHz, after which it decreases with increasing frequency reaching -15.3 dB at 40 GHz. The S_{21} of the Zr1 device's CPW through structure (solid red line) barely depends on the frequency, starting at -8.0 dB and reaching -8.9 dB at 40 GHz.

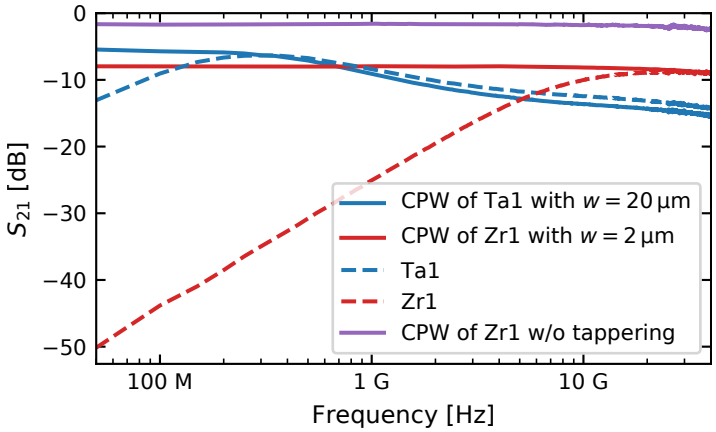

Figure 3.7.: CPW through structure's forward transmissions of the Ta1 (blue solid line) and the Zr1 (red solid line) device having a width of $w = 20\,\mu m$ and $w = 2\,\mu m$, respectively. The length of the narrowed area amounts to $50\,\mu m$ for the Ta1 device and to $10\,\mu m$ for the Zr1 device. The forward transmission S_{21} of the Ta1 and Zr1 device (from fig. 3.6b) is shown as dashed line, in blue and red, respectively. The S_{21} of a CPW through structure without width reduction and a length of $590\,\mu m$ (from $930\,\mu m$) is shown as solid violet line (from fig. 2.10a).

The blue dashed line in fig. 3.7 corresponds to S_{21} of the Ta1 device. At about 300 MHz, the S_{21} of both structures coincide, marking the frequency, at which S_{21} is no longer limited by the capacitance of the VCM device, but by the usable bandwidth of the CPW structure. The slight deviation of S_{21} at higher frequencies might originate from the top electrode's material stack. The S_{21} of the Ta1 device's CPW through structure was only measured with the bottom electrode's material, which might by different from the S_{21} of the top electrode. Although, the thickness of the Pt layers is identical (25 nm as shown in table 3.1), they were deposited differently: once by RF magnetron sputtering (BE) and once by physical vapor deposition (TE), as described in chapter 3.1.

A similar argumentation can explain the trend of the S_{21} of the Zr1 device, which is shown as red dashed line in fig. 3.7 (also in fig. 3.6b). At about 20 GHz, the S_{21} of the Zr1 device and its CPW through structure coincide, marking again the frequency, at which the Zr1 device's S_{21} is no longer limited by the capacitance of the VCM device, but by the bandwidth of its CPW structure. No deviation occurs at frequencies above 20 GHz, which might originate from the similarity of the Zr1 device's top and bottom electrodes. Both contain a 30 nm thick Pt layer and both were deposited by means of RF magnetron sputtering. The main reason for the better bandwidth of the Zr1 device compared to the bandwidth of the Ta1 device is the shorter length of the narrowed area.

The S_{21} of both narrowed CPW through structures is much lower than S_{21} of a CPW structure without narrowed area (shown as violet line in fig. 3.7), which has a S_{21} above -3 dB at all frequencies. This was already shown in fig. 2.10a from chapter 2.1.3. The through structure without narrowed area is identical to the Zr1 device's through structure, with regard to the length of the CPW structure (amounting to $590\,\mu m$) and to the bottom

electrode's material stack. As the constant width of $w = 100\,\mu m$ is the only difference between those two through structures, the decrease of S_{21} must originate from the reduction in width of the inner conductor.

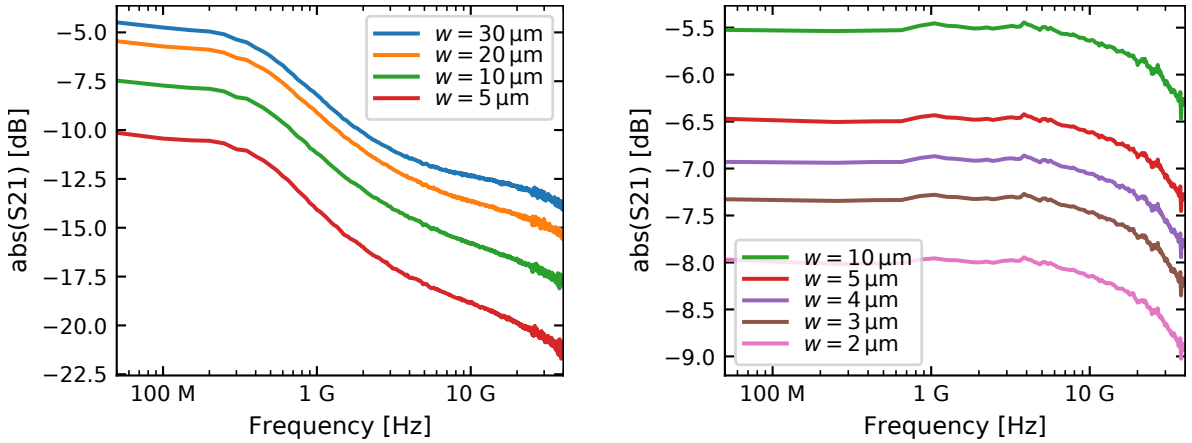

(a) CPW through structures on the Ta1 device's wafer.

(b) CPW through structures on the Zr1 device's wafer.

Figure 3.8.: Forward transmission S_{21} for different linewidths of the CPW through structures on the (a) Ta1 device's and on the (b) Zr1 device's wafer. No VCM device was integrated in the CPW structure.

This is also illustrated in fig. 3.8, in which the forward transmission S_{21} of the CPW through structures on the (a) Ta1 device's wafer and on the (b) Zr1 device's wafer are shown. The Ta1 device's CPW through structures were fabricated with mask A, having an overall length of 930 µm and a narrowed area's length of 50 µm. The Zr1 device's CPW through structures were fabricated with mask B, having an overall length of 590 µm and a narrowed area's length of 10 µm. The CPW through structures' S_{21} on both wafers scales inversely with the linewidth w. This confirms the dependence of the VCM devices' S_{21} at higher frequencies (see fig 3.6b) on the bandwidth of their CPW structure.

In general, the S_{21} of the CPW through structures on the Zr1 device's wafer is higher than the CPW through structures on the Ta1 device's wafer. CPW through structures with a narrowed areas' width of $w = 10\,\mu m$ (shown in green) and $w = 5\,\mu m$ (shown in red) exit on both wafers. At $w = 10\,\mu m$, S_{21} varies between -7.5 dB at 50 MHz and -17.9 dB at 40 GHz on the Ta1 device's wafer, while it varies between -5.5 dB at 50 MHz and -6.3 dB at 40 GHz on the Zr1 device's wafer. A similar observation can be made at $w = 5\,\mu m$. The better performance of the CPW through structures on the Zr1 device's wafer can be explained in part by the shorter overall length of the CPW structure, which reduces the capacitance between the inner and the outer conductors from 1.27 pF to 0.82 pF (see chapter 3.2.2). This reduction of 35.4 %, however, cannot explain the reduction of S_{21} by more than 12 dB at 40 GHz, as observed at a linewidth of $w = 10\,\mu m$ and $w = 5\,\mu m$. Also, the slight difference in the thicknesses of the Pt bottom electrodes (25 nm on the Ta1 device's wafer and 30 nm on the Zr1 device's wafer) cannot explain the change in S_{21} to this extend. The fabrication

of both bottom electrodes is very similar (see chapter 3.1). The only remaining explanation is the length of the narrowed area, which was reduced on mask B from 50 µm to 10 µm.

TaC and ZrC devices

The scattering parameters of the Ta-C (blue solid line) and Zr-C (orange solid line) device are shown in fig. 3.9. These two devices are very similar to the Ta3 and Zr1 devices (plotted as dashed line for comparison) and differ only by the additional C layer in the Ta-C and Zr-C devices. A $3 \times 2\,\mu m^2$ device was used for the Ta-C device, because the $2 \times 2\,\mu m^2$ devices on the Ta-C device's wafer were not operational. Both, the forward reflection S_{11} and the forward transmission S_{21}, behave similarly for all four devices, showing that the additional C layer has only a minor influence on the scattering parameters. For the Zr1 and ZrC device also values above 0 dB were measured, which result from an imprecise calibration of the VNA.

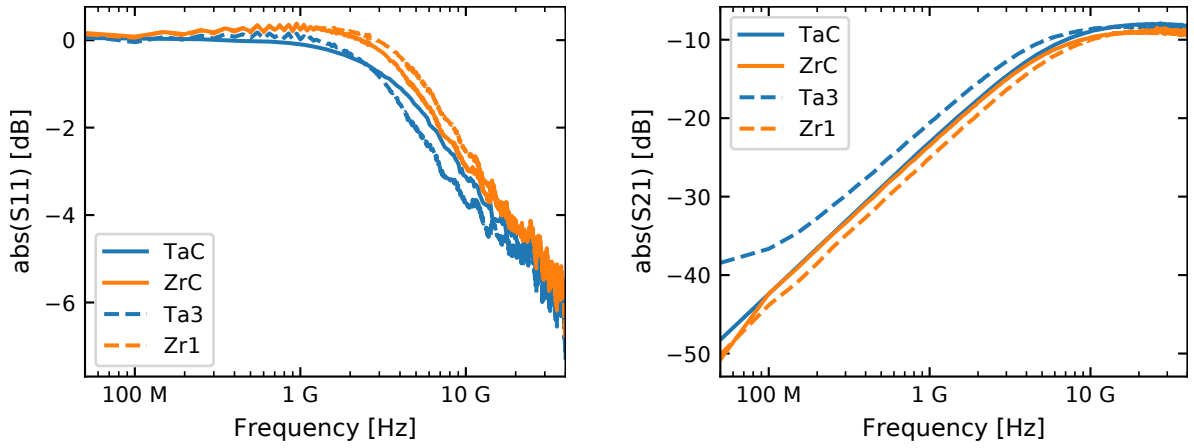

(a) S_{11} (b) S_{21}

Figure 3.9.: Absolute values of the (a) forward reflection S_{11} and (b) the forward transmission S_{21} of the Ta-C and Zr-C devices (solid lines). The scattering parameters of the Ta3 and Zr1 device from fig. 3.6 are also plotted as dashed lines for comparison.

HfAx and HfBx devices

The scattering parameters of the devices on the HfAx and HfBx wafer are shown in fig. 3.10 and fig. 3.11, respectively. Again, higher capacitances lead to a lower forward reflection S_{11} and a higher forward transmission S_{21}, following the trend of the other devices. The forward transmission S_{21} has again a maximum for all studied devices on the HfAx and HfBx wafer, which indicates that they are also limited by the bandwidth of their CPW structure at higher frequencies. The maximum is, however, always in the gigahertz regime. This results from the improvements on mask B, which are the smaller device size and the smaller dimensions of the CPW structure.

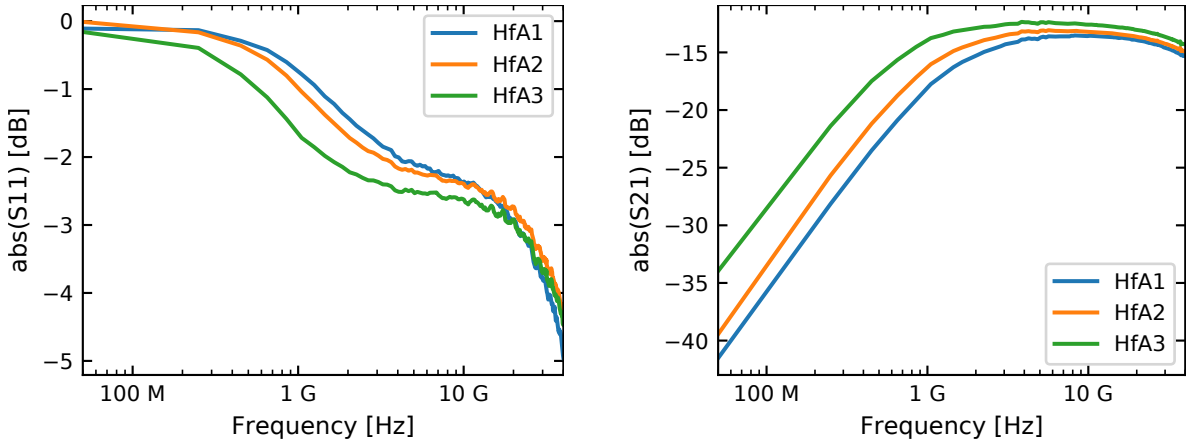

(a) S_{11} (b) S_{21}

Figure 3.10.: Absolute values of the (a) forward reflection S_{11} and (b) the forward transmission S_{21} of the HfAx wafer's devices.

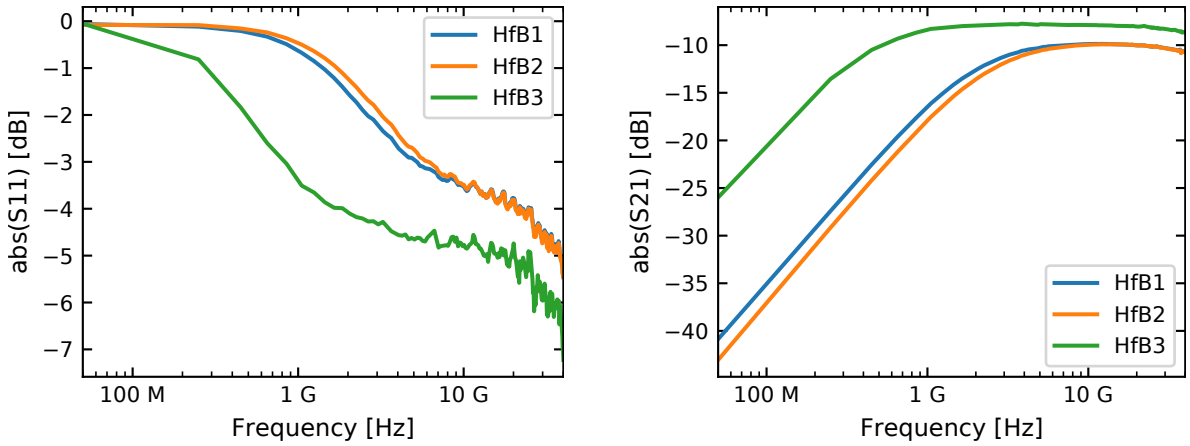

(a) S_{11} (b) S_{21}

Figure 3.11.: Absolute values of the (a) forward reflection S_{11} and (b) the forward transmission S_{21} of the HfBx devices.

Surprisingly the forward reflection S_{11} has two poles. The first occurs above 1 GHz and the second one above 10 GHz for all devices on the HfAx and HfBx wafer. All other devices only have one cut-off frequency, occurring above 1 GHz (except for the Ta1 and Ta2 device on mask A). This cannot be explained by the bandwidth of the CPW structure. The forward transmission S_{21} of the CPW through structure of the HfAx wafer, which is without VCM device, is shown in fig. 3.12 as blue line. The width of the inner conductor of the CPW through structure was reduced to 10 µm at the center. Its S_{21} is flat up to 10 GHz and can, therefore, not be the origin of the second pole. Its S_{21} is also similar to the CPW through structure of the Zr1 device (orange line).

The occurrence of the two cut-off frequencies originates from the HfO_x/TiO_x bilayer structure of the HfAx and HfBx devices, which constitutes two different capacitors in series. Firstly, the cut off frequency of the first capacitor is reached, at which it becomes conducting for these frequencies. This first cut-off frequency is reached at lower frequencies than

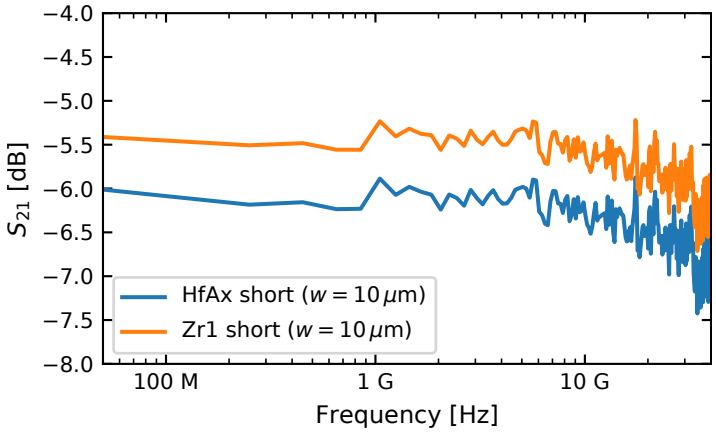

Figure 3.12.: CPW through structure's forwards transmissions S_{21} of the HfAx (blue solid line) and the Zr1 (orange solid line) device. Both structures have a narrowed width of $w = 10\,\mu$m.

for the other devices fabricated with mask B, due to the thinner layer thickness of 3 nm. Frequencies below 10 GHz, however, cannot yet pass the second capacitor and are, therefore, reflected, which explains the flattening of the forward reflection, after the first cut-off frequencies. At frequencies above 10 GHz the cut-off frequency of the second capacitor is reached and these frequencies are also transmitted through the second capacitor. This is supported by the fact that the first cut-off frequency depends on the device size. This is most prominent for the $10 \times 10\,\mu m^2$ large HfB3 device, for which the first cut-off frequency occurs much earlier as for the other devices on the HfAx and HfBx wafers (see fig. 3.11a). Both TiO_x and HfO_x have similar permittivities ($\epsilon_{r,TiOx} = 12.3$ [163], $\epsilon_{r,HfOx} = 12.0 - 14.0$ [165], both measured at 1 MHz) and consequently both layers should have a similar capacitance. Deviations from the layer thicknesses (3 nm) can also have an impact on the capacitance and, therefore, it remains unclear which layer has the larger capacitance and is responsible for the first cut-off frequency. As shown in the next section, the occurrence of two cut-off frequencies has a noticeable influence on the electrical charging time.

3.2.4. Electrical charging times

The scattering parameters obtained in the previous section, will be used in this section to derive the devices' electrical charging times. The method for deriving the time dependent voltage at the device $V_{DUT}(t)$ is explained in detail in chapter 2.2.2. The voltage at the device consists of the superposition of the incoming signal $v_1^+(t)$ and its reflection $v_1^-(t)$ at port 1 of the device, minus the transmitted signal $v_2^-(t)$ at port 2. This is described by eq. 2.15:

$$V_{DUT}(t) = v_1^+(t) + v_1^-(t) - v_2^-(t).$$

The incoming signal $v_1^+(t)$ is measured with the oscilloscope, and $v_1^-(t)$ and $v_2^-(t)$ are calculated using eq. 2.11 and eq. 2.16, respectively:

$$v_1^-(t) = \mathcal{F}^{-1}\left(\mathcal{F}(v_1^+(t)) \cdot S_{11}(f)\right),$$

$$v_2^-(t) = \mathcal{F}^{-1}\left(\mathcal{F}(v_1^+(t)) \cdot S_{21}(f)\right).$$

The forward reflection S_{11} and forward transmission S_{21} were derived in the previous section for each device in table 3.1. As described in chapter 1.4.2, the rise time (10 % - 90 %) is used as measure for the electrical charging time. Identically to chapter 2.2.2, a 10 ns long pulse[1] with an amplitude of -0.52 V serves as $v_1^+(t)$, having a rise time of 359 ps. To reduce the impact of the pulse generator's rise time on the device's rise time, a 250 ps long pulse with an amplitude of -0.79 V emitted by the PG5 pulse generator was used as $v_1^+(t)$ for devices with a rise time faster than 250 ps.

Ta1, Ta2, Ta3, and Zr1 devices

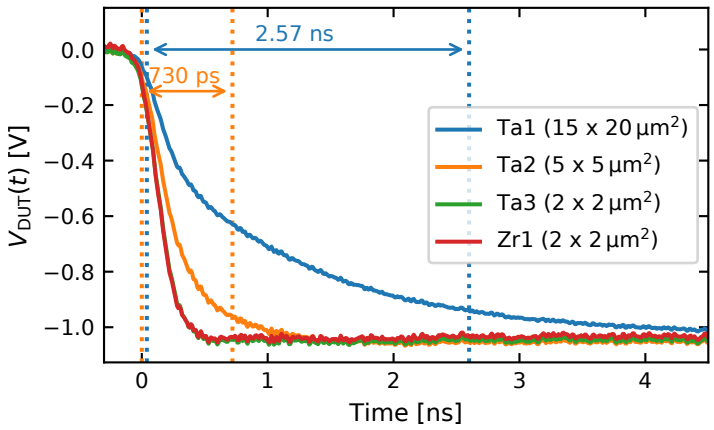

Figure 3.13.: $V_{DUT}(t)$ of the Ta1, Ta2, Ta3, and Zr1 device. Derived with eq. 3.2.4. The vertical dotted lines indicate the rise times (10 % - 90 %) of the Ta1 and Ta2 device. Adapted from [100].

The results for $V_{DUT}(t)$ of the Ta1, Ta2, Ta3, and Zr1 device are shown in fig. 3.13. The scattering parameters from fig. 3.6 were used. The result of the Ta1 device (blue line) was already shown in chapter 2.2.2. It has the slowest rise time with 2.57 ns, which is expected as this device's VCM stack is the largest ($15 \times 20\,\mu m^2$) and, consequently, also has the largest capacitance (4.60 pF, see table 3.3). This results in an increase in the forward transmission and a decrease in the forward reflection, as shown in fig. 3.6. The reflection at the VCM device, therefore, contains fewer high frequency components, which are necessary for steep rising edges.

[1] emitted by the PSPL 2600C pulse generator

The rise time of the Ta2 devices (orange line) is much shorter and amounts to 730 ps. This results from its smaller VCM stack ($5 \times 5\,\mu m^2$) and the resulting smaller capacitance (1.11 pF). The Ta3 and Zr1 devices are the smallest devices ($2 \times 2\,\mu m^2$) and, consequently, have the smallest capacitances (0.38 pF and 0.29 pF, respectively). This results in the steepest rising edges of $V_{DUT}(t)$ (green and red line), which are much shorter than the rise time of the used pulse generator (PSPL 2600C, $T_{PG} \approx 359$ ps).

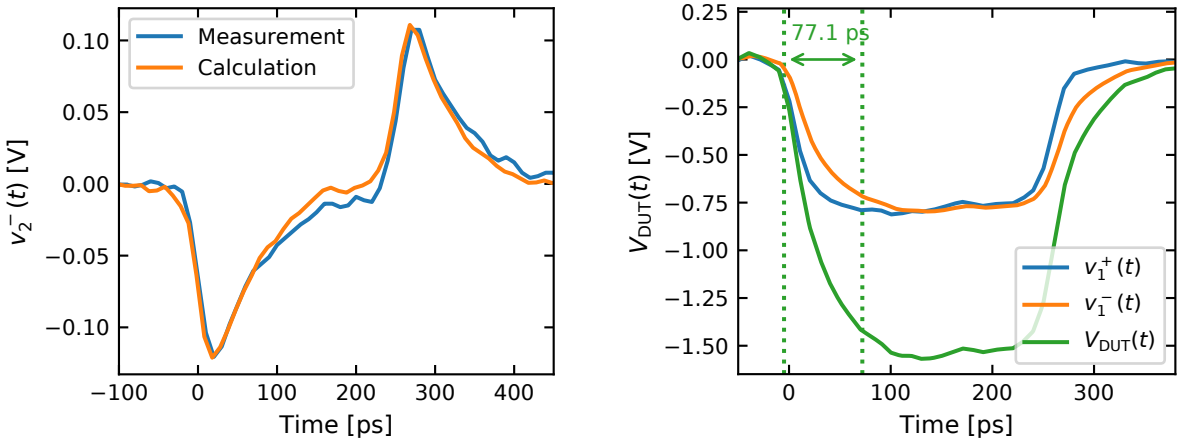

(a) $v_2^-(t)$ of the Ta3 device.

(b) $v_1^+(t)$, $v_1^-(t)$, and $V_{DUT}(t)$ of the Ta3 device.

Figure 3.14.: (a) Measured (blue) and calculated (orange) transmission $v_2^-(t)$ through the Ta3 device. The calculated transmission takes the cables' influence into account, as described in chapter 2.2.2. (b) Pulse $v_1^+(t)$ emitted by the pulse generator, reflection $v_1^-(t)$ and voltage $V_{DUT}(t)$ at the Ta3 device. Adapted from [100].

To circumvent this issue, the rise times of the Ta3 and Zr1 device were determined from a 250 ps pulse with an amplitude of -0.79 V emitted by the pulse generator PG5. It is shown in blue in fig. 3.14b. A voltage amplitude of -0.79 V was chosen, because it is the highest available voltage, at which both devices did not switch during the pulses' application. To verify that this approach is still valid on a subnanosecond timescale, the measured and calculated transmitted signals through the Ta3 device are shown in fig. 3.14a in blue and orange, respectively. For the calculated transmission the influence of the cables was taken into account (see chapter 2.2.2). The good overlap of the measured and the calculated transmitted voltage validates the approach also on a subnanosecond timescale.

In fig. 3.14b, the subsequent analysis is demonstrated on a subnanosecond timescale. In blue the pulse $v_1^+(t)$ emitted by the PG5 pulse generator is shown. Its reflection $v_1^-(t)$ (orange line) at the Ta3 device is calculated using eq. 3.2.4 and its transmission $v_2^-(t)$ using eq. 3.2.4. Using these three quantities and eq. 3.2.4, the voltage at the device $V_{DUT}(t)$ is calculated and shown as green line.

To determine the rise time (10 %-90 %), it is crucial that the device gets fully charged during the application of the pulse. As described in chapter 1.3.1, the voltage at the device should amount to twice the pulse amplitude after the electrical charging time. In this case, the maximum absolute voltage amounts to 1.57 V, which is almost identical to twice the pulse

amplitude (1.58 V). Nevertheless, not all devices reached a maximum absolute voltage close to 1.58 V. To achieve a suitable comparison for all rise times, evaluated with the 250 ps pulse, the 10 % and 90 % levels for the determination the rise time were multiplied with 1.58 V, instead of the maximum absolute voltage of the device's $V_{\mathrm{DUT}}(t)$. In this case, it takes 77.1 ps to charge the Ta3 device, which is faster than the Ta2 device (730 ps) by almost one order of magnitude. Please note that this is not a suitable comparison, because the pulse's rise time was not yet considered, which is done at the end of this section.

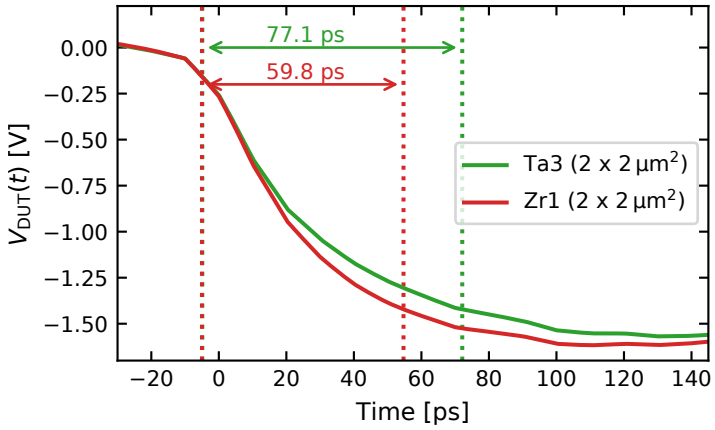

Figure 3.15.: Zoom into the beginning of $V_{\mathrm{DUT}}(t)$ of the Ta3 and Zr1 device. Derived with eq. 3.2.4. The vertical dotted lines indicate the rise times (10 % - 90 %) of both devices.

In fig. 3.15, a zoom into the beginning of $V_{\mathrm{DUT}}(t)$ is shown for the Ta3 and Zr1 device in green and red, respectively. The Ta3 device's $V_{\mathrm{DUT}}(t)$ was already shown in fig. 3.14b and its rise time amounts to 77.1 ps. The Zr1 device's rise time is the fastest and amounts to 59.8 ps. This can be explained by the slightly higher forward reflection (see fig. 3.6a) and slightly lower forward transmission (see fig. 3.6a), which originates from the larger capacitance of the Ta3 device (see table 3.3). Both, the Ta3 and Zr1 device, are faster than the Ta1 and Ta2 device by one order of magnitude or more, which is due to the use of mask B in the fabrication process of the Ta3 and Zr1 device.

TaC and ZrC devices

In fig. 3.16, a zoom into the beginning of $V_{\mathrm{DUT}}(t)$ is shown for the Ta-C and Zr-C device in green and red, respectively. The scattering parameters from fig. 3.9 were used. Their rise times amount to 68.3 ps and 63.0 ps for the Ta-C and Zr-C device, respectively, and are close to the rise times of the Ta3 and Zr1 device (77.1 ps and 59.8 ps). This shows that the additional C-layer has only a minor influence on the device's electrical charging time.

HfAx and HfBx devices

The voltage at the device $V_{\mathrm{DUT}}(t)$ of the HfA1, HfA2, and HfA3 device has been determined with the scattering parameters from fig. 3.10 and $V_{\mathrm{DUT}}(t)$ of the HfB1, HfB2, and HfB3 de-

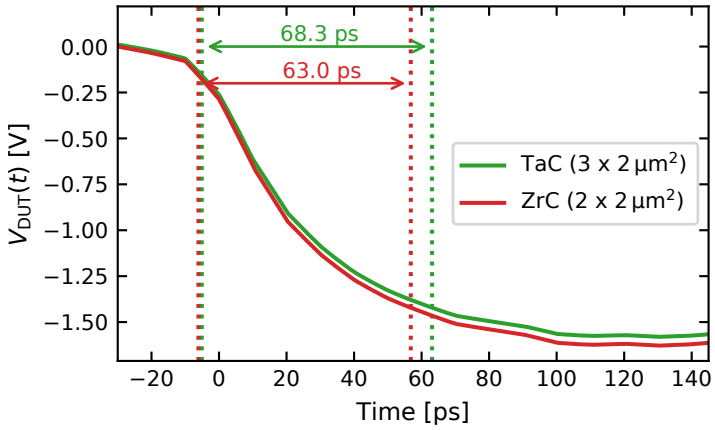

Figure 3.16.: Zoom into the beginning of $V_{DUT}(t)$ of the Ta-C and Zr-C device. Derived with eq. 3.2.4. The vertical dotted lines indicate the rise times (10 % - 90 %) of both devices.

vice with the scattering parameters from fig. 3.11. The rise times of the HfA1, HfB1, and HfB2 device were again determined with the 250 ps voltage pulse from the pulse generator PG5 with an amplitude of -0.79 V as $v_1^+(t)$. The $V_{DUT}(t)$ of the HfA2, HfA3, and HfB3 device have, however, not reached the 90 % threshold during the 250 ps pulse application and, therefore, their rise times were determined with the 10 ns pulse from the PSPL 2600C pulse generator with an amplitude of -0.52 V, which was also for the determination of the rise time of the Ta1 and Ta2 device.

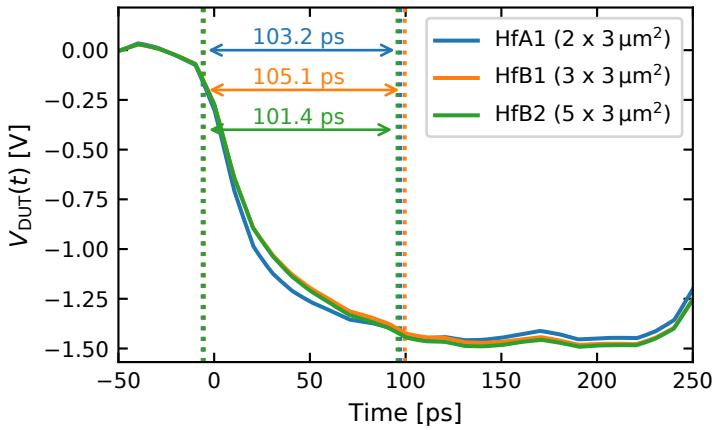

Figure 3.17.: Zoom into the beginning of $V_{DUT}(t)$ of the HfA1, HfA2, and HfA3 device. Derived with eq. 3.2.4. The vertical dotted lines indicate the rise times (10 % - 90 %) of all three devices.

The rising edges of the HfA1, HfB1, and HfB2 device are shown in fig. 3.17 and are almost identical amounting to 103.2 ps for the HfA1 device, to 105.1 ps for the HfB1 device and to 101.4 ps for the HfB2 device. The deposition of the HfAx and HfBx device's Pt bottom electrode has been performed differently. As they reach similar rise times at comparable device sizes, the different deposition processes of the Pt electrodes have only a minor impact on the rise time.

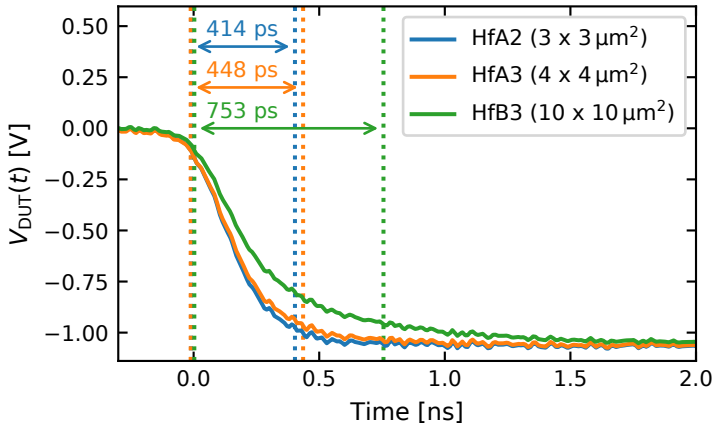

Figure 3.18.: Zoom into the beginning of $V_{\mathrm{DUT}}(t)$ of the HfA1, HfB1, and HfB2 device. Derived with eq. 3.2.4. The vertical dotted lines indicate the rise times (10 % - 90 %) of all three devices.

The rising edges of the HfA2, HfA3 and HfB3 device are shown in fig. 3.18 and amount to 414 ps for the HfA2 device, to 448 ps for the HfA3 device, and to 753 ps for the HfB3 device, which is significantly slower than the rise time of the other devices on the HfAx and HfBx wafer. This is due to the HfB3 device's size ($10 \times 10\,\mu\mathrm{m}^2$), which is larger than the other tested devices on the HfAx and HfBx wafer. Consequently, the HfB3 device has also the largest capacitance, which leads to the slow rise time. It is, however, noticeable that the rise time of the HfB3 device is similar to the rise time of the Ta2 device (730 ps), although the Ta2 device is much smaller ($5 \times 5\,\mu\mathrm{m}^2$). The HfB3 device, consequently, has a larger capacitance (1.94 pF, see table 3.3) than the Ta2 device (1.11 pF), which is smaller by 43.3 %. This rise time of the Ta2 device is, however, only 3.1 % shorter than the rise time of the HfB3 device. This indicates that the improvements of mask B (shortening the narrowed area's length and the CPW structure's length) compensates the losses originating from the larger device capacitance in this case.

Influence of pulse generators' rise times

To compare all rise times, the influence of the pulse generators' rise times needs to be considered. The PSPL 2600C and PG5 pulse generator's rise times amount to 359 ps and to 34.5 ps, respectively. By means of eq. 2.13, the rise time of the device, T_{Rise}, can be determined from the calculated rise times, T_{Calc}, and the rise times of the pulse generators, T_{PG}:

$$T_{\mathrm{Rise}} = \sqrt{T_{\mathrm{Calc}}^2 - T_{\mathrm{PG}}^2}. \tag{3.3}$$

The results for T_{Rise} for all devices are listed in table 3.4, sorted by the device size to demonstrate its influence on T_{Rise}. Almost all devices have a rise time below 100 ps. The fastest device fabricated with mask A is the Ta2 device with 636 ps, being slower by more than one order of magnitude than the fastest devices fabricated with mask B, which is the

Zr1 device with a rise time of 48.8 ps. This shows the benefits of mask B and underlines the importance of small CPW structures. Suggestions for the optimization of the CPW structures with integrated VCM devices are, therefore, given in the next section. The HfA2, HfA3 and HfB1 device are the only devices fabricated with mask B and having a rise time of more than 100 ps, which is due to their large size.

To show that all devices were almost fully charged during the pulses' application, the quotient of the maximum absolute voltage of $V_{\mathrm{DUT}}(t)$ and twice the pulse amplitude V_{P} is built and shown as $|^{V_{\max}}/_{2V_{\mathrm{P}}}|$ in the last column of table 3.4. The pulse amplitude amounts to -0.52 V for the PSPL 2600C pulse generator and to -0.79 V for the PG5 pulse generator. If the device was charged by less than 90 % of $2V_{\mathrm{P}}$ during the application of the 250 ps pulse of the PG5 pulse generator, its rise time was determined with the 10 ns pulse from the PSPL 2600C pulse generator. Therefore, the quotient $|^{V_{\max}}/_{2V_{\mathrm{P}}}|$ always amounts to 90 % or more. During the application of the 10 ns pulse from the PSPL 2600C pulse generator, all devices were charged completely. Also, most of the devices excited with the PG5 pulse generator were charged to almost 100 %. Only the devices on the HfAx and HfBx wafers were charged by less than 95 %, which is due to their longer rise times, resulting from the occurrence of two cut-off frequencies in the forward reflection, as described in section 3.2.3. The first cut-off frequency occurs much earlier as for the other devices fabricated with mask B. Frequencies above this first cut-off frequency are, consequently, missing in the reflection and do not contribute to the rising edge of $V_{\mathrm{DUT}}(t)$.

Table 3.4.: Calculated rise times T_{Rise} for all devices listed in table 3.1. T_{Rise} was determined with eq. 3.3 from T_{Calc} and T_{PG}. The devices are sorted by their size.

Device	Size	Mask	Pulse generator	T_{PG}	T_{Calc}	T_{Rise}	$\lvert^{V_{\max}}/_{2V_{\mathrm{P}}}\rvert$
Ta3	$2 \times 2\,\mu\mathrm{m}^2$	B	PG5	34.5 ps	77.1 ps	69.0 ps	99.3 %
Zr1	$2 \times 2\,\mu\mathrm{m}^2$	B	PG5	34.5 ps	59.8 ps	48.8 ps	100.0 %
Zr-C	$2 \times 2\,\mu\mathrm{m}^2$	B	PG5	34.5 ps	63.0 ps	52.1 ps	100.0 %
Ta-C	$3 \times 2\,\mu\mathrm{m}^2$	B	PG5	34.5 ps	68.3 ps	58.9 ps	100.0 %
HfA1	$2 \times 3\,\mu\mathrm{m}^2$	B	PG5	34.5 ps	103.2 ps	96.9 ps	92.3 %
HfA2	$3 \times 3\,\mu\mathrm{m}^2$	B	PSPL 2600C	359 ps	414 ps	206.2 ps	100.0 %
HfB1	$3 \times 3\,\mu\mathrm{m}^2$	B	PG5	34.5 ps	105.1 ps	99.0 ps	93.8 %
HfB2	$5 \times 3\,\mu\mathrm{m}^2$	B	PG5	34.5 ps	101.4 ps	95.0 ps	94.4 %
HfA3	$4 \times 4\,\mu\mathrm{m}^2$	B	PSPL 2600C	359 ps	448 ps	268 ps	100.0 %
Ta2	$5 \times 5\,\mu\mathrm{m}^2$	A	PSPL 2600C	359 ps	730 ps	636 ps	100.0 %
HfB3	$10 \times 10\,\mu\mathrm{m}^2$	B	PSPL 2600C	359 ps	753 ps	662 ps	100.0 %
Ta1	$15 \times 20\,\mu\mathrm{m}^2$	A	PSPL 2600C	359 ps	2.57 ns	2.54 ns	100.0 %

The rise times, T_{Rise}, from table 3.4 are plotted in fig. 3.19 against the device size. The rise times of the devices fabricated with mask A are shown as blue points and the rise times of the devices fabricated with mask B as orange points. Due to the different permittivities and layer thicknesses, the data points are not perfectly comparable. Nevertheless, the device size has a crucial nonlinear impact on the rise time for both masks. Fabricating smaller

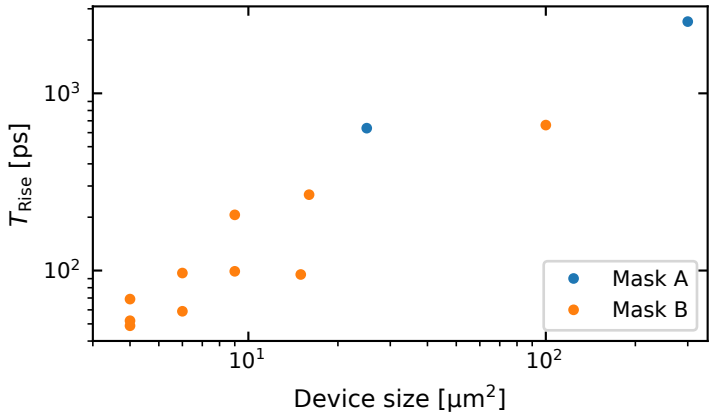

Figure 3.19.: Rise times (10 %-90 %) T_{Rise} from table 3.4 against the device size. The rise times of the devices fabricated with mask A are plotted in blue and the rise times of the devices fabricated with mask B are plotted in orange.

devices than $2 \times 2\,\mu\mathrm{m}^2$ is not possible with the optical lithography process. Smaller devices would not necessarily have faster rise times, as other limiting factors, such as the bandwidth of the CPW structure, will become more limiting at a certain point. Although, only two data points are available for mask A, they show a tendency for higher rise times at the same device size, which shows the benefit of the optimized mask B. Most prominent is the rise time of the HfB3 device ($10 \times 10\ \mu\mathrm{m}^2$), which is four times larger than the Ta2 device ($5 \times 5\ \mu\mathrm{m}^2$), but has almost the same rise time (see table 3.4).

3.3. Optimization

In the previous section, it was shown that the optimization of CPW structure with integrated VCM device is crucial for fast experiments as the electrical charging time can easily vary by one order of magnitude or more. Employing a fast pulse generator cannot compensate for the use of a slow device, which can easily be shown by transforming eq. 3.3:

$$T_{\mathrm{Calc}} = \sqrt{T_{\mathrm{Rise}}^2 + T_{\mathrm{PG}}^2}, \tag{3.4}$$

in which T_{Calc} corresponds to the charging time of the device, taking into account the pulse generator's rise time, T_{PG}, and the device's charging time T_{Rise}. If an ideal pulse generator with a negligible rise time ($T_{\mathrm{PG}} \ll T_{\mathrm{Rise}}$) was used, eq. 3.4 would simplify to $T_{\mathrm{Calc}} \approx T_{\mathrm{Rise}}$, and the electrical charging time of the device would be the only limitation.

As shown in the previous section, the charging time of the fastest devices fabricated with mask B was reduced by more than one order of magnitude compared to the fasted device fabricated with mask A. The reduction of the device size to $2 \times 2\,\mu\mathrm{m}^2$ (from $5 \times 5\,\mu\mathrm{m}^2$) has the largest influence followed by the shortening of the narrowed area's length to 10 µm (from 50 µm) and shortening the CPW structure's overall length to 590 µm (from 930 µm). This section explains different methods to optimize the integration of VCM device into

CPW structures and also discusses possible limitations [100]. The suggestions made are also transferable to other memory technologies, such as PCM devices.

3.3.1. Smaller structures

To achieve faster electrical charging times several parameters of the CPW structure can be shortened:

1. The size of the VCM device itself is the most crucial factor on the electrical charging time, as shown in table 3.4 and fig. 3.19. Reducing the width of the VCM device, also reduces the width of the inner conductor of the CPW structure in the narrowed area. As shown in fig. 3.7, a smaller inner conductor's width decreases the bandwidth of the CPW structure, which also leads to a slower electrical charging. Below a certain device size, the rise time will no longer be limited by the device size, but by the bandwidth of the CPW structure. The optimum device would, therefore, have a short length, but a broader width. Shortening the length of the VCM device is only limited by the resolution of the optical lithography, which is in this case at 2 µm.

2. The length of the narrowed area is also crucial for the bandwidth of the CPW structures. This is shown in fig. 3.7, in which the bandwidths of electrically short-circuited CPW structures without integrated VCM device are compared. The CPW structures fabricated with mask A had a narrowed length of 50 µm and had a significant lower bandwidth than the devices fabricated with mask B, on which the narrowed length has been shortened to 10 µm. The only limitation is the length of the VCM device, which depends on the resolution of the optical lithography, as mentioned above.

3. The overall length of the CPW structure has only a small effect on the electrical charging time. Shortening its length reduces the angular capacitances between the inner and outer conductors of the CPW structure, as shown in chapter 3.2.2. The CPW structure's length should, therefore, be shortened to the minimum size of the contacting pads, which also constitutes a limitation.

3.3.2. Thicker electrodes

Thicker electrodes would increase the bandwidth of the CPW structure, as stated in [32]. All devices listed in table 3.1 have Pt conductors with a thickness between 20 nm and 30 nm, which is far below the skin depth of Pt. As shown in chapter 1.3, Pt has a skin depth of 816 nm at a frequency of 40 GHz. The use of thicker electrodes was tried, but resulted in short circuits at the edges of the VCM device. To avoid these edges, the bottom and top electrode needed to lie in one plane, which requires a completely different device fabrication. To realize a vertical material stack without edges, the use of chemical mechanical polishing or similar methods are required.

3.3.3. Lateral devices

As the VCM device's stack has a major influence on the device's capacitance (see table 3.3) and, consequently, on the electrical charging time (see fig. 3.19), removing this stack could reduce the electrical charging time. This would require the use of lateral devices, which are, however, difficult to realize for VCM devices. For other memory technologies, such as PCM, lateral devices are more prominent [59]. Angular capacitances between the inner and outer conductors of the CPW structure (as described in chapter 3.2.2) and between the bottom and top electrode would, however, remain. The latter scales with the lateral distance of the two electrodes and the width of the inner conductor. This width could again be reduced by narrowing the inner conductor, which would, however, again result in a trade-off between the device's remaining angular capacitance and the usable bandwidth of the CPW structure.

4. SET kinetics of VCM devices

This chapter summarizes the results of the SET kinetics of TaO_x-, ZrO_x-, and HfO_x/TiO_x-based devices. All of them could be driven from the HRS to the LRS by applying 50 ps pulses with an amplitude of 5.0 V. To the author's knowledge, this is the fastest SET time reported for ReRAM devices. Also, the influence of the electrical charging time on the measured SET kinetics is analyzed.

The SET kinetics of the Ta1, Ta2, Ta3, Zr1, HfA2, and HfB1 device (see table 3.1) were measured. Firstly, the influence of the VCM device's capacitance on the SET kinetics at timescales below 10 ns is demonstrated. Here, the SET kinetics were measured and evaluated manually as described in chapter 2.2.1, showing that the SET kinetics are mainly limited by the VCM device's capacitance. Later in chapter 4.2, the results achieved with the automated setup and evaluation method are shown. For the Ta3, Zr1, HfA2, and HfB1 device, the SET kinetics could be measured on a timescale of 5 ps. SET times down to 50 ps could be shown in all devices, if sufficiently high voltages were applied. Also, fast transition times from the HRS to the LRS down to 5 ps could be observed for the HfA2 device. Finally, a model is developed in chapter 4.3, which considers the electrical charging times from chapter 3.2.4, which constitutes the main limitation of the SET kinetics in the subnanosecond regime. Finally, the two other possible limits —the migration of oxygen vacancies and the heating time of the conductive filament —are discussed.

4.1. Influence of capacitances on SET kinetics

The manual measurement procedure for the Ta2 device was in analogy to the one of the Ta1 device (see chapter 2.1.1) and is sketched in fig. 4.1. The results are published in [100]. Prior to the application of the pulse, the device was driven to the HRS by applying a voltage sweep of 2.0 V at a sweep rate of 0.1 $^{V}/_{s}$ (red line in fig. 4.1) with a Keithley 2634B SMU. The device's resistance was read at 0.5 V during the descending part of the sweep (marked in blue). Afterwards, 10 ns pulses with various amplitudes between -1.2 V and -3.2 V, emitted by the pulse generator PSPL 2600C, were applied to the active Pt electrode of the Ta2 device (green pulse). Finally, the Ta2 device was driven back to the LRS by applying a voltage sweep of -1.5 V at a sweep rate of 0.1 $^{V}/_{s}$ (right green line). The device's resistance was read again at -0.5 V during the descending part of the sweep (marked in blue). The second sweep is conducted to verify the device's functionality and to drive it into a comparable state at

the beginning of each cycle. The Ta2 device was connected with the DC probes during the application of the sweeps (green shaded area) and with the RF probes during the pulse's application (orange shaded area).

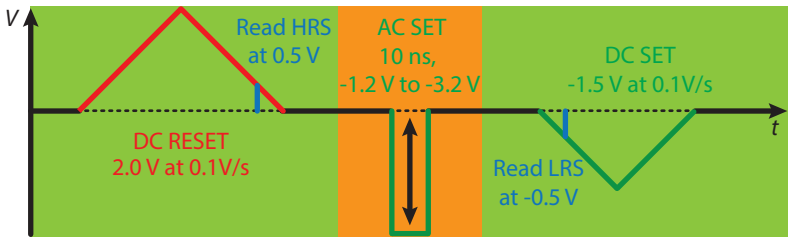

Figure 4.1.: Measurement cycle to determine the Ta2 device's SET kinetics ($2 \times 2\,\mu m^2$, Pt \TaO$_x$ \Ta, see table 3.1). During the green shaded area the device is connected to the DC probes and during the orange shaded area to the RF probes.

An exemplary voltage pulse with an amplitude of -1.3 V (blue) and its current response (red) is shown in fig. 4.2a. After the occurrence of a capacitive peak at the beginning of the pulse's application, the measured current is near zero, which indicates that the device is still in the HRS. The start of the pulse is defined as the time at which 20 % of the capacitive peak's maximum is reached, as explained in chapter 2.2.1. After 2.68 ns the current suddenly increases, marking the SET event.

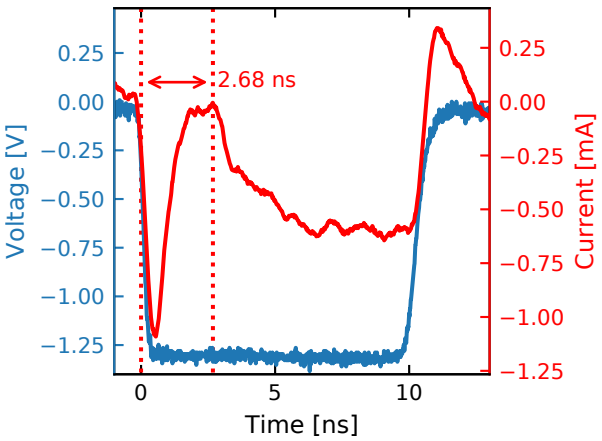

(a) V_P = -1.3 V.

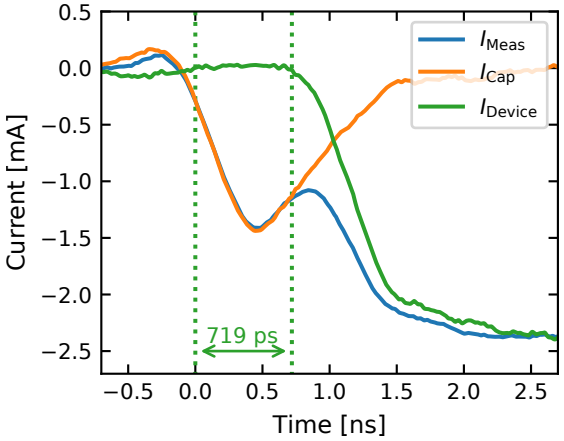

(b) V_P = -1.8 V.

Figure 4.2.: (a) Voltage pulse (blue) with a duration of 10 ns and an amplitude of -1.3 V and its current response (red). The SET event occurs after 2.68 ns. (b) Current response (I_{Meas}, blue) of a 10 ns pulse with an amplitude of -1.8 V with its capacitive component (I_{Cap}, orange) and the current through the device (I_{Device}, green). The SET event occurs after about 719 ps. All currents were smoothened with a Savitzky-Golay filter. Adapted from [100].

At faster timescales, the Ta2 device switches within the capacitive charging of the Ta2 device. This is demonstrated in fig. 4.2b, in which the beginning of a current response, I_{Meas}, of a voltage pulse with an amplitude of -1.8 V is shown in blue. As explained in chapter 2.2.1, the capacitive current, I_{Cap} (orange), is determined using eq. 2.5 and the current through

the device, I_{Device}, using eq. 2.6. It increases after about 719 ps, which indicates the SET event.

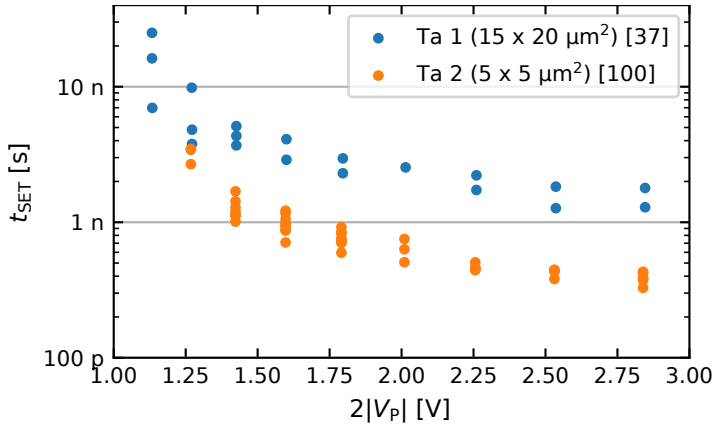

Figure 4.3.: SET kinetics for the Ta1 and the Ta2 device. On the abscissa, twice the adjusted pulse voltage, V_{P}, is indicated. Data from [37, 100]

The SET kinetics of the Ta1 and Ta2 device are shown in fig. 4.3. On the abscissa, twice the adjusted pulse voltage, V_{P}, is indicated, because this is the voltage, which is effectively applied to the VCM device after the electrical charging time. Although, the VCM stack of both devices was identical, the Ta2 device achieved significant faster SET times. The only plausible reason for the bending of the kinetics below 10 ns is the electrical charging of the VCM device. As the Ta2 device is significantly smaller than the Ta1 device ($5 \times 5\,\mu\mathrm{m}^2$ and $15 \times 20\,\mu\mathrm{m}^2$, respectively), it also has a smaller capacitance (1.11 pF and 4.60 pF, respectively, see chapter 3.2.2). This smaller capacitance in turn leads to a faster electrical charging of the Ta2 device, which leads to faster SET kinetics. As calculated in chapter 3.2.4 and shown in table 3.4, the rise time of the Ta1 device amounts to 2.54 ns and the rise time of the Ta2 device to 636 ps. This is close to the time at which the SET kinetics of both devices start to bend towards slower SET times.

To achieve faster SET times mask B was designed, which includes smaller devices down to $2 \times 2\,\mu\mathrm{m}^2$ (see fig. 3.2) and other optimizations such as a shorter overall length of the CPW structure (590 µm, instead of 930 µm) and a shorter narrowed length (10 µm, instead of 50 µm).

4.2. SET kinetics on a sub-10-ps timescale

In this section, the results of the SET kinetics measured with the automated setup are shown. Differently to the previous method, the pulse generator PG5 was used and the device was connected to the RF probes during the entire cycle (see chapter 2.1.2).

4.2.1. Ta3 and Zr1 devices

The measurements of the Ta3 ($2 \times 2\,\mu m^2$, Pt\TaO$_x$\Ta) and Zr1 device ($2 \times 2\,\mu m^2$, Pt\ZrO$_x$\Ta) were published in [38]. The results show that both devices can reach a SET time of 50 ps at 5.01 V and 3.16 V, respectively. The Zr1 device can also reach a transition time from the HRS to the LRS of 10 ps. Such fast SET and transition times were, to the author's knowledge, not yet reported for VCM devices.

The measurement procedure is depicted in fig. 4.4. The device is firstly driven to the HRS with a positive voltage sweep (in red) with a maximum of 1.6 V at a sweep rate of 0.5 V/s. A faster sweep rate compared to the previous measurement was chosen to accelerate the measurement procedure. As shown in fig. 2.8, the leakage current of the bias tee is still relatively small (less than 1 µA) at this sweep rate. Afterwards, a short voltage pulse is applied with the PG5 pulse generator (green). This pulse is the only signal applied to the AC port of the bias tee during one cycle (orange shaded area). All other measurements were conducted with the Keithley 2634B SMU (green shaded area) at the DC port. The resistance is read at a voltage of -0.2 V before and after the pulse's application (in blue). The resistance was not read during the sweep, as in the previous measurement, to reduce the impact of the leakage current on the resistance measurement. Finally, the device is driven back to the LRS with a negative voltage sweep (green) with a minimum of -1.2 V at a sweep rate of 0.5 V/s and a current compliance of 300 µA.

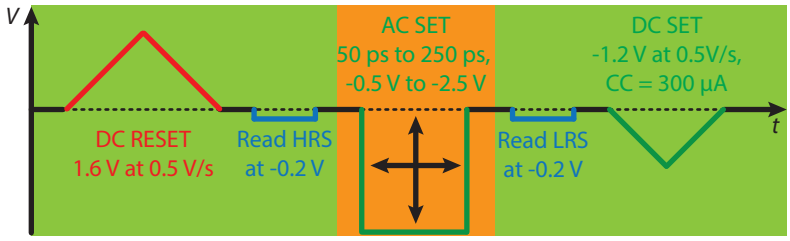

Figure 4.4.: Measurement cycle to determine the Ta3 and Zr1 device's SET kinetics. The green shaded area marks the part, measured by the Keithley 2634B SMU at the DC port of the bias tee and the orange shaded area marks the part, in which the pulse from the PG5 pulse generator is applied to the AC port of the bias tee.

Starting from 50 ps, the pulse width was increased in steps of 5 ps, until a pulse width of 250 ps is reached. This cycle is repeated at least 10 times at each pulse width. If the resistance in the HRS was not in the range between 10 kΩ and 30 kΩ, the cycle was discarded in the subsequent evaluation and repeated until 10 cycles had an HRS resistance in this range. This is done to achieve a suitable comparison. As shown in [161], the HRS of a HfO$_x$/TiO$_x$-based VCM device has an impact on its SET kinetics. The voltage amplitude is varied with different broadband attenuators placed between the pulse generator and the bias tee. With these attenuators, the pulse voltage can be adjusted between -5.0 V without attenuation and -0.5 V with an attenuation of 20 dB. The attenuation values used in this section are 6 dB (-2.5 V), 10 dB (-1.6 V), 13 dB (-1.1 V), 16 dB (-0.8 V), and 20 dB (-0.5 V). For every cycle,

the ratio $R_{\mathrm{LRS}}/R_{\mathrm{HRS}}$ has been built. The device's resistance did not change during the cycle, if $R_{\mathrm{LRS}}/R_{\mathrm{HRS}}$ is around unity. The device switched from the HRS to the LRS, if $R_{\mathrm{LRS}}/R_{\mathrm{HRS}}$ is close to zero. To achieve smoother transients for the ratio $R_{\mathrm{POST}}/R_{\mathrm{PRE}}$, the measurements were repeated until smooth lines at each pulse amplitude were achieved.

The results for the Ta3 device at all applied pulse voltages are shown in fig. 4.5 as boxplots. On the abscissa the FWHM of the applied pulse is plotted. To calculate the FWHM, the measured transmitted voltage was first interpolated linearly, as explained in chapter 2.1.2. Otherwise, the FWHM could only take discrete multiples of the oscilloscope's sampling time (10 ps). If the FWHM is shorter than the adjusted pulse width (which can occur as shown below), the adjusted pulse width is used instead. On the ordinate, the ratio $R_{\mathrm{LRS}}/R_{\mathrm{HRS}}$ is given. Each boxplot contains at least 10 values for $R_{\mathrm{LRS}}/R_{\mathrm{HRS}}$, and all R_{HRS} values were in the range between 10 kΩ and 30 kΩ as explained above. The red bar in the boxplots marks the median value.

The results for the Zr1 device are shown in fig. 4.6. At the lowest voltage, the ratio $R_{\mathrm{LRS}}/R_{\mathrm{HRS}}$ of both devices remains at unity for all pulse widths, which means that the devices did not switch to the LRS. This is shown in fig. 4.5d for the Ta3 device at $2V_{\mathrm{P}} = -1.6\,\mathrm{V}$ and in fig. 4.6d for the Zr1 device at $2V_{\mathrm{P}} = -1.0\,\mathrm{V}$. At higher voltages, $R_{\mathrm{LRS}}/R_{\mathrm{HRS}}$ begins to decrease after a certain time. This is illustrated for the Ta3 device in fig. 4.5c at a voltage of $2V_{\mathrm{P}} = -2.2\,\mathrm{V}$. At short FWHMs, $R_{\mathrm{LRS}}/R_{\mathrm{HRS}}$ remains again near unity. At a FWHM of 85 ps, the box plot starts to broaden, reaching also values close to zero, which means that at this FWHM, the SET event occurs randomly. The median value is, however, still close to unity, meaning that the Ta3 device did not switch to the LRS during most cycles. At longer FWHMs of 95 ps, the median value of $R_{\mathrm{LRS}}/R_{\mathrm{HRS}}$ starts to decrease, reaching a value of 0.12 at a FWHM of 120 ps. Also, the broadening of the boxplot decreases significantly, which means that during almost all cycles the Ta3 device switched to the LRS. A similar observation can be made for the Zr1 device at a voltage of $2V_{\mathrm{P}} = -1.6\,\mathrm{V}$ in fig. 4.6c. Both measurements were aborted after the devices switched to the LRS at every cycle in order to reduce the stress on the devices.

By increasing the absolute pulse voltage, the SET event occurs at even shorter FWHMs. Both devices begin to switch at 50 ps at a voltage of $2V_{\mathrm{P}} = -3.2\,\mathrm{V}$ for the Ta3 device (see fig. 4.5b) and at a voltage of $2V_{\mathrm{P}} = -2.2\,\mathrm{V}$ for the Zr1 device (see fig. 4.6b). At the highest absolute voltage both devices switch to the LRS at the shortest available FWHM of 50 ps during each cycle. The measurement was, therefore, again aborted to reduce the stress on the devices. This is shown in fig. 4.5a for the Ta3 device at a voltage of $2V_{\mathrm{P}} = -5.0\,\mathrm{V}$ and in fig. 4.6a for the Zr1 device at a voltage of $2V_{\mathrm{P}} = -3.2\,\mathrm{V}$.

A disadvantage of the data representation in fig. 4.5 and fig. 4.6 is that the ratio $R_{\mathrm{LRS}}/R_{\mathrm{HRS}}$ yields no absolute values of the HRS and the LRS. The HRS was chosen for both devices in the range from 10 kΩ to 30 kΩ. To get more information on the absolute LRS values, they were plotted in fig. 4.7 as boxplots for the Ta3 device. The LRS values have the same trend

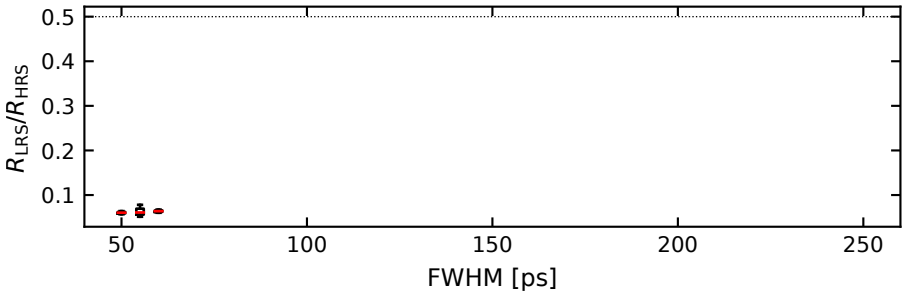

(a) Ta3 device, $V_P = -2.5\,V$.

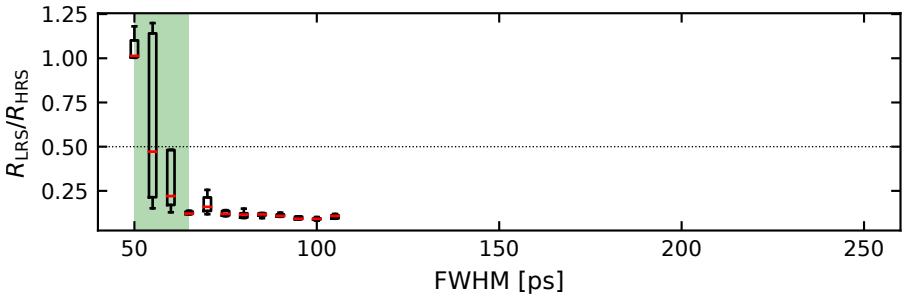

(b) Ta3 device, $V_P = -1.6\,V$.

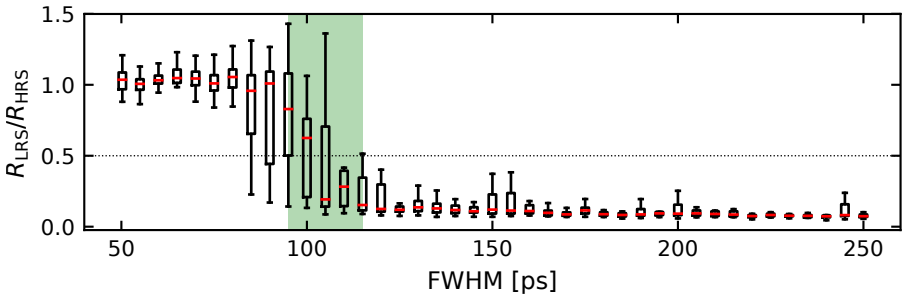

(c) Ta3 device, $V_P = -1.1\,V$.

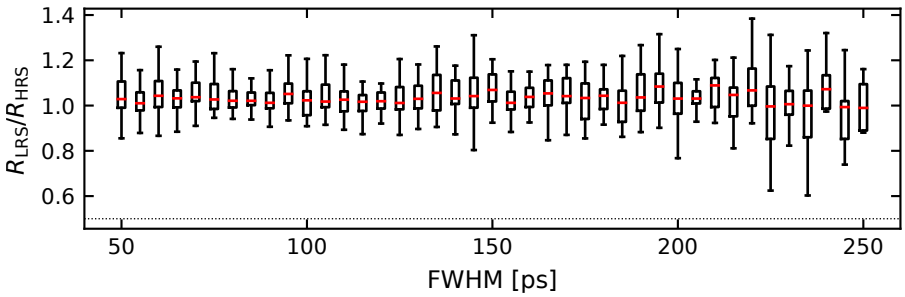

(d) Ta3 device, $V_P = -0.8\,V$.

Figure 4.5.: SET kinetics of the Ta3 device (see table 3.1). The SET event has been defined as the time at which the median value (red bar) reaches values below 0.5 (horizontal dashed line). The green shaded areas in (b) and (c) mark the transition time (20 %-80 %). Reprinted from [38], with the permission of AIP Publishing.

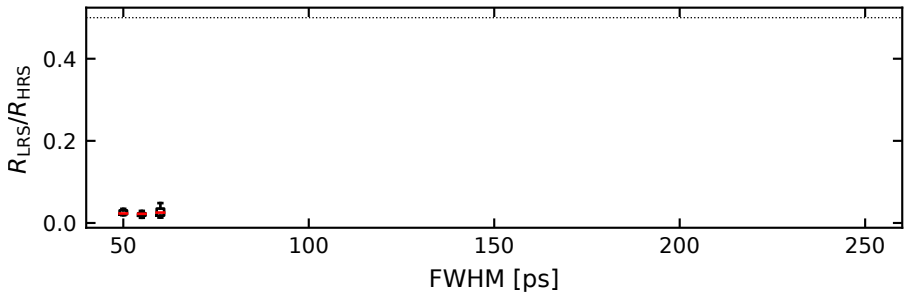

(a) Zr1 device, $V_P = -1.6\,V$.

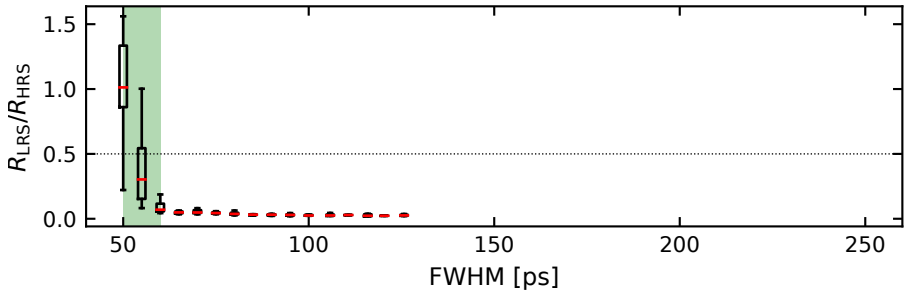

(b) Zr1 device, $V_P = -1.1\,V$.

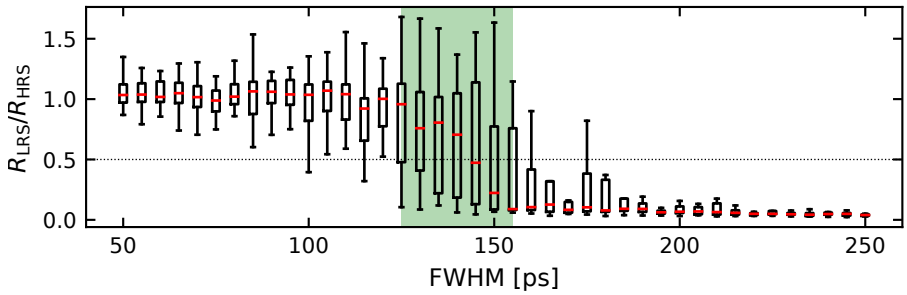

(c) Zr1 device, $V_P = -0.8\,V$.

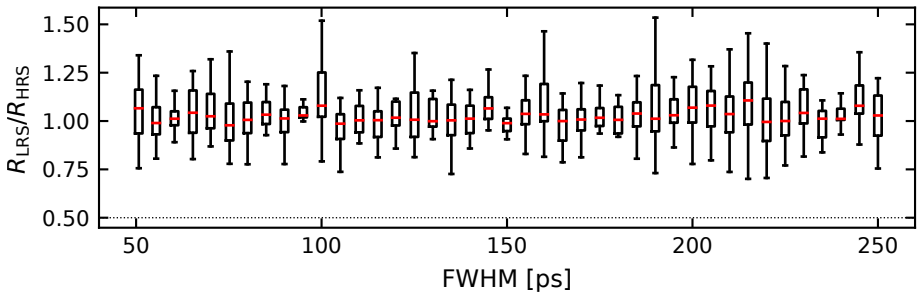

(d) Zr1 device, $V_P = -0.5\,V$.

Figure 4.6.: SET kinetics of the Zr1 device (see table 3.1). The SET event has been defined as the time at which the median value (red bar) reaches values below 0.5 (horizontal dashed line). The green shaded areas in (b) and (c) mark the transition time (80 %-20 %). Reprinted from [38], with the permission of AIP Publishing.

as the ratio $R_{\mathrm{LRS}}/R_{\mathrm{HRS}}$. They start at short FWHMs in the range from 10 kΩ to 30 kΩ and decrease with increasing FWHMs down to 1.54 kΩ. In the following, only the $R_{\mathrm{LRS}}/R_{\mathrm{HRS}}$ will be shown to maintain conciseness. The LRS values will, however, be shown in the appendix section B. The LRS values of the Zr1 device are, for example, shown in fig. B.1, reaching LRS values down to 482 Ω.

Two exemplary current responses of a 50 ps long pulse are shown in fig. 4.8. The Ta3 device switched from the HRS at 24.6 kΩ to the LRS at 1.58 kΩ during the application of a pulse with an amplitude of $2V_{\mathrm{P}} = -5.0\,\mathrm{V}$ (see fig. 4.8a) and the Zr1 device switched from the HRS at 19.4 kΩ to the LRS at 653 Ω during the application of a pulse with an amplitude of $2V_{\mathrm{P}} = -3.2\,\mathrm{V}$ (see fig. 4.8b). The FWHM of the captured current responses amount to 42.1 ps for the Ta3 device and to 43.1 ps for the Zr1 device. The SET time, however, does not amount to these values, because the effectively applied voltage has a longer FWHM. The shorter values for the FWHM in the current response result from the higher forward transmission of higher frequencies and higher forward reflection of lower frequencies in the scattering parameters of the Ta3 and Zr1 device (see fig. 3.6). In turn, the transmitted signal comprises higher frequencies than the reflected signal, which results in the short FWHM. As mentioned above, in this case the adjusted pulse width is used as FWHM.

The median values for the ratio $R_{\mathrm{LRS}}/R_{\mathrm{HRS}}$ are plotted in fig. 4.9. The data of the Ta3 device (solid lines) are from fig. 4.5 and the data of the Zr1 device (dashed line) from fig. 4.6. The color of the curves indicates the pulse amplitudes. From these curves, the SET times and transition times of the Ta3 and Zr1 device were determined. The SET time is defined as the shortest FWHM, at which $R_{\mathrm{LRS}}/R_{\mathrm{HRS}}$ reaches a value below 0.5. For this purpose, a horizontal line is drawn in fig. 4.9 (also in fig. 4.5 and fig. 4.6), which marks the SET time. The transition time from the HRS to the LRS is defined as the timespan from the last value of $R_{\mathrm{LRS}}/R_{\mathrm{HRS}}$ above 0.8 and the first below 0.2. It is marked as green shaded area in fig. 4.5 and fig. 4.6 for the Ta3 device and the Zr1 device, respectively. The most prominent transition time is the one observed for the Zr1 device at a pulse voltage of $V_{\mathrm{P}} = -1.1\,\mathrm{V}$ (see also fig. 4.6b). The median of $R_{\mathrm{LRS}}/R_{\mathrm{HRS}}$ at 50 ps remains at unity, which indicates that during most of the 50 ps cycles, the Zr1 device remained in the HRS. At 60 ps, however, the median of $R_{\mathrm{LRS}}/R_{\mathrm{HRS}}$ drops below 0.1. The narrowness of the boxplot at 60 ps also indicates that the Zr1 device switched to the LRS during every cycle. The Zr1 device never switched completely to the LRS at 50 ps, but always at 60 ps. Consequently, the transition from the HRS to the LRS must have occurred during the additional 10 ps.

The SET times in fig. 4.10 could be determined on a picosecond timescale. Again, twice the adjusted absolute pulse amplitude $|2V_{\mathrm{P}}|$ is plotted on the abscissa, as this is the effective voltage seen by the VCM device at the end of its electrical charging. Also, determining the SET time from the ratio $R_{\mathrm{LRS}}/R_{\mathrm{HRS}}$ is advantageous, compared to determining it from the current through the device (see chapter 2.2.1), because it can also be evaluated automatically. Furthermore, a much larger data set is evaluated. Consequently, this evaluation method also

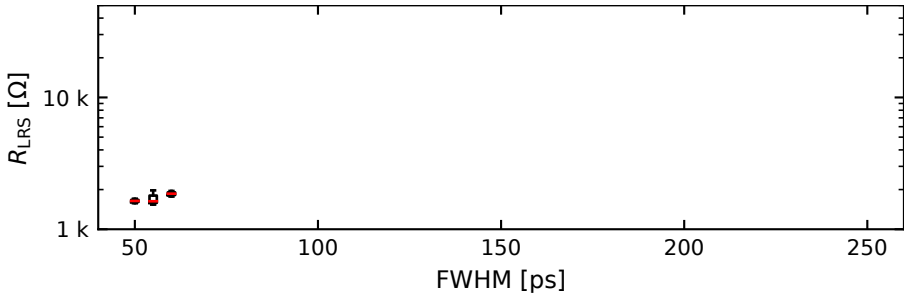

(a) Ta3 device, $V_P = -2.5\,V$.

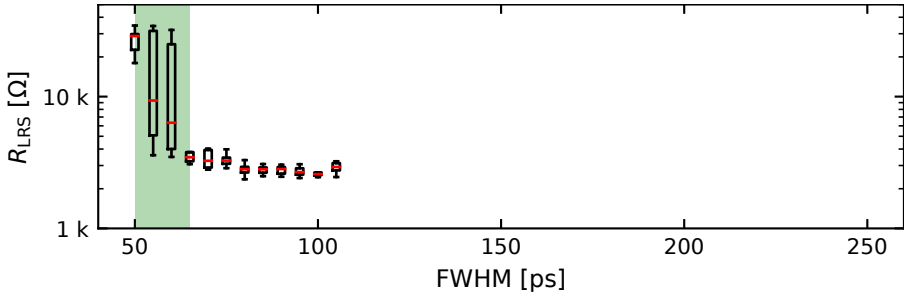

(b) Ta3 device, $V_P = -1.6\,V$.

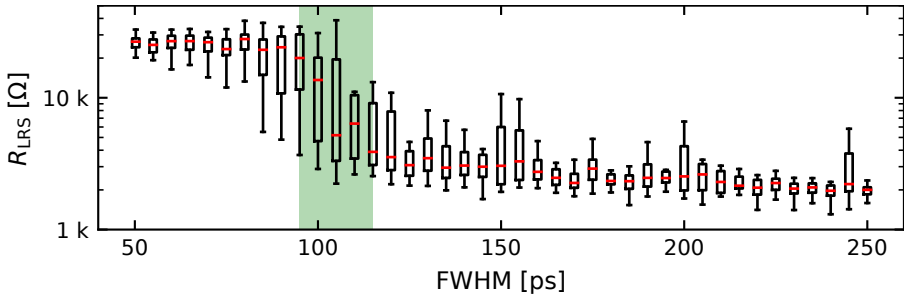

(c) Ta3 device, $V_P = -1.1\,V$.

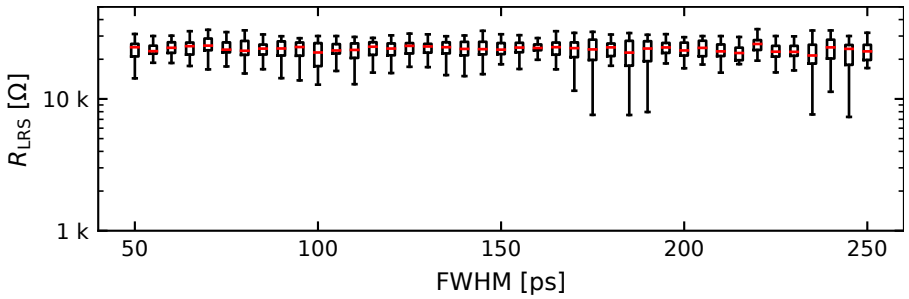

(d) Ta3 device, $V_P = -0.8\,V$.

Figure 4.7.: SET kinetics of the Ta3 device (see table 3.1) representing the LRS values. The data set is identical to the one from fig. 4.5. The red bar in the boxplot marks the median. The green shaded areas in (b) and (c) mark the transition time (80 %-20 %). Reprinted from the supplementary information of [38], with the permission of AIP Publishing.

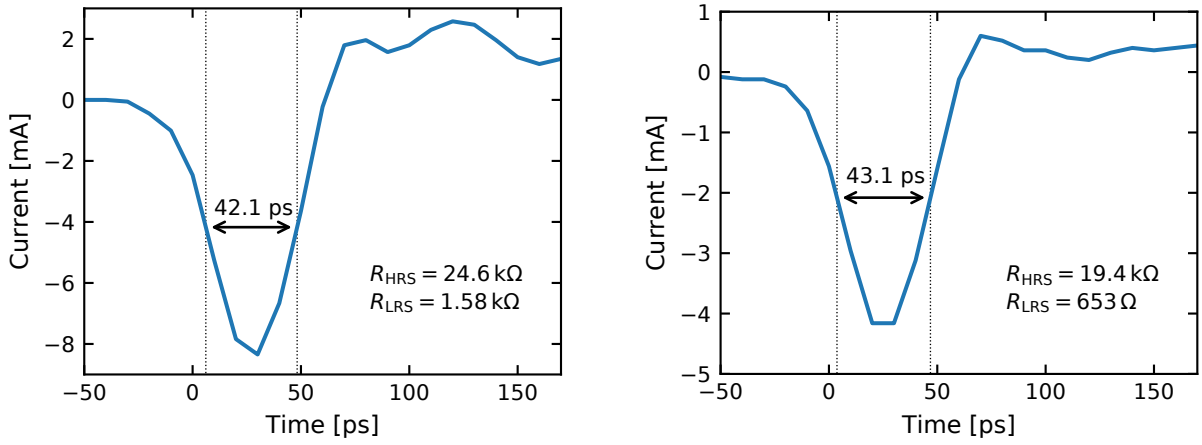

(a) Ta3 device, $V_P = -2.5\,V$, FWHM = 50 ps. (b) Zr1 device, $V_P = -1.6\,V$, FWHM = 50 ps.

Figure 4.8.: (a) Ta3 device's current responses of a 50 ps pulse with an amplitude of $2V_P = -5.0\,V$. (b) Zr1 device's current responses of a 50 ps pulse with an amplitude of $2V_P = -3.2\,V$. The change in resistance is indicated on the lower left for both devices. Adapted from [38], with the permission of AIP Publishing.

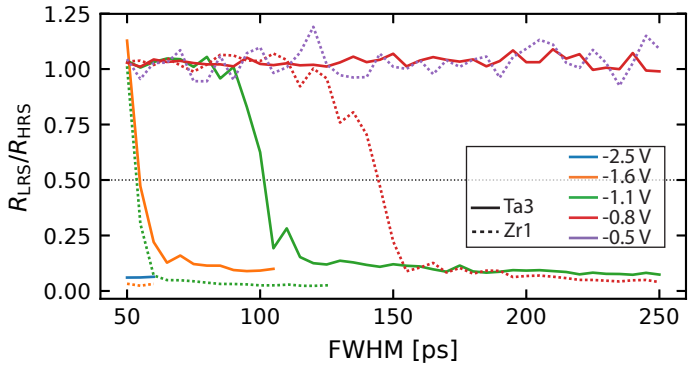

Figure 4.9.: Median values of the ratio R_{LRS}/R_{HRS} for the Ta3 device (solid lines, data from fig. 4.5) and the Zr1 device (dashed lines, data from fig. 4.6). The color of the lines indicates the pulse amplitude. Reprinted from [38], with the permission of AIP Publishing.

takes the device's cycle-to-cycle variability into account. Measuring the transition time is even possible down to 10 ps, as shown in the previous paragraph.

Nevertheless, determining the SET event from the current responses is also possible. The smaller dimensions on mask B also lead to lower capacitive peaks in the devices' current responses. This is demonstrated for the Zr1 device in fig. 4.11, in which the current response I_{Meas} (blue line) of a 250 ps pulse with an amplitude of -0.8 V is shown. After the first capacitive peak, the current decreases to almost zero, indicating that the device is in the HRS. After 145 ps, I_{Meas} increases again, which marks the SET event. To further illustrate this, the capacitive current I_{Cap} (orange line) is determined with eq. 2.5. Finally, the current through the device I_{Device} (green line) is determined with eq. 2.6, in which the SET event is even more prominent. The transient of R_{LRS}/R_{HRS} of the Zr1 device at a pulse amplitude of $V_P = -0.8\,V$ (see red-dashed line in fig. 4.9) also crosses the 0.5 threshold at a FWHM of 145 ps. This shows that both methods to determine the SET time yield similar results.

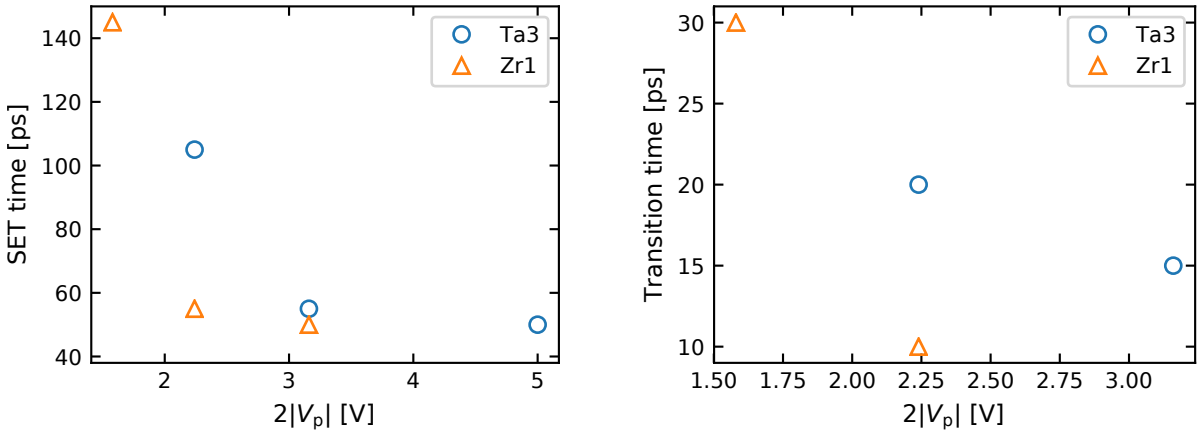

(a) SET times.

(b) Transition times (80 %-20 %).

Figure 4.10.: (a) SET times of the Ta3 and Zr1 device, determined in fig. 4.9 (see horizontal line). (b) Transition times (80 %-20 %) of the Ta3 and the Zr1 device. Only two data points per device are shown, because the transition time can only be determined if the device starts in the HRS at short FWHMs and ends in the LRS at long FWHMs. This is only the case for two measurements for each device. Twice the adjusted absolute pulse amplitude $|2V_P|$ is plotted on the abscissa, as this is the effective voltage at the end of the electrical charging. Adapted from [38], with the permission of AIP Publishing.

Determining the SET time from the transient of $^{R_{LRS}}/_{R_{HRS}}$ is, however, less elaborately and is, therefore, used in the following.

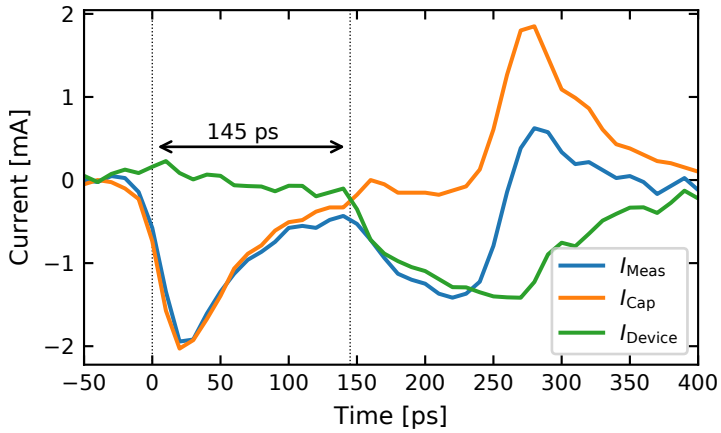

Figure 4.11.: Measured current response I_{Meas} (blue line) of the Zr1 device after the application of a 250 ps pulse with an amplitude of $V_P = -0.8$ V. The capacitive current I_{Cap} (orange line) was determined with eq. 2.5 and the current through the device I_{Device} (green line) with eq. 2.6. The SET event occurring after approximately 145 ps is indicated. Adapted from [38], with the permission of AIP Publishing.

The SET and transition times of the Zr1 device are shorter than the ones of the Ta3 device, as shown in fig. 4.10. Several possible origins for this observation are discussed in the following:

1. The SET kinetics of VCM devices depend strongly on the chosen RESET voltage [142] and on the value of the HRS [161]. To eliminate these influences the RESET voltage

was chosen identically for both devices (1.6 V, see fig. 4.4) and it was made sure that the devices' HRS is in the range from 10 kΩ to 30 kΩ. A deeper discussion, showing that the devices' HRS cannot be the origin of the shift in the SET kinetics of the Ta3 and Zr1 device, can be found in the supplement of [38].

2. As shown in chapter 3.2.4, the electrical charging times of the Ta3 and Zr1 device amount to 69.0 ps and to 48.8 ps (see table 3.4), respectively. At $|2V_P| = 2.2$ V in fig. 4.10a the SET times of the Ta3 and Zr1 device amount to 105 ps, and 55 ps, respectively. This large discrepancy of the SET times cannot be explained by the different electrical charging times to this extend.

3. A higher SET voltage shifts the SET kinetics towards higher voltages, which is equivalent to slower SET times at the same applied voltage. For this purpose, 410 additional sweeps were conducted for both devices at a sweep rate of 0.5 V/s. The settings of the sweeps are identical to the ones from table 3.2. Two exemplary sweeps of the Ta3 and Zr1 device were already shown in fig. 3.4c and fig. 3.4d, respectively. The SET voltage was defined as the voltage at which the device's current surpasses a threshold of 250 µA. The results for the SET voltage of both devices are shown in fig. 4.12. The mean of the Ta3 device's SET voltage amounts to 0.75 V and the median to 0.74 V. The mean and median of the Zr1 device's SET voltage amount to 0.64 V.

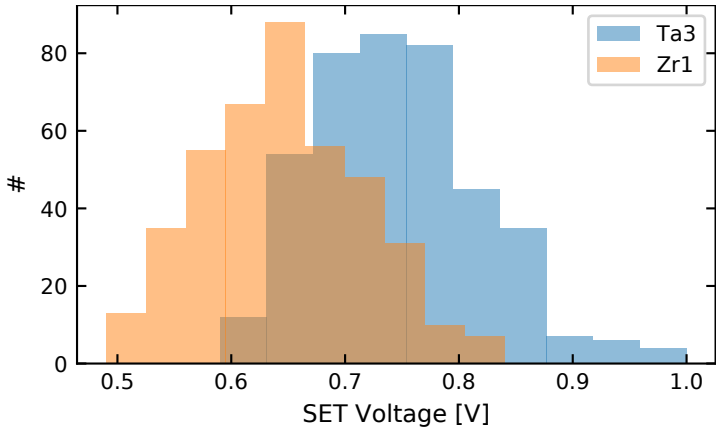

Figure 4.12.: SET voltages of the Ta3 (blue) and Zr1 device (orange). For each device, 410 sweeps were conducted with settings from table 3.2. The SET event is defined as the voltage at which the device's current surpasses the threshold of 250 µA. The mean of the Ta3 device's SET voltage amounts to 0.75 V and the median to 0.74 V. The mean and median of the Zr1 device's SET voltage amount to 0.64 V.

To demonstrate the impact of the SET voltage on the SET kinetics (point 3), the SET times from fig. 4.10a were again plotted in fig. 4.13, but this time the absolute pulse voltage $|V_P|$ of the Ta3 device has been shifted by -0.1 V, which corresponds to the difference of the Ta3 and Zr1 device's median SET voltage. As the SET voltage was determined with quasistatic sweeps (sweep rate: 0.5 V/s), charging effects can be neglected. The SET kinetics

of the Ta3 device are now much closer to the SET kinetics of the Zr1 device, which indicates the strong influence of the SET voltage. The still slightly slower SET times of the Ta3 device can be explained by the difference in the electrical charging time, as described by point 2.

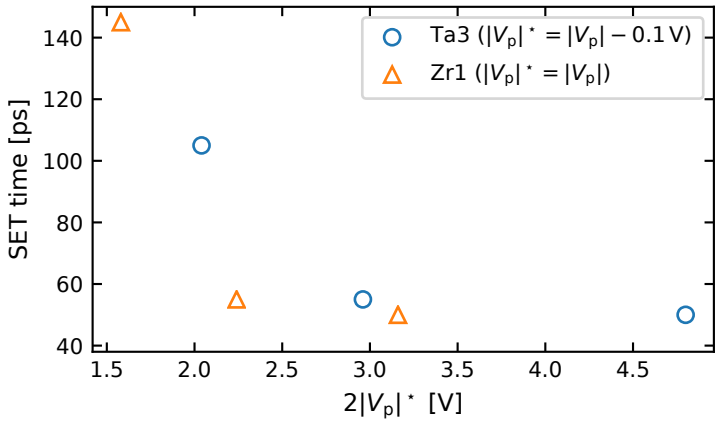

Figure 4.13.: SET times from fig. 4.10a. However, this time absolute pulse voltage $|V_P|$ of the Ta3 device has been shifted by -0.1 V to take the SET voltage's influence on the SET kinetics into account.

The lower SET voltage of the Zr1 device could be attributed to its lower migration barrier for oxygen vacancies. For yttrium-stabilized ZrO_x with low yttrium concentrations, the migration barrier is always below 0.6 eV [166]. In TaO_x, in contrast, the migration barrier is reported to be above 1 eV [167, 168]. In addition, different thermal conductivities in ZrO_x and TaO_x could influence the temperature in the device and, thereby, have an impact on the SET voltage.

4.2.2. HfAx and HfBx devices

To demonstrate that the devices on the HfAx and HfBx wafer can also achieve fast SET times, the SET kinetics of the HfA2 and HfB1 device (both: $3 \times 3\,\mu m^2$, Pt\$HfO_x$\$TiO_x$\Ti) are shown in this section.

The measurement procedure is shown in fig. 4.14. It is very similar to the one used for the Ta3 and Zr1 device (see fig. 4.4). As mentioned in section 3.2.1, a lower RESET voltage of -1.2 V had to be used, because the devices on the HfBx wafer reached significantly higher HRSs. Nevertheless, the HRSs scattered in the range from 10 kΩ to 200 kΩ for the HfA2 device and from 30 kΩ to 500 kΩ for the HfB1 device, which makes a comparison to the Zr1 and Ta3 devices' SET kinetics impossible (ranging from 10 kΩ to 30 kΩ). As mentioned above, the SET kinetics strongly depend on the chosen RESET voltage [142] and on the HRS [161]. Also, a current compliance of 500 µA was used instead of 300 µA. The pulse amplitudes (ranging from -0.8 V to -2.5 V) and durations (ranging from 50 ps to 250 ps in steps of 5 ps) are, however, identical to the ones applied to the Ta3 and Zr1 device. Each cycle was repeated at least 10 times until a smooth curve was achieved.

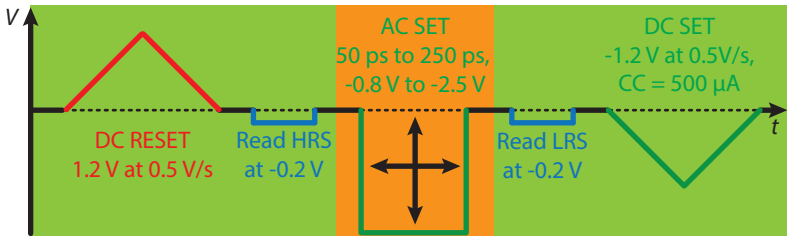

Figure 4.14.: Measurement cycle to determine the HfA2 and HfB1 devices' SET kinetics. The green shaded area marks the parts measured by the Keithley 2634B SMU at the DC port of the bias tee and the orange shaded area the part, in which the pulse from the PG5 pulse generator is applied to the AC port of the bias tee.

The results of the ratio $R_{\mathrm{LRS}}/R_{\mathrm{HRS}}$ of the HfA2 and HfB1 device are shown in fig. 4.15 and fig. 4.16, respectively, in form of boxplots. The LRS values can be found in the appendix section B. The minimum LRS value amounts to 817 Ω for the HfA2 device (see fig. B.2) and to 976 Ω for the HfB1 device (see fig. B.3). At the lowest applied pulse voltage of $2V_{\mathrm{P}} = -1.6\,\mathrm{V}$, both devices did not switch to the LRS. At a FWHM of 250 ps, the HfA2 device's $R_{\mathrm{LRS}}/R_{\mathrm{HRS}}$ median shifted towards 0.5 (see fig. 4.15d), but did not fall below 0.5 and, therefore, no SET time could be derived. Meanwhile, the median value of the HfB1 device remained at unity for all FWHMs (see fig. 4.16d), although the boxplots also broadened towards 0.5.

At a voltage of $2V_{\mathrm{P}} = -2.2\,\mathrm{V}$, both devices switched to the LRS. The HfA2 device (see fig. 4.15c) switched at a FWHM of 150 ps and the HfB1 device switched a little earlier at 140 ps (see fig. 4.16c). It is striking that the transition of the HfB1 device's median has a step like function and jumps from values close to unity to values close to zero, which corresponds to a transition time of only 5 ps. The broadening of the box plots in the region of the SET event indicates, however, a stochastic process at this timescale and, therefore, this observation does not prove that the transition occurs truly within 5 ps. A similar observation can be made at a voltage of $2V_{\mathrm{P}} = -3.2\,\mathrm{V}$. The HfA2 device switched at 100 ps to the LRS (see fig. 4.15b) and the HfB1 device again a little earlier at 90 ps (see fig. 4.16b).

At the highest applied voltage of $2V_{\mathrm{P}} = -5.0\,\mathrm{V}$, the HfA2 device switched to the LRS within 55 ps (see fig. 4.15a) and the HfB1 device already switched at a FWHM of 50 ps to the LRS (see fig. 4.16a). To show that the HfA2 device can also switch faster than 55 ps, an additional 50 ps pulse with an amplitude of $2V_{\mathrm{P}} = -7.1\,\mathrm{V}$ has been applied to the HfA2 device, during which it switched from the HRS (165 kΩ) to the LRS (2.11 kΩ). The current response is shown in fig. 4.17a, which indicates that the FWHM of the applied pulse (50 ps) has been preserved. An exemplary current response of a 50 pulse with an amplitude of $2V_{\mathrm{P}} = -5.0\,\mathrm{V}$ applied to the HfB1 device is shown in fig. 4.17b. Again, the FWHM has been preserved and the device switched from the HRS (88.3 kΩ) to the LRS (5.15 kΩ).

The median values of the ratio $R_{\mathrm{LRS}}/R_{\mathrm{HRS}}$ of the HfA2 and HfB1 device are shown in fig. 4.18 as solid and dashed lines, respectively. The median values are also indicated in fig. 4.15 and fig. 4.16 as red bars. The horizontal dotted line at 0.5 marks the threshold for the SET time,

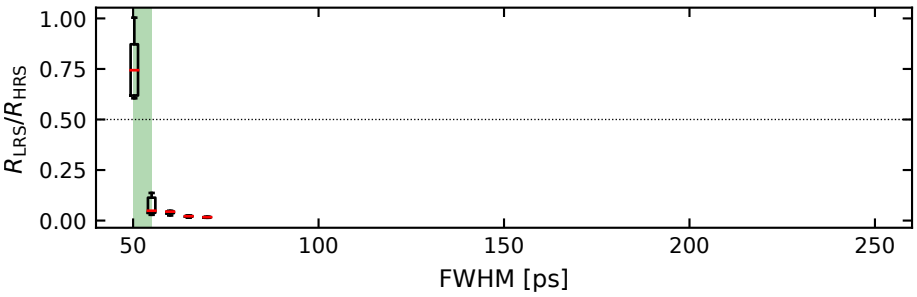

(a) HfA2 device, $V_P = -2.5\,V$.

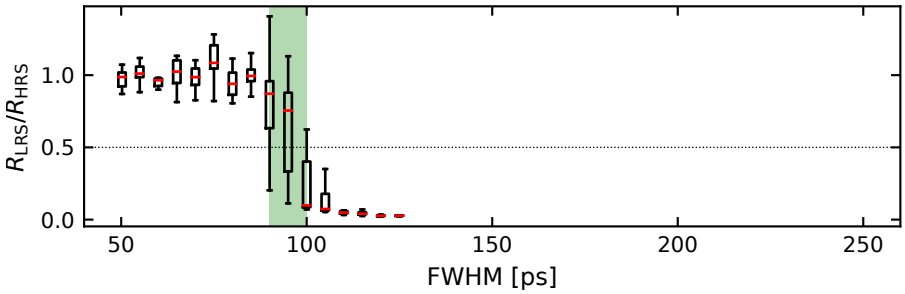

(b) HfA2 device, $V_P = -1.6\,V$.

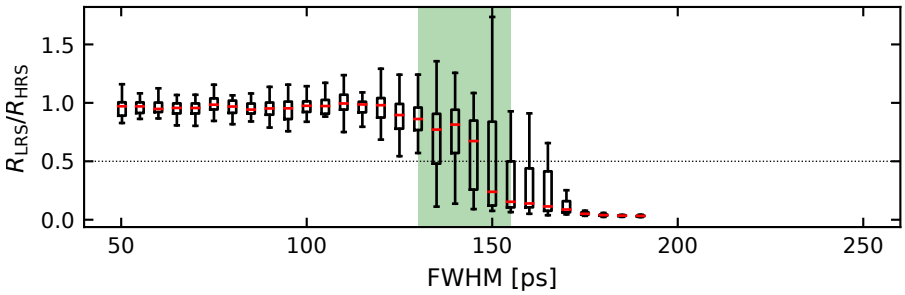

(c) HfA2 device, $V_P = -1.1\,V$.

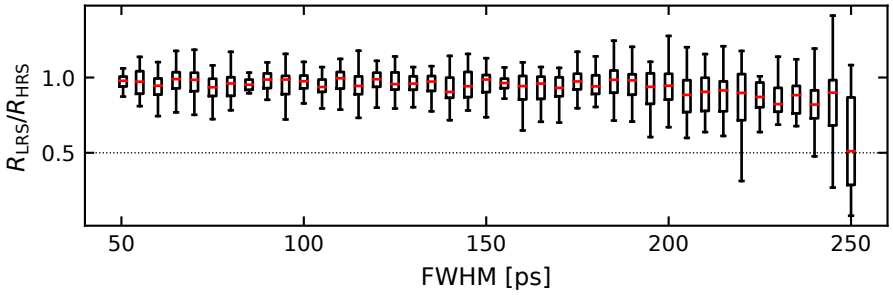

(d) HfA2 device, $V_P = -0.8\,V$.

Figure 4.15.: SET kinetics of the HfA2 device (see table 3.1). The SET event has been defined as the time at which the median value (red bar) reaches values below 0.5 (horizontal dashed line). The green shaded areas in (a), (b), and (c) mark the transition time (20 %-80 %).

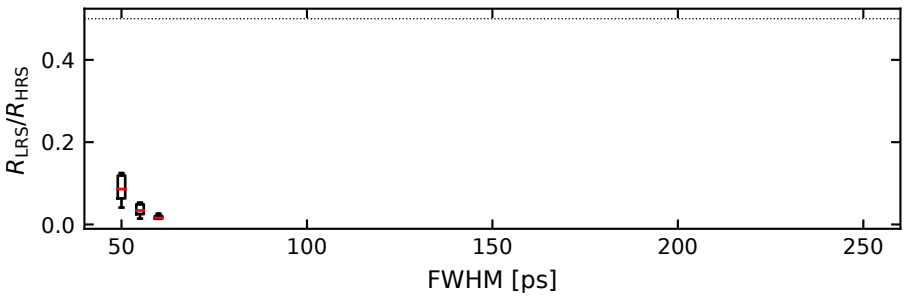

(a) HfB1 device, $V_P = -2.5\,V$.

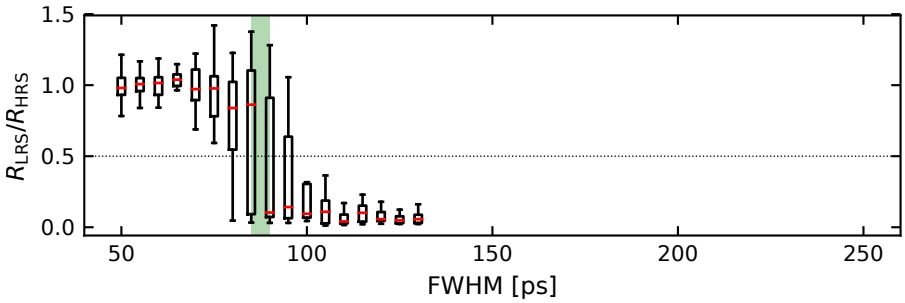

(b) HfB1 device, $V_P = -1.6\,V$.

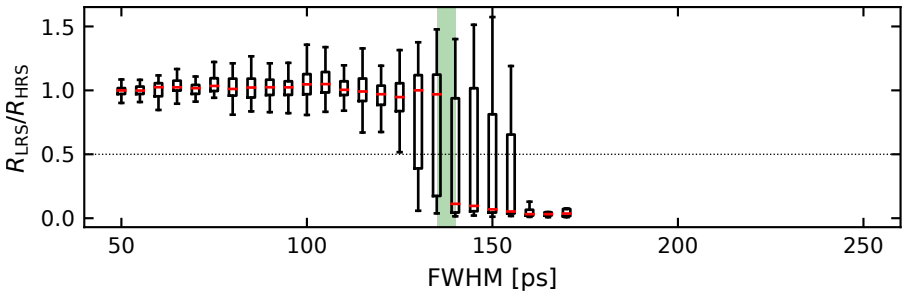

(c) HfB1 device, $V_P = -1.1\,V$.

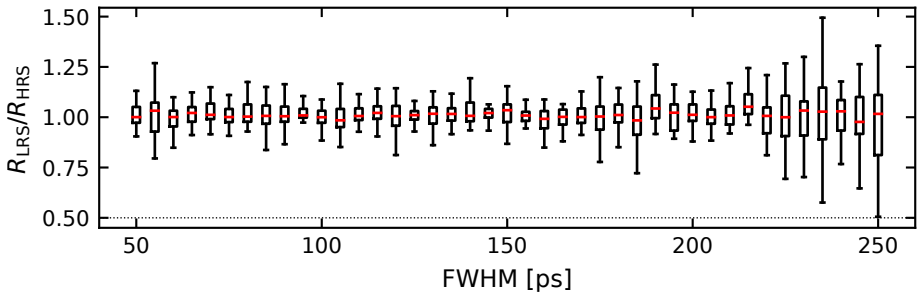

(d) HfB1 device, $V_P = -0.8\,V$.

Figure 4.16.: SET kinetics of the HfB1 device (see table 3.1). The SET event has been defined as the time at which the median value (red bar) reaches values below 0.5 (horizontal dashed line). The green shaded areas in (b) and (c) mark the transition time (80 %-20 %).

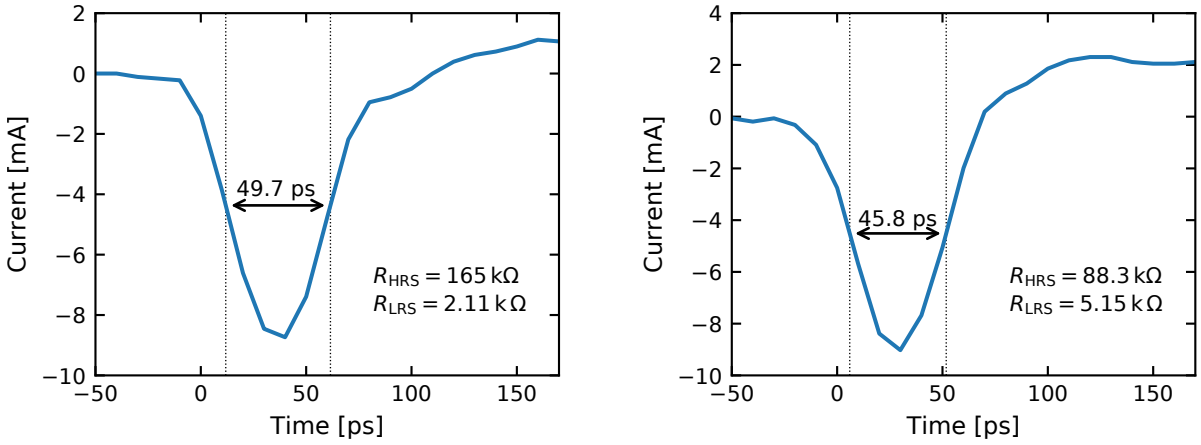

(a) HfA2 device, $V_P = -3.5\,V$, FWHM = 50 ps.

(b) HfB1 device, $V_P = -2.5\,V$, FWHM = 50 ps.

Figure 4.17.: (a) HfA2 device's current responses of a 50 ps pulse with an amplitude of $2V_P = -7.1\,V$. (b) HfB1 device's current responses of a 50 ps pulse with an amplitude of $2V_P = -5.0\,V$. The change in resistance is indicated on the lower left for both devices.

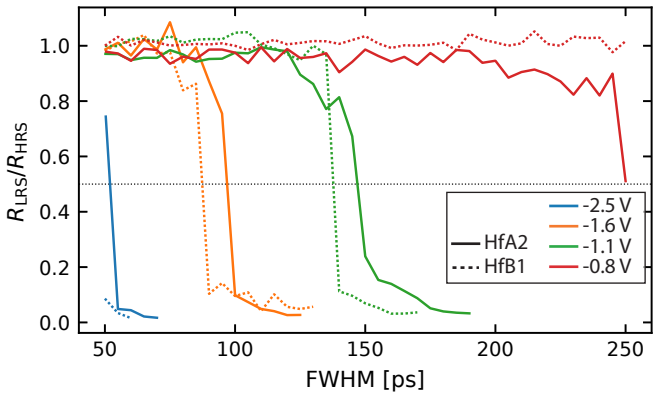

Figure 4.18.: Median values of the ratio R_{LRS}/R_{HRS} for the HfA2 device (solid lines, data from fig. 4.15) and the HfB1 device (dashed lines, data from fig. 4.16). The color of the lines indicates the pulse amplitude.

which is almost identical for both devices. The transition to the LRS of the HfB1 device occurs much more abruptly than the transition to the LRS of the HfA2 device. This can be attributed to the higher HRS of the HfB1 device, which leads to a more abrupt SET transition. This was also observed for crossbar equivalents of the HfA2 and HfB1 devices [161].

The derived SET and transition times for the HfA2 and HfB1 device are shown in fig. 4.19. The SET time for the HfA2 device at $|2V_P| = 7.1\,V$ was determined with the single pulse from fig. 4.17a. As already mentioned above, the SET kinetics are very similar, which is expected, because the material stacks of both devices are almost identical. It was, however, shown in chapter 3.2.4 that the electrical charging time of the HfA2 and HfB1 device amount to 206.2 ps and 99.0 ps, respectively. Consequently, a faster SET kinetic for the HfB1 device is expected. The higher HRS of the HfB1 device also influences the SET kinetics [161], which may compensate for the HfB1 device's shorter electrical charging time.

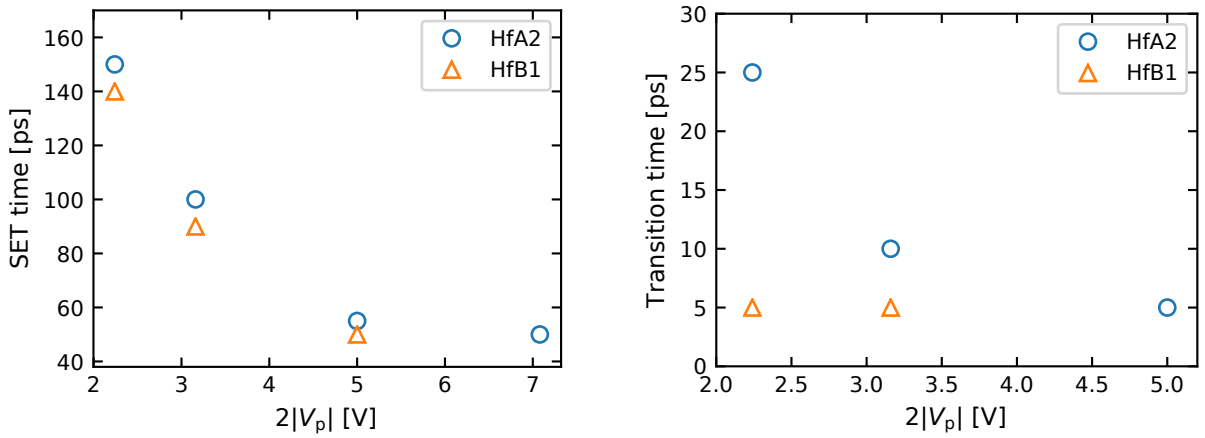

(a) SET times.

(b) Transition times (80 %-20 %).

Figure 4.19.: (a) SET times of the HfA2 and the HfB1 device, determined from fig. 4.18 (see horizontal line). (b) Transition times (80 %-20 %) of the HfA2 and the HfB1 device. Determined from fig. 4.15 and fig. 4.16 (see green shaded area). Twice the adjusted absolute pulse amplitude $|2V_P|$ is plotted on the abscissa, as this is the effective voltage at the end of the electrical charging.

As shown in fig. 4.19b, the HfA2 device's transition time depends on the applied voltage and it amounts to only 5 ps at $2V_P = -5.0$ V. All values of R_{LRS}/R_{HRS} at a FWHM of 50 ps were above the 0.5 threshold of the SET time (see dashed line in fig. 4.15a) and all values of R_{LRS}/R_{HRS} at a FWHM of 55 ps were below this threshold. This indicates that the transition from the HRS to the LRS can truly occur within 5 ps. For the HfB1 device, the transition was always abrupt, which might correlate with the higher HRS state, which facilitates abrupt SET transitions [161]. The boxplots in this area are, however, very broad and, therefore, the determined transition times of the HfB1 device of 5 ps cannot be confirmed. The time-span of the determined transition times of the HfA2 and HfB1 device is marked as green shaded areas in fig. 4.15 and fig. 4.16, respectively.

4.3. Switching speed limit of VCM devices

Different limiting mechanism of the SET kinetics are summarized in [36]. The argumentation in this section was published in [100]. At slow timescales (above 10 ns), the migration of oxygen vacancies is limiting the SET [80] and RESET kinetics [94].

In the fast regime (below 10 ns), the electrical charging time or the heating time of the VCM device dominates the switching kinetics. So far, the heating time has only been estimated with finite element simulations. These models have, however, several uncertainties, such as the geometry of the filament and the thermal properties (thermal conductivity, heat capacity, and mass density), which are difficult to estimate for thin films, as they differ from their bulk values. So far, simulation results indicate that the heating could occur only within tens of picoseconds [36, 97] or several nanoseconds [80]. The electrical charging time was

already determined in chapter 3.2.4 and can reach values down to 48.8 ps for VCM devices incorporated into CPW structures (see table 3.4).

To test the impact of the electrical charging time on the SET kinetics, the results of Ta1 ($15 \times 20\,\mu m^2$), Ta2 ($5 \times 5\,\mu m^2$), and Ta3 device ($2 \times 2\,\mu m^2$) are summarized in fig. 4.20. The blue dots of the Ta1 device mark the slow regime above 10 ns [37, 130]. The SET times in the fast regime of the Ta1 (orange dots) and Ta2 device (green dots) were already shown in fig. 4.3 and the SET times of the Ta3 device (red dots) in fig. 4.10a. The electric charging times of these three devices amount to 2.54 ns for the Ta1, to 636 ps for the Ta2, and to 69.0 ps for the Ta3 device. The influence of this electric charging time on the SET times in the fast regime (below 10 ns) is clearly visible, as the devices with shorter electrical charging times, also achieve faster SET times.

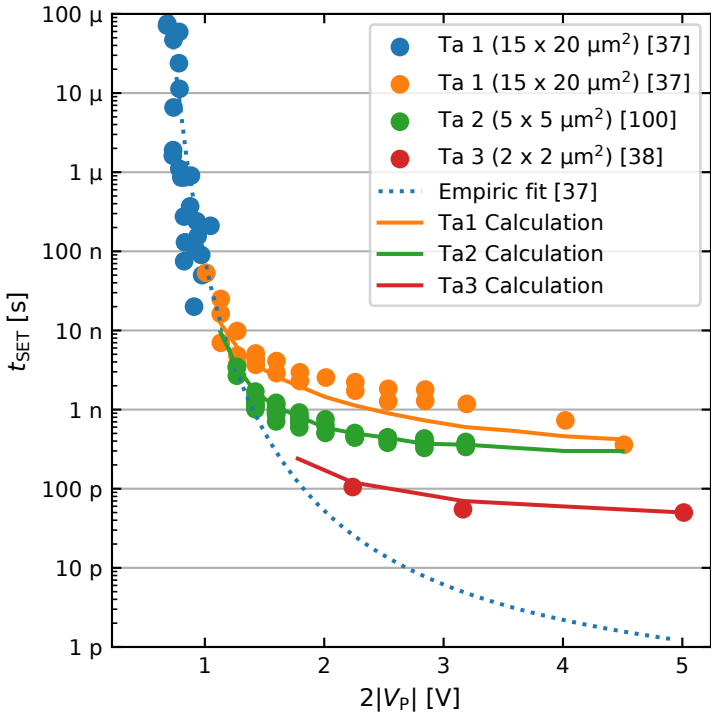

Figure 4.20.: SET kinetics of the Ta1 device [37] (blue and orange points), the Ta2 device [100] (green points), and the Ta3 device [38] (red points). These data were already shown in fig. 4.3 and fig. 4.10a. Eq. 4.1 is drawn as blue dotted line corresponding to an empiric fit to the Ta1 device's slow regime (blue points). With this equation, the influence of the electrical charging time on the device's SET kinetics was calculated and the results are drawn as solid lines. Twice the pulse amplitude is indicated on the abscissa corresponding to the voltage at the device at the end of its electrical charging. Adapted from [100].

Physically, the SET kinetics are limited by the migration of oxygen vacancies in the slow regime [80] (blue dots in fig. 4.20) and are only little influenced by the device's electrical charging or heating time. Therefore, this slow regime reflects the intrinsic speed limit of

ReRAM devices. An empiric function was fitted to this regime in [37]:

$$t_{\mathrm{SET}}(t) = t_0 \cdot \exp\left(\frac{\kappa}{|V_{\mathrm{DUT}}(t)| - V_0}\right), \tag{4.1}$$

with $\kappa = 11.2\,\mathrm{V}$ and $V_0 = 0.162\,\mathrm{V}$ serving as fitting parameters. The reciprocal value of the attempt frequency of amorphous TaO_x amounts to $t_0 = 1.19 \cdot 10^{-13}$ [169]. Eq. 4.1 is plotted as blue dotted line in Fig. 4.20. To prove that the bending of the SET kinetics in the fast regime towards slower SET times originates from the electrical charging time, the SET times were calculated by using eq. 4.1, while considering the electrical charging time, which is explained in the following.

For every applied pulse in Fig. 4.20, the voltage at the device $V_{\mathrm{DUT}}(t)$ was calculated with the device's scattering parameters, as described in chapter 2.1. The SET time for the first value in time of $|V_{\mathrm{DUT}}(t)|$ above $V_0 = 0.162\,\mathrm{V}$ (referred to as V_1) is calculated with eq. 4.1 ($t_{\mathrm{SET}}(V_1)$). Then, the quotient $q_1 = \frac{t_{\mathrm{S}}}{t_{\mathrm{SET}}(V_1)}$, with the oscilloscope's sampling time $t_{\mathrm{S}} = 10\,\mathrm{ps}$, is built, which corresponds to a state variable, describing the current state of the VCM devices. For $q_1 < 1$, the SET time is longer than t_{S} and, consequently, the VCM device did not switch during this time frame. $|V_{\mathrm{DUT}}(t)|$ is low at the beginning of a pulse and, therefore, the value of q_1 is always below 1.

In the next step, the following values of $|V_{\mathrm{DUT}}(t)|$ are analyzed. The i-th value above $0.162\,\mathrm{V}$ is referred to as V_i. For all values of V_i, the quotients $q_i = \frac{t_{\mathrm{S}}}{t_{\mathrm{SET}}(V_i)}$ are built, and added up until their sum reaches 1 ($\Sigma_{i=1}^{n} q_i \geq 1$). Finally, the SET time is calculated by multiplying the number of iterations n with t_{S}, which is done for all three devices.

The calculated SET times are plotted as solid lines in fig. 4.20. They match the measured SET times well, which indicates that the SET kinetics are only limited by the electrical charging of the VCM devices. A similar procedure was used in a previous study to demonstrate that the SET kinetics of $SrTiO_3$ devices are limited in the slow regime by the migration of oxygen vacancies [105].

As the electrical charging is the limiting factor of the SET kinetics down to 50 ps, the heating of the VCM device must occur on a faster timescale. A finite element study conducted by S. Menzel suggests heating times between 120 ps and tens of picoseconds [36]. The results of this section confine this interval to a maximum heating time of 50 ps for filamentary TaO_x-based devices. As mentioned above, the heating time also depends on the filament's geometry and the thermal properties of the device and, therefore, this conclusion cannot be made for other VCM devices. The heating time scales with the volume of the heated area, which is mainly the conductive filament [80]. The filament's diameter is, however, significantly smaller than the device's feature sizes (*e.g.* having a diameter of 1 nm to 3 nm in HfO_x-based devices [78] or 2 nm to 4 nm in $SrTiO_3$-based devices [77]) and, therefore, no change in the heating time is expected for smaller devices than $2 \times 2\,\mu\mathrm{m}^2$, down to sub-

10-nm scaled devices. The charging time can, however, be further reduced by nanoscaling VCM devices [36].

5. RESET kinetics of VCM devices

In the previous chapter 4, fast SET operations within 50 ps were demonstrated with TaO_x-, ZrO_x-, and HfO_x/TiO_x-based devices. To the author's knowledge this is the fastest SET time observed in VCM devices. As shown in this chapter, achieving similar fast RESET times with these devices proved, however, to be more challenging and 50 ps fast RESET times could only be realized reproducibly on HfO_x/TiO_x-based devices. Nevertheless, the observed RESET failure was analyzed and could be identified as a unipolar switching mode. Due to the nonlinearity of the RESET kinetics, faster RESET times require higher voltages. These higher voltages trigger, however, a unipolar SET event, which prohibits faster RESET times.

Firstly, the RESET times were determined for the Ta3 ($2 \times 2\,\mu m^2$, Pt\$TaO_x$\Ta, more details in table 3.1), and Zr1 device ($2 \times 2\,\mu m^2$, Pt\$ZrO_x$\Ta) in the sub-100 ns time regime, which is shown in section 5.1.1. In this regime, reproducible fast switching times down to 480 ps could be observed for both devices. No reproducible RESET operations could be achieved on the timescale between 50 ps and 250 ps (see section 5.1.2). Instead of switching to a higher resistance during the application of a positive voltage pulse to the active Pt electrodes, the devices' resistance decreased. It was even possible to switch both devices from the HRS to the LRS with a positive voltage pulse to the active Pt electrode (see section 5.1.2). Combining these results allowed the construction of a programming window for the RESET operation (see section 5.1.4), showing that the Ta3 and Zr1 device's RESET kinetics is intrinsically limited by the coexistence of the unipolar switching mode. By introducing an oxygen-blocking C layer between the active Pt electrode and the Ta_x or ZrO_x layer, 50 ps fast RESET times could be shown for both ZrO_x- and TaO_x-based devices, but not reproducibly.

Later, in section 5.2, the RESET kinetics of the HfA1, HfA3, HfB2 and HfB3 device (all Pt\$HfO_x$\$TiO_x$\Ti, see table 3.1) are shown. Some devices on the HfAx and most devices on the HfBx wafer switched reproducibly from the LRS to the HRS at FWHMs below 60 ps. On the other devices, also unipolar SET operations were observed. The only difference between the two samples (HfAx and HfBx) is the deposition method of the active Pt electrode, which was once deposited using a standard RF magnetron sputtering technique, and once with an off-axis sputtering tool. The devices on the HfBx wafer were fabricated with the off-axis sputtering tool and most of them could be switched to the HRS.

The unipolar SET voltage was characterized for several devices on the Ta3, Zr1, HfAx and HfBx device's wafers. The devices on the HfBx wafer had the highest unipolar SET voltage

indicating a correlation with the facilitation of fast RESET times. Higher unipolar SET voltages could remove the RESET speed limit. For this purpose, suggestions to achieve higher unipolar SET voltages are given. Finally, an analogy to the SET programming window of PCM devices is given, which compares the intrinsic speed limiting processes of both memory types.

5.1. RESET kinetics of TaO_x- and ZrO_x-based devices

5.1.1. Sub-100 ns time regime

The measurement procedure to determine the Ta3 and Zr1 device's RESET kinetics on a sub-100 ns timescale is sketched in fig. 5.1. Firstly, the device was driven to the LRS with a negative voltage sweep with an amplitude of -1.2 V at a sweep rate of 0.5 V/s. A current compliance of 300 µA was used to prevent the devices from taking damage and to reach a resistance window from 1.0 kΩ to 3.0 kΩ. Positive voltage pulses were, subsequently, applied with the PSPL 2600C pulse generator to the active Pt electrode of the devices. The pulse width was varied between 3 ns and 100 ns and the pulse amplitude between 0.6 V and 1.0 V. As explained below, the RESET time is determined from the measured current response, which was measured with the Tektronix DPO77704D oscilloscope. The devices' resistance was read before and after the application of the pulse at a voltage of -0.2 V, which are referred to as R_{PRE} and R_{POST}, respectively, throughout this chapter. Finally, a sweep with a positive voltage of 1.6 V was conducted at a sweep rate of 0.5 V/s. This sweep ensures that the devices start each cycle in a similar state.

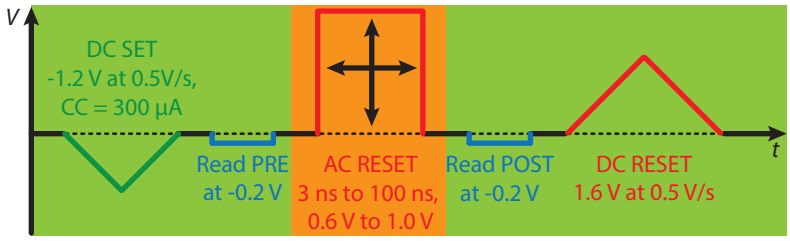

Figure 5.1.: Sketch of the measurement cycle to determine the Ta3 and Zr1 device's RESET kinetics on a sub-100 ns timescale. The green shaded area marks the parts measured by the Keithley 2634B SMU at the DC port of the bias tee and the orange shaded area the part, in which the pulse from the PSPL 2600C pulse generator is applied to the AC port of the bias tee.

The resulting RESET kinetics of both devices are plotted in fig. 5.2. The determination of the RESET time is explained in chapter 2.2.1 (see fig. 2.13). Both devices show a strong nonlinear dependence of the RESET time on the applied pulse voltage. The RESET times of the Zr1 device (orange triangles) are a little faster than the ones of the Ta3 device. At an amplitude of $2V_{\mathrm{P}} = 1.6\,\mathrm{V}$, the RESET kinetics of the Zr1 device start to bend due to the relative long rise time of the PSPL 2600C pulse generator ($\approx 359\,\mathrm{ps}$). The Zr1 device's

rise time of 48.8 ps (see table 3.4) contributes only little to this bending. At an amplitude of $2V_P = 1.8\,V$, no RESET time could be determined for the Ta3 device, which is explained below.

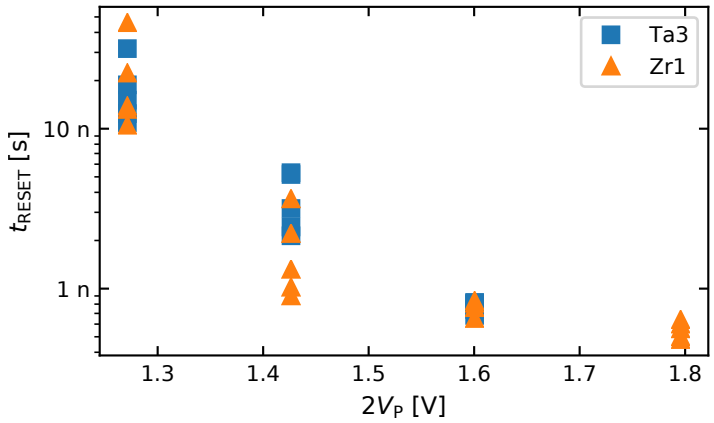

Figure 5.2.: RESET kinetics of the Ta3 (blue squares) and Zr1 device (orange triangles). Twice the adjusted absolute pulse amplitude $2V_P$ is plotted on the abscissa, as this is the effective voltage at the end of the electrical charging.

The two fastest detected RESET times of the Ta3 and Zr1 device are shown in fig. 5.3a and fig. 5.3b, respectively. The pulse width of both pulses was reduced to prevent the devices from damage. A 10 ns voltage pulse with an amplitude of $2V_P = 1.6\,V$ was applied to the Ta3 device and a 2 ns voltage pulse with an amplitude of $2V_P = 1.8\,V$ was applied to the Zr1 device. During the pulse's application the Ta3 device switched from 1.39 kΩ to 18.23 kΩ and the Zr1 device from 1.55 kΩ to 132 kΩ. The determined RESET time amounts to 760 ps for the Ta3 device and to 480 ps for the Zr1 device. The current peak at the beginning of the Zr1 device's current response has a much larger amplitude than the capacitive peak and the end of the pulse. The integral below a capacitive peak corresponds to the electric charge and it must be identical at the beginning and at the end of the pulse. As the current peak at beginning of the pulse is much larger, this shows that the peak at the beginning can only be little influenced by the capacitive current and, therefore, corresponds mainly to the current through the device.

As mentioned above, the RESET time of the Ta3 device could only be determined up to an amplitude of $2V_P = 1.6\,V$ (see fig. 5.2). During the application of a 4 ns pulse with an amplitude of $2V_P = 1.8\,V$ the Ta3 device's resistance surprisingly decreased from 1.39 kΩ to 990 Ω, instead of increasing, as it did for the pulses with a lower amplitude. The corresponding current response is shown in fig. 5.4. Different to the previously shown current responses, the current increased to 3.0 mA (instead of 1.5 mA), which indicates that a sudden increase in conductivity must have occurred at the beginning of the pulse's application, which prevents the device from switching to the HRS. Fortunately, the occurrence of this current increase did not destroy the Ta3 device. Nevertheless, the measurement was aborted to prevent the

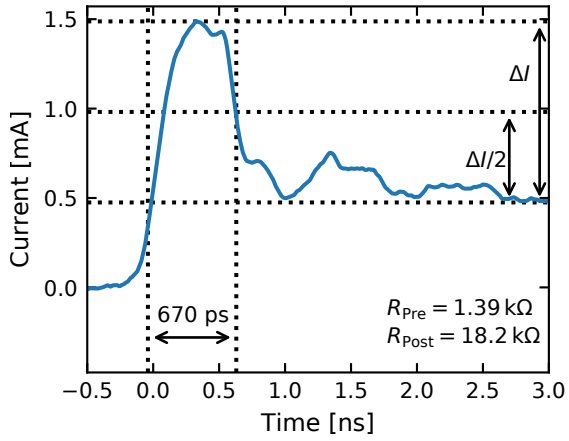

(a) Ta3 device, 10 ns pulse, $2V_P = 1.6\,V$

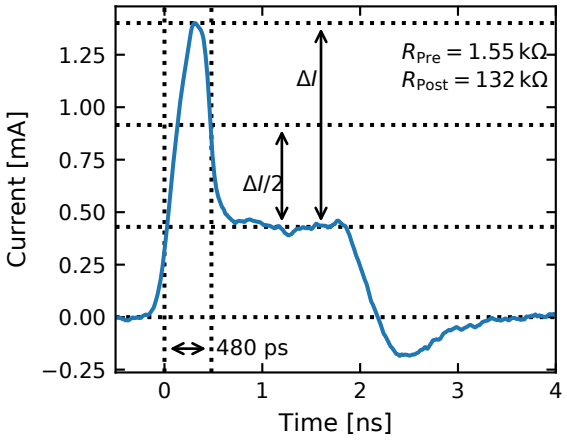

(b) Zr1 device, 2 ns pulse, $2V_P = 1.8\,V$

Figure 5.3.: (a) Current response of the Ta3 device, during the application of a 10 ns pulse with an amplitude of $2V_P = 1.6\,V$. The RESET event was detected at 670 ps. (b) Current response of the Zr1 device, during the application of a 2 ns pulse with an amplitude of $2V_P = 1.8\,V$. The RESET event was detected at 480 ps. The current responses of both devices were smoothened with a Savitzky-Golay filter.

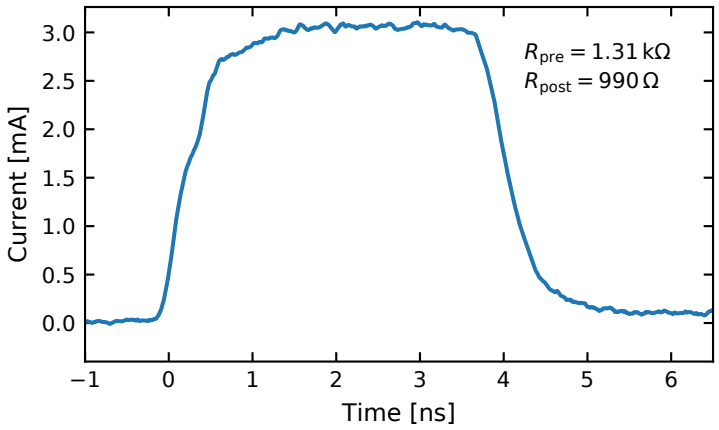

Figure 5.4.: Ta3 device's current response to a 4 ns pulse with an amplitude of $2V_P = 1.8\,V$.

device from taking damage. This phenomenon was also observed for the Zr1 device at faster timescales, which is shown in the following.

5.1.2. Time regime from 50 ps to 250 ps

Regular RESET mode

The measurement procedure of the Ta3 and Zr1 device's RESET kinetics in the time regime from 50 ps to 250 ps is sketched in fig. 5.5. Differently to the measurement procedure of the RESET kinetics in the sub-100 ns regime, the PG5 pulse generator is used to apply the RESET pulse. Its width was varied between 50 ps and 250 ps in steps of 5 ps and its amplitude was varied from 0.8 V to 2.5 V. The resistance before the pulse's application R_{PRE} was again set in the range from 1.0 kΩ to 3.0 kΩ. Each combination of pulse width and amplitude was repeated at least 10 times.

Similar to the SET kinetics, the ratio of the resistance after the pulse's application (R_{POST}) and the resistance before its application (R_{PRE}) is built and referred to as ${}^{R_{\mathrm{POST}}}/_{R_{\mathrm{PRE}}}$. Values of ${}^{R_{\mathrm{POST}}}/_{R_{\mathrm{PRE}}} > 1$ indicate an increase of the resistance after the pulse's application and a value of ${}^{R_{\mathrm{POST}}}/_{R_{\mathrm{PRE}}} < 1$ a decrease of resistance.

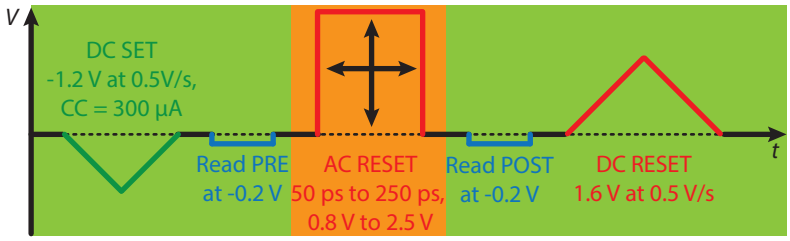

Figure 5.5.: Measurement cycle to determine the Ta3 and Zr1 device's RESET kinetics in the time regime from 50 ps to 250 ps. The green shaded area marks the part measured by the Keithley 2634B SMU at the DC port of the bias tee and the orange shaded area the part in which the pulse from the PG5 pulse generator is applied to the AC port of the bias tee.

The results for ${}^{R_{\mathrm{POST}}}/_{R_{\mathrm{PRE}}}$ of the Ta3 and Zr1 device are shown in fig. 5.6 and fig. 5.7, respectively. As the ratio does not yield concrete information on the absolute POST resistance value, these values are shown in the appendix section C to maintain conciseness. In this case, the POST resistance values of the Ta3 device are shown in fig. C.1 and the ones for the Zr1 device in fig. C.2.

Pulses with the lowest amplitude of $2V_{\mathrm{P}} = 1.6\,\mathrm{V}$ were only applied to the Zr1 device. As shown in fig. 5.7d, ${}^{R_{\mathrm{POST}}}/_{R_{\mathrm{PRE}}}$ moves slightly to higher values for longer FWHMs. The highest achieved POST resistance only amounts to 4 kΩ, which does not correspond to a complete RESET operation.

At a pulse amplitude of $2V_{\mathrm{P}} = 2.2\,\mathrm{V}$, the Ta3 device's ${}^{R_{\mathrm{POST}}}/_{R_{\mathrm{PRE}}}$ remained at unity up to a FWHM of 240 ps at which ${}^{R_{\mathrm{POST}}}/_{R_{\mathrm{PRE}}}$ started to decrease (see fig. 5.6c). A similar tendency was observed for the Zr1 device: Its ${}^{R_{\mathrm{POST}}}/_{R_{\mathrm{PRE}}}$ decreased with increasing FWHMs (see fig. 5.7c).

At a higher amplitude of $2V_{\mathrm{P}} = 3.2\,\mathrm{V}$, a small increase of ${}^{R_{\mathrm{POST}}}/_{R_{\mathrm{PRE}}}$ was observed for the Ta3 device up to a FWHM of 190 ps, after which ${}^{R_{\mathrm{POST}}}/_{R_{\mathrm{PRE}}}$ started to decrease back to unity, indicating that the Ta3 device also does not switch to the HRS in this time regime (see fig. 5.6b). The Zr1 device's ${}^{R_{\mathrm{POST}}}/_{R_{\mathrm{PRE}}}$ decreased again with increasing FWHM (see fig. 5.7b) but much faster than at a pulse amplitude of $2V_{\mathrm{P}} = 2.2\,\mathrm{V}$. The measurement was, therefore, aborted at a FWHM of 100 ps to prevent the Zr1 device from taking damage.

At the highest amplitude of $2V_{\mathrm{P}} = 5.0\,\mathrm{V}$, the Ta3 device's ${}^{R_{\mathrm{POST}}}/_{R_{\mathrm{PRE}}}$ remained at unity for short FWHMs and then abruptly decreased to values down to 0.5 (see fig. 5.6a). This corresponds to R_{POST} values down to 500 Ω. At this amplitude, the Zr1 device's ${}^{R_{\mathrm{POST}}}/_{R_{\mathrm{PRE}}}$ yielded values below one, even at a FWHM of 50 ps (see fig. 5.6a). The lowest values for R_{POST} amounted to 350 Ω.

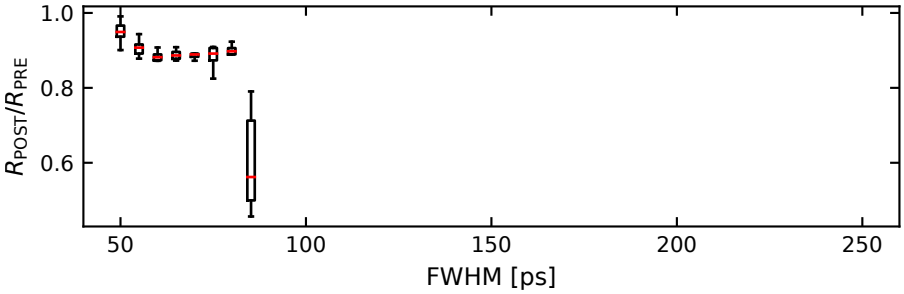

(a) Ta3 device, $V_P = 2.5\,V$.

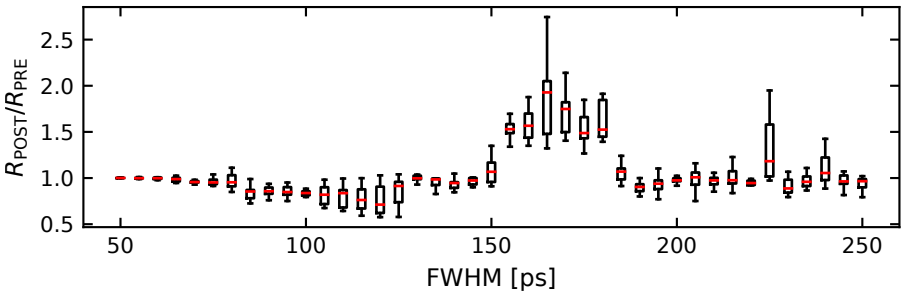

(b) Ta3 device, $V_P = 1.6\,V$.

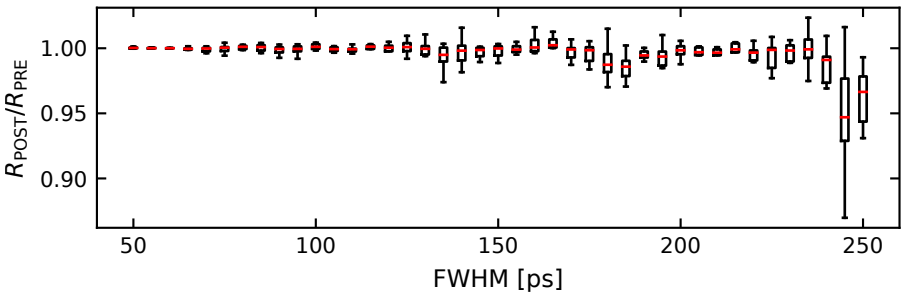

(c) Ta3 device, $V_P = 1.1\,V$.

Figure 5.6.: Regular RESET kinetics of the Ta3 device (see table 3.1). The red bar in the boxplot marks the median.

These results show that it is not possible to successfully switch the Ta3 and Zr1 device to the HRS with pulses shorter than 250 ps. The devices' resistance is rather decreasing, which is identified below as a unipolar switching mode. At almost all pulse amplitudes and FWHMs the boxplots were broad, which indicates that the R_{POST} values scatter significantly, which corresponds to large cycle-to-cycle variability. As the devices' resistance is rather decreasing for the considered pulse amplitudes and FWHMs, it was tested in the following section to realize a unipolar SET kinetic measurement of the Ta3 and Zr1 device with positive voltage pulses.

Unipolar SET kinetics

The measurement procedure to determine the Ta3 and Zr1 device's unipolar SET kinetics is shown in fig. 5.8. It is almost identical to the measurement procedure, which was used in chapter 4.2.1 to determine the Ta3 and Zr1 device's SET kinetics with negative SET

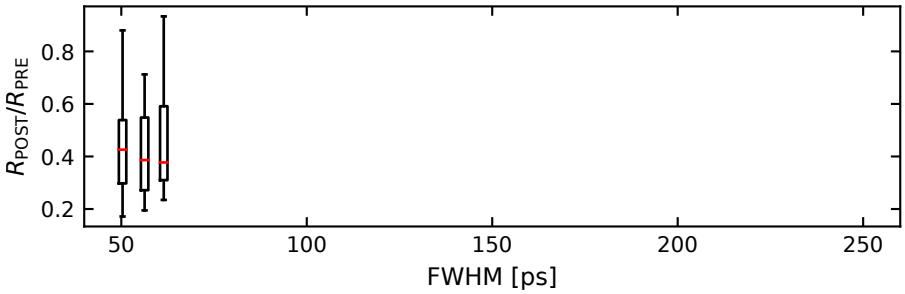

(a) Zr1 device, $V_P = 2.5\,V$.

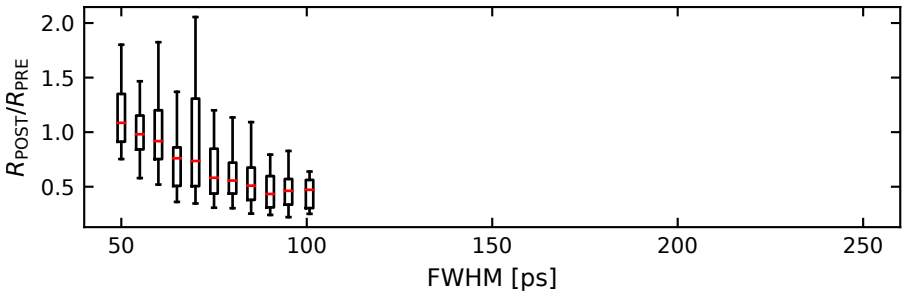

(b) Zr1 device, $V_P = 1.6\,V$.

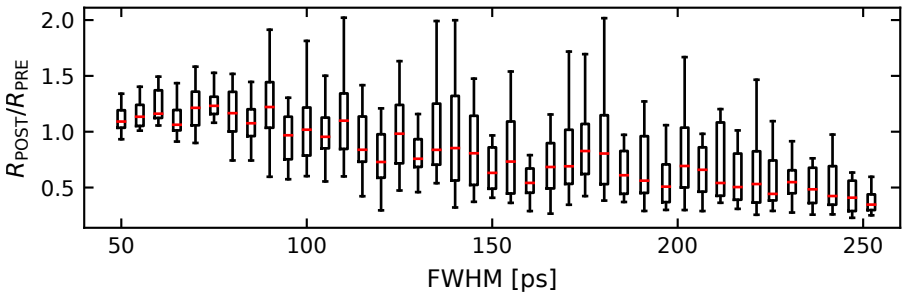

(c) Zr1 device, $V_P = 1.1\,V$.

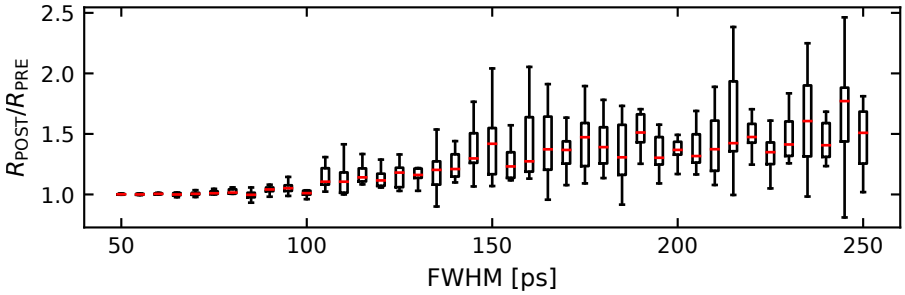

(d) Zr1 device, $V_P = 0.8\,V$.

Figure 5.7.: Regular RESET kinetics of the Zr1 device (see table 3.1). The red bar in the boxplot marks the median.

polarity (see fig. 4.4), corresponding to the usual bipolar operations of VCM devices. The only difference is the positive polarity of the SET pulse. Its pulse width was again varied in steps of 5 ps from 50 ps to 250 ps and its amplitude from 0.8 V to 2.5 V. As for the SET kinetics, the measurement cycles were only considered if the initial resistance R_{PRE} was in the range from 10 kΩ to 30 kΩ. Otherwise, the cycle was repeated. Due to the large cycle-

to-cycle variability of the ratio $R_{\mathrm{POST}}/R_{\mathrm{PRE}}$, the measurement cycles were repeated until a continuous line for the median values of $R_{\mathrm{POST}}/R_{\mathrm{PRE}}$ was achieved.

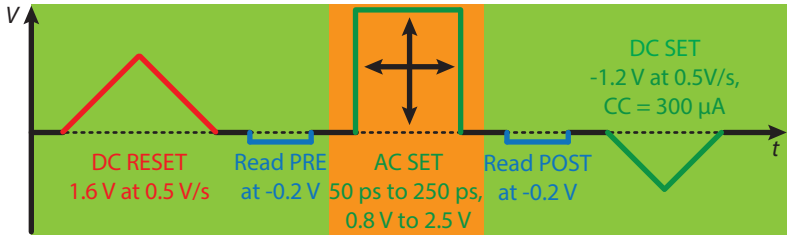

Figure 5.8.: Measurement cycle to determine the Ta3 and Zr1 device's unipolar SET kinetics with positive SET polarity.

These values for the ratio $R_{\mathrm{POST}}/R_{\mathrm{PRE}}$ of the Ta3 and Zr1 device are shown in fig. 5.9 and fig. 5.10, respectively. The corresponding absolute values of R_{POST} values are shown in the appendix section C in fig. C.3 and in fig. C.4 for the Ta3 and Zr1 device, respectively. The observed results for the SET kinetics are very similar to the ones of the regular bipolar SET kinetics presented in chapter 4. At lower voltages, the ratio $R_{\mathrm{POST}}/R_{\mathrm{PRE}}$ of both devices remains at unity, which indicates that they also remain in the HRS. At higher voltages, they switched to the LRS.

At the highest applied pulse voltage of $2V_{\mathrm{P}} = 5.0\,\mathrm{V}$, the Ta3 device started to switch to the LRS at a FWHM of 55 ps (see fig. 5.9a). To show that it is also possible to switch the Ta3 device to the LRS within 50 ps, an additional cycle with a pulse amplitude of $2V_{\mathrm{P}} = 7.1\,\mathrm{V}$ and a FWHM of 50 ps was conducted. The corresponding current response is shown in fig. 5.11a, during which the device switched from 21.5 kΩ to 393 Ω. The Zr1 device already switched to the LRS within 50 ps at a pulse voltage of $2V_{\mathrm{P}} = 5.0\,\mathrm{V}$. An exemplary current response of a 50 ps pulse with an amplitude of $2V_{\mathrm{P}} = 5.0\,\mathrm{V}$ is shown in fig. 5.11b, in which the Zr1 device switched from 18.6 kΩ to 538 Ω.

The resulting transients of the medians of $R_{\mathrm{POST}}/R_{\mathrm{PRE}}$ are shown in fig. 5.12. These values were derived from fig. 5.9 and fig. 5.10 for the Ta3 and Zr1 device, respectively. The colors indicate the pulse amplitude. Both devices switched faster to the LRS at higher voltage amplitudes. The SET and transition times are calculated as in chapter 4: The SET times are again derived by taking the FWHM, at which the transient of $R_{\mathrm{POST}}/R_{\mathrm{PRE}}$ falls below the value 0.5, which is marked as dotted horizontal line in fig. 5.12. The transition time from the HRS to the LRS is defined as the timespan from the last value of $R_{\mathrm{POST}}/R_{\mathrm{PRE}}$ above 0.8 and the first below 0.2.

The resulting SET and transition times of the Ta3 and Zr1 device are plotted in fig. 5.13a and fig. 5.13b, respectively, against twice the adjusted pulse amplitude $2V_{\mathrm{P}}$, which corresponds to the effective voltage at the end of the electrical charging. Only, the SET time at $2V_{\mathrm{P}} = 7.1\,\mathrm{V}$ was determined from a single pulse (see fig. 5.11a). The usual bipolar switching mode of VCM devices is realized by applying negative voltage pulses to the active Pt electrode. In this bipolar switching mode, the fastest SET time amounts to 50 ps and the fastest

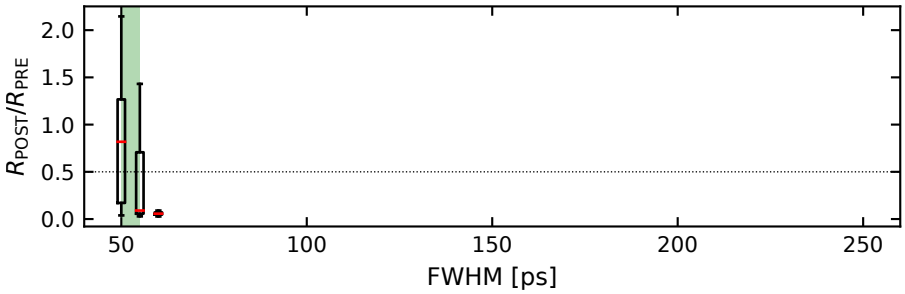

(a) Ta3 device, $V_P = 2.5\,V$.

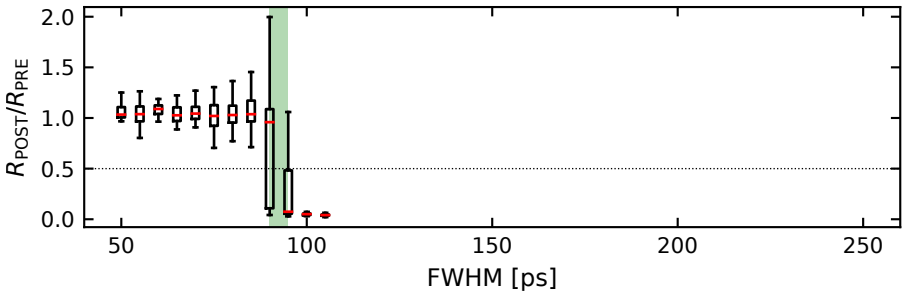

(b) Ta3 device, $V_P = 1.6\,V$.

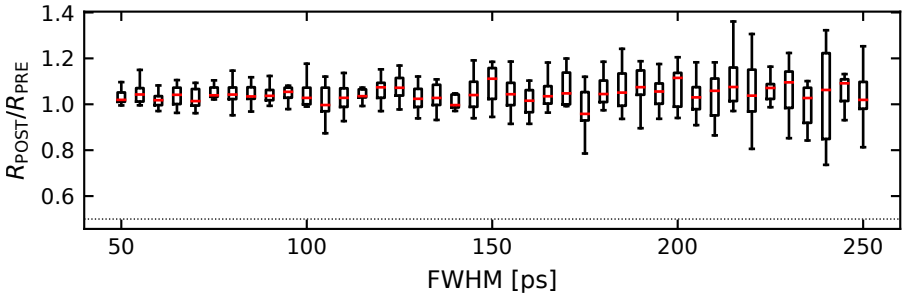

(c) Ta3 device, $V_P = 1.1\,V$.

Figure 5.9.: Unipolar SET kinetics of the Ta3 device (see table 3.1) with positive voltage pulses applied to the Pt bottom electrode. The unipolar SET time has been defined as the time at which the median value (red bars) reaches values below 0.5 (horizontal dashed line). The green shaded area marks the transition time (80 %-20 %).

transition time to 10 ps (see fig. 4.10). This is also possible with the unipolar switching mode (positive voltage pulses). In this mode, the fastest SET time also amounts to 50 ps and the fastest transition time was derived to 5 ps. The voltage, at which a SET time of 50 ps is achieved, is higher than in the bipolar switching mode. The boxplots of which the transition times have been derived are broad (see green shaded area in fig. 5.9 and fig. 5.10), reaching from values of R_{POST}/R_{PRE} around unity to values close to zero and, therefore, no clear statement about the transition time can be made. This broadness of the boxplots probably results from a large cycle-to-cycle variability.

The occurrence of a SET operation during the application of a positive voltage to the active Pt electrode corresponds to a unipolar switching operation, which is usually observed for TCM- or PCM-based devices [56]. It was, however, already observed in TaO_x- [170] and ZrO_x-based [91] devices and also in other VCM devices (see section 5.1.3). The results of

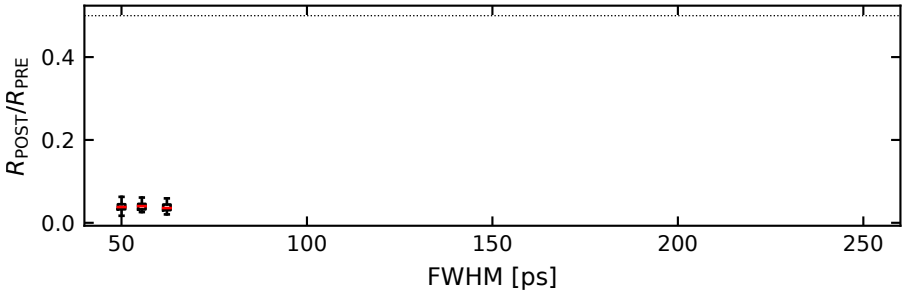

(a) Zr1 device, $V_P = 2.5\,V$.

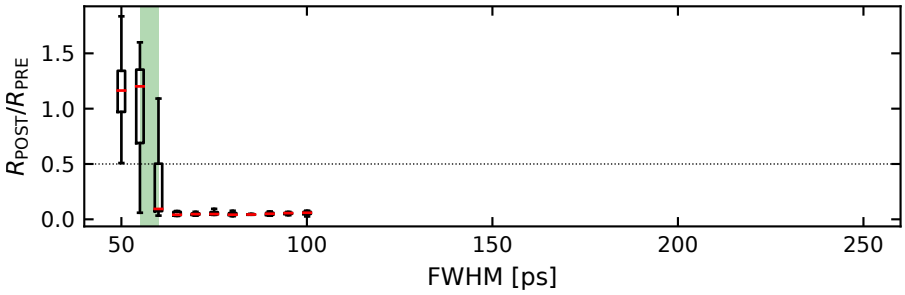

(b) Zr1 device, $V_P = 1.6\,V$.

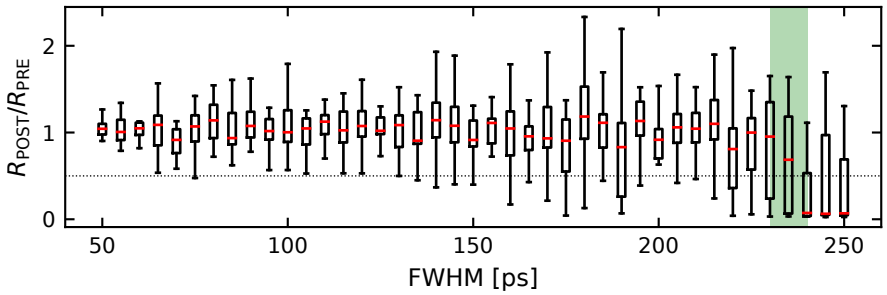

(c) Zr1 device, $V_P = 1.1\,V$.

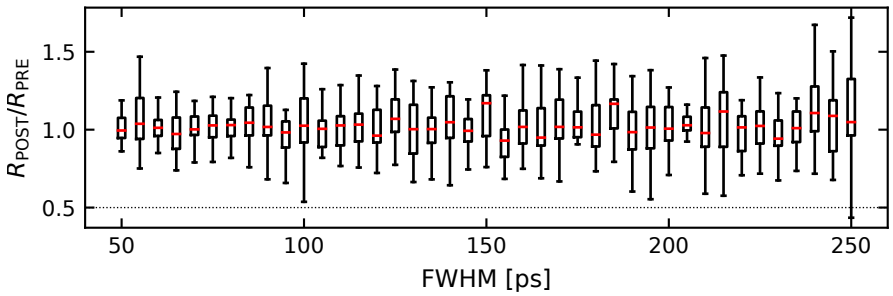

(d) Zr1 device, $V_P = 0.8\,V$.

Figure 5.10.: Unipolar SET kinetics of the Zr1 device (see table 3.1) with positive voltage pulses applied to the Pt bottom electrode. The unipolar SET time has been defined as the time at which the median value (red bars) reaches values below 0.5 (horizontal dashed line). The green shaded area marks the transition time (80 %-20 %).

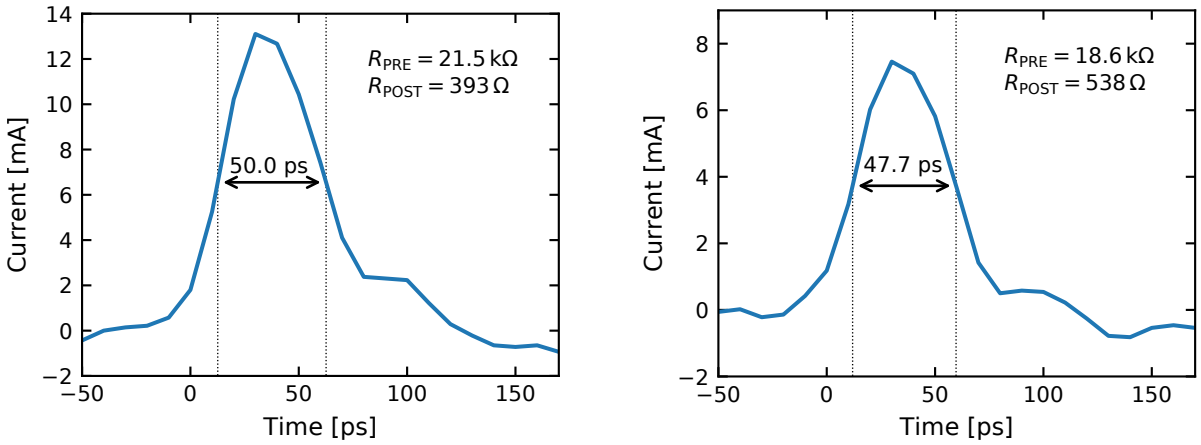

(a) Ta3 device, $V_P = 3.5\,V$, FWHM = 50 ps.

(b) Zr1 device, $V_P = 2.5\,V$, FWHM = 50 ps.

Figure 5.11.: (a) Ta3 device's current responses of a 50 ps pulse with an amplitude of $2V_P = 7.1\,V$. (b) Zr1 device's current responses of a 50 ps pulse with an amplitude of $2V_P = 5.0\,V$. The change in resistance is indicated on the upper right for both devices. Both devices switched from the HRS to the LRS, during the pulse's application.

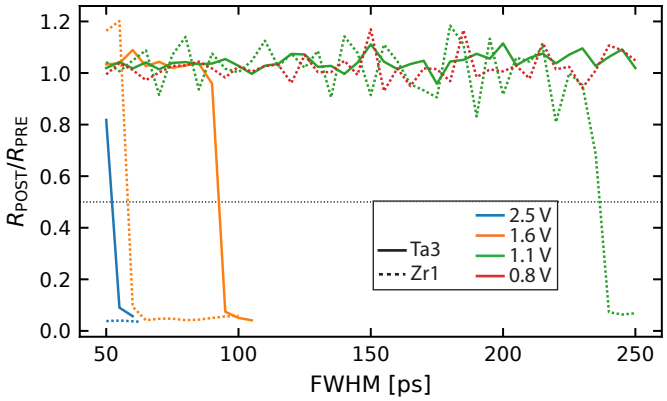

Figure 5.12.: Median values of the ratio R_{POST}/R_{PRE} for the Ta3 device (solid lines, data from fig. 5.9) and the Zr1 device (dashed lines, data from fig. 5.10). The colors of the line indicate the pulse amplitude.

this section have proven that the SET operation of the unipolar switching mode can also occur within 50 ps in TaO_x- and ZrO_x-based devices. To the author's knowledge, this has also not yet been shown by any other study. The presence of the unipolar switching mode, however, prevents faster RESET times as shown in section 5.1.4. The unipolar SET kinetics could only be determined in the time regime from 50 ps to 250 ps. To get more information on the unipolar SET kinetics at slower timescales, this switching mode was studied with quasi-static sweeps, as shown in the following section.

Quasi-static sweeps

The measurement procedure of the quasi-static sweeps is sketched in fig. 5.14. These measurements were conducted on larger devices, ranging from $2 \times 10\,\mu m^2$ to $30 \times 10\,\mu m^2$. All devices were again formed by applying a sweep with an amplitude of -4.0 V at a sweep rate of

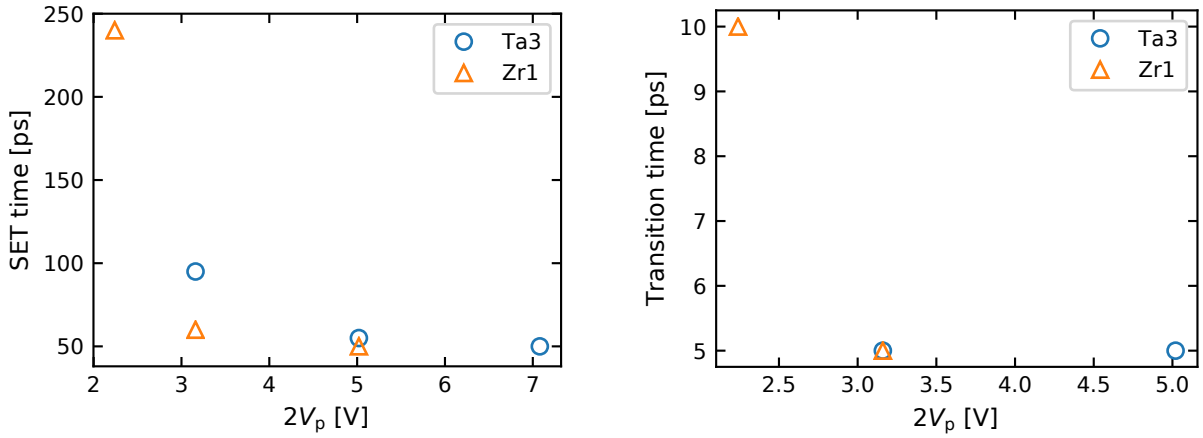

(a) SET times.

(b) Transition times (80 %-20 %).

Figure 5.13.: (a) Unipolar SET times of the Ta3 and Zr1 device, determined from fig. 5.12 (see horizontal line). (b) Transition times (80 %-20 %) of the Ta3 and Zr1 device, determined from fig. 5.9 and fig. 5.10 (see green shaded area). Twice the adjusted pulse amplitude $2V_P$ is plotted on the abscissa, as this is the effective voltage at the end of the electrical charging.

0.5 V/s to the Pt bottom electrode. Afterwards, a positive voltage sweep with an amplitude of 4.0 V was conducted at a sweep rate of 0.5 V/s, during which the devices firstly switched to the HRS and subsequently broke through at a higher voltage. After this breakthrough, all devices were stuck in the LRS.

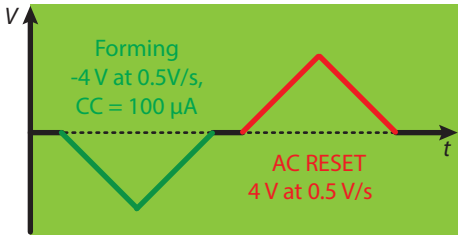

Figure 5.14.: Measurement cycle to determine the Ta3 and Zr1 device's unipolar SET times on slower timescales. The measurement was conducted with a Keithley 2634B SMU.

An exemplary measurement on a 2 × 10 µm^2 device on the Zr1 device's wafer is shown in fig. 5.15a. At the beginning, the device is in the LRS and the measured current depends linearly on the applied voltage. At a voltage of 0.60 V, the current starts to decrease, which corresponds to the RESET operation, which has already been observed in the bipolar switching mode. The current keeps decreasing until a voltage of 2.31 V is reached, at which it increases abruptly. The voltage at which this increase in current occurs is referred to as unipolar SET voltage.

All measured unipolar SET voltages are summarized in fig. 5.15b. The unipolar SET voltage scatters for both devices on a large voltage interval, indicating a significant device-to-device variability. The resulting mean values, standard deviations, and median values are listed in table 5.1. Both mean and median values are in the range from 2.12 V to 2.35 V,

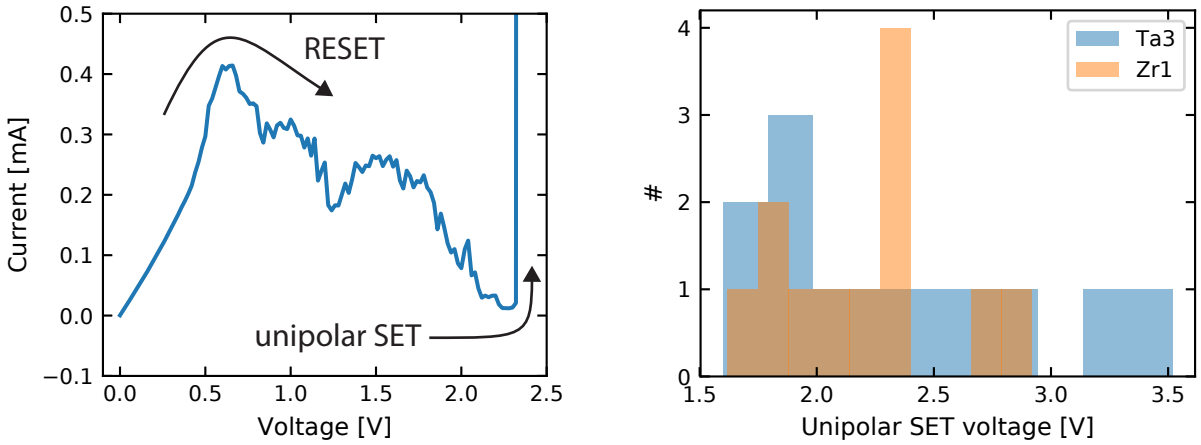

(a) Exemplary unipolar SET of the Zr1 device.

(b) Distribution of unipolar SET voltages.

Figure 5.15.: (a) Exemplary unipolar SET cycle of a $2 \times 10\,\mu m^2$ device on the Zr1 device's wafer. (b) Histogram of the measured unipolar SET voltage for 12 devices on each of the Ta3 (blue) and Zr1 device's (orange) wafer.

which is very close to unipolar SET voltages reported in other studies for TaO_x- [171–173] and ZrO_x-based devices [174, 175]. These literature values are given in the last column of table 5.1. The standard deviation of the unipolar SET voltage amounts to 0.58 V and 0.36 V for the Ta3 and Zr1 devices, respectively. In case of the Ta3 device, this corresponds to 24.7 % of the mean value, which reflects the large variability. Similar large variability values for the unipolar SET voltage were also already observed in TaO_x- [173] and ZrO_x-based devices [174–177]. This large variability is also the reason for the broadness of the box plots observed in the unipolar SET kinetics (see fig. 5.9 and fig. 5.10).

Table 5.1.: Measured values for the unipolar SET voltage and comparison to other literature values.

Wafer	Mean	Std. dev.	Median	Literature
Ta3	2.35 V	0.58 V	2.25 V	1.4 V - 2.7 V [173], 2.0 V [171, 172]
Zr1	2.12 V	0.36 V	2.29 V	2.2 V-2.7 V [174, 175], 1.1 V-1.6 V [176], 1 V-6 V [177]

5.1.3. Endurance of unipolar switching mode

The coexistence of the bipolar and unipolar switching mode has been demonstrated for many other transition VCM-based devices, such as NiO_x [178,179], TiO_x [180,181], HfO_x [182,183], SiO_x [184] and $SrTiO_x$ [185, 186]. In all of these studies a current compliance was used to protect the devices from damage. The advantage of achieving a unipolar switching mode with sub-250 ps pulses is that it does not require a current compliance, because the electrical excitation is stopped, before any damage at the device occurs. The used pules widths are

much shorter than the reaction time of most active current compliances. For example, the reaction time of the active current compliance of a Keithley 2634B SMU amounts to tens of microseconds [121, 187].

The characteristics of the unipolar switching mode resembles the TCM mechanism, which was also reported to occur at high voltages and high currents [69]. The so-called "eightwise" switching mode could also be responsible for the occurrence of a SET event, if a positive voltage is applied to the active Pt electrode, which was observed in TaO_x-based devices [85]. Here, an exchange of oxygen [82] at the active Pt electrode is suggested. The unipolar SET occurs, however, at much higher voltages and currents than the "eightwise" switching mode. It is, therefore, unclear if the exchange of charged traps at the active Pt electrode also contributes to the observed unipolar SET event. This switching mode has been observed in HfO_x- [84], $SrTiO_3$- [82], and TiO_x-based [188] devices, too.

So far, all measurements of the unipolar SET voltage were conducted with a measurement procedure, which involves the application of a negative voltage sweep to the active Pt electrode. To demonstrate that a true unipolar switching mode can be achieved, an endurance measurement was conducted with the Ta3 and Zr1 device, which involves only positive voltages applied to the active Pt electrode.

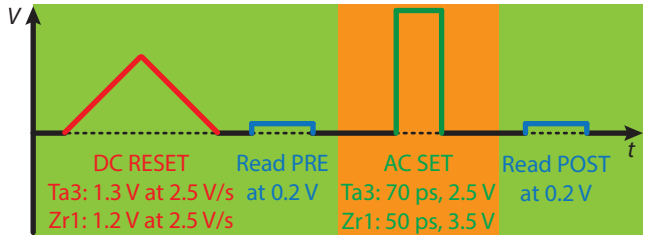

Figure 5.16.: Measurement cycle to determine the Ta3 and Zr1 device's endurance in the unipolar operation mode. Only positive voltages were applied.

The measurement procedure is sketched in fig. 5.16. The device is firstly, driven to the HRS with a positive voltage sweep with an amplitude of 1.3 V for the Ta3 device and 1.2 V for the Zr1 device. Both sweeps were conducted at a sweep rate of 2.5 V/s. Compared to the RESET sweeps of the previous measurements, the amplitude was reduced and the sweep rate accelerated to reduce the stress on the devices. After this sweep, the device's resistance R_{PRE} is read at a voltage of 0.2 V prior to the application of the pulse. Its width was chosen to 70 ps for the Ta3 device and to 50 ps for the Zr1 device. The pulse amplitude was chosen to 2.5 V for the Ta3 and to 3.5 V for the Zr1 device. Finally, the change in resistance R_{POST} is read at a voltage of 0.2 V.

The resulting values for R_{PRE} and R_{POST} are shown in fig. 5.17. As this measurement is very time consuming (several days), it was aborted for the Ta3 device at the 10^4-th cycle until which it switched consistently. After 3590 cycles, the Zr1 device got stuck in the HRS, which is marked as bolt orange dot. Nevertheless, the device could be brought back by forming it again with a second forming sweep (amplitude: -4 V, sweep rate: 0.5 V/s,

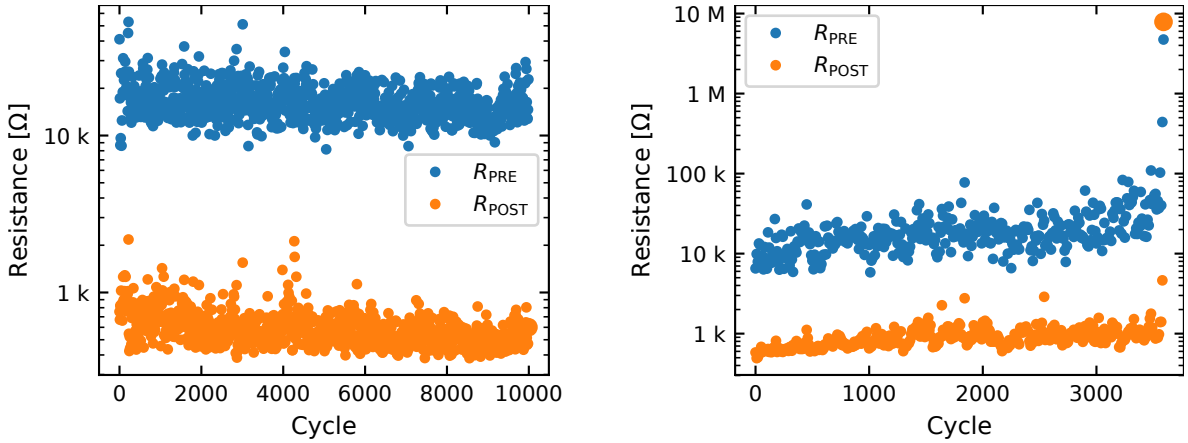

(a) Endurance of the Ta3 device.

(b) Endurance of the Zr1 device.

Figure 5.17.: Endurance measurements of the (a) Ta3 and (b) Zr1 device in a unipolar operation mode. Every 10-th value is plotted.

CC: 100 µA). It switched back to the LRS at a voltage of -1.78 V. This bipolar SET voltage is significantly higher than the usual SET voltage of -0.74 V (see fig. 4.12). The device was afterwards still operational in the bipolar and unipolar mode. The unipolar SET operation works reproducibly as both devices show an endurance of more than 10^3 cycles in this mode.

The fact that the Zr1 device was stuck in the HRS indicates that a depletion of oxygen vacancies occurred, which increased the device's conductivity. During bipolar endurance measurements on VCM devices, the concentration of oxygen vacancies in the transition metal oxide usually increases with the cycle number [90]. This is due to the fact that oxygen vacancies are more easily generated during the SET operation, than annihilated during the RESET operation [155, 158]. In the presented unipolar switching mode, on the other hand, the oxygen vacancies are always forced towards the Ta top electrode, which also contains oxygen. The oxygen vacancies in the oxide can, consequently, be annihilated at the interface to the Ta top electrode with the oxygen from the Ta top electrode. This brings the oxide back to an oxygen-rich state. This also explains the higher SET voltage, which had to be used to bring the device back to the LRS after the endurance measurement. The higher voltage was required to reincorporate oxygen into the Ta top electrode to form new oxygen vacancies in the oxide.

While endurance measurements of the unipolar operation mode with up to 10^4 cycles could be achieved, an endurance of up to 10^7 cycles could be achieved on the same device stack as the Zr1 device in the bipolar mode [90]. Also, literature values on the endurance of the unipolar switching mode are less promising than literature values on the endurance of the bipolar mode. The most promising known endurance measurement of the unipolar switching mode was reported for a NiO_x-based device, with an endurance of 10^6 cycles [189]. The highest reported endurance value of the unipolar switching mode for TaO_x-based devices amounts to 10^5 cycles [173] and the highest value for ZrO_x-based devices to 3.8×10^4 cycles [175]. These endurance values were achieved with voltage pulses with different amplitudes

and pulse widths. By using shorter pulses, the overall excitation of the device during the RESET becomes shorter than by applying slower sweeps. Consequently, less oxygen can be incorporated into the ohmic electrode by using shorter pulses. As the PG5 pulse generator is only operated with fixed attenuators and a maximum pulse width of 250 ps, this measurement cannot be conducted with the setup at hand.

Nevertheless, it could be shown that the unipolar SET operation is as fast as the bipolar SET operation, having a SET time down to 50 ps. So far, only unipolar SET times in the range of tens of nanoseconds [190–193] were reported. The fasted observed SET time amounted to 16 ns for a NiO_x-based device [194].

5.1.4. RESET programming window

In fig. 5.2 the RESET kinetics in the time regime from 100 ns to 480 ps of the Ta3 and Zr1 device are shown. These kinetic measurements provide voltage-time combinations at which the devices start to switch to the HRS. The unipolar SET kinetics of fig. 5.13a, on the other hand, provide voltage-time combinations at which the devices start to switch to the LRS. The results of both kinetic measurements are summarized in fig. 5.18, forming a RESET programming window. The RESET times (red points) are extracted from fig. 5.6 and the unipolar SET times (green points) from fig. 5.13a. The green and red shaded areas are drawn by the eye and define the programming windows for the RESET and the unipolar SET operation.

For the Ta3 device, the unipolar SET and RESET kinetics intersect at a voltage of 1.80 V. During the measurement of the RESET kinetics in the sub-100 ns regime, a unipolar SET event was also observed at an effective voltage of $2V_P = 1.80\,V$ (see fig. 5.4), which is in the measured span of the unipolar SET voltages measured on other devices on the Ta3 device's wafer (see fig. 5.15b). The voltage of 1.80 V corresponds to a potential RESET time of 510 ps, marking the intrinsic RESET speed limit of the Ta3 device. This observation is in contradiction to the results of Torrezan *et al.*, who reported a RESET time of 120 ps in a TaO_x-based device. This contradiction is addressed below.

The potential intrinsic RESET speed limit of the Zr1 device is derived in a similar manner. Here, the unipolar SET and RESET kinetics intersect at a voltage of 2.20 V. During the RESET kinetic measurements in the sub-100 ns regime, the Zr1 device still switched to the HRS at $2V_P = 1.80\,V$, indicating a higher unipolar SET voltage than for the Ta3 device. During the unipolar SET kinetics measurements, the Zr1 device still switched to the LRS at $2V_P = 2.24\,V$, which is also in the range of the unipolar SET voltages measured on other devices on the Zr1 device's wafer (see fig. 5.15b). The intersection at 2.20 V indicates a potential intrinsic speed limit of 400 ps, which is only little below the fastest measured RESET time of 480 ps (see fig. 5.3b).

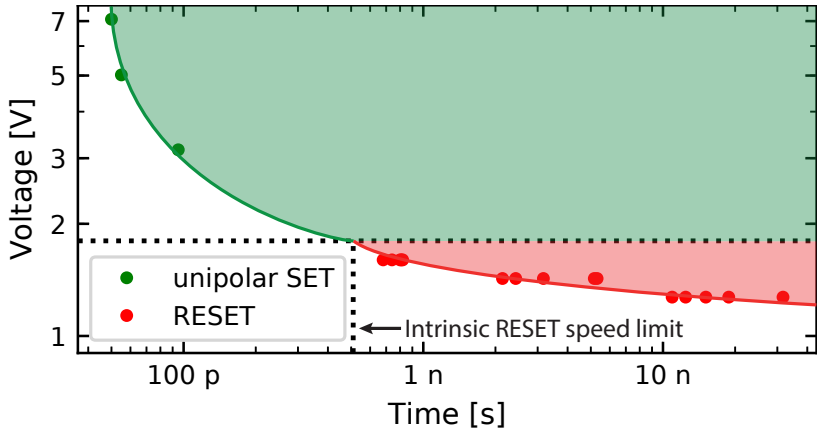

(a) Ta3 device's programming window.

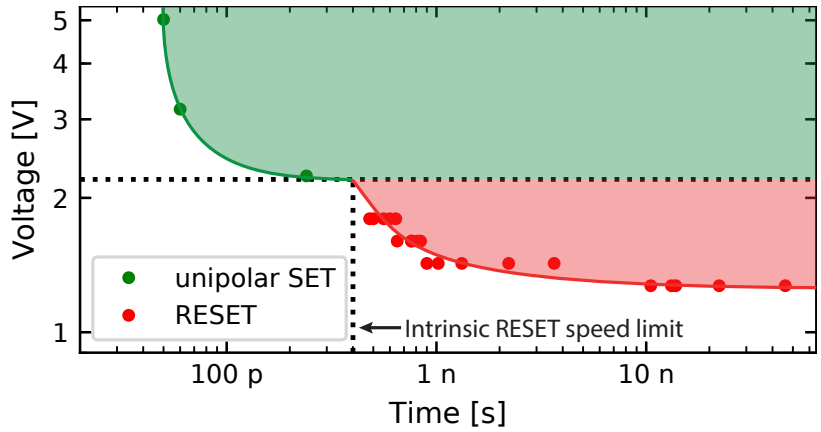

(b) Zr1 device's programming window.

Figure 5.18.: (a) Ta3 and (b) Zr1 device's programming mode. The indicated voltage is applied to the Pt bottom electrode. The RESET times (red points) are extracted from fig. 5.6 and the unipolar SET times from fig. 5.13a.

An important note is that due to the large device-to-device variability of the unipolar SET voltage, the measured RESET and unipolar SET programming windows from fig. 5.18 will vary significantly for other devices on the Ta3 and Zr1 device's wafer, which will also have a significant impact on the devices intrinsic RESET speed limit. The broadness of the boxplots during the kinetic measurements of the unipolar SET voltage (see *e.g.* fig. 5.10c) also indicate a large cycle-to-cycle variability. Furthermore, the unipolar SET kinetics will also be affected by the devices' electrical charging times, which has been demonstrated for the bipolar SET kinetics in the previous chapter (see fig. 4.20). As there are no kinetic data on the unipolar SET kinetics at slower timescales available, the contribution of the electrical charging time cannot be separated.

Unfortunately, it is not possible to measure the RESET kinetics in the range between 250 ps and 500 ps, because at this timescale, it becomes more challenging to derive the RESET time from the measured current response. Also, it is not possible to perform automated measurements in this time regime, because the PG5 pulse generator's maximum pulse width amounts to 250 ps.

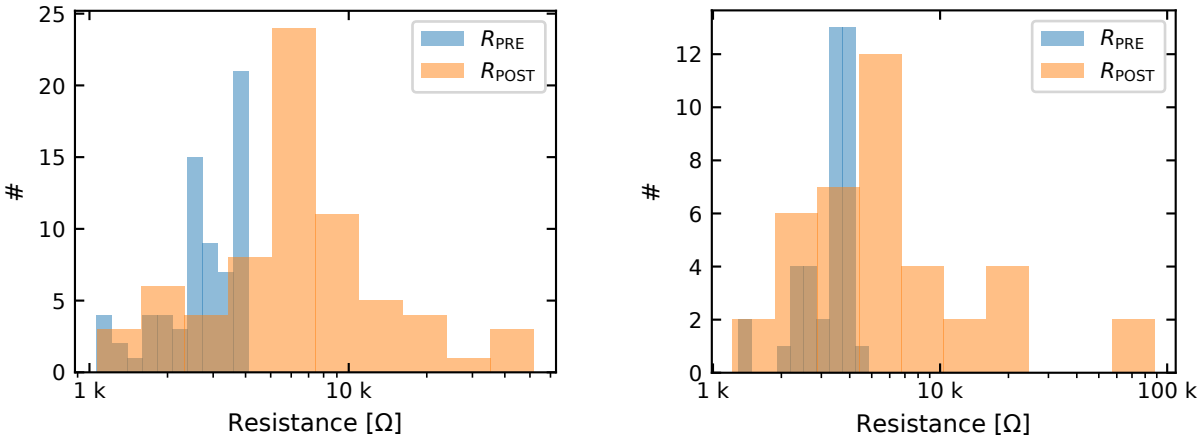

(a) Ta-C device, $V_P = 1.8\,V$, FWHM = 50 ps.

(b) Zr-C device, $V_P = 2.5\,V$, FWHM = 50 ps.

Figure 5.19.: Histograms of the resistance before R_{PRE} (blue) and after R_{POST} (orange) the application of a 50 ps pulse for (a) the Ta-C and (b) the Zr-C device.

Although, the "eightwise" switching mode has significantly different attributes than the unipolar SET event (regarding the observed voltages and currents), 50 ps RESET pulses were tested on the Ta-C and Zr-C device. These two devices have an additional C layer between the active Pt electrode and the oxide, which prohibits the exchange of oxygen vacancies and, thus, suppresses the "eightwise" switching mode [85]. The measurement procedure was identical to the tested regular RESET kinetics on the Ta3 and Zr1 device (see fig. 5.5), only that this time a fixed pulse width of 50 ps and a fixed amplitude of $2V_P = 3.6\,V$ for the Ta3 device and of $2V_P = 5.0\,V$ for the Zr1 device was used. The resulting values R_{PRE} and R_{POST} are shown in fig. 5.19. During several cycles, the value of R_{POST} shifted to the HRS. This shift to the HRS was, however, not reproducible and the transition occurred stochastically. Nevertheless, it shows that it is possible to reach the HRS within 50 ps in TaO_x- and ZrO_x-based devices. Two exemplary current responses are shown in fig. 5.20, during which the Ta-C and Zr-C device switched to the HRS.

Although, this RESET operation at 50 ps still occurs stochastically at a pulse width of 50 ps, it is a significant improvement compared to the measurements on the Ta3 and Zr1 device. At a voltage of $2V_P = 3.6\,V$, the Ta3 device always remained in the LRS (see fig. 5.6b) or switched from the HRS to the LRS (see fig. 5.9b). A similar observation was made for the Zr1 device at a voltage of $2V_P = 5.0\,V$ (see fig. 5.7a and fig. 5.10a). The presence of the oxygen-blocking 1.5 nm thick C layer at the active Pt electrode in the Ta-C and Zr-C device, therefore, fosters fast RESET operations in TaO_x- and ZrO_x-based devices. This also indicates that during the unipolar SET not only TCM, but also the exchange of oxygen vacancies or other mobile donors at the active Pt electrode may play a role. Further device optimizations may result in reproducible RESET operations in TaO_x- and ZrO_x-based devices within 50 ps.

As mentioned above, Torrezan *et al.* have observed a RESET time of 120 ps in a TaO_x-based device [32], which is in contradiction to the observed intrinsic RESET speed limitation

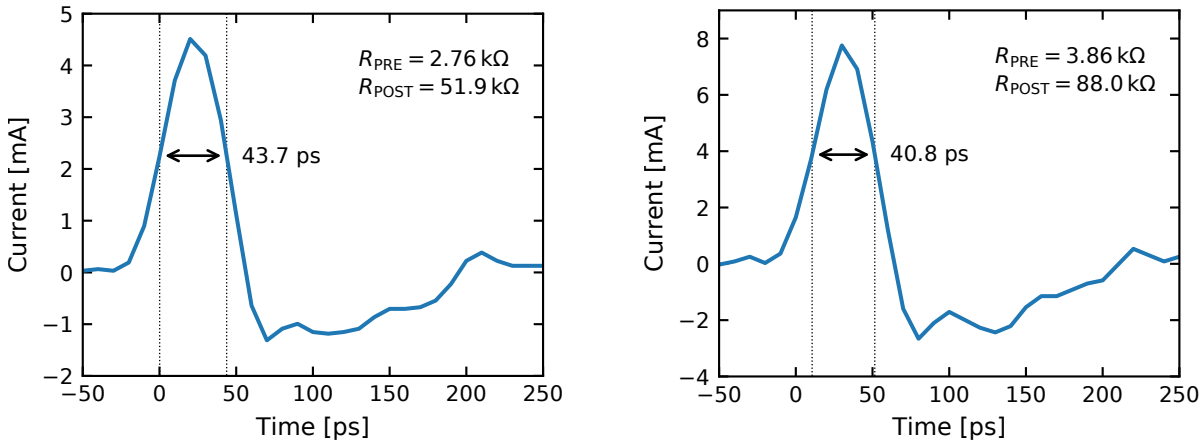

(a) Ta-C device, $V_P = 1.8\,V$ (9 dB), FWHM = 50 ps. (b) Zr-C device, $V_P = 2.5\,V$ (6 dB), FWHM = 50 ps.

Figure 5.20.: (a) Ta-C device's current response of a 50 ps pulse with an amplitude of $V_P = 1.8\,V$. (b) Zr-C device's current response of a 50 ps pulse with an amplitude of $V_P = 2.5\,V$. The change in resistance is indicated on the upper right for both devices.

at about 510 ps in the RESET programming window. The effective amplitude of their applied pulses amounted to approx. 4 V, which would be far above the unipolar SET voltage threshold observed in the Ta3 device (see table 5.1). Unknown differences in the fabrication process or during the electroforming process probably suppress the occurrence of the unipolar switching mode. A significant difference can be observed in the RESET voltage in the *IV* characteristics of the TaO_x-based devices. The Ta3 and Zr1 device started to switch at a voltage of about 0.6 V to the HRS (see fig. 3.4). For the TaO_x-based device of Torrezan *et al.*, on the other hand, the transition to the HRS started at a voltage below 0.4 V [195], which enlarges the RESET window significantly.

5.2. RESET kinetics of $HfO_X\backslash TiO_X$-bilayer devices

In the previous section, no reproducible RESET operation could be achieved in TaO_x and ZrO_x-based VCM devices at a timescale below 480 ps. In this section, results on the RESET kinetics of the HfO_x/TiO_x-bilayer are shown. Reproducible RESET kinetics at timescales down to 50 ps could be shown for the HfB2 and HfB3 device, which is attributed to their lower RESET voltages and higher unipolar SET voltages. In chapter 4.2.2, it could be shown that fast SET times down to 50 ps are also realizable with this material stack. In this section, firstly the RESET and unipolar SET voltages are compared, which have a significant influence on the RESET programming window.

5.2.1. RESET and unipolar SET voltage

The RESET programming window (see section 5.1.4) can be used as guide to optimize VCM devices towards faster RESET times. The intrinsic RESET speed is limited by the

intersection of the unipolar SET and the bipolar RESET kinetic curve, which corresponds to an intrinsic speed limitation. This intersection is, therefore, highly dependent on the RESET voltage and the unipolar SET voltage. By either reducing the RESET voltage or increasing the unipolar SET voltage, this RESET speed limitation can be shifted towards faster RESET times. It was already shown in fig. 3.5 that the RESET transition of the devices on the HfAx and HfBx wafer require a lower voltage to switch completely to the HRS (1.2 V) than the TaO_x- and ZrO_x-based devices (1.6 V, see fig. 3.4). This already enlarges the RESET window and should facilitate faster RESET operations.

The unipolar SET voltage was also tested for several devices on the HfAx and HfBx wafer. To realize multiple measurements on a single device, a different setup was used [187, 196, 197]. It compromises a Rigol DG5102 arbitrary waveform generator, a Picoscope 6403C oscilloscope and a self-built current amplification board. The main advantage of this setup is the integrated current compliance of the current amplification board, which reacts within 10 ns and is much faster than the current compliance of a Keithley 2634B SMU, which reacts only within tens of microseconds [121]. This faster current compliance allowed to cycle some devices in the unipolar switching mode.

The devices were formed with a -4.0 V sweep at a sweep rate of 814 $^{kV}/_{s}$, using a current compliance of 100 µA. Some devices did not form at this voltage and were, therefore, formed with the Keithley 2634B SMU with a -6.0 V sweep at sweep rate of 0.5 $^{V}/_{s}$. Instead of using the active current compliance, a 22 kΩ series resistor was used to prevent the device from damage. The unipolar SET voltage was then determined by applying a 3 V sweep at a sweep rate of 814 $^{kV}/_{s}$ and a current compliance of 1.0 mA. This high value of the current compliance was necessary, because with lower values the devices did not switch to the LRS, which was also reported in [70]. After the devices switched to the LRS, they were driven back to the HRS with a voltage sweep with an amplitude of 1.6 V.

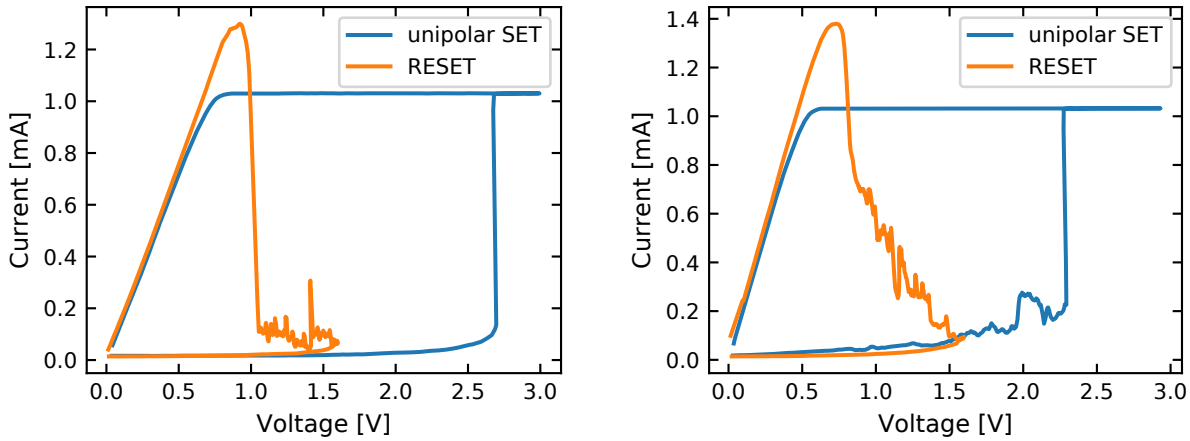

(a) 2 × 10 µm² device on the HfAx wafer.

(b) 15 × 10 µm² device on the HfBx wafer

Figure 5.21.: Exemplary unipolar sweeps conducted on a device on the (a) HfAx wafer and a device on the (b) HfBx wafer. The RESET (orange) sweep was conducted after the unipolar SET sweep (blue).

An exemplary unipolar SET sweep (blue) and the subsequent RESET sweep (orange) are shown for a device on the HfAx and HfBx wafer in fig. 5.21. Again, several devices could only be switched once to the LRS, but with some multiple unipolar cycles could be achieved. The maximum number of cycles conducted on a single device amounts to 16 on the HfAx wafer and to 15 on the HfBx wafer.

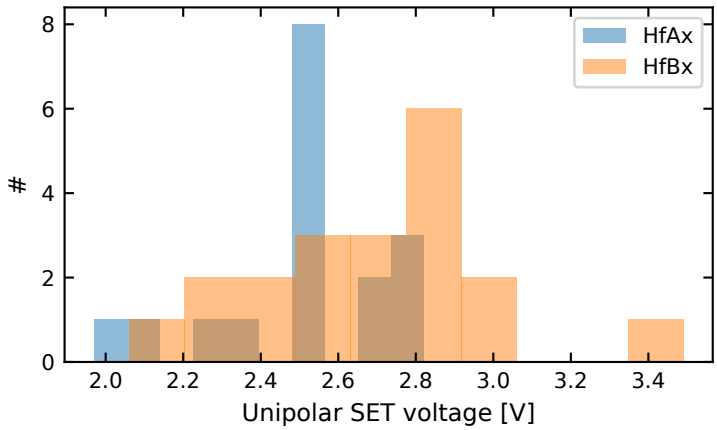

Figure 5.22.: Distribution of the unipolar SET voltage on devices on the HfAx (blue) and the HfBx (orange) wafer. Overall, 15 devices on the HfAx wafer and 19 devices on the HfBx wafer were tested. Their sizes varied from $1 \times 10\,\mu m^2$ to $30 \times 10\,\mu m^2$.

The distribution of the HfAx and HfBx device's unipolar SET voltage is shown in fig. 5.22 in blue and orange, respectively. If a device could be cycled several times, its median unipolar SET voltages was taken. Their resulting mean and median values for the unipolar SET voltage are shown in table 5.2. One more study with on the unipolar switching mode with a TiO_x/HfO_x-bilayer exists [198] and their measured unipolar SET voltages are shown in the last column of table 5.2.

Table 5.2.: Measured values of the unipolar SET voltage for devices on the HfAx and HfBx wafer and comparison to other literature values.

Wafer	Mean	Std. dev.	Median	Literature
HfAx	2.52 V	0.26 V	2.56 V	2.4 V - 2.6 V [198]
HfBx	2.66 V	0.35 V	2.73 V	2.4 V - 2.6 V [198]

Both, the devices on the HfAx wafer and the devices on the HfBx wafer, achieve higher values for the unipolar SET voltage than the Ta3 or Zr1 device (see table 5.1). Nevertheless, both values are within or close to the range measured by Wang *et al.* [198]. The standard deviation is little smaller than the one for the Ta3 or Zr1 device, but still the values of the unipolar SET voltage spread over a range of more than 0.5 V, which indicates that still a significant device-to-device variability exists.

The benefit of this setup is its fast current compliance, which allowed the conduction of several cycles on a single device. Unfortunately, most devices got either stuck in the LRS or HRS after only a few cycles. As mentioned above, a maximum of 16 cycles could be achieved

on a device on the HfAx wafer and a maximum of 15 cycles on a device on the HfBx wafer. The resulting distributions of the unipolar SET voltage are shown in fig. 5.23. Although the standard deviation only amounts to 0.10 V and 0.05 V for the device on the HfAx wafer and the device on the HfBx wafer, respectively, but the values still spread over a range of 0.35 V and 0.50 V. Therefore, it can be stated that even though the cycle-to-cycle variability is smaller than the device-to-device variability, it still has a significant impact on the kinetic measurements.

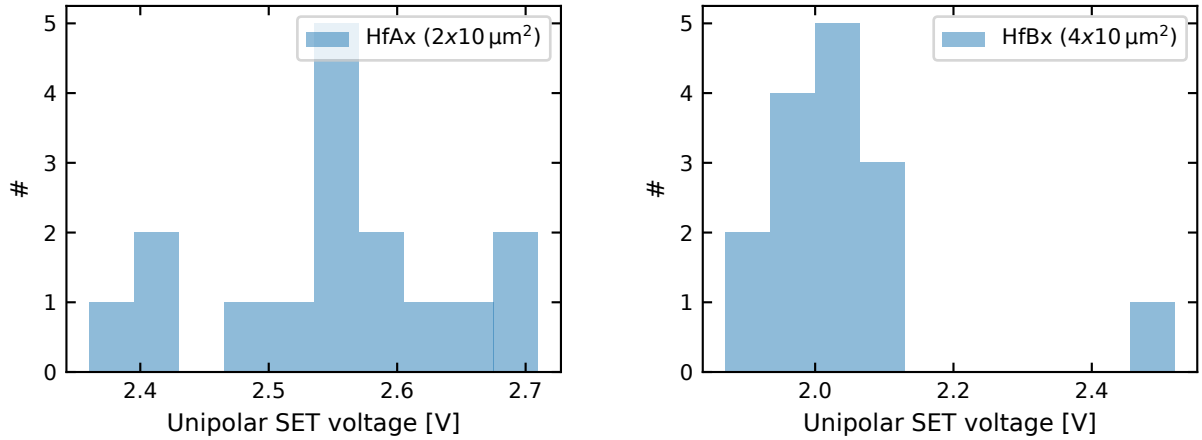

(a) 2 × 10 µm² device on the HfAx wafer.

(b) 15 × 10 µm² device on the HfBx wafer.

Figure 5.23.: Cycle-to-cycle variability of a single device on the (a) HfAx wafer and on the (b) HfBx wafer. The standard deviation amounts to only 0.1 V and 0.05 V, respectively.

5.2.2. Time regime from 50 ps to 250 ps

The devices on the HfAx and HfBx wafers not only have a smaller RESET voltage, but also a higher unipolar SET voltage than the devices on the Ta3 and on the Zr1 wafer. This enlarges their RESET programming window significantly and, as show in the following sections, allows reproducible fast RESET operations in the range from 50 ps to 250 ps. Nevertheless, the significant device-to-device variability prohibited the RESET operation on some devices on the HfAx and HfBx wafer. The HfAx wafer's unipolar SET voltage was lower than the one of the HfBx wafer, which made it more difficult to achieve 50 ps fast RESET times with devices on the HfAx wafer. Much better results could be achieved with devices on the HfBx wafer, which is shown subsequently.

The measurement procedure for the tested devices (HfA1, HfA3, HfB2 and HfB3) is sketched in fig. 5.24. It is very similar to the one used to investigate Ta3 and Zr1 device's RESET kinetics (see fig. 5.5). Only the RESET voltage during the second DC sweep has been reduced to 1.2 V and higher pulse amplitudes (up to $V_P = 2.5$ V) were used to reset the devices. Each cycle was again repeated at least 10 times. Again, the resistance in the LRS was chosen in the range from 1.0 kΩ to 3.0 kΩ.

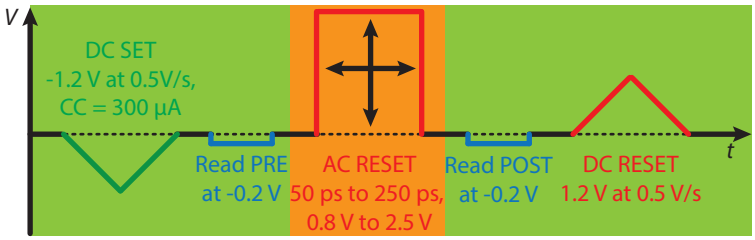

Figure 5.24.: Measurement cycle to determine the HfA1, HfA3, HfB2 and HfB3 device's RESET kinetics in the time regime from 50 ps to 250 ps.

Devices on HfAx wafer

The measurement of the HfA1 device (see fig. 5.25) yielded broad scattered results for the ratio R_{POST}/R_{PRE} at all pulse widths and pulse amplitudes. The absolute values for R_{POST} are shown in the appendix section C (see fig. C.5). At the lowest voltage of $2V_P = 2.2\,V$, which is still lower than the measured average unipolar SET voltage, almost no effect of the applied pulse could be seen (see fig. 5.25d). At higher amplitudes of $2V_P = 3.2\,V$ and $2V_P = 5.0\,V$ (see fig. 5.25c and fig. 5.25b, respectively), the HfA1 device switched sometimes to the HRS or remained in the LRS. Unfortunately, the HfA1 device did not switch repeatedly to the HRS at any pulse width and also values of R_{POST}/R_{PRE} below 1 were observed, which indicates that the presence of the unipolar SET mode also affects these measurements.

This became most obvious at $2V_P = 7.1\,V$ (see fig. 5.25c). From pulse widths of 55 ps to 70 ps, the HfA1 device switched repeatedly to the HRS. At longer pulse widths also smaller values for R_{POST}/R_{PRE} occurred and at pulse widths of 90 ps or longer, R_{POST}/R_{PRE} was at most of the cycles below 1, which indicates that the unipolar switching mode becomes more dominant at these pulse widths. This observation may be affected by the HfA1 device's electrical charging time, which amounts to 96.9 ps (see table 3.4). Possibly, the maximum of V_{DUT} at pulse widths below 90 ps is too low to initiate the unipolar SET operation.

The high device-to-device variability of the unipolar SET voltage also results in a high device-to-device variability of the measured RESET kinetics. This is demonstrated for the HfA3 device. The results for R_{POST}/R_{PRE} are shown in fig. 5.26 and the absolute values for R_{POST} are again shown in the appendix section C (see fig. C.6). At all pulse amplitudes, no switching to the HRS could be observed and the device was drifting to values of R_{POST}/R_{PRE} below 1, which shows that for the HfA3 device the unipolar SET operation is even more dominant than in the HfA1 device. Both tendencies could also be observed on other devices on the HfAx wafer.

Devices on HfBx wafer

The devices on the HfBx wafer had the highest unipolar SET voltages of all samples tested in the framework of this thesis. Consequently, their devices should have the largest RESET

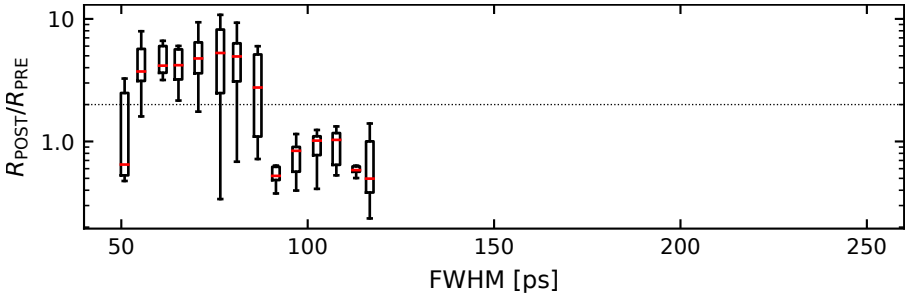

(a) HfA1 device, $V_P = 3.5\,V$.

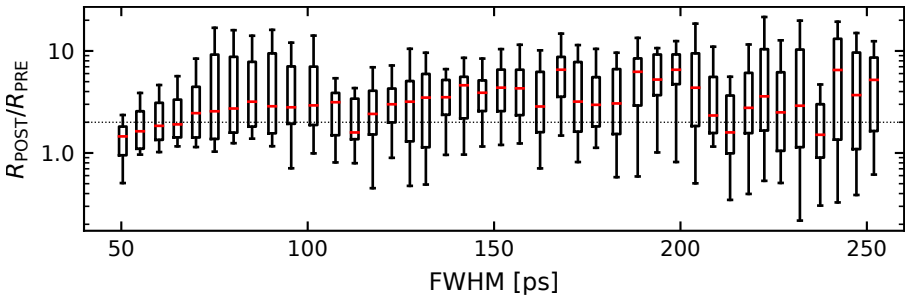

(b) HfA1 device, $V_P = 2.5\,V$.

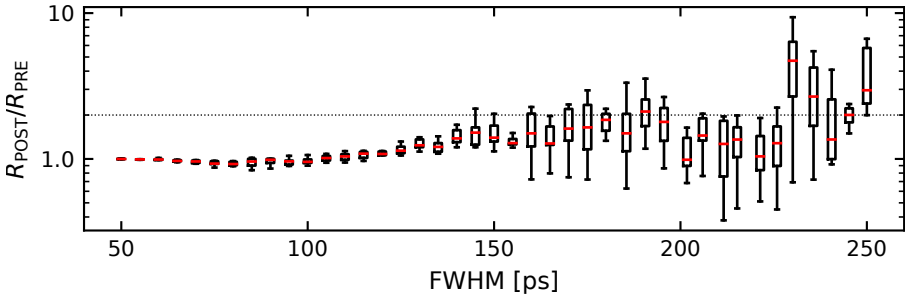

(c) HfA1 device, $V_P = 1.6\,V$.

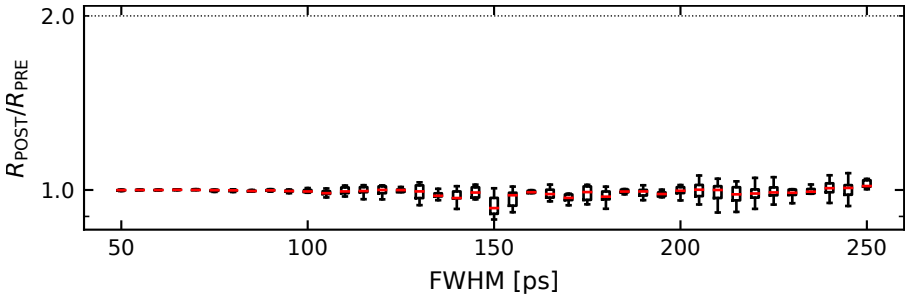

(d) HfA1 device, $V_P = 1.1\,V$.

Figure 5.25.: RESET kinetics of the HfA1 device (see table 3.1). The red bar in the boxplot marks the median.

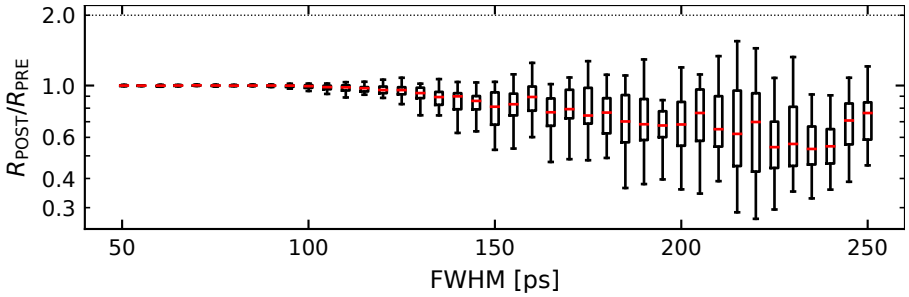

(a) HfA3 device, $V_P = 1.8\,V$.

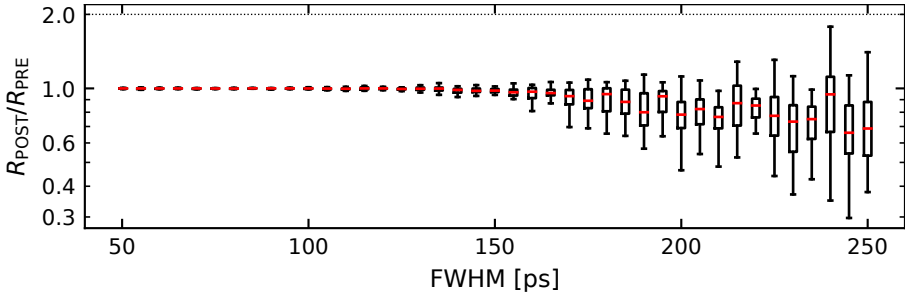

(b) HfA3 device, $V_P = 1.6\,V$.

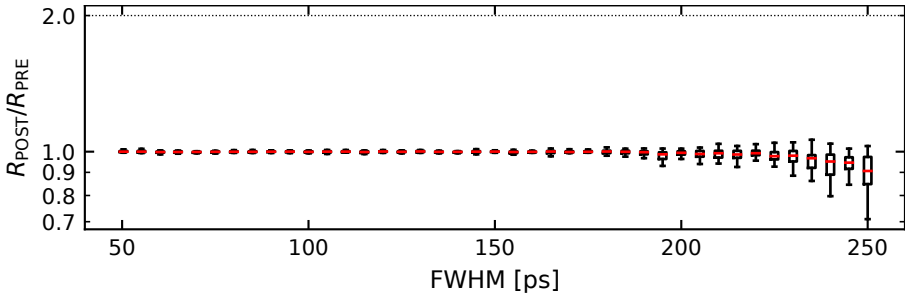

(c) HfA3 device, $V_P = 1.1\,V$.

Figure 5.26.: RESET kinetics of the HfA3 device (see table 3.1). The red bar in the boxplot marks the median.

window in the RESET programming window and, therefore, successful RESET operations should be achievable.

The RESET kinetics of the HfB3 device could be measured successfully, which is shown in fig. 5.27. To reduce the stress on the device, the pulse width was increased in steps of 20 ps (instead of 5 ps), if the ratio R_{POST}/R_{PRE} was at unity. If changes in R_{POST}/R_{PRE} occurred, the pulse width was varied in steps of 5 ps and the measurements were repeated until a smooth curve for the median values of R_{POST}/R_{PRE} was achieved. The absolute values for R_{POST} are plotted in fig. C.7 of the appendix section C. As expected, R_{POST}/R_{PRE} increases with the measured FWHM at all amplitudes. This increase of resistance occurred faster at higher pulse amplitudes and also changes of R_{POST}/R_{PRE} by more than one order of magnitude could be achieved.

The median values of R_{POST}/R_{PRE} at all amplitudes and pulse widths are shown in fig. 5.28a. The faster RESET operations at higher voltages become more obvious in this representation. The RESET time was defined as the time, at which R_{POST}/R_{PRE} reaches values above two,

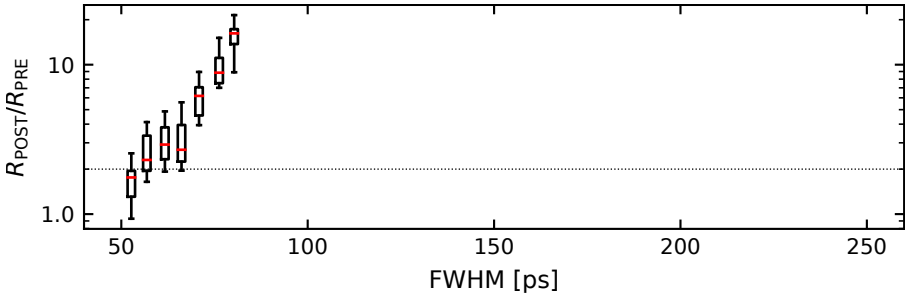

(a) HfB3 device, $V_P = 5.0\,V$.

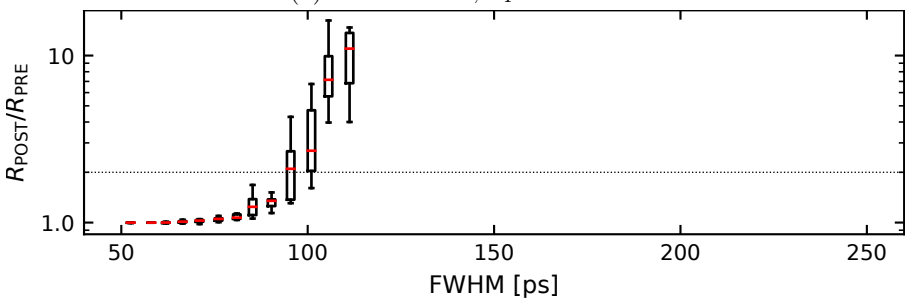

(b) HfB3 device, $V_P = 3.5\,V$.

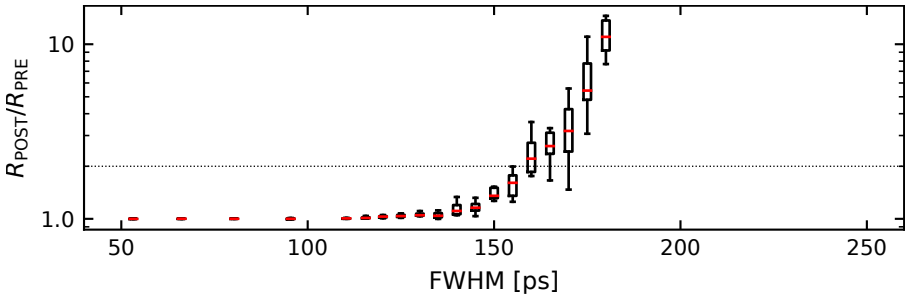

(c) HfB3 device, $V_P = 2.5\,V$.

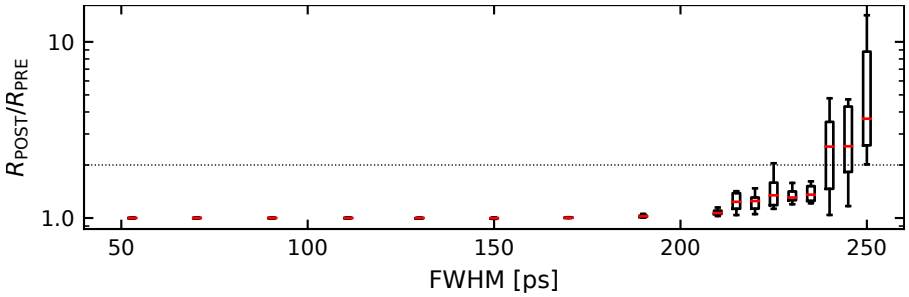

(d) HfB3 device, $V_P = 1.8\,V$.

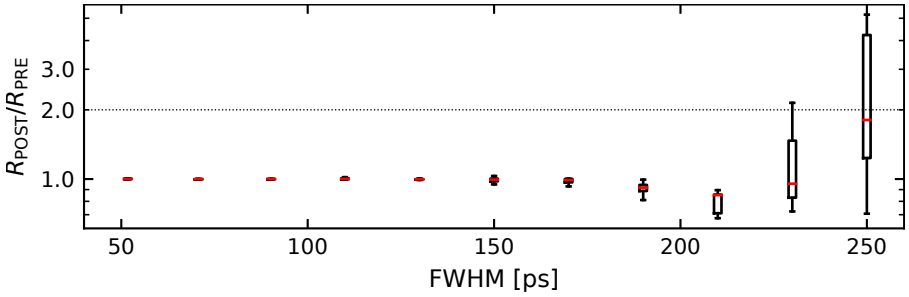

(e) HfB3 device, $V_P = 1.6\,V$.

Figure 5.27.: RESET kinetics of the HfB3 device (see table 3.1). The red bar in the boxplot marks the median. The horizontal dotted line marks the definition of the RESET time.

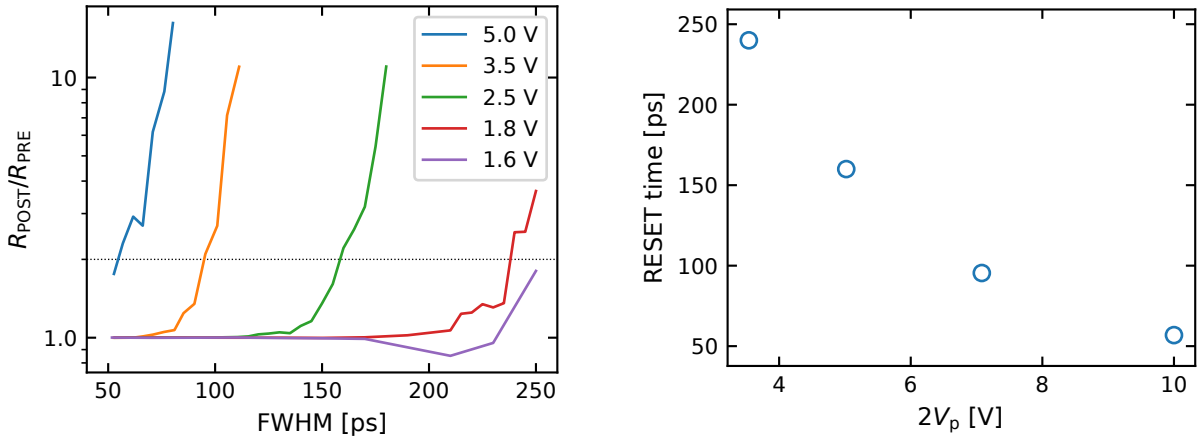

(a) HfB3 device's transients for R_{POST}/R_{PRE}.

(b) RESET times of the HfB3 device.

Figure 5.28.: (a) Median values of the ratio R_{POST}/R_{PRE} for the HfB3 device (data from fig. 5.27). The colors of the line indicate the pulse amplitude. The horizontal dotted line marks the definition of the RESET time. (b) Resulting RESET times of the HfB3 device. Twice the adjusted absolute pulse amplitude $2V_P$ is plotted on the abscissa, as this is the effective voltage at the end of the electrical charging.

which is the reciprocal of the threshold used for the SET kinetics. The horizontal dotted lines in fig. 5.27 and fig. 5.28a mark $R_{POST}/R_{PRE} = 2$ and, therefore, the threshold for the measured RESET time.

The resulting RESET times are plotted in fig. 5.28b against twice the applied pulse voltage, which corresponds to the effectively applied voltage at the end of the electrical charging. Compared to the results on the SET kinetics in chapter 4, much higher voltages are required to achieve fast RESET times. The fasted measured RESET time amounts to 55 ps. This might also be related to the comparable large size ($10 \times 10\,\mu m^2$) of the HfB3 device and the resulting long electrical charging time (662 ps, see table 3.4). Reproducibly 50 ps fast RESET times could be demonstrated on the much smaller HfB2 device ($5 \times 3\,\mu m^2$), which has, consequently, also a much faster electrical charging time of only 95.0 ps.

To demonstrate reproducible fast RESET times, the measurement procedure was changed and is sketched in fig. 5.29. Similar to the previous measurements, the device was driven to the LRS at the beginning of each cycle and the resistance was read before and after the pulse's application. In contrast to the previous measurements, neither the pulse width nor the amplitude were varied. Instead, they were fixed at 50 ps and 5.0 V, respectively. The high amplitude was chosen to ensure that the HfB2 device switches to the HRS at every cycle. Consequently, no positive sweep was needed at the end of the cycle. Overall, 1000 cycles were conducted.

An exemplary current response is shown in fig. 5.30a, during which the HfB2 device switched from 4.37 kΩ to 1.81 MΩ. The pulse width was chosen to 50 ps and the FWHM of the current response was even shorter (48.8 ps), which proves that the RESET can be realized within 50 ps or faster.

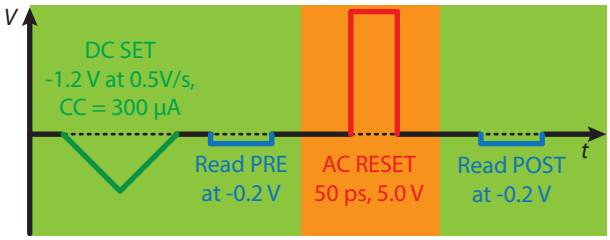

Figure 5.29.: Measurement cycle to demonstrate the HfB2 device's RESET repeatability with 50 ps pulses at an amplitude of $V_P = 5.0\,V$.

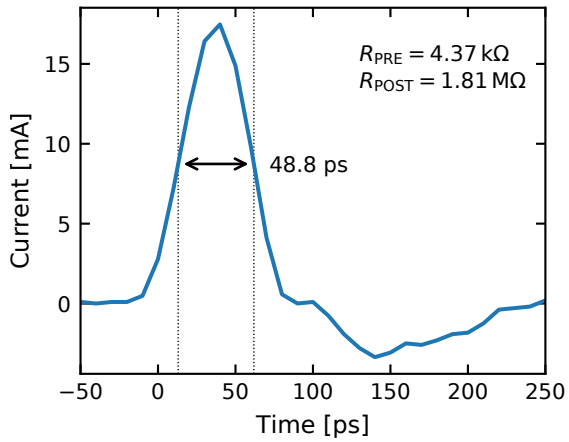

(a) HfB2 device, $V_P = 5.0\,V$, FWHM = 50 ps.

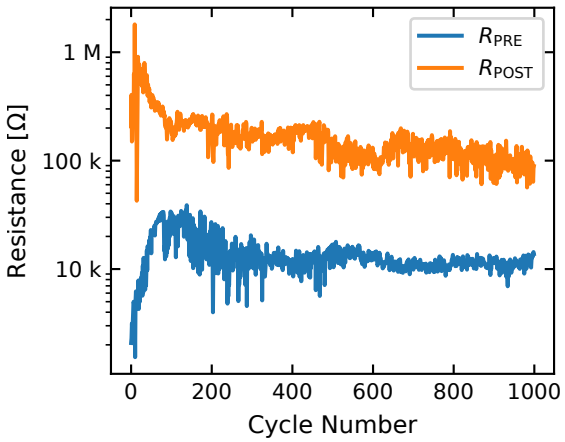

(b) RESET repeatability of the HfB2 device.

Figure 5.30.: (a) HfB2 device's current responses of a 50 ps pulse with an amplitude of $2V_P = 10.0\,V$. The change in resistance is indicated on the upper right. The device switched to the HRS during the pulse's application. (b) RESET repeatability of the HfB2 device. The RESET operation was also conducted by applying a 50 ps pulse with an amplitude of $2V_P = 10.0\,V$. The measurement was aborted after 1000 cycles.

The resulting values for R_{PRE} and R_{POST} are shown in fig. 5.30b. At the beginning, the values of both, the R_{PRE} and the R_{POST} drifted. The drift might have been triggered by the relatively high voltage amplitude of $2V_P = 10\,V$. It was already shown in fig. 3.5d that for the HfBx devices, the LRS's resistance shifts from linear to nonlinear with the number of cycles. This is also the origin of the shift of R_{PRE} at the beginning of the endurance measurement (see fig. 5.30b). Overall, the values of R_{PRE} and R_{POST} were always separated by one order of magnitude, which confirms the repeatability of the 50 ps fast RESET operation.

Fast RESET times of 50 ps and 55 ps on two devices of the HfBx wafer could be demonstrated. Similar results could also be shown on more devices on the HfBx wafer, but this was not the case for all devices on the HfBx wafer. On some devices also values below unity for R_{POST}/R_{PRE} were observed, indicating that the presence of the unipolar SET mode again prohibits faster RESET times. The high device-to-device variability in the RESET measurements probably also results from the high device-to-device variability of the unipolar SET voltage (see fig. 5.22).

5.3. Optimizations for faster RESET times

During the measurements of the RESET kinetics, it could be shown that the RESET time of VCM devices is often intrinsically limited by the presence of a unipolar switching mode, which is initiated at higher voltages. This results in a RESET programming window, which was measured for the Ta3 and Zr1 device (see fig. 5.18). It has, however, to be stated that due to the large device-to-device variability of the unipolar SET voltage, this RESET programming window also differs from device to device and possibly from cycle to cycle. Therefore, it was not measured for the HfO_x/TiO_x-based devices. Nevertheless, two possibilities to remove or reduce this intrinsic RESET speed limitation could be identified: reducing the RESET voltage or increasing the unipolar SET voltage. Suggestions on how to achieve these two attributes are given in the following sections.

5.3.1. Lowering the RESET voltage

It was shown that the RESET voltage can be lowered by heating a TaO_x-based VCM device [199]. By selecting materials with thermal properties that foster a better heating within the filamentary region (*e.g.* lower heat capacity, lower heat conductivity, and lower mass density), lower RESET voltages may be realizable. The unipolar switching mode, however, may also be temperature dependent [69] and this approach might therefore result in a lower unipolar SET voltage as well, which would still prohibit faster RESET times.

Another way to reduce the RESET voltage is to choose an ohmic electrode that induces a low defect formation energy for oxygen vacancies in the oxide [158]. It could be shown for ZrO_x-based devices that by replacing Ta with Ti as ohmic electrode, the RESET voltage can be reduced by about 0.1 V [90]. The ohmic electrode, on the other hand, could also have an influence on the unipolar SET voltage (as shown in the next section). For example, changing the Ta top electrode of a Pt\TaO_x\Ta device with a Pt top electrode (symmetrical stack) resulted in higher RESET and higher unipolar SET voltages [170].

Also, the surface roughness of the oxide layer has an influence on the SET and RESET voltage. A higher surface roughness resulted in lower SET and RESET voltages for a ZnO_x-based device with symmetric Pt electrodes [200].

5.3.2. Increasing the unipolar SET voltage

It is crucial to achieve a deeper understanding of the unipolar switching mode. The presence of thermodiffusion was postulated [69, 201]. The results achieved in this chapter, however, indicate that also the exchange of oxygen vacancies or other charged defects could have an influence on the unipolar switching mode. The introduction of an oxygen blocking C layer in TaO_x and ZrO_x-based devices resulted in 50 ps fast RESET operations. Also, the shift of the unipolar SET voltage from 2.56 V (HfAx wafer) to 2.73 V (HfBx wafer, see median

values in table 5.2) probably results from a different deposition method of the Pt bottom electrode. As mentioned above, several studies suggest an exchange of charges at the active Pt electrode during a so-called "eightwise" switching mode [82, 83, 85]. Therefore, different active electrodes or other oxygen blocking layers could be tested. In [202], the use of a pure active C electrode and 5 nm SiO_x as active layer prohibited the occurrence of the unipolar SET up to 10 V.

An interesting study was conducted by Yanagida *et al.* [70]. They have shown for NiO_x-, CoO_x-, and TiO_x-based devices with symmetric Pt electrodes that the switching mode depends on the adjusted current compliance during the electroforming. The unipolar switching mode requires higher current compliances than the bipolar switching mode. They also showed that the required current compliance for the bipolar switching mode scales with the device size, while the current compliance required for the unipolar switching mode was almost constant. Consequently, the current compliance required for the bipolar switching mode was below the current compliance required for the unipolar switching mode for small devices (submicrometer scale). For larger devices, the current compliance required for the bipolar switching mode was larger than the current compliance required for the unipolar switching mode and, consequently, bipolar switching was not possible. Other studies have also shown that it is difficult to realize a bipolar switching mode with a symmetric device stack, having two Pt electrodes [170, 203, 204].

Yanagida *et al.* showed as well that the electric field required for unipolar switching decreases exponentially with increasing device sizes [70]. It could, consequently, be possible to achieve higher unipolar SET voltages with smaller devices. The unipolar SET voltages for the devices investigated in this thesis had no dependency on the device size, but this effect might only be relevant for submicrometer scaled devices. The last observation of Yanagida *et al.* was that the electrical field required for the unipolar switching of NiO_x-based devices was higher if the NiO_x was crystalline. If this observation is transferable to other VCM devices, higher unipolar SET voltages could be achieved in crystalline devices.

Gao *et al.* have shown that in a symmetric $Pt/Ta_2O_5/Pt$ stack, the unipolar SET voltage amounts to 2.1 V and is much higher than the unipolar SET voltage of an asymmetric $Pt/Ta_2O_5/Ta$ stack, which amounts to 1.6 V [170]. Using an inert top electrode could, therefore, increase the unipolar SET voltage. This is in accordance with another study, investigating the impact of the ohmic electrode on the endurance and switching kinetics of Ta_2O_5-based devices [155]. Here, higher unipolar SET voltages were observed for ohmic electrodes with lower oxygen affinity. Using an inert top electrode has, however, also several disadvantages, such as a higher forming voltage [90], lower endurance [170], and a larger cycle-to-cycle variability [170]. A similar observation was made by Lin *et al.* for ZrO_x-based devices, who replaced the Pt top electrode with an Au top electrode and thereby, decreased the unipolar SET voltage from 2.8 V to 2.6 V [204]. The origin of the large cycle-to-cycle

variability in symmetrical stacks is attributed to new conductive filaments, which are formed during every cycle [91, 170].

The unipolar SET event could also be triggered by an electric breakdown and, consequently, depend on the dielectric breakdown strength of the active switching layer. Materials with higher electrical strength might, thus, have a higher unipolar SET voltage. An overview of the electric breakdown strength of different metal oxides is given in [205], according to which AlO_x is supposed to have a comparable strong electric breakdown field. This is supported by a study on AlO_x-based devices, in which a unipolar SET voltage of 3.0 V was observed [206], which is higher than the unipolar SET voltages observed for the devices investigated in this thesis. In devices with strong electric breakdown fields, it could, consequently, be possible to achieve reproducible 50 ps fast RESET times.

5.4. Analogy to switching times in PCM devices

In chapter 4, it could be shown that it is possible to switch VCM devices within 50 ps to the LRS. This was so far only limited by extrinsic effects, such as the minimum available pulse width or the device's electrical charging time. The intrinsic properties of VCM devices probably allow much faster SET times. Achieving RESET times down to 50 ps was more difficult and could only be achieved repeatedly on a few devices.

In contrast to VCM devices, reaching fast RESET operations in PCM devices is more easily achieved than a fast SET operation. Several studies investigating the switching kinetics of PCM devices reported slower SET than RESET times [207–209]. The fastest measured RESET time amounts to 200 ps [60]. The fastest observed SET time, however, amounts to 500 ps, which could only be realized by pre-heating the device [62]. Another study observed 550 ps fast SET times without pre-heating the device [61]. With optical THz measurements, electrical fields could be induced into PCM devices with a duration of 1 ps [63]. By inducing 900 of these pulses, the device was driven from the HRS to the LRS.

The SET time of PCM devices is limited by the crystallization speed, which is strongly temperature dependent [56, 210, 211]. Faster SET times can, consequently, only be achieved at higher temperatures. The heating in PCM devices also results from Joule heating. To achieve higher temperatures, it is necessary to induce a larger current by applying a higher voltage. Similar to the RESET kinetics of VCM devices, the SET kinetics of PCM devices can, consequently, be accelerated up to a certain point by increasing the applied voltage. This only works in VCM devices up to the point at which the unipolar SET mode sets in and for PCM devices up to the point at which the melting sets in. The melted part can only be recrystallized by slowly decreasing the temperature, which also prohibits fast SET times.

The programming window of a PCM and a VCM device are compared in fig. 5.31. The SET programming window of the PCM device was measured on a GeTe-based device, starting in the HRS and was taken from [208]. As explained above, at a voltage threshold of about 1.6 V,

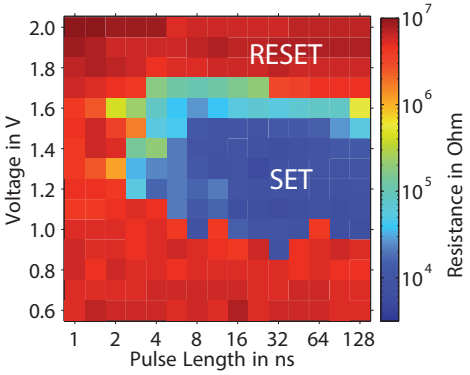

(a) SET programming window of a GeTe-based PCM device. Reprinted from [208], with the permission of AIP Publishing.

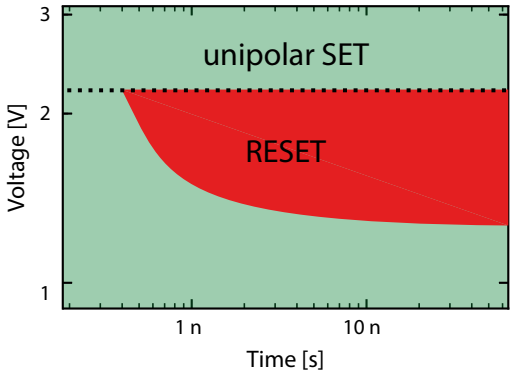

(b) RESET programming window of a ZrO_x-based VCM device.

Figure 5.31.: Comparison of the (a) SET programming window of a GeTe-based PCM device and (b) RESET programming window of a ZrO_x-based VCM device (from fig. 5.18b). The PCM device was initially in the HRS, while the VCM device was initially in the LRS.

the conducting region in the GeTe-layer starts to melt, which prohibits a faster crystallization and, consequently, also faster SET times. The RESET programming window of the VCM device is an adaption of fig. 5.18b. It was measured on the Zr1 device starting in the LRS. At voltages above 2.2 V, the unipolar switching mode sets in, prohibiting faster RESET times.

It could be shown in this section that by increasing the unipolar SET voltage, this RESET speed limit of VCM devices can be shifted towards faster RESET times down to 50 ps. The fastest electronically measured SET time of PCM devices without pre-heating amounts to 550 ps [61]. Nevertheless, the unipolar SET process is not yet fully understood and further studies are required to identify attributes, with which the unipolar SET voltage can be increased towards higher amplitudes.

6. Outlook

Before presenting the conclusion of this thesis, suggestions for future experiments are given: In chapter 5, it could be shown that the RESET kinetics of VCM devices are limited intrinsically by the presence of a unipolar SET switching mode, which is triggered at higher positive voltages (applied to the active Pt electrode). Realizing faster RESET times requires, thus, a deeper understanding of this unipolar switching mode. So far, the unipolar SET voltage was determined with manual voltage sweeps on single VCM devices, in which a high cycle-to-cycle and device-to-device variability was observed. An approach to achieve higher statistics on the unipolar SET voltage is presented in section 6.1. Suggestions for future applications of VCM devices are given in section 6.2, which are their realization in neuromorphic applications [25] and as RF switch. Finally, exemplary measurements on fast switching times in other memories technologies are presented.

6.1. Determining and optimizing the RESET speed limit

The RESET kinetics could only be measured in the range from 50 ps to 250 ps and in the range from 480 ps to 100 ns. It could, however, be shown in fig. 5.18 that the intrinsic RESET speed limit of investigated TaO_x and ZrO_x occurs in the gap between these two ranges. To also cover the range from 250 ps to 480 ps, and thereby determining the intrinsic RESET speed limit, an additional pulse generator was ordered from the SYMPULS GmbH. It is able to generate pulses with a width from 50 ps to 100 ns at an amplitude of 2.5 V. The reduction of the amplitude from 5.0 V to 2.5 V was chosen, because higher voltages are only relevant in the regime form 50 ps to 250 ps. The HfB3 device (HfO_x/TiO_x, see table 3.1), for example, switches within 250 ps at a pulse voltage of 1.8 V to the HRS (see fig. 5.28). As shown in section 6.2.1, this pulse generator can also be useful to test, if an analog switching mode can be realized, within VCM devices on a subnanosecond timescale.

More information on the unipolar SET voltage is required. So far, the device-to-device variability of the unipolar SET voltage has been investigated with setups that can only contact one device at once. This makes the measurement not only time-consuming, but also yields lower statistics. To gain more comprehensive statistics on the unipolar SET voltage, these measurements could be repeated with array testers.

One exemplary measurement of the unipolar SET voltage is shown in fig. 6.1. It was conducted with a custom array tester from the aixACCT Systems GmbH, with which 32 de-

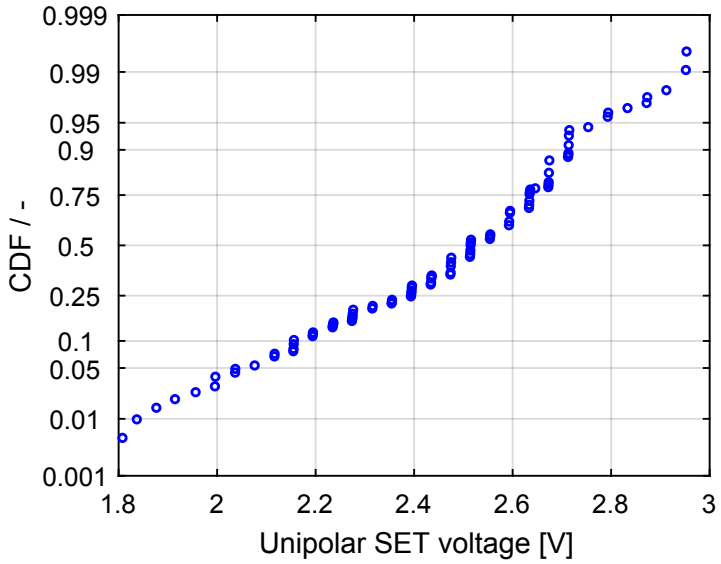

Figure 6.1.: Exemplary measurement of the unipolar SET voltage of a ZrO_x-based VCM device with a custom array tester from the aixACCT Systems GmbH. The measurement was conducted by S. Liberda under the supervision of S. Wiefels.

vices can be measured at once [90, 212]. The tested device has a Pt\ZrO_x\Ta stack and the deposition processes are identical to the ones of the Zr1 device (see chapter 3.1). Again, a 4.0 V sweep was applied at a sweep rate of 800 V/s to the active Pt electrode and the voltage, at which the sudden current increase occurred, was taken as unipolar SET voltage. Overall, 209 devices were tested. Similar to the measured values on the Zr1 device's wafer (see fig. 5.15b), the unipolar SET voltage scatters over a broad voltage range from 1.8 V to 3.0 V. The median value amounts to 2.52 V, which is close to the measured value of 2.29 V on the Zr1 device's wafer (see table 5.1). The small shift to higher voltages may result from the higher sweep rate (800 V/s for the results in this section and 0.5 V/s from chapter 5) or from the different device structure. The tested devices from fig. 6.1 have a planar Pt bottom electrode [90]. The deposition methods and layer thicknesses were identical to the ones of the Zr1 device (see chapter 3.1).

A disadvantage of this array tester is that no current compliance is available. In future, the unipolar SET voltage could be investigated with a new array tester from the aixACCT systems GmbH. It is able to measure 32 x 32 devices at once and comprises a fast current compliance. With this array tester, it may be possible to not only measure the device-to-device, but also the cycle-to-cycle variability. Acquiring statistics of the unipolar SET voltage on different VCM devices, may help to gain a deeper understanding of the unipolar SET processes and also to build VCM devices that have 50 ps fast SET and RESET times.

6.2. Future applications

6.2.1. Neuromorphic applications

In this section, two suggestions are presented on how neuromorphic applications could be realized with VCM devices by using subnanosecond pulses. The first is to realize an analog switching mode, which is required to emulate synaptic weights. The second is an approach to use the VCM device's capacitance to realize short term plasticity (STP) and long term potentiation (LTP).

Analog switching mode

Several studies have presented approaches on how an analog switching mode or intermediate resistive states can be realized in VCM devices by using single short pulses [37] or sequences of short pulses [41, 160, 161]. An analog switching mode requires the presence of irreversible processes such as the migration of mobile donors. This irreversible process needs to be conducted in as small as possible steps, which can be realized by applying short pulses. An exemplary measurement, conducted on a AlO_x/TiO_x-based VCM device, of Stathopoulos *et al.*, is shown in fig. 6.2 [41]. The device's resistance could by increased in small steps by applying a sequence of 7 pulses with a pulse width of 100 ns and an amplitude of 2 V. The overall change in resistance is almost identical to the case in which a single pulse with a width of 1 µs and an amplitude of 2 V is applied. With the presented setup much shorter pulses than in any of the above-mentioned studies can be applied to the VCM device.

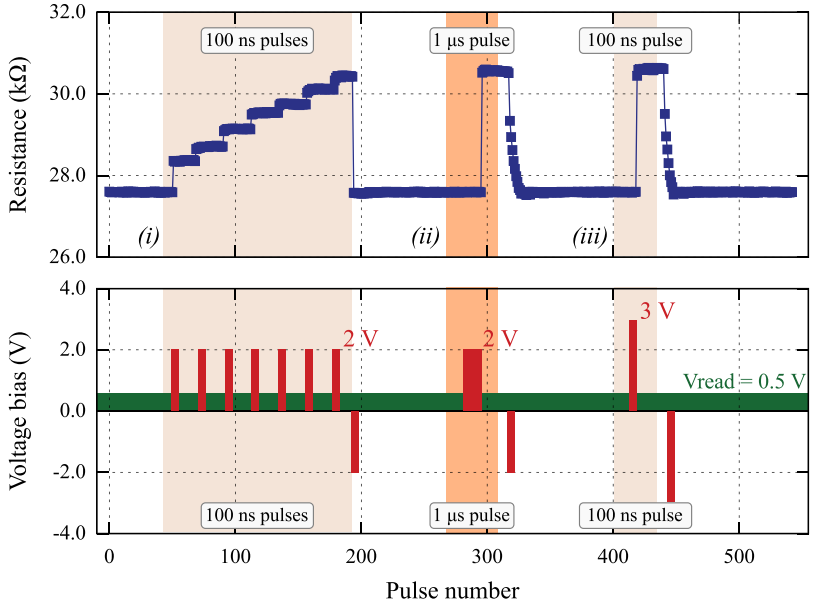

Figure 6.2.: Realization of an analog switching mode on a AlO_x/TiO_x-based VCM device. Taken from [41].

Short term plasticity and long term potentiation

Short term plasticity and long term potentiation describes the brain's ability to forget stimuli occurring at a low repetition rate and to memorize stimuli occurring at a high repetition rate [213]. This can be described by the model of Atkinson and Shiffrin [214] and is sketched in fig. 6.3, which was taken from [213]. Both, frequent (red) and less-frequent (blue) inputs are firstly registered and stored in the sensory memory (SM) and then transferred to the short term memory (STM). Frequent inputs are being rehearsed and will, therefore, be stored in the long term memory (LTM). Less-frequent inputs, on the other hand, are not being rehearsed and will, consequently, be forgotten.

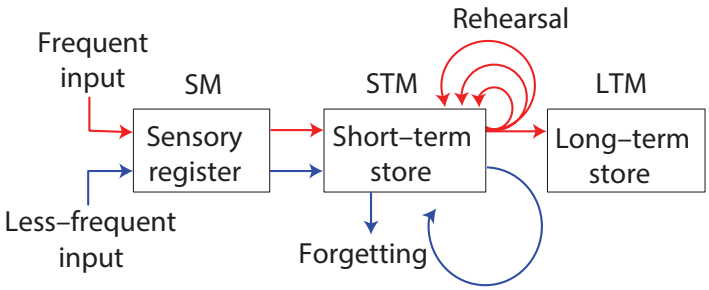

Figure 6.3.: Illustration of the model of Atkinson and Shiffrin [214] describing the short term memory (STM) and long term memory (LTM). Reprinted by permission from Springer Nature Customer Service Centre GmbH: Nature Materials [213], © 2011 Macmillan Publishers Limited. All rights reserved (2011).

To realize STP and LTP, reversible processes need to be present in the memory device. For VCM devices this could be the heating time. As shown in chapter 4.3, for filamentary TaO_x devices, the heating time is shorter than 50 ps during the SET. This could be different for the RESET: Differently to the HRS, in the LRS, the entire filament is electrically conducting and the heating occurs along the entire filament [94]. During the SET, this heating occurs mainly at the active interface. As the heating time scales also with the volume, the heating time during the RESET might be longer than during the SET. Pulsed-IV measurements conducted on HfO_x-based devices suggest that the heating must occur on slower timescales than 100 ps [97]. Using different materials than TaO_x might also result in larger heating times during the SET operation. For example, FEM simulations of eightwise switching $SrTiO_x$ devices suggest heating times between few nanoseconds [80] and up to 50 ns [144] during the SET operation.

Realizing STP and LTP requires a pattern generator with adjustable pulse widths and adjustable breaks between the pulses. An ideal exemplary pattern is depicted in fig. 6.4 as blue line. The pattern comprises pulses, with an amplitude of 1.0 V, a pulse width of 50 ps, and a spacing time of $t_{sw} = 50$ ps. The rise and fall times amount to 10 ps. As shown in table 3.4, the Zr1 device (ZrO_x) has the fastest electric charging time and its scattering parameters are, therefore, used to calculate the resulting effective voltage at the VCM device $V_{DUT}(t)$. This technique is explained in chapter 2.2.2. The result for $V_{DUT}(t)$ is shown as

orange line in fig. 6.4. The Zr1 device's charging time is fast enough (48.8 ps) to become almost completely charged during the application of a pulse and to become almost completely discharged during the time between two pulses. A separation between the electrical charging time and the heating time down to 50 ps is, consequently, possible with the Zr1 device.

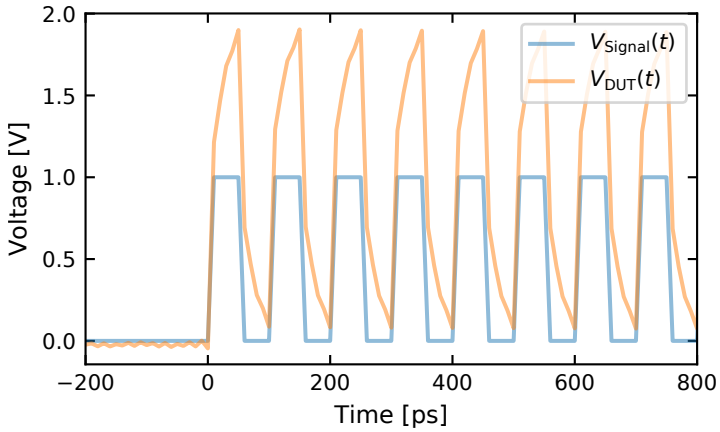

Figure 6.4.: Exemplary pulse pattern ($V_{\mathrm{Signal}}(t)$, blue) to realize STP and LTP in VCM devices and the calculated effective voltage at the VCM device ($V_{\mathrm{DUT}}(t)$, orange).

STP and LTP were already demonstrated in VCM [215, 216] and ECM devices [213, 217–219], however, in most cases on a slow timescale of milliseconds or seconds. To the author's knowledge, the fastest realizations in VCM and ECM devices were on a timescale of 200 ns [216] and 10 µs [219], respectively. The fastest realization of STP and LTP was demonstrated by Sengupta *et al.* on a 2.5 ns timescale with a magnetic tunnel junction [220]. A similar technique to STP and LTP is spike-timing-dependent plasticity (STDP), which were realized on VCM [221] and ECM devices [222, 223] on a microsecond timescale. Only for tunneling junction based devices, STDP was realized within 600 ps [39].

Measurements on the STP and LTP of VCM devices could also be realized by using the device's capacitance. For example, for VCM devices with heating times faster than 50 ps. Two possible measurements are shown in fig. 6.5. In (a), an imaginary pulse sequence of 50 ps pulses with an amplitude of 1.0 V and a pulse separation of 50 ps is shown. It represents a frequent input and is identical to the one shown in fig. 6.4, except this time, the effective voltage at the device $V_{\mathrm{DUT}}(t)$ (orange) is calculated for the Ta1 device instead of for the Zr1 device. The Ta1 device has the largest capacitance and, consequently, also the longest electrical charging time, which amounts to 2.54 ns (see table 3.4). The effective voltage at the device $V_{\mathrm{DUT}}(t)$, therefore, increases gradually with each applied pulse. An assumed threshold, for the information to be written, at 1.2 V (dotted line) would be reached after 2.1 ns and the information would be stored permanently. In (b), an imaginary pulse sequence of 50 ps pulses with an amplitude of 1.0 V, but a pulse separation of 500 ps is shown (in blue) and represents a less-frequent input. The calculated $V_{\mathrm{DUT}}(t)$ never reaches the assumed threshold at 1.2 V, and the information would, consequently, be forgotten.

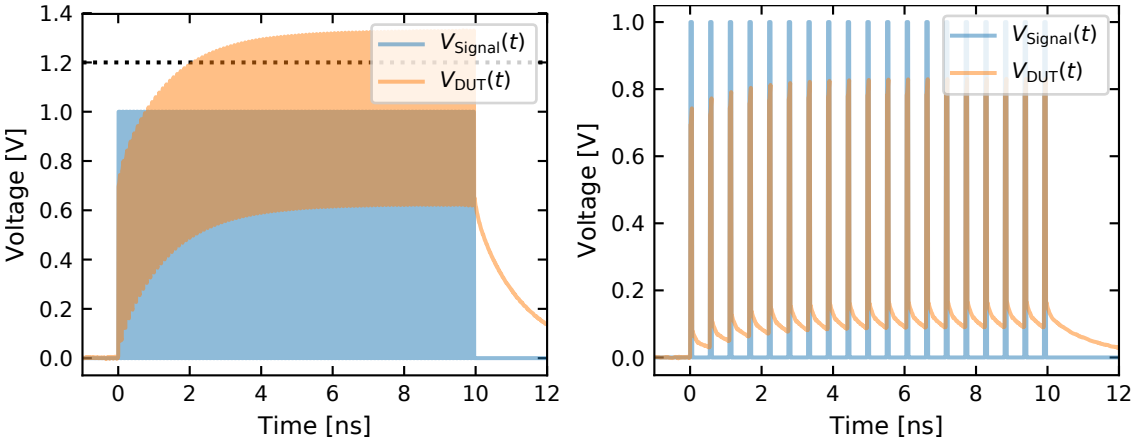

(a) 50 ps pulses with a separation of 50 ps.

(b) 50 ps pulses with a separation of 500 ps.

Figure 6.5.: Exemplary pulse sequences (blue) to realize STP and LTP with the Ta1 device. The orange line marks the calculated voltage at the device $V_{\mathrm{DUT}}(t)$. (a) Represents a frequent input and the pulses are separated by 50 ps. The horizontal dotted line at 1.2 V marks an imaginary threshold for the information to be written. (b) Represents a less-frequent input and the pulses are separated by 500 ps.

There would be several advantages in comparison to the previous studies on STP and LTP (see above):

1. The considered timescale is much shorter than the ones of the previous studies. To the author's knowledge, the fastest STP and LTP measurements were conducted with a pulse separation of 2.5 ns [220].

2. The short pulse widths of only 50 ps would make the product $P(t) \times \mathrm{d}t$ small and, consequently, also reduce the energy consumption.

3. Using the device's capacitance to realize STP and LTP yields a high repeatability as no or only little ionic migration occurs during the charging of the device's capacitance.

6.2.2. RF switch

A disadvantage of the used CPW structures is their size, which makes applications with them difficult to realize and expensive. A potential technical realization could be an RF switch [224]. The use of ReRAM and PCM devices as RF switch was already demonstrated in [225] and [226], respectively. In the HRS, the RF switch is in the off state and signals cannot be transmitted through the VCM device. In the LRS, on the other hand, the RF switch is in the on state and signals can transmit through the VCM device. Two features of VCM devices, however, need to be addressed for their realization as RF switch [227]:

1. For the transmission of low frequencies, the device's resistance in the LRS needs to be very low. In this thesis, the LRS was usually in the range from 1.0 kΩ to 3.0 kΩ, which would hinder the transmission of low frequencies. The Ta1 device yielded also

LRS values around 200 Ω [37], which would probably still be too high for a realization as RF switch. Therefore, RF switches have, so far, mainly been built with ECM devices [228–230]. With the unipolar switching mode, however, also a LRS in the range of only a few ohms are possible with VCM devices [170]. This LRS has also metallic attributes [91]. As the fast pulses used in this thesis are much faster than any commercial active current compliance, the unipolar switching mode could be improved with regard to the endurance and thereby help to achieve very low LRSs.

2. In the HRS, the VCM device needs to block also high frequencies. This is, however, difficult as the VCM device itself constitutes a parallel plate capacitor, which has a low reactance for high frequencies. This can be illustrated with fig. 3.6b. The Ta3 and Zr1 device have the lowest capacitance, but nevertheless their forward transmission S_{21} increases with frequency and reaches at about 10 GHz the bandwidth limit of the CPW structure. The RF switch would in this case only be isolating in the off-state (HRS) up to a frequency of 10 GHz. The realization of an RF switch with VCM devices, consequently, requires VCM devices with low capacitances. Ideally, lateral devices should be used, as it is done for RF switches using PCM devices [226].

6.3. Other memory technologies

The measurement setup used for this thesis can also be used to test the switching kinetics of other memory technologies than VCM. In the following, exemplary measurements on ECM, PCM and FeRAM devices are shown. All devices were integrated into a CPW structure and the current responses were measured with the Tektronix DPO77704D oscilloscope.

6.3.1. Electrochemical metallization memory

Firstly, an exemplary measurement of an ECM device (Cu\SiO$_2$\Pt) is shown, which was also published in the supplementary information of [219]. A 10 ns pulse[1] with an amplitude of $2V_\mathrm{P} = 4.0\,\mathrm{V}$ was applied to the active Cu electrode and is shown in blue in fig. 6.6. The recorded current response is shown in red. After about 1.4 ns a sudden increase in the current could be observed, which corresponds to the SET event [231]. Simulations of the ion migration in ECM devices even suggest switching times down to 50 ps [232].

6.3.2. Phase change memory

Additionally, the RESET time of a PCM device was tested. It is a lateral device, which was fabricated by X. T. Vu. It consists of a 100 nm long and 125 nm wide AgInSbTe layer with a thickness of 25 nm. At its sides, it is contacted with 40 nm thick Pt electrodes. A 50 ps

[1] Generated with the PSPL 2600C pulse generator.

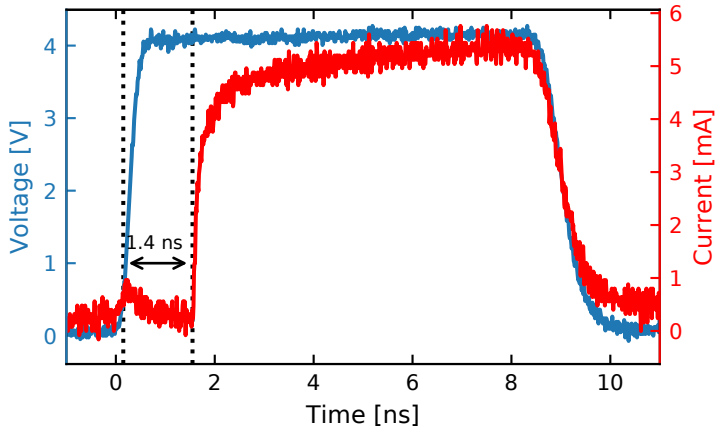

Figure 6.6.: 10 ns voltage pulse with an effective amplitude of 4.0 V (blue) applied to a Cu\SiO_2\Pt ECM device. Its current response is shown in red. After about 1.4 ns, the current increases abruptly, which indicates the SET event. Adapted from [219] (Supplementary information).

pulse[2] with an amplitude of $2V_P = 10.0\,\mathrm{V}$ was applied to this device. The measured current response is shown in fig. 6.7. The measured FWHM amounts to 49.5 ps. The resistance was recorded before (R_{PRE}) and after (R_{POST}) the pulse's application with a Keithley 2634B SMU. The resistance increased from 4.55 kΩ to 1.25 MΩ, which proves the successful RESET within 50 ps.

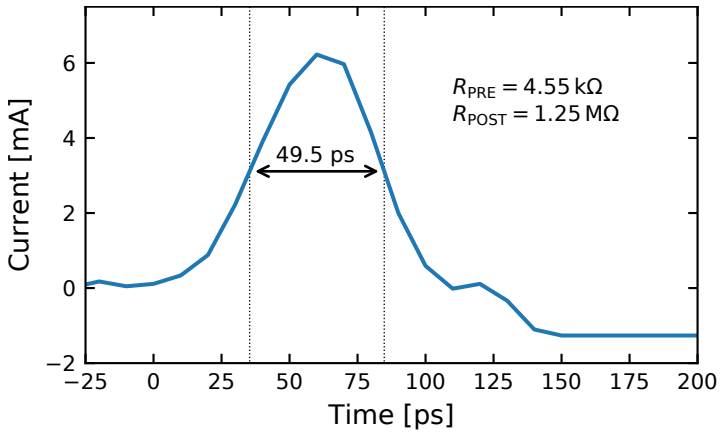

Figure 6.7.: Current response of a AgInSbTe-based PCM device to a 50 ps pulse with an amplitude of $2V_P = 10.0\,\mathrm{V}$. On the upper right, the change in resistance during the pulse's application is indicated.

To the author's knowledge this is the fastest electrically measured RESET time on a PCM device. The fastest measured RESET time so far amounts to 200 ps [60].

6.3.3. Ferroelectric switching

Finally, the switching time of a ferroelectric Pt\Y:HfO_x(45 nm)\Pt capacitor with a size of $4 \times 5\,\mu\mathrm{m}^2$ was tested, which can potentially be used in FeRAM [233]. Two consecutive 10 ns

[2]Generated with the PG5 pulse generator.

pulses[3] with an amplitude of $2V_P = 15.4\,V$ were applied to the devices, after it was polarized with a 10 ns voltage pulse with the opposite polarity of $2V_P = -15.4\,V$. The resulting two current responses are shown in fig. 6.8. During the first pulse (blue) the current peak at the beginning of the pulse was significantly larger than the peak at the end of the pulse, which indicates that the measured current does not only correspond to the capacitive current, but also to the polarization switching current. This is confirmed in the current response of the consecutive pulse (orange), in which the current peak at the beginning is significantly smaller than the peak at the beginning of the first pulse.

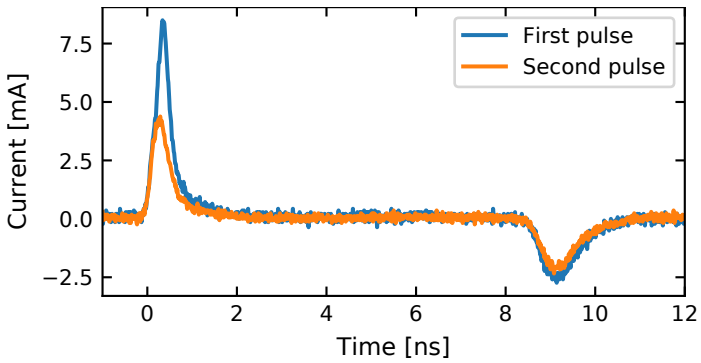

Figure 6.8.: Current responses of two consecutive 10 ns pulses with an amplitude of $2V_P = -15.4\,V$ applied to a $4 \times 5\,\mu m^2$ Pt\Y:HfO_x\Pt capacitor. The current peak at the beginning of the first pulse (blue) is significantly larger than the current peak at the beginning of the second pulse (orange), which indicates the occurring of the device's repolarization. The measurement was conducted in cooperation with F. Berg.

This measurement shows that it is possible to repolarize (or switch) ferroelectric capacitors within less than 10 ns. By further decreasing the pulse width or using other pulse generators, even faster switching times may be observable. To the author's knowledge, the fastest reported switching time of FeRAM devices amounts to 925 ps, and was measured on HfO_x-based devices [234].

[3]Generated by the PSPL 2600C pulse generator.

Conclusion

In this thesis, the SET and RESET kinetics of VCM-based devices were studied on a timescale between 50 ps and 100 ns. Firstly, the RF setup was automated by employing a programmable pulse generator and a broadband bias tee. For this purpose, this pulse generator and an oscilloscope were integrated in a python-based software, which allowed automated measurements in the time regime from 50 ps to 250 ps. With this automation comprehensive data sets could be collected, which lead to a picosecond precise determination of the SET and RESET times. In addition, the evaluation of the data could be conducted in an automated fashion.

To minimize the electrical charging time of VCM devices, an improved optical mask was designed. Shortening the overall length of the CPW structure and the length of the narrowed area increased the CPW structure's bandwidth. Also, the device size was reduced significantly, which decreased the devices' capacitances and, consequently, also their electrical charging times by more than one order of magnitude.

This electrical charging time was determined with the devices' scattering parameters, which were measured up to a frequency of 40 GHz. Multiplying the Fourier transform of the applied pulse with the forward reflection and finally inversely Fourier transforming this product yields the reflected signal. The transmitted signal was calculated by using the forward transmission instead of the forward reflection and matches the measured transmitted signal well, confirming the validity of this approach. By superimposing the incoming signal with the calculated reflected signal and subtracting the transmitted signal, the effective voltage at the VCM device could be determined. The advantage of this approach is that the frequency dependency of all components (capacitances, inductances and serial resistances) is considered and no circuit-based modelling is necessary.

From this calculated voltage at the VCM device, the electrical charging time could be determined. It could be shown that the devices' electrical charging times scale significantly with the device size. By comparing devices fabricated with the improved mask to devices fabricated with a preliminary mask, a significant improvement could be seen. The fastest device fabricated with the preliminary mask has an electrical charging time of 636 ps and the fastest device fabricated with the improved mask an electrical charging time of 48.8 ps. This constitutes an improvement by more than one order of magnitude.

The SET and RESET kinetics were measured on TaO_x-, ZrO_x-, and HfO_x/TiO_x-based VCM devices. The SET kinetics of these three devices could be measured down to 50 ps.

By comparing the SET kinetics of three differently sized TaO_x-based devices, it could be shown that in the sub-10 ns regime the SET time is strongly influenced by the device sizes or their capacitances. By fitting an exponential function to the SET kinetics in the time regime above 10 ns, in which the SET kinetics are mainly limited by the migration of mobile donors (*e.g.* oxygen vacancies), and using the devices' calculated electrical charging times, it could be shown that the SET kinetics in the sub-10 ns regime are mainly limited by the electrical charging time. These results suggest that the migration of mobile donors and the heating of the filament occur on a faster timescale than 50 ps.

The measurement of the RESET kinetics proved to be more difficult in the subnanosecond regime. The RESET times also depend nonlinearly on the applied voltage in this regime and, consequently, faster RESET times require higher voltages. However, above a certain voltage, in all devices a unipolar SET occurs, which prohibits faster RESET times and constitutes an intrinsic RESET speed limit. With these measurements, a RESET programming window could be determined for TaO_x- and ZrO_x-based devices, which is similar to the SET programming window of PCM devices. Nevertheless, RESET times down to 50 ps could be achieved for some TaO_x-, ZrO_x-, and HfO_x/TiO_x-based VCM devices, but with low repeatability. In case of the TaO_x- and ZrO_x-based devices, an additional C layer had to be introduced at the active Pt electrode. Only some of the HfO_x/TiO_x-based devices could be switched repeatedly to the HRS within 50 ps.

Overcoming the intrinsic RESET speed limit requires an in-depth understanding of the unipolar switching mode. For this purpose, the unipolar SET voltage was determined for all samples, showing that the HfO_x/TiO_x-based devices have the highest unipolar SET voltage. Only with these devices, repeatedly 50 ps fast RESET times are accessible. Therefore, the feasibility of fast RESET operations may depend on the unipolar SET voltage. For all tested devices, the unipolar SET voltage has a large device-to-device variability. In future, the statistics on the unipolar SET voltage will, consequently, be measured with array testers.

Finally, suggestions for other future measurements are given in the outlook. The RESET kinetics in the range from 250 ps to 490 ps could be measured with a new pulse generator. This would allow a more precise determination of the intrinsic RESET speed limit. Realizing neuromorphic applications on a subnanosecond timescale, such as an analogous switching mode or STP and LTP, should also be possible. First measurements on the switching kinetics of ECM, PCM, and FeRAM were conducted with the presented setup on a sub-10 ns time scale.

Today's CMOS devices are operated at gigahertz frequencies by generating the required signals on-chip. Fabricating similar fast on-chip pulse generators is difficult for scientific groups, but with the presented setup, failure mechanisms for fast writing times can also be found in the gigahertz regime. In the case of this thesis, one failure mechanism in the RESET kinetics of VCM devices could be identified as the unipolar switching mode. Suggestions on how the unipolar switching mode could be suppressed are given in this thesis and repeatedly

50 ps fast SET and RESET operations are shown for HfO_x/TiO_x-based devices. To the author's knowledge, this has not yet been demonstrated in any other study. With the presented setup it is, therefore, not only possible to detect technological barriers for fast writing times in advance, but it also helps to provide solutions to overcome these barriers.

Acronyms

AC	Alternating current
AE	Active electrode
BE	Bottom electrode
CC	Current compliance
CMOS	Complementary metal-oxide-semiconductor
CPU	Central processing unit
CPW	Coplanar waveguide
DC	Direct current
DRAM	Dynamic random access memory
DUT	Device under test
ECM	Electrochemical metallization memory
FeRAM	Ferroelectric random access memory
FEM	Finite element model
FWHM	Full width half maximum
GPIB	General purpose interface bus
HDD	Hard drive disk
HRS	High resistive state
LRS	Low resistive state
LTM	Long term memory
LTP	Long term potentiation
MOS	Metal-oxide-semiconductor
OC	Outer conductor
PCM	Phase change memory
ReRAM	Redox-based random access memory
RF	Radio frequency
SM	Sensory memory
SMU	Source measure unit
SOLT	Short open load trough
SSD	Solid state drive
STM	Short term memory
STP	Short term plasticity

STDP Spike-timing-dependent plasticity

STTRAM Spin-transfer-torque random access memory

TCM Thermochemical memory

TE Top electrode

TEM Transversal electromagnetic mode

USB Universal serial bus

VCM Valence change memory

VNA Vector network analyzer

List of Publications

Peer Reviewed Journals

M. von Witzleben, S. Walfort, R. Waser, S. Menzel and U. Böttger, "Determining the electrical charging speed limit of ReRAM devices," *IEEE J. Electron Devices Soc.*, vol. 9, pp. 667-678, 2021

S. Wiefels, **M. von Witzleben**, M. Hüttemann, U. Böttger, R. Waser, and S. Menzel, "Impact of the Ohmic Electrode on the Endurance of Oxide Based Resistive Switching Memory," *IEEE Trans. Electron Devices*, vol. 68, no. 3, pp. 1024-1030, 2021

M. von Witzleben, T. Hennen, A. Kindsmüller, S. Menzel, R. Waser, and U. Böttger, "Study of the SET switching event of VCM-based memories on a picosecond timescale," *J. Appl. Phys.*, vol. 127, no. 20, p. 204501, 2020

U. Böttger, **M. von Witzleben**, V. Havel, K. Fleck, V. Rana, R. Waser, and S. Menzel, "Picosecond multilevel resistive switching in tantalum oxide thin films," *Sci. Rep.*, vol. 10, no. 1, p. 16391, 2020

M. Lübben, F. Cüppers, J. Mohr, **M. von Witzleben**, U. Breuer, R. Waser, C. Neumann, and I. Valov, "Design of defect-chemical properties and device performance in memristive systems," *Sci. Adv.*, vol. 6, no. 19, p. eaaz9079, 2020

S. Siegel, C. Bäumer, A. Gutsche, **M. von Witzleben**, R. Waser, S. Menzel, R. Dittmann, "Trade-Off Between Data Retention and Switching Speed in Resistive Switching ReRAM Devices," *Adv. Electron. Mater.*, p. 2000815, 2020

C. Bengel, A. Siemon, F. Cüppers, S. Hoffmann-Eifert, A. Hardtdegen, **M. von Witzleben**, L. Hellmich, R. Waser, and S. Menzel, "Variability-Aware Modeling of Filamentary Oxide based Bipolar Resistive Switching Cells Using SPICE Level Compact Models," *IEEE Trans. Circuits Syst. I*, pp. 1-13, 2020

F. Cüppers, S. Menzel, C. Bengel, A. Hardtdegen, **M. von Witzleben**, U. Böttger, R. Waser, and S. Hoffmann-Eifert, "Exploiting the switching dynamics of HfO_2-based ReRAM devices for reliable analog memristive behavior," *APL Mater.*, vol. 7, no. 9, pp. 91105/1-9, 2019

S. Menzel, **M. von Witzleben**, V. Havel, and U. Böttger , "The ultimate switching speed limit of redox-based restive switching devices," *Faraday Discuss.*, vol. 213, pp. 197-213, 2018

M. von Witzleben, K. Fleck, C. Funck, B. Baumkötter, M. Zuric, A. Idt, T. Breuer, R. Waser, U. Böttger, and S. Menzel, "Investigation of the Impact of High Temperatures on the Switching Kinetics of Redox-based Resistive Switching Cells using a Highspeed Nanoheater," *Adv. Electron. Mat.*, vol. 3, no. 12, p. 1700294, 2017

Conference Proceedings

A. Hardtdegen, F. Cüppers, **M. von Witzleben**, U. Böttger, S. Menzel, R. Waser, and S. Hoffmann-Eifert, "Characterization of HfO_2/TiO_x ReRAM Cells in Pulse Operation Mode," *Proc. 2018 IEEE Conference on Nanotechnology*, 2018

M. von Witzleben, E. Wichmann, C. Funck, K. Fleck, R. Waser, U. Böttger, T. Breuer, and S. Menzel, "Thermal effects on the I-V characteristics of filamentary VCM based ReRAM-cells using a nanometer-sized heater," *2017 17th Non-Volatile Memory Technology Symposium (NVMTS)*, 2017

Conference Talks and Posters

M. von Witzleben, V. Havel, K. Fleck, A. Kindsmüller, R. Waser, S. Menzel, U. Böttger, "Switching kinetics of VCM-based resistive memories at ultrafast time scales," *DPG-Frühjahrstagung 2018 of the Condensed Matter Section*, Berlin, Germany, 11-16 March 2018

M. von Witzleben, K. Fleck, C. Funck, E. Wichmann, B. Baumkötter, A. Idt, T. Breuer, M. Zuric, R. Waser, U. Böttger, and S. Menzel, "SET kinetics and I-V characteristics of VCM-based ReRAM cells at high temperatures using a nanometer-sized heater," *2017 17th Non-Volatile Memory Technology Symposium (NVMTS)*, Aachen, Germany, 30 August - 01 September 2017

Bibliography

[1] M. Aubert, A. Brumm, M. Ramli, T. Sutikna, E. W. Saptomo, B. Hakim, M. J. Morwood, G. D. van den Bergh, L. Kinsley, and A. Dosseto. Pleistocene cave art from Sulawesi, Indonesia. *Nature*, 514:223–227, 2014. doi:10.1038/nature13422.

[2] H. Haarmann. *Die Geschichte der Schrift*. C.H. Beck Verlag, 2 edition, 2004.

[3] J. Assmann. *Stein und Zeit: Mensch und Gesellschaft im alten Ägypten*. Verlag Wilhelm Fink, 3 edition, 2003.

[4] E. J. Himelfarb. First Alphabet Found in Egypt. *Archaeology*, 53(1):21, 2000.

[5] G. Sampson. *Writing Systems: A Linguistic Introduction*. Stanford University Press, 1985.

[6] D. Buisseret. *Envisioning the City: Six Studies in Urban Cartography*. University Of Chicago Press, 1998.

[7] J. Needham and T. Tsuen-Hsuin. *Science and Civilisation in China: Paper and Printing*, volume 5. Cambridge University Press, 1985.

[8] H. Steinberg. *Five Hundred Years of Printing*. Pelican S. Penguin Books Ltd, 3 edition, 1974.

[9] Hans Heger. *Die Geschichte der maschinellen Datenverarbeitung*, volume 1. IBM Deutschland GmbH, 1990.

[10] E. R. Teja. *The Designer's Guide to Disk Drives*. Reston Pub Co, 1984.

[11] K. Itoh. The History of DRAM Circuit Designs – At the Forefront of DRAM Development –. *IEEE Solid-State Circuits Society Newsletter*, 13(1):27–31, 2008. doi:10.1109/N-SSC.2008.4785688.

[12] Micron. *Micron 16-Nanometer NAND Technology Wins Flash Memory Summit Best of Show Award*, 2013. http://investors.micron.com/node/31001/pdf.

[13] Samsung. *Samsung Now Mass Producing Industry's First 2nd-generation, 10-Nanometer Class DRAM*, 2017. https://news.samsung.com/global/wp-content/themes/btr_newsroom/download.php?id=a1NV5LzA32eHN1IlQKRu53cIe2h9FIPFzKNa3EsW0Ao%3D.

[14] J. J. Yang, D. B. Strukov, and D. R. Stewart. Memristive Devices for Computing. *Nat. Nanotechnol.*, 8(1):13–24, 2013. doi:10.1038/nnano.2012.240.

[15] S. Yu and P. Chen. Emerging Memory Technologies: Recent Trends and Prospects. *IEEE Solid-State Circuits Mag.*, 8(2):43–56, 2016. doi:10.1109/MSSC.2016.2546199.

[16] D. Reinsel, J. Gantz, and J. Rydning. The Digitization of the World - From Edge to Core. Technical report, https://www.seagate.com/files/www-content/our-story/trends/files/idc-seagate-dataage-whitepaper.pdf, 2018.

[17] S. Stapnes. Detector challenges at the LHC. *Nature*, 448:290–296, 2007. doi:10.1038/nature06078.

[18] T. Critchlow and K. K.van Dam. *Data-Intensive Science*. CRC Press, 1 edition, 2013.

[19] D. Britton and S. L. Lloyd. How to deal with petabytes of data: the LHC Grid project. *Rep. Prog. Phys.*, 77(6):065902, 2014. doi:10.1088/0034-4885/77/6/065902.

[20] D. Abdurachmanov, B. Bockelman, P. Elmer, G. Eulisse, R. Knight, and S. Muzaffar. Heterogeneous High Throughput Scientific Computing with APM X-Gene and Intel Xeon Phi. *J. Phys.: Conference Series*, 608:012033, 2015. doi:10.1088/1742-6596/608/1/012033.

[21] S. Liu, J. Tang, Z. Zhang, and J. Gaudiot. Computer Architectures for Autonomous Driving. *Computer*, 50(8):18–25, 2017. doi:10.1109/MC.2017.3001256.

[22] S. Kumar and E. Goel. Changing the world of Autonomous Vehicles using Cloud and Big Data. *2018 Second International Conference on Inventive*, pages 368–376, 2018. doi:10.1109/ICICCT.2018.8473347.

[23] R. K. Venkatesan, S. Herr, and E. Rotenberg. Retention-aware placement in DRAM (RAPID): software methods for quasi-non-volatile DRAM. In *The Twelfth International Symposium on High-Performance Computer Architecture, 2006*, pages 155–165, 2006. doi:10.1109/HPCA.2006.1598122.

[24] J. von Neumann. First Draft of a Report on EDVAC. Technical report, Moore School of Electrical Engineering University of Pennsylvania, 1945.

[25] M. A. Zidan, J. P. Strachan, and W. D. Lu. The future of electronics based on memristive systems. *Nat. Electron.*, 1:22–29, 2018. doi:10.1038/s41928-017-0006-8.

[26] AMD. *AMD EPYC 7000 Series Processors: Revolutionary Performance for the Cloud Era*, 2019. https://www.amd.com/system/files/2017-06/AMD-EPYC-Data-Sheet.pdf.

[27] Intel. *Intel Core i9 i7 Extreme Edition Comparison Chart*, 2019. https://www.intel.com/content/dam/support/us/en/documents/processors/core/intel-core-i9-i7-extreme-edition-comparison-chart.pdf.

[28] R. Waser, R. Dittmann, G. Staikov, and K. Szot. Redox-Based Resistive Switching Memories - Nanoionic Mechanisms, Prospects, and Challenges. *Adv. Mater.*, 21(25-26):2632–2663, 2009. doi:10.1002/adma.200900375.

[29] H. Akinaga and H. Shima. Resistive Random Access Memory (ReRAM) Based on Metal Oxides. *Proc. IEEE*, 98(12):2237–2251, 2010. doi:10.1109/JPROC.2010.2070830.

[30] I. L. Markov. Limits on fundamental limits to computation. *Nature*, 512(7513):147–154, 2014. doi:10.1038/nature13570.

[31] D. Ielmini. Resistive switching memories based on metal oxides: mechanisms, reliability and scaling. *Semicond. Sci. Tech.*, 31(6):063002, 2016. doi:10.1088/0268-1242/31/6/063002.

[32] A. C. Torrezan, J. P. Strachan, G. Medeiros-Ribeiro, and R. S. Williams. Sub-nanosecond switching of a tantalum oxide memristor. *Nanotechnology*, 22:485203, 2011. doi:10.1088/0957-4484/22/48/485203.

[33] B. J. Choi, A. C. Torrezan, K. J. Norris, F. Miao, J. P. Strachan, M.-X. Zhang, D. A. A. Ohlberg, N. P. Kobayashi, J. J. Yang, and R. S. Williams. Electrical Performance and Scalability of Pt Dispersed SiO_2 Nanometallic Resistance Switch. *Nano Letters*, 13(7):3213–3217, 2013. doi:10.1021/nl401283q.

[34] B. J. Choi, A. C. Torrezan, S. Kumar, J. P. Strachan, P. G. Kotula, A. J. Lohn, M. J. Marinella, Z. Li, R. S. Williams, and J. J. Yang. High-Speed and Low-Energy Nitride Memristors. *Adv. Funct. Mater.*, 26(29):5290–5296, 2016. doi:10.1002/adfm.201600680.

[35] C. Wang, H. Wu, B. Gao, W. Wu, L. Dai, X. Li, and H. Qian. Ultrafast RESET Analysis of HfO_x-Based RRAM by Sub-Nanosecond Pulses. *Adv. Electron. Mat.*, 3(12):1700263–n/a, 2017. doi:10.1002/aelm.201700263.

[36] S. Menzel, M. von Witzleben, V. Havel, and U. Böttger. The ultimate switching speed limit of redox-based restive switching devices. *Faraday Discuss.*, 2018. doi:10.1039/C8FD00117K.

[37] U. Böttger, M. von Witzleben, V. Havel, K. Fleck, V. Rana, R. Waser, and S. Menzel. Picosecond multilevel resistive switching in tantalum oxide thin films. *Sci. Rep.*, 10(1):16391, 2020. doi:10.1038/s41598-020-73254-2.

[38] M. Witzleben, T. Hennen, A. Kindsmüller, S. Menzel, R. Waser, and U. Böttger. Study of the SET switching event of VCM-based memories on a picosecond timescale. *J. Appl. Phys.*, 127(20):204501, 2020. doi:10.1063/5.0003840.

[39] C. Ma, Z. Luo, W. Huang, L. Zhao, Q. Chen, Y. Lin, X. Liu, Z. Chen, C. Liu, H. Sun, X. Jin, Y. Yin, and X. Li. Sub-nanosecond memristor based on ferroelectric tunnel junction. *Nat. Commun.*, 11(1):1439, 2020. doi:10.1038/s41467-020-15249-1.

[40] A. Schönhals, J. Mohr, D. J. Wouters, R. Waser, and S. Menzel. 3-bit Resistive RAM Write-Read Scheme Based on Complementary Switching Mechanism. *IEEE Electron Device Lett.*, 38(4):449–452, 2017. doi:10.1109/LED.2017.2670642.

[41] S. Stathopoulos, A. Khiat, M. Trapatseli: S. Cortese, A. Serb, I. Valov, and T.Prodromakis. Multibit memory operation of metal-oxide bi-layer memristors. *Sci. Rep.*, 7:17532, 2017. doi:10.1038/s41598-017-17785-1.

[42] A. Hardtdegen, C. La Torre, F. Cüppers, S. Menzel, R. Waser, and S. Hoffmann-Eifert. Improved Switching Stability and the Effect of an Internal Series Resistor in HfO_2/TiO_x Bilayer ReRAM Cells. *IEEE Trans. Electron Devices*, 65(8):3229–3236, 2018. doi:10.1109/TED.2018.2849872.

[43] R. Dittmann and J. P. Strachan. Redox-based memristive devices for new computing paradigm. *APL Materials*, 7(11):110903/1–10, 2019. doi:10.1063/1.5129101.

[44] O. Krestinskaya, A. P. James, and L. O. Chua. Neuromemristive Circuits for Edge Computing: A Review. *IEEE Trans. Neural Netw. Learn. Syst.*, pages 1–20, 2019. doi:10.1109/TNNLS.2019.2899262.

[45] K. Takeuchi. Memory system architecture for the data centric computing. *Jpn. J. Appl. Phys.*, 55(4S):04EA02, 2016. doi:10.7567/JJAP.55.04EA02.

[46] A. Chen. A review of emerging non-volatile memory (NVM) technologies and applications. *Solid-State Electronics*, 125:25–38, 2016. doi:10.1016/j.sse.2016.07.006.

[47] M. H. Park, Y. H. Lee andT. Mikolajick, U. Schröder, and C. S. Hwang. Review and perspective on ferroelectric HfO_2-based thin films for memory applications. *MRS Communications*, pages 1–14, 2018. doi:10.1557/mrc.2018.175.

[48] A. G. Chernikova, M. G. Kozodaev, D. V. Negrov, E. V. Korostylev, M. H. Park, U. Schröder, C. S. Hwang, and A. M. Markeev. Improved Ferroelectric Switching Endurance of La-Doped $Hf_{0.5}Zr_{0.5}O_2$ Thin Films. *ACS Appl. Mater. Interfaces*, 10(3):2701–2708, 2018. doi:10.1021/acsami.7b15110.

[49] J. Müller, T. S. Boscke, U. Schröder, R. Hoffmann, T. Mikolajick, and L. Frey. Nanosecond Polarization Switching and Long Retention in a Novel MFIS-FET Based on Ferroelectric HfO_2. *IEEE Electron Device Lett.*, 33:185–187, 2012. doi:10.1109/LED.2011.2177435.

[50] S. Dünkel, M. Trentzsch, R. Richter, P. Moll, C. Fuchs, O. Gehring, M. Majer, S. Wittek, B. Müller, T. Melde, H. Mulaosmanovic, S. Slesazeck, S. Müller, J. Ocker, M. Noack, D.-A. Löhr, P. Polakowski, J. Müller, T. Mikolajick, J. Höntschel, B. Rice, J. Pellerin, and S. Beyer. A FeFET based super-low-power ultra-fast embedded NVM technology for 22nm FDSOI and beyond. In IEEE, editor, *2017 IEEE International Electron Devices Meeting (IEDM)*, pages 19.7.1–19.7.4. IEEE, 2017. doi:10.1109/IEDM.2017.8268425.

[51] G. Walters, A. Shekhawat, N. G. Rudawski, S. Moghaddam, and T. Nishida. Tiered deposition of sub-5 nm ferroelectric $Hf_{1-x}Zr_xO_2$ films on metal and semiconductor substrates. *Appl. Phys. Lett.*, 112:192901, 2018. doi:10.1063/1.5027516.

[52] S. Bhatti, R. Sbiaa, A. Hirohata, H. Ohno, S. Fukami, and S. N. Piramanayagam. Spintronics based random access memory: a review. *Mater. Today*, 20(9):530–548, 2017. doi:10.1016/j.mattod.2017.07.007.

[53] Jimmy J. Kan, Chando Park, Chi Ching, Jaesoo Ahn, Yuan Xie, Mahendra Pakala, and Seung H. Kang. A Study on Practically Unlimited Endurance of STT-MRAM. *IEEE Trans. Electron Devices*, 64:3639–3646, 2017. doi:10.1109/TED.2017.2731959.

[54] G. E. Rowlands, T. Rahman, J. A. Katine, J. Langer, A. Lyle, H. Zhao, J. G. Alzate, A. A. Kovalev, Y. Tserkovnyak, Z. M. Zeng, H. W. Jiang, K. Galatsis, Y. M. Huai, P. K. Amiri, K. L. Wang, I. N. Krivorotov, and J. Wang. Deep subnanosecond spin torque switching in magnetic tunnel junctions with combined in-plane and perpendicular polarizers. *Appl. Phys. Lett.*, 98:102509, 2011. doi:10.1063/1.3565162.

[55] C. Cong Xu, Yang Zheng, Dimin Niu, Xiaochun Zhu, Seung H. Kang, and Yuan Xie. Impact of Write Pulse and Process Variation on 22 nm FinFET-Based STT-RAM Design: A Device-Architecture Co-Optimization Approach. *IEEE Trans. Multi-Scale Comput. Syst.*, 1:195–206, 2015. doi:10.1109/TMSCS.2015.2509960.

[56] S. Menzel, U. Böttger, M. Wimmer, and M. Salinga. Physics of the Switching Kinetics in Resistive Memories. *Adv. Funct. Mater.*, 25(40):6306–6325, 2015. doi:10.1002/adfm.201500825.

[57] G. W. Burr, M. J. Brightsky, A. Sebastian, H. Cheng, J. Wu, S. Kim, N. E. Sosa, N. Papandreou, H. Lung, H. Pozidis, E. Eleftheriou, and C. H. Lam. Recent Progress in Phase-Change Memory Technology. *IEEE J. Emerging Sel. Top. Circuits Syst.*, 6(2):146–162, 2016. doi:10.1109/JETCAS.2016.2547718.

[58] M. Wimmer and M. Salinga. The gradual nature of threshold switching. *New Journal of Physics*, 16:113044, 2014. doi:10.1088/1367-2630/16/11/113044.

[59] M. Salinga, B. Kersting, I. Ronneberger, V. P. Jonnalagadda, X. T. Vu, M. Le Gallo, I. Giannopoulos, O. Cojocaru-Mirédin, R. Mazzarello, and A. Sebastian. Monatomic phase change memory. *Nat. Mater.*, page 1, 2018. doi:10.1038/s41563-018-0110-9.

[60] D. Q. Huang, X. S. Miao, Z. Li, J. J. Sheng, J. J. Sun, J. H. Peng, J. H. Wang, Y. Chen, and X. M. Long. Nonthermal phase transition in phase change memory cells induced by picosecond electric pulse. *Appl. Phys. Lett.*, 98(24):242106, 2011. doi:10.1063/1.3597792.

[61] S. K. Pandey and A. Manivannan. Sub-nanosecond threshold-switching dynamics and set process of In_3SbTe_2 phase-change memory devices. *Appl. Phys. Lett.*, 108:233501, 2016. doi:10.1063/1.4953196.

[62] D. Loke, T. H. Lee, W. J. Wang, L. P. Shi, R. Zhao, Y. C. Yeo, T. C. Chong, and S. R. Elliott. Breaking the Speed Limits of Phase-Change Memory. *Science*, 336(6088):1566–1569, 2012. doi:10.1126/science.1221561.

[63] P. Zalden, M. J. Shu, F. Chen, X. Wu andY. Zhu, H. Wen, S. Johnston, Z.-X. Shen, P. Landreman, M. Brongersma, S. W. Fong, H.-S. P. Wong, M.-J. Sher, P. Jost, M. Käs, M. Salinga, A. von Hoegen, M. Wuttig, and A. M. Lindenberg. Picosecond Electric-Field-Induced Threshold Switching in Phase-Change Materials. *Phys. Rev. Lett.*, 117(6):067601, 2016. doi:10.1103/PhysRevLett.117.067601.

[64] S. Lai and T. Lowrey. OUM - A 180 nm nonvolatile memory cell element technology for stand alone and embedded applications. In *IEEE International Electron Devices Meeting. Technical Digest*, pages 36.5.1–4, 2001. doi:10.1109/IEDM.2001.979636.

[65] D. H. Im, J. I. Lee, S. L. Cho, H. G. An, D. H. Kim, I. S. Kim, H. Park, D. H. Ahn, H. Horii, S. O. Park, U. Chung, and J. T. Moon. A unified 7.5nm dash-type confined cell for high performance PRAM device. In *2008 IEEE International Electron Devices Meeting*, pages 1–4, 2008. doi:10.1109/IEDM.2008.4796654.

[66] R. Waser, R. Bruchhaus, and S. Menzel. Redox-based Resistive Switching Memories. In R. Waser, editor, *Nanoelectronics and Information Technology (3rd edition)*, pages 683–710. Wiley-VCH, 2012. doi:10.1002/adma.200900375.

[67] L. Goux and I. Valov. Electrochemical processes and device improvement in conductive bridge RAM cells. *Phys. Status Solidi A*, 213:274–288, 2016. doi:10.1002/pssa.201532813.

[68] I. Valov and Y. Yang. Memristors with alloyed electrodes. *Nat. Nanotechnol.*, 15(7):510–511, 2020.

[69] D. Ielmini, R. Bruchhaus, and R. Waser. Thermochemical resistive switching: materials, mechanisms, and scaling projections. *Phase Transit.*, 84(7):570–602, 2011. doi:10.1080/01411594.2011.561478.

[70] T. Yanagida, K. Nagashima, K. Oka, M. Kanai, A. Klamchuen, B.H. Park, and T. Kawai. Scaling Effect on Unipolar and Bipolar Resistive Switching of Metal Oxides. *Scientific reports*, 3(1657), 2013. doi:10.1038/srep01657.

[71] K. Skaja, C. Bäumer, O. Peters, S. Menzel, M. Moors, H. Du, M. Bornhöfft, C. Schmitz, C.-L. Jia, C. M. Schneider, J. Mayer, R. Waser, and R. Dittmann. Avalanche-Discharge-Induced Electrical Forming in Tantalum Oxide-Based Metal-Insulator-Metal Structures. *Advanced Functional Materials*, 25:7154–7162, 2015. doi:10.1002/adfm.201502767.

[72] C. Bäumer, C. Schmitz, A. H. H. Ramadan, H. Du, K. Skaja, V. Feyer, P. Müller, B. Arndt, C. Jia, J. Mayer, R. A. De Souza, C. M. Schneider, R. Waser, and R. Dittmann. Spectromicroscopic insights for rational design of redox-based memristive devices. *Nat. Commun.*, 6:9610, 2015. doi:10.1038/ncomms9610.

[73] A. Kindsmüller, C. Schmitz, C. Wiemann, K. Skaja, D. J. Wouters, R. Waser, C. M. Schneider, and R. Dittmann. Valence change detection in memristive oxide based heterostructure cells by hard X-ray photoelectron emission spectroscopy. *APL Materials*, 6(046106), 2018. doi:10.1063/1.5026063.

[74] A. Wedig, M. Lübben, D.-Y. Cho, M. Moors, K. Skaja, V. Rana, T. Hasegawa, K. Adepalli, B. Yildiz, R. Waser, and I. Valov. Nanoscale cation motion in TaO_x, HfO_x and TiO_x memristive systems. *Nat. Nanotechnol.*, 11(1):67–74, 2016. doi:10.1038/nnano.2015.221.

[75] Y. Ma, D. Li, A. A. Herzing, D. A. Cullen, B. T. Sneed, K. L. More, N. T. Nuhfer, J. A. Bain, and M. Skowronski. Formation of the Conducting Filament in TaO_x-Resistive Switching Devices by Thermal-Gradient-Induced Cation Accumulation. *ACS Appl. Mater. Interfaces*, 10(27):23187–23197, 2018. doi:10.1021/acsami.8b03726.

[76] Carlos M. M. Rosário, Bo Thöner, Alexander Schönhals, Stephan Menzel, Alexander Meledin, Nuno P. Barradas, Eduardo Alves, Joachim Mayer, Matthias Wuttig, Rainer Waser, Nikolai A. Sobolev, and Dirk J. Wouters. Metallic filamentary conduction in valence change-based resistive switching devices: the case of TaO_x thin film with $x \sim 1$. *Nanoscale*, 2019. doi:10.1039/C9NR05285B.

[77] K. Szot, R. Dittmann, W. Speier, and R. Waser. Nanoscale resistive switching in $SrTiO_3$ thin films. *Phys. Status Solidi-Rapid Res. Lett.*, 1(2):R86–R88, 2007. doi:10.1002/pssr.200701003.

[78] S. Privitera, G. Bersuker, S. Lombardo, C. Bongiorno, and D. Gilmer. Conductive filament structure in HfO_2 resistive switching memory devices. *Solid-State Electronics*, 111:161–165, 2015. doi:10.1016/j.sse.2015.05.044.

[79] S. Pi, C. Li, H. Jiang, W. Xia, H. Xin, J. J. Yang, and Q. Xia. Memristor crossbar arrays with 6-nm half-pitch and 2-nm critical dimension. *Nat. Nanotechnol.*, 14(1):35–39, 2019. doi:10.1038/s41565-018-0302-0.

[80] S. Menzel, M. Waters, A. Marchewka, U. Böttger, R. Dittmann, and R. Waser. Origin of the Ultra-nonlinear Switching Kinetics in Oxide-Based Resistive Switches. *Adv. Funct. Mater.*, 21(23):4487–4492, 2011. doi:10.1002/adfm.201101117.

[81] K. Fleck, C. La Torre, N. Aslam, S. Hoffmann-Eifert, U. Böttger, and S. Menzel. Uniting Gradual and Abrupt SET Processes in Resistive Switching Oxides. *Phys. Rev. Applied*, 6(6):064015, 2016. doi:10.1103/PhysRevApplied.6.064015.

[82] D. Cooper, C. Bäumer, N. Bernier, A. Marchewka, C. La Torre, R. E. Dunin-Borkowski, S. Menzel, R. Waser, and R. Dittmann. Anomalous Resistance Hysteresis in Oxide ReRAM: Oxygen Evolution and Reincorporation Revealed by in situ TEM. *Adv. Mater.*, 29(23):1700212, 2017. doi:10.1002/adma.201700212.

[83] H. Zhang, S. Yoo, S. Menzel, C. Funck, F. Cüppers, D. J. Wouters, C. S. Hwang, R. Waser, and S. Hoffmann-Eifert. Understanding the Coexistence of Two Bipolar Resistive Switching Modes with Opposite Polarity in $Pt/TiO_2/Ti/Pt$ Nanosized ReRAM Devices. *ACS Appl. Mater. Interfaces*, 10(35):29766–29778, 2018. doi:10.1021/acsami.8b09068.

[84] S. Petzold, E. Miranda, S. U. Sharath, J. Muñoz-Gorriz, T. Vogel, E. Piros, N. Kaiser, R. Eilhardt, A. Zintler, L. Molina-Luna, J. Suñé, and L. Alff. Analysis and simulation of the multiple resistive switching modes occurring in HfO_x-based resistive random access memories using memdiodes. *J. Appl. Phys.*, 125(23):234503, 2019. doi:10.1063/1.5094864.

[85] A. Schönhals, C. M. M. Rosario, S. Hoffmann-Eifert, R. Waser, S. Menzel, and D. J. Wouters. Role of the Electrode Material on the RESET Limitation in Oxide ReRAM Devices. *Adv. Electron. Mater.*, 4(2):1700243/1–11, 2017. doi:10.1002/aelm.201700243.

[86] R. Waser, R. Dittmann, S. Menzel, and T. Noll. Introduction to new memory paradigms: memristive phenomena and neuromorphic applications. *Faraday Discuss.*, 213:11–27, 2019. doi:10.1039/c8fd90058b.

[87] C. Bäumer, T. Heisig, B. Arndt, K. Skaja, F. Borgatti, F. Offi, F. Motti, G. Panaccione, R. Waser, S. Menzel, and R. Dittmann. Spectroscopic elucidation of ionic motion processes in tunnel oxide-based memristive devices. *Faraday Discuss.*, 213:215–230, 2019. doi:10.1039/c8fd00108a.

[88] M.-J. Lee, C. B. Lee, D. Lee, S. R. Lee, M. Chang, J. H. Hur, Y.-B. Kim, C. J. Kim, D. H. Seo, S. Seo, U.-I. Chung, I.-K. Yoo, and K. Kim. A fast, high-endurance and scalable non-volatile memory device made from asymmetric Ta_2O_{5-x}/TaO_{2-x} bilayer structures. *Nat. Mater.*, 10(8):625–630, 2011. doi:10.1038/nmat3070.

[89] P. Huang, B. Chen, Y. Wang, F. Zhang, L. Shen, R. Liu, L. Zeng, G. Du, X. Zhang, B. Gao, J. Kang, X. Liu, X. Wang, B. Weng, Y. Tang, G. Lo, and D. Kwong. Analytic model of endurance degradation and its practical applications for operation scheme optimization in metal oxide based RRAM. In *Electron Devices Meeting (IEDM), 2013 IEEE International*, pages 22.5.1–22.5.4, 2013. doi:10.1109/IEDM.2013.6724685.

[90] S. Wiefels, M. von Witzleben, M. Hüttemann, U. Böttger, R. Waser, and S. Menzel. Impact of the Ohmic Electrode on the Endurance of Oxide-Based Resistive Switching Memory. *IEEE Transactions on Electron Devices*, 68(3):1024–1030, 2021. doi:10.1109/TED.2021.3049765.

[91] I. Kärkkänen, A. Shkabko, M. Heikkilä, M. Vehkamaki, J. Niinistö, N. Aslam, P. Meuffels, M. Ritala, M. Leskela, R. Waser, and S. Hoffmann-Eifert. Impedance spectroscopy study of the unipolar and bipolar resistive switching states of atomic layer deposited polycrystalline ZrO_2 thin films. *Phys. Status Solidi A-Appl. Mat.*, 212(4):751–766, 2015. doi:10.1002/pssa.201431489.

[92] A. Prakash, D. Jana, and S. Maikap. TaO_x-based resistive switching memories: Prospective and challenges. *Nanoscale Research Letters*, 8(1):1–17, 2013. doi:10.1186/1556-276X-8-418.

[93] D. B. Strukov and R. S. Williams. Exponential ionic drift: fast switching and low volatility of thin-film memristors. *Appl. Phys. A-Mater. Sci. Process.*, 94(3):515–519, 2009. doi:10.1007/s00339-008-4975-3.

[94] A. Marchewka, B. Rösgen, K. Skaja, H. Du, C. L. Jia, J. Mayer, V. Rana, R. Waser, and S. Menzel. Nanoionic Resistive Switching Memories: On the Physical Nature of the Dynamic Reset Process. *Adv. Electron. Mater.*, 2(1):1500233/1–13, 2016. doi:10.1002/aelm.201500233.

[95] M. Witzleben, K. Fleck, C. Funck, B. Baumkötter, M. Zuric, A. Idt, T. Breuer, R. Waser, U. Böttger, and S. Menzel. Investigation of the Impact of High Temperatures on the Switching Kinetics of Redox-based Resistive Switching Cells using a Highspeed Nanoheater. *Adv. Electron. Mat.*, 3(12):1700294, 2017. doi:10.1002/aelm.201700294.

[96] E. Yalon, S. Cohen, A. Gavrilov, and D. Ritter. Evaluation of the local temperature of conductive filaments in resistive switching materials. *Nanotechnology*, 23(46):465201/1–, 2012. doi:10.1088/0957-4484/23/46/465201.

[97] E. Yalon, A. A. Sharma, M. Skowronski, J. A. Bain, D. Ritter, and I. V. Karpov. Thermometry of Filamentary RRAM Devices. *IEEE Trans. Electron Devices*, 62(9):2972–2977, 2015. doi:10.1109/TED.2015.2450760.

[98] M. Uenuma, Y. Ishikawa, and Y. Uraoka. Joule heating effect in nonpolar and bipolar resistive random access memory. *Appl. Phys. Lett.*, 107:073503, 2015. doi:10.1063/1.4928661.

[99] J. M. Goodwill, G. Ramer, D. Li, B. D. Hoskins, G. Pavlidis, J. J. McClelland, A. Centrone, J. A. Bain, and M. Skowronski. Spontaneous current constriction in threshold switching devices. *Nature Communications*, 10(1628), 2019. doi:10.1038/s41467-019-09679-9.

[100] M. von Witzleben, S. Walfort, R. Waser, S. Menzel, and U. Böttger. Determining the electrical charging speed limit of ReRAM devices. *IEEE J. Electron Devices Soc.*, 9:667–678, 2021. doi:10.1109/JEDS.2021.3095389.

[101] D. M. Pozar. *Microwave Engineering*. John Wiley & Sons, 4 edition, 2012.

[102] GigaLane Co. Ltd. *GL Series Flexible Low Loss Microwave Cable Assembly*, 2011. http://gigarf.firstmall.kr/data/pdf/329.pdf.

[103] D. R. Lide. *CRC handbook of chemistry and physics*, volume 84. CRC press, 2004.

[104] D. Ielmini, F. Nardi, and S. Balatti. Evidence for Voltage-Driven Set/Reset Processes. *IEEE Trans. Electron Devices*, 59:2049–2055, 2012. doi:10.1109/TED.2012.2199497.

[105] K. Fleck, U. Böttger, R. Waser, and S. Menzel. Interrelation of Sweep and Pulse Analysis of the SET Process in $SrTiO_3$ Resistive Switching Memories. *IEEE Electron Device Lett.*, 35(9):924 – 926, 2014. doi:10.1109/LED.2014.2340016.

[106] Y. Nishi, S. Schmelzer, U. Böttger, and R. Waser. Weibull Analysis of the Kinetics of Resistive Switches based on Tantalum Oxide Thin Films. *Proceedings of the 43rd European Solid-State Device Research Conference (ESSDERC)*, pages 174–177, 2013. doi:10.1109/ESSDERC.2013.6818847.

[107] N. Ciocchini, M. Cassinerio, D. Fugazza, and D. Ielmini. Evidence for Non-Arrhenius Kinetics of Crystallization in Phase Change Memory Devices. *IEEE Trans. Electron Devices*, 60(11):3767–3774, 2013. doi:10.1109/TED.2013.2282637.

[108] A.A. Sharma, M. Noman, M. Skowronski, and J.A. Bain. High-speed in-situ pulsed thermometry in oxide RRAMs. In *2014 International Symposium on VLSI Technology, Systems and Applications (VLSI-TSA)*, pages 1–2, 2014. doi:10.1109/VLSI-TSA.2014.6839687.

[109] J. S. Brockman, L. Gao, B. Hughes, C. T. Rettner, M. G. Samant, K. P. Roche, and S. S. P. Parkin. Subnanosecond incubation times for electric-field-induced metallization of a correlated electron oxide. *Nat. Nanotechnol.*, 9:453–458, 2014. doi:10.1038/nnano.2014.71.

[110] A. A. Sharma, I. V. Karpov, R. Kotlyar, J. Kwon, M. Skowronski, and J. A. Bain. Dynamics of electroforming in binary metal oxide-based resistive switching memory. *J. Appl. Phys.*, 118(11):114903/1–, 2015. doi:10.1063/1.4930051.

[111] J. Kwon, A. A. Sharma, C. M. Chen, A. Fantini, M. Jurczak, A. A. Herzing, J. A. Bain, Y. N. Picard, and M. Skowronski. Transient thermometry and HRTEM analysis of filamentary resistive switches. *ACS Applied Materials & Interfaces*, 8:20176–20184, 2016. doi:10.1021/acsami.6b05034.

[112] Api technologies corp. *Adapters, in-series DC-26.5 & 40 GHz 2.9mm*, 2018. https://www.apitech.com/globalassets/documents/products/rf-microwave-microelectronics-power-solutions/rf-components/coaxial-adapters--connector-systems/5162.pdf.

[113] V. Milanovic, M. Gaitan, E. D. Bowen, and M. E. Zaghloul. Micromachined coplanar waveguides in CMOS technology. *IEEE Microwave and Guided Wave Letters*, 6(10):380–382, 1996. doi:10.1109/75.536952.

[114] Y. Dong, T. K. Johansen, and V. Zhurbenko. Ultra-wideband coplanar waveguide-to-asymmetric coplanar stripline transition from dc to 165 ghz. *Int. J. Microw. Wirel. Technol.*, 10(8):870–876, 2018.

[115] Brian C. Wadell. *Transmission line design handbook*. Artech House, 1991.

[116] I. Rosu. Impedance Matching. Technical Report YO3DAC-VA3IUL, https://www.qsl.net/va3iul/, 2014.

[117] David Yevick and Hannah Yevick. *Fundamental math and physics for scientists and engineers*. Wiley, 2014. doi:10.1002/9781118979792.

[118] Y. Lu, Jong Ho Lee, and I-Wei Chen. Nanofilament Dynamics in Resistance Memory: Model and Validation. *ACS Nano*, 9:7649, 2015. doi:10.1021/acsnano.5b03032.

[119] U. Böttger, M. v. Witzleben, V. Havel, K. Fleck, V. Rana, R. Waser, and S. Menzel. Picosecond Multilevel Resistive Switching in Tantalum Oxide Thin Films. https://arxiv.org/abs/2002.00700, 2019.

[120] H. W. Johnson and M. Grahm. *High Speed Digital Design: A Handbook of Black Magic*, volume 1. Prentice Hall, 1993.

[121] V. Havel. Transient Processes in Resistive Switching Memory Devices at Ultimate Time Scale Down to Sub-Nanosecond Range. Phd thesis, RWTH Aachen University, 2016. doi:10.18154/RWTH-2016-02755.

[122] Tektronix. *DPO7000C Series Digital Phosphor Oscilloscopes User Manual*. Tektronix, 071-2980-04 edition, 2014. https://de.tek.com/product-support?series=MSO/DPO70000&type=manual.

[123] Picosecond Pulse Labs. *Model 2600C Pulse Generator Instruction Manual*. Tektronix, 2001. https://www.tek.com/product-support?series=Signal%20Pulse%20Generators&type=manual.

[124] Agilent. *Agilent 8720E Family Microwave Vector Network Analyzers Data Sheet*. Agilent, 2004. https://literature.cdn.keysight.com/litweb/pdf/5968-5163E.pdf.

[125] FormFactor. *Probes Selection Guide*. FormFactor, 2017. https://www.formfactor.com/download/probe-selection-guide.

[126] H. Nyquist. Certain Topics in Telegraph Transmission Theory. *Transactions of the American Institute of Electrical Engineers*, 47(2):617–644, 1928. doi:10.1109/T-AIEE.1928.5055024.

[127] C. E. Shannon. Communication in the Presence of Noise. *Proceedings of the IRE*, 37:10–21, 1949. doi:10.1109/JRPROC.1949.232969.

[128] Api technologies. *A/AH Attenuators 2.9mm up to 40 GHz up to 2 Watts*. Api technologies, 2017. https://www.apitech.com/products/rf-solutions/passive-coaxial-products/fixed-attenuators/low-power-fixed-attenuators/2.92mm/40ah-fixed-coaxial-attenuator/.

[129] V. Havel, K. Fleck, B. Rösgen, V. Rana, S. Menzel, U. Böttger, and R. Waser. Ultrafast Switching in Ta_2O_5-based Resistive Memories. In *Silicon Nanoelectronics Worshop SNW 2016, Honolulu, HI, USA, 12-13 June 2016*, pages 82–83, 2016. doi:10.1109/SNW.2016.7577995.

[130] Karsten Fleck. The Influence of Local Heating on the Switching Kinetics of Resistive Switching Oxides. Phd thesis, RWTH Aachen University, 2018.

[131] K. Fleck, U. Böttger, R. Waser, N. Aslam, S. Hoffmann-Eifert, and S. Menzel. Energy dissipation during pulsed switching of strontium-titanate based resistive switching memory devices. In *Proceedings of the 43th European Solid-State Device Research Conference (ESSDERC), Lausanne, Switzerland, September 12-15, 2016*, pages 160–163, 2016. doi:10.1109/ESSDERC.2016.7599611.

[132] K. Fleck, N. Aslam, S. Hoffmann-Eifert, V. Longo, F. Roozeboom, W. M. M. Kessels, U. Böttger, R. Waser, and S. Menzel. The influence of non-stoichiometry on the switching kinetics of strontium-titanate ReRAM devices. *J. Appl. Phys.*, 120(24):244502, 2016. doi:10.1063/1.4972833.

[133] API Technologies Corp. *BIAS TEES 2.9mm UP TO 40 GHz 25 VOLTs*. API Technologies Corp., 2017. https://datasheet.octopart.com/8812KFF2-26-API-Technologies-datasheet-136500798.pdf.

[134] Yonghyun Shim, Gwendolyn Hummel, and Mina Rais-Zadeh. RF switches using phase change materials. In *2013 IEEE 26th International Conference on Micro Electro Mechanical Systems (MEMS)*, pages 237–240. IEEE, 2013. doi:10.1109/MEMSYS.2013.6474221.

[135] H. Madan, H-T. Zhang, M. Jerry, D. Mukherjee, N. Alem, R. Engel-Herbert, and S. Datta. 26.5 Terahertz electrically triggered RF switch on epitaxial VO_2-on-Sapphire (VOS) wafer. In *2015 IEEE International Electron Devices Meeting (IEDM)*, pages 9.3.1–9.3.4. IEEE, 2015. doi:10.1109/IEDM.2015.7409661.

[136] Rohde & Schwarz. *R&S ZVL Vector Network Analyzer Specifications*, 2019. https://scdn.rohde-schwarz.com/ur/pws/dl_downloads/dl_common_library/dl_brochures_and_datasheets/pdf_1/ZVL_dat-sw_en_5213-8150-22_v1200.pdf.

[137] S. Yu, Y. Wu, R. Jeyasingh, D. Kuzum, and H. P. Wong. An Electronic Synapse Device Based on Metal Oxide Resistive Switching Memory for Neuromorphic Computation. *IEEE Trans. Electron Devices*, 58:2729–2737, 2011. doi:10.1109/TED.2011.2147791.

[138] Y. Bai, H. Wu, R. Wu, Y. Zhang, N. Deng, Z. Yu, and H. Qian. Study of Multilevel Characteristics for 3D Vertical Resistive Switching Memory. *Scientific Reports*, 4:5780–5780, 2014. doi:10.1038/srep05780.

[139] Artem Zaidman. Impact of ohmic electrode material variation on the switching kinetics of ZrO_2-based resistive memory cells. Bachelor's thesis, RWTH Aachen University, 2017.

[140] Stefan Leisten. Influence of the ohmic electrode on the switching kinetics and endurance of ZrO_2-based resisitive memory cells. Bachelor's thesis, RWTH Aachen University, 2018.

[141] Y. Nishi, S. Menzel, K. Fleck, U. Böttger, and R. Waser. Origin of the SET Kinetics of the Resistive Switching in Tantalum Oxide Thin Films. *IEEE Electron Device Lett.*, 35(2):259–261, 2013. doi:10.1109/LED.2013.2294868.

[142] Y. Nishi, K. Fleck, U. Böttger, R. Waser, and S. Menzel. Effect of RESET Voltage on Distribution of SET Switching Time of Bipolar Resistive Switching in a Tantalum Oxide Thin Film. *IEEE Trans. Electron Devices*, 62(5):1561–1567, 2015. doi:10.1109/TED.2015.2411748.

[143] Y. Nishi, U. Böttger, R. Waser, and S. Menzel. Crossover From Deterministic to Stochastic Nature of Resistive-Switching Statistics in a Tantalum Oxide Thin Film. *IEEE Trans. Electron Devices*, 2018. doi:10.1109/TED.2018.2866127.

[144] S. Siegel, C. Bäumer, A. Gutsche, M. von Witzleben, R: Waser, S. Menzel, and R. Dittmann. Trade-Off Between Data Retention and Switching Speed in Resistive Switching ReRAM Devices. *Adv. Electron. Mater.*, 2020. doi:10.1002/aelm.202000815.

[145] J. P. Strachan, A. C. Torrezan, G. Medeiros-Ribeiro, and R. S. Williams. Measuring the switching dynamics and energy efficiency of tantalum oxide memristors. *Nanotechnology*, 22(50):505402/1–5, 2011. doi:10.1088/0957-4484/22/50/505402.

[146] Thomas Schanze. Sinc interpolation of discrete periodic signals. *IEEE Transactions on Signal Processing*, 43:1502–1503, 1995. doi:10.1109/78.388863.

[147] FormFactor. *—Z— Probe High-Frequency Wafer Probe*. FormFactor, 2010. https://www.formfactor.com/product/probes/z-probe/z-probe-coaxial/.

[148] A. Schönhals. Non-Standard Switching Phenomena and Interface Effects in Resistive Switching Devices. Phd thesis, RWTH Aachen University, 2019. doi:10.18154/RWTH-2019-08592.

[149] A. Schönhals, S. Menzel, V. Rana, and R. Waser. 3-bit Read Scheme for Single Layer Ta_2O_5 ReRAM. In *Non-Volatile Memory Technology Symposium (NVMTS), 2014 14th Annual*, 2014. doi:10.1109/NVMTS.2014.7060845.

[150] A. Schönhals, A. Kindsmüller, C. La Torre, H. Zhang, S. Hoffmann-Eifert, S. Menzel, R. Waser, and D. J. Wouters. Overcoming the RESET Limitation in Tantalum Oxide-Based ReRAM Using an Oxygen-Blocking Layer. In *Memory Workshop (IMW), 2017 IEEE International*, 2017. doi:10.1109/IMW.2017.7939096.

[151] A. Kindsmüller. The role of interface and exchange processes in forming and switching of ZrO_2 based ReRAM devices. Phd thesis, RWTH Aachen University, 2020. doi:10.18154/RWTH-2020-07858.

[152] C. La Torre, A. Kindsmüller, D. J. Wouters, C. E. Graves, G. A. Gibson, J. P. Strachan, R. S. Williams, R. Waser, and S. Menzel. Volatile HRS asymmetry and subloops in resistive switching oxides. *Nanoscale*, 9:14414–14422, 2017. doi:10.1039/C7NR04896C.

[153] A. Hardtdegen, H. Zhang, and S. Hoffmann-Eifert. Tuning the Performance of Pt/HfO_2/Ti/Pt ReRAM Devices obtained from Plasma-Enhanced Atomic Layer Deposition for HfO_2 Thin Films. *ECS Transactions*, 75(6):177–184, 2016. doi:10.1149/07506.0177ecst.

[154] Stephan Aussen, Alexander Hardtdegen, Katharina Skaja, and Susanne Hoffmann-Eifert. Interfaces Formed by ALD Metal Oxide Growth on Metal Layers. *ECS Trans.*, 80(3):87–95, 2017. doi:10.1149/08003.0087ecst.

[155] W. Kim, S. Menzel, D. J. Wouters, Y. Guo, J. Robertson, B. Rösgen, R. Waser, and V. Rana. Impact of oxygen exchange reaction at the ohmic interface in Ta_2O_5-based ReRAM devices. *Nanoscale*, 8(41):17774–17781, 2016. doi:10.1039/c6nr03810g.

[156] M. Lübben, P. Karakolis, V. Ioannou-Sougleridis, P. Normand, and P. Dimitrakis andI. Valov. Graphene-Modified Interface Controls Transition from VCM to ECM Switching Modes in Ta/TaO_x Based Memristive Devices. *Adv. Mater.*, 27(40):6202–6207, 2015. doi:10.1002/adma.201502574.

[157] W. Kim, S. Menzel, D. J. Wouters, R. Waser, and V. Rana. 3-Bit Multi Level Switching by Deep Reset Phenomenon in Pt/W/TaO_x/Pt-ReRAM Devices. *IEEE Electron Device Lett.*, 37(5):564–567, 2016. doi:10.1109/LED.2016.2542879.

[158] Y. Guo and J. Robertson. Material selection for oxide-based resistive random access memories. *Appl. Phys. Lett.*, 105(22):223516, 2014. doi:10.1063/1.4903470.

[159] C. Bengel, A. Siemon, F. Cüppers, S. Hoffmann-Eifert, A. Hardtdegen, M. von Witzleben, L. Helllmich, R. Waser, and S. Menzel. Variability-Aware Modeling of Filamentary Oxide based Bipolar Resistive Switching Cells Using SPICE Level Compact Models. *TCAS 1*, 2020. doi:10.1109/TCSI.2020.3018502.

[160] A. Hardtdegen, F. Cüppers, M. von Witzleben, U. Böttger, S. Menzel, R. Waser, and S. Hoffmann-Eifert. Characterization of HfO_2/TiO_x ReRAM Cells in Pulse Operation Mode. In *Proc. 2018 IEEE Conference on Nanotechnology*, pages 1–4. IEEE, 2018. doi:10.1109/NANO.2018.8626314.

[161] F. Cüppers, S. Menzel, C. Bengel, A. Hardtdegen, M. von Witzleben, U. Böttger, R. Waser, and S. Hoffmann-Eifert. Exploiting the switching dynamics of HfO_2-based ReRAM devices for reliable analog memristive behavior. *APL Mater.*, 7(9):91105/1–9, 2019. doi:10.1063/1.5108654.

[162] J. McPherson, J. Kim, A. Shanware, H. Mogul, and J. Rodriguez. Trends in the ultimate breakdown strength of high dielectric-constant materials. *IEEE Trans. Electron Devices*, 50(8):1771–1778, 2003. doi:10.1109/TED.2003.815141.

[163] C.T. Dervos, Thirios, J. Novacovich, P. Vassiliou, and P. Skafidas. Permittivity properties of thermally treated TiO_2. *Mater. Lett*, 58(9):1502 – 1507, 2004. doi:10.1016/j.matlet.2003.10.012.

[164] K. Kukli, M. Ritala, J. Sundqvist, J. Aarik, J. Lu, T. Sajavaara, M. Leskelä, and A. Hårsta. Properties of hafnium oxide films grown by atomic layer deposition from hafnium tetraiodide and oxygen. *J. Appl. Phys.*, 92:5698–5703, 2002. doi:10.1063/1.1515107.

[165] J. F. Conley, Y. Ono, D. J. Tweet, W. Zhuang, and R. Solanki. Atomic layer deposition of thin hafnium oxide films using a carbon free precursor. *J. Appl. Phys.*, 93:712–718, 2003. doi:10.1063/1.1528306.

[166] R. Devanathan, W. Weber, S. Singhal, and J. Gale. Computer simulation of defects and oxygen transport in yttria-stabilized zirconia. *Solid State Ionics 2006*, 177(15):1251–1258, 2006. doi:10.1016/j.ssi.2006.06.030.

[167] S. Choi, J. Lee, S. Kim, and W. D. Lu. Retention failure analysis of metal-oxide based resistive memory. *Appl. Phys. Lett.*, 105:113510, 2014. doi:10.1063/1.4896154.

[168] R. Nakamura, T. Toda, S. Tsukui, M. Tane, M. Ishimaru, T. Suzuki, and H. Nakajima. Diffusion of oxygen in amorphous Al_2O_3, Ta_2O_5, and Nb_2O_5. *J. Appl. Phys.*, 116(3):033504, 2014. doi:10.1063/1.4889800.

[169] H. Ono and K. i. Koyanagi. Infrared absorption peak due to Ta=O bonds in Ta_2O_5 thin films. *Appl. Phys. Lett.*, 77:1431–1433, 2000. doi:10.1063/1.1290494.

[170] S. Gao, G. Liu, Q. Chen, W. Xue, H. Yang, J. Shang, B. Chen, F. Zeng, C. Song, F. Pan, and R. W. Li. Improving Unipolar Resistive Switching Uniformity with Cone Shaped Conducting Filaments and Its Logic-In-Memory Application. *ACS Appl. Mater. Interfaces*, 10(7):6453–6462, 2018. doi:10.1021/acsami.7b19586.

[171] H. K. Yoo, S. B. Lee, J. S. Lee, S. H. Chang, M. J. Yoon, Y. S. Kim, B. S. Kang, M. Lee, C. J. Kim, B. Kahng, and T. W. Noh. Conversion from unipolar to bipolar resistance switching by inserting Ta_2O_5 layer in Pt/TaO_x/Pt cells. *Appl. Phys. Lett.*, 98(18):183507/1–3, 2011. doi:10.1063/1.3587809.

[172] M. J. Yoon, S. B. Lee, H. K. Yoo, S. Sinn, and B. S. Kang. Dielectric-breakdown-like forming process in the unipolar resistance switching of Ta_2O_{5-x} thin films. *Curr. Appl. Phys.*, 12(3):846–848, 2012. doi:10.1016/j.cap.2011.11.017.

[173] Y. Sakotsubo, M. Terai, S. Kotsuji, Y. Saito, M. Tada, Y. Yabe, and H. Hada and. A new approach for improving operating margin of unipolar ReRAM using local minimum of reset voltage. *IEEE Symp. on VLSI Tech.*, page 87, 2010. doi:10.1109/IEDM.2010.5703391.

[174] X. Wu, P. Zhou, J. Li, L. Y. Chen, H. B. L. Y. Y. Lin, and T. A. Tang. Reproducible unipolar resistance switching in stoichiometric ZrO_2 films. *Appl. Phys. Lett.*, 90(18):183507/1–3, 2007. doi:10.1063/1.2734900.

[175] C. Lin and T. Lin. Superior unipolar resistive switching in stacked ZrO_x/ZrO_2/ZrO_x structure. *AIP Advances*, 6:035103, 2016. doi:10.1063/1.4943508.

[176] M. C. Wu, T. H. Wu, and T. Y. Tseng. Robust unipolar resistive switching of Co nano-dots embedded ZrO_2 thin film memories and their switching mechanism. *J. Appl. Phys.*, 111(1):14505/1–6, 2012. doi:10.1063/1.3674322.

[177] C. Lin, Y. Chang, H. Lin, and C. Lin. Effect of non-lattice oxygen on ZrO_2-based resistive switching memory. *Nanoscale Res. Lett.*, 7(1):187, 2012. doi:10.1186/1556-276X-7-187.

[178] F. Nardi, D. Ielmini, C. Cagli, S. Spiga, M. Fanciulli, L. Goux, and D. J. Wouters. Control of filament size and reduction of reset current below 10 μA in NiO resistance switching memories. *Solid-State Electron.*, 58(1):42–47, 2011. doi:10.1016/j.sse.2010.11.031.

[179] L. Goux, R. Degraeve, J. Meersschaut, B. Govoreanu, D. J. Wouters, S. Kubicek, and M. Jurczak. Role of the anode material in the unipolar switching of TiN\NiO\Ni cells. *J. Appl. Phys.*, 113, 2013. doi:10.1063/1.4790596.

[180] D. S. Jeong, H. Schröder, and R. Waser. Coexistence of bipolar and unipolar resistive switching behaviors in a Pt/TiO_2/Pt stack. *Electrochem. Solid State Lett.*, 10(8):G51–G53, 2007. doi:10.1149/1.2742989.

[181] K. J. Yoon, S. J. Song, J. Y. Seok, J. H. Yoon, G. H. Kim, J. H. Lee, and C. S. Hwang. Ionic bipolar resistive switching modes determined by the preceding unipolar resistive switching reset behavior in Pt/TiO_2/Pt. *Nanotechnology*, 24(14):145201/1–8, 2013. doi:10.1088/0957-4484/24/14/145201.

[182] Y. Yin Chen, G. Pourtois, C. Adelmann, L. Goux, B. Govoreanu, R. Degreave, M. Jurczak, J. A. Kittl, G. Groeseneken, and D. J. Wouters. Insights into Ni-filament formation in unipolar-switching Ni/HfO_2/TiN resistive random access memory device. *Appl. Phys. Lett.*, 100:113513, 2012. doi:10.1063/1.3695078.

[183] X. Tran, W. Zhu, W. Liu, Y. Yeo, B. Nguyen, and H. Yu. Self-selection unipolar HfO_x-Based RRAM. *IEEE Trans. Electron Devices*, 60(1):391–395, 2013. doi:10.1109/TED.2012.2223821.

[184] C. Schindler, S. C. P. Thermadam, R. Waser, and M. N. Kozicki. Bipolar and unipolar resistive switching in Cu-doped SiO_2. *IEEE Trans. Electron Devices*, 54(10):2762–2768, 2007. doi:10.1109/TED.2007.904402.

[185] W. Shen, R. Dittmann, and R. Waser. Reversible alternation between bipolar and unipolar resistive switching in polycrystalline barium strontium titanate thin films. *J. Appl. Phys.*, 107(9):94506/1–4, 2010. doi:10.1063/1.3369285.

[186] S. B. Lee, D. H. Kwon, K. Kim, H. K. Yoo, S. Sinn, M. Kim, B. Kahng, and B. S. Kang. Avoiding fatal damage to the top electrodes when forming unipolar resistance switching in nano-thick material systems. *J. Phys. D Appl. Phys.*, 45(25):255101/1–6, 2012. doi:10.1088/0022-3727/45/25/255101.

[187] T. Hennen, E. Wichmann, A. Elias, J. Lille, O. Mosendz, R. Waser, D. J. Wouters, and b) D. Bedau2. Current-limiting amplifier for high speed measurement of resistive switching data. https://arxiv.org/abs/2102.05770v1, 2021.

[188] L. Zhang, A. Janotti, A. C. Meng, K. Tang, C. G. Van de Walle, and P. C. McIntyre. Interfacial Cation-Defect Charge Dipoles in Stacked TiO_2/Al_2O_3 Gate Dielectrics. *ACS Appl. Mater. Interfaces*, 10(6):5140–5146, 2018. doi:10.1021/acsami.7b19619.

[189] I. G. Baek, M. S. Lee, S. Seo, M. J. Lee, D. H. Seo, D.-S. Suh, J. C. Park, S. 0. Park, H. S. Kim, I. K. Yoo, U.-I. Chung, and I. T. Moon. Highly Scalable Non-volatile Resistive Memory using Simple Binary Oxide Driven by Asymmetric Unipolar Voltage Pulses. *IEDM Technical Digest. IEEE International Electron Devices Meeting*, pages 587–590, 2004. doi:10.1109/IEDM.2004.1419228.

[190] Y. Hosoi, Y. Tamai, T. Ohnishi, K. Ishihara, T. Shibuya, Y. Inoue, S. Yarnazaki, T. Nakano, S. Ohnishi, N. Awaya, I. H. Inoue, H. Shima, H. Akinaga, H. Takagi, H. Akoh, and Y. Tokura. High speed unipolar switching resistance RAM (RRAM) technology. In *IEEE International Electron Devices Meeting, San Francisco, CA*, pages 547–550, 2006. doi:10.1109/IEDM.2006.346732.

[191] K. Tsunoda, K. Kinoshita, H. Noshiro, Y. Yarnazaki, T. Lizuka, Y. Ito, A. Takahashi, A. Okano, Y. Sato, T. Fukano, M. Aoki, and Y. Sugiyama. Low power and high speed switching of Ti-doped NiOReRAM under the unipolar voltage source of less than 3 V. In *IEEE International Electron Devices Meeting, Washington, DC*, pages 767–770, 2007. doi:10.1109/IEDM.2007.4419060.

[192] L. Zhang, R. Huang, M. Zhu, S. Qin, Y. Kuang, D. Gao, C. Shi, and Y. Wang. Unipolar TaO_x-Based Resistive Change Memory Realized With Electrode Engineering. *IEEE Electron Device Lett.*, 31:966–968, 2010. doi:10.1109/LED.2010.2052091.

[193] G. Kim, J. Lee, Y. Ahn, W. Jeon, S. Song, J. Seok, J. Yoon, K. Yoon, T. Park, and C. Hwang. 32×32 crossbar array resistive memory composed of a stacked schottky diode and unipolar resistive memory. *Advanced Functional Materials*, 23(11):1440–1449, 2013. doi:10.1002/adfm.201202170.

[194] C. Cagli, F. Nardi, and D. Ielmini. Modeling of Set/Reset Operations in NiO-Based Resistive Switching Memory devices. *IEEE Trans. Electron Devices*, 56(8):1712, 2009. doi:10.1109/TED.2009.2024046.

[195] J. P. Strachan, G. Medeiros-Ribeiro, J. J. Yang, M.-X. Zhang, F. Miao, I. Goldfarb, M. Holt, V. Rose, and R. S. Williams. Spectromicroscopy of tantalum oxide memristors. *Appl. Phys. Lett.*, 98(24):242114, 2011. doi:10.1063/1.3599589.

[196] T. Hennen, D. Bedau, J. A. J. Rupp, C. Funck, S. Menzel, M. Grobis, R. Waser, and D. J. Wouters. Forming-free Mott-oxide threshold selector nanodevice showing s-type NDR with high endurance ($> 10^{12}$ cycles), excellent Vth stability ($< 5\%$), fast (< 10 ns) switching, and promising scaling properties. In *2018 IEEE International Electron Devices Meeting (IEDM), 1-5 December 2018, San Francisco, USA*. IEEE, 2018. doi:10.1109/IEDM.2018.8614618.

[197] T. Hennen, D. Bedau, J. A. J. Rupp, C. Funck, S. Menzel, M. Grobis, R. Waser, and D. J. Wouters. Switching Speed Analysis and Controlled Oscillatory Behavior of a Cr-doped V_2O_3 Threshold Switching Device for Memory Selector and Neuromorphic Computing Application. *2019 Ieee 11th International Memory Workshop (IMW 2019)*, pages 44–47, 2019. doi:10.1109/IMW.2019.8739556.

[198] X. P. Wang, Y. Y. Chen, L. Pantisano, L. Goux, M. Jurczak, G. Groeseneken, and D. J. Wouters. Effect of anodic interface layers on the unipolar switching of HfO_2-based resistive RAM. In *Proceedings of 2010 International Symposium on VLSI Technology, System and Application*, pages 140–141, 2010. doi:10.1109/VTSA.2010.5488914.

[199] M. von Witzleben, E. Wichmann, C. Funck, K. Fleck, R. Waser, U. Böttger, T. Breuer, and S. Menzel. Thermal effects on the I-V characteristics of filamentary VCM based ReRAM-cells using a nanometer-sized heater. In *2017 17th Non-Volatile Memory Technology Symposium (NVMTS), Aachen, Germany, August 30 - September 01, 2017*, pages 1–5, 2017. doi:10.1109/NVMTS.2017.8171313.

[200] J. J. Ke, K. Namura, J. R. D. Retamal, C. H. Ho, H. Minamitake, T. C. Wei, D. S. Tsai, C. H. Lin, M. Suzuki, and J. H. He. Surface-Controlled Metal Oxide Resistive Memory. *IEEE Electron Device Lett.*, 36(12):1307–1309, 2015. doi:10.1109/LED.2015.2493343.

[201] D. B. Strukov, F. Alibart, and R. S. Williams. Thermophoresis/diffusion as a plausible mechanism for unipolar resistive switching in metal-oxide-metal memristors. *Appl. Phys. A Mater. Sci. Process.*, 107(3):509–518, 2012. doi:10.1007/s00339-012-6902-x.

[202] E. Ambrosi, A. Bricalli, M. Laudato, and D. Ielmini. Impact of oxide and electrode materials on the switching characteristics of oxide ReRAM devices. *Faraday Discuss.*, 213:87–98, 2019. doi:10.1039/c8fd00106e.

[203] I. Kärkkänen, A. Shkabko, M. Heikkilä, J. Niinistö, M. Ritala, M. Leskelä, S. Hoffmann-Eifert, and R. Waser. Study of atomic layer deposited ZrO_2 and ZrO_2/TiO_2 films for resistive switching application. *Phys. Status Solidi A-Appl. Mat.*, 211(2):301–309, 2014. doi:10.1002/pssa.201330034.

[204] C.-Y. Lin, C.-Y.Wu, C.-Y. Wu, T.-C. Lee, F.-L. Yang, C. Hu, and T.-Y. Tseng. Effect of Top Electrode Material on Resistive Switching Properties of ZrO_2 Film Memory Devices. *IEEE Electron Device Lett.*, 28(5):366–368, 2007. doi:10.1109/LED.2007.894652.

[205] J. McPherson, J. Kim, A. Shanware, and H. Mogul. Thermochemical description of dielectric breakdown in high dielectric constant materials. *Appl. Phys. Lett.*, 82(13):2121–2123, 2003. doi:10.1063/1.1565180.

[206] K. Jung, S. Song, K. Park, J. Sok, K. Kim, and Y. Park. Observation of AlO_x material in electrical resistive switching for nonvolatile random access memory application. *J. Kor. Phys. Soc*, 70(5):489–493, 2017. doi:10.3938/jkps.70.489.

[207] J. W. Wang, L.P. Shi, R. Zhao, K. G. Lim, H. K. Lee, T. C. Chong, and Y. H. Wu and. Fast phase transitions induced by picosecond electrical pulses on phase change memory cells. *Appl. Phys. Lett.*, 93(4):043121, 2008. doi:10.1063/1.2963196.

[208] G. Bruns, P. Merkelbach, C. Schlockermann, M. Salinga, M. Wuttig, T. D. Happ, J. B. Philipp, and M. Kund. Nanosecond switching in GeTe phase change memory cells. *Appl. Phys. Lett.*, 95(4):43108/1–3, 2009. doi:10.1063/1.3191670.

[209] W. Wang, D. Loke, L. Shi, R. Zhao, H. Yang, L. Law, L. Ng, K. Lim, Y. Yeo, T. Chong, and A. L. Lacaita. Enabling Universal Memory by Overcoming the Contradictory Speed and Stability Nature of Phase-Change Materials. *Sci. Rep.*, 2(1):360, 2012. doi:10.1038/srep00360.

[210] D. Lencer, M. Salinga, and M. Wuttig. Design Rules for Phase-Change Materials in Data Storage Applications. *Advanced Materials*, 23(18):2030–2058, 2011. doi:10.1002/adma.201004255.

[211] M. Salinga, E. Carria, A. Kaldenbach, M. Bornhöfft, J. Benke, J. Mayer, and M. Wuttig. Measurement of crystal growth velocity in a melt-quenched phase-change material. *Nature Communications*, 4:2371/1–, 2013. doi:10.1038/ncomms3371.

[212] S. Wiefels, C. Bengel, N. Kopperberg, K. Zhang, R. Waser, and S. Menzel. HRS Instability in Oxide based Bipolar Resistive Switching Cells. *IEEE Trans. Electron Devices*, 67(10):4208–4215, 2020. doi:10.1109/TED.2020.3018096.

[213] T. Ohno, T. Hasegawa, T. Tsuruoka, K. Terabe, J. K. Gimzewski, and M. Aono. Short-term plasticity and long-term potentiation mimicked in single inorganic synapses. *Nat. Mater.*, 10:591–595, 2011. doi:10.1038/nmat3054.

[214] R.C. Atkinson and R.M. Shiffrin. *Human Memory: A Proposed System and its Control Processes*, volume 2, pages 89–195. Academic Press, 1968. doi:10.1016/S0079-7421(08)60422-3.

[215] R. Yang, K. Terabe, Y. Yao, T. Tsuruoka, T. Hasegawa, J. K. Gimzewski, and M. Aono. Synaptic plasticity and memory functions achieved in a WO_{3-x}-based nanoionics device by using the principle of atomic switch operation. *Nanotechnology*, 24(38):384003, 2013. doi:10.1088/0957-4484/24/38/384003.

[216] S. Kim, C. Du, P. Sheridan, W. Ma, S. Choi, and W. D. Lu. Experimental Demonstration of a Second-Order Memristor and Its Ability to Biorealistically Implement Synaptic Plasticity. *Nano Letters*, 15:2203–2211, 2015. doi:10.1021/acs.nanolett.5b00697.

[217] A. Nayak, T. Ohno, T. Tsuruoka, K. Terabe, T. Hasegawa, J. K. Gimzewski, and M. Aono. Controlling the Synaptic Plasticity of a Cu_2S Gap-Type Atomic Switch. *Advanced Functional Materials*, 22(17):3606–3613, 2012. doi:10.1002/adfm.201200640.

[218] M. Ignatov, M. Ziegler, M. Hansen, and H. Kohlstedt. Memristive stochastic plasticity enables mimicking of neural synchrony: Memristive circuit emulates an optical illusion. *Sci. Adv.*, 3(10):e1700849, 2017. doi:10.1126/sciadv.1700849.

[219] M. Lübben, F. Cüppers, J. Mohr, M. von Witzleben, U. Breuer, R. Waser, C. Neumann, and I. Valov. Design of defect-chemical properties and device performance in memristive systems. *Sci. Adv.*, 6(19):eaaz9079/1–10, 2020. doi:10.1126/sciadv.aaz9079.

[220] A. Sengupta and K. Roy. Short-Term Plasticity and Long-Term Potentiation in Magnetic Tunnel Junctions: Towards Volatile Synapses. *Phys. Rev. Applied*, 5:024012, 2016. doi:10.1103/PhysRevApplied.5.024012.

[221] H. Hwang, J. Woo, T. Lee, S. Park, T. Lee, W. Lee, and S. Nahm. Synaptic plasticity and preliminary-spike-enhanced plasticity in a CMOS-compatible Ta_2O_5 memristor. *Mater. Des.*, 187:108400, 2020. doi:10.1016/j.matdes.2019.108400.

[222] V. Kornijcuk, O. Kavehei, H. Lim, J. Y. Seok, S. K. Kim, I. Kim, W.-S. Lee, B. J. Choi, and D. S. Jeong. Multiprotocol-induced plasticity in artificial synapses. *Nanoscale*, page in press, 2014. doi:10.1039/C4NR03405H.

[223] X. Zhang, S. Liu, X. Zhao, F. Wu, Q. Wu, W. Wang, R. Cao, Y. Fang, H. Lv, S. Long, Q. Liu, and M. Liu. Emulating Short-Term and Long-Term Plasticity of Bio-Synapse Based on Cu/a-Si/Pt Memristor. *IEEE Electron Device Lett.*, 38(9):1208–1211, 2017. doi:10.1109/LED.2017.2722463.

[224] N. Wainstein, G. Adam, E. Yalon, and S. Kvatinsky. Radiofrequency Switches Based on Emerging Resistive Memory Technologies - A Survey. *Proceedings of the IEEE*, 109(1):77–95, 2021. doi:10.1109/JPROC.2020.3011953.

[225] R. Ge, X. Wu, M. Kim, J. Shi, S. Sonde, L. Tao, Y. Zhang, J. C. Lee, and D. Akinwande. Atomristor: Nonvolatile Resistance Switching in Atomic Sheets of Transition Metal Dichalcogenides. *Nano Letters*, 18(1):434–441, 2018. doi:10.1021/acs.nanolett.7b04342.

[226] Nabil El-Hinnawy, Pavel Borodulin, Brian P. Wagner, Matthew R. King, John S. Mason, Evan B. Jones, Victor Veliadis, Robert S. Howell, Robert M. Young, and Michael J. Lee. A 7.3 THz Cut-Off Frequency, Inline, Chalcogenide Phase-Change RF Switch Using an Independent Resistive Heater for Thermal Actuation. In *2013 IEEE Compound Semiconductor Integrated Circuit Symposium (CSICS)*, pages 1–4. IEEE, 2013. doi:10.1109/CSICS.2013.6659195.

[227] N. Wainstein and S. Kvatinsky. TIME—Tunable Inductors Using MEmristors. *IEEE Trans. Circuits Syst. I Regul. Pap.*, 65(5):1505–1515, 2018. doi:10.1109/TCSI.2017.2760625.

[228] J. A. Nessel, R. Q. Lee, C. H. Mueller, M. N. Kozicki, M. Ren, and J. Morse. A Novel Nanoionics-based Switch for Microwave Applications. In *2008 IEEE Mtt-S International Microwave Symposium Digest, Vols 1-4*, pages 1312–1315, 2008. doi:10.1109/MWSYM.2008.4633016.

[229] A. Vena, E. Perret, S. Tedjini, C. Vallée, P. Gonon, and C. Mannequin. A fully passive RF switch based on nanometric conductive bridge. In *2012 IEEE/MTT-S International Microwave Symposium Digest*, pages 1–3, 2012. doi:10.1109/MWSYM.2012.6258428.

[230] S. Pi, M. Ghadiri-Sadrabadi, J. C. Bardin, and Q. Xia. Nanoscale memristive radiofrequency switches. *Nat. Commun.*, 6(1):7519, 2015. doi:10.1038/ncomms8519.

[231] Michael Lübben. Redox Processes at Interfaces and Ionic Motion in Resistively Switching Materials. Phd thesis, RWTH Aachen University, 2020.

[232] A. Roy and P. Cha. Electric field induced charge migration and formation of conducting filament during resistive switching in electrochemical metallization (ECM) memory cells. *J. Appl. Phys.*, 128:205102, 2020. doi:10.1063/5.0026350.

[233] Sergej Starschich. Ferroelectric, Pyroelectric and Piezoelectric Effects of Hafnia and Zirconia Based Thin Films. Phd thesis, RWTH Aachen University, 2017. doi:10.18154/RWTH-2017-10511.

[234] X. Lyu, M. Si, P. R. Shrestha, K. P. Cheung, and P. D. Ye. First Direct Measurement of Sub-Nanosecond Polarization Switching in Ferroelectric Hafnium Zirconium Oxide. In *2019 IEEE International Electron Devices Meeting (IEDM)*, pages 15.2.1–15.2.4. IEEE, 2019. doi:10.1109/IEDM19573.2019.8993509.

Appendix

A. Fabrication protocols

On the following pages, the protocols describing the fabrication procedure of the Ta1, Ta2, HfAx, and HfBx devices (see tab. 3.1) can be found. The Ta1 and Ta2 device's protocol has been written by Alfred Steffen and the one of the HfAx and HfBx device by Alexander Hardtdegen.

Protokoll: 10a A.Steffen 13.10.2014

LITHO CPW

Von:	A.Steffen
Für:	Victor Havel (IWE-II) Tel.: 0241-802-7829, Dr. Vikas Rana (PGI-7)
Lithographie:	**Bottom Electrode** Positivprozess mit AZ 6632-1.2
Probenname:	# 014. BE-Test
Proben:	1“x 1“ Siliziumwafer, oxidiert ~ 450nm, 5 nm Ti u. 30 nm Pt gesputtert
Reinigung:	Entfernung Schutzlack (Säge): Aceton (Ultraschall: Zeit 5 min, Power Stufe 1) Propanol (Ultraschall: Zeit 5 min, Power Stufe 1) Plasma 300W, 10 min, Sauerstoff (Tepla 300)
Belackung:	Resist AZ 6632-1.2 0,5 ml Resist mittels Eppendorf-Pipette Spinner: Prog. C-RCP-4 (4000 U/min, mit Vorbeschleunigung zur Lackverteilung)
Trocknen:	5 min, 90 °C, Heizplatte vorne links (Einstellwert 85°C)
Belichten:	Maskaligner Süss MA 6 Constant Power Mode 350 W, (Intensity ~10 mW/cm²) Vacuum Contact Mode Exposure time 25 sec
Maske:	CPW-V01-20130710_L1 (Bottom Electrode)
Entwickeln:	120 sec in AZ 326 MIF bei Raumtemperatur kräftig bewegen!
Stoppen:	5 min in Reinstwasser
Ätzen BE:	IBE (René B.)
Entfernung Resist:	Plasma 600W, 30 min, Sauerstoff (Tepla 300)
Entfernung „fences“:	mittels SWAP unter Propanol abreiben

Lithographie:	**Oxid**
Beschichtung Oxid:	5 nm TaOx von IWE RWTH-Aachen
Belackung:	Resist AZ 5214E 0,5 ml Resist mittels Eppendorf-Pipette Spinner: Prog. C-RCP-4 (4000 U/min, mit Vorbeschleunigung zur Lackverteilung)
Trocknen:	5 min, 90 °C, Heizplatte vorne links (Einstellwert 85°C)
Rehydrierung:	mind. 1 Stunde
Belichten:	Maskaligner Süss MA 6 Constant Power Mode 350 W, (Intensity ~10 mW/cm²) Vacuum Contact Mode Exposure time 25 sec
Maske:	CPW-V01-20130710_L1 (Oxid)
Entwickeln:	120 sec in AZ 326 MIF bei Raumtemperatur kräftig bewegen!
Stoppen:	5 min in Reinstwasser
RIBE Ätzen:	von TaOx (R. Borowski) CF_4@0^0; t: 1 min
Entfernung Lack:	nach IBE Ätzung DMSO 90°C, 1 h über Nacht in DMSO legen 5 min mit DI spülen Plasma 600W, 30 min, Sauerstoff (Tepla 300)

Lithographie:	**Top Electrode**
Prozess:	Lift-Off Prozess Umkehrprozess mit AZ 5214E
Probenname:	# 014-CPW-RF-Test
Belackung:	Resist AZ 5214E 0,5 ml Resist mittels Eppendorf-Pipette Spinner: Prog. C-RCP-4 (4000 U/min, mit Vorbeschleunigung zur Lackverteilung)
Trocknen:	5 min, 90 °C, Heizplatte vorne links (Einstellwert 85°C)
Rehydrierung:	mind. 1 Stunde
Maske:	CPW-V01-20130710_L1 (TE)
Belichten:	Maskaligner Süss MA 6 Constant Power Mode 350 W, (Intensity ~10 mW/cm²) Vacuum Contact Mode Exposure time 10 sec
Umkehrbacken:	60 sec, 120 °C, Heizplatte, 3 min abkühlen
Rehydrierung:	mind.1 Stunde
Flutbelichtung:	Maskaligner Süss MA/BA 6 Constant Power Mode 350 W LAMP TEST MODE Exposure Time 60 sec
Entwickeln:	90 sec in AZ 326 MIF
Stoppen:	5 min in Reinstwasser
Trocknen:	mit Stickstoff abblasen

Metallisierung Top Electrode

Deposition:	Elektronenstrahlverdampfung 30 nm Titan (2 Å/s) 100 nm Platin (3 Å/s)
Lift-Off:	60 min in Technistrip Micro D350 (DMSO) bei 90°C und über Nacht in Technistrip Micro D350 (DMSO) stehen lassen
Spülen:	min. 5 min in Reinstwasser

Fertig!!!!!

Probe: CPW_HOTO_1

Goals: CPW-Microstructures for ps-pulse measurements by M. von Witzleben, 1" x 1"

MASK: CPW Small v1.3 2018

Layer stack: 5 nm Ti / 25 nm Pt / 3 nm HfO2 / 3 nm TiO2 / 10 nm Ti / 20 nm Pt

Nr.	Process step	Parameters	Comment/Operator	Date
1	Cleaning: thermal oxidized Si substrate	2x Aceton (AC) 5 min; US intensity 1 Isoprpanol (IP) 5 min; US intensity 1 drying with nitrogen gas pistole O2 plasma 30 min 600 W	Alexander Hardtdegen	17.04.19
2	BE metal sputtering	5 nm Ti, 25 nm Pt @ UVEX Tool	René Borowski	17.04.19
3	Belackung BE Litho	Resist: AZ 5214E Spinner: C-RCP-4 (4000 U/min) Trocken: Heizplatte unten links, 5 min @ 90°C	Stephan Aussen, Alexander Hardtdegen	30.04.19
4	Belichtung BE Litho	Maskaligner Süss MA 6 Constant Power Mode, 350 W Vacuum Contact Mode Exposure Time: 25 s (intensity: 2.2 mW/cm²) MASK: CPW Small B (Ganz rechts)	Stephan Aussen, Alexander Hardtdegen	30.04.19
5	Development BE Litho	AZ 326 MIF @ RT; 70 sec (kräftig bewegen)! stopped in water (overflow rinse) drying with nitrogen gas pistole	Stephan Aussen, Alexander Hardtdegen	30.04.19
6	Control BE Litho	NIKON Microscope	Stephan Aussen, Alexander Hardtdegen	30.04.19
7	RIBE Etching for BE	Ar@-10°: 120 s Ar@-50°:30 s (Fence reduction) Ar @0°: 86 s; Pt etching	Stephan Aussen	02.05.19
8	Resist Removal BE Litho	DMSO @ 80 °C 3h, Wasser abspülen Aceton Swab 2 min Isoprop. Spülen 5 min Kontrolle im NIKON	Stephan Aussen	03.05.19
9	ALD Oxide Deposition	3 nm HfO2 Plasma @ 300 °C Run No. 1348 3 nm TiO2 Thermal @ 300 °C Run No. 1349 FlexAL @ Nanocluster	Alexander Hardtdegen	09.05.19
10	Belackung Oxidätzung	Resist: AZ 5214E Spinner: C-RCP-4 (4000 U/min) Trocknen: Heizplatte unten links, 5 min @ 90°C	Alexander Hardtdegen / Stephan Außen	14.05.19
11	Belichtung Oxidätzung	Maskaligner Süss MA 6 Constant Power Mode, 350 W Vacuum Contact Mode Exposure Time: 25s (intensity: 2.2 mW/cm²) MASK: CPW Small Ox (Mitte)	Alexander Hardtdegen / Stephan Außen	14.05.19
12	Development Oxidätzun	AZ 326 MIF @ RT; 70 sec (kräftig bewegen)! stopped in water (overflow rinse) drying with nitrogen gas pistole	Alexander Hardtdegen / Stephan Außen	14.05.2019
13	RIBE Oxidätzung		Stephan Außen	15.05.2019
14	Resist Removal Oxidätzung	DMSO @ 80 °C 3h, Wasser abspülen Aceton Swab 2 min Isoprop. Spülen 5 min Kontrolle im NIKON	Stephan Außen	15.05.2019
15	Belackung TE Liftoff	Resist: AZ 5214E Spinner: C-RCP-4 (4000 U/min) Trocken: Heizplatte unten links, 5 min @ 90°C	Alexander Hardtdegen	22.05.2019
16	Belichtung TE Liftoff	Maskaligner Süss MA 6 Constant Power Mode, 350 W Vacuum Contact Mode Exposure Time: 10 s (intensity: 2.2 mW/cm²) MASK: CPW Small B (Ganz rechts)	Alexander Hardtdegen	22.05.2019
17	Umkehrbacken	60 s @ 120 °C (vorne rechts)	Alexander Hardtdegen	22.05.2019
18	Flutbelichtung	60s, MA/BA 60 (360W), Lamp test mode	Alexander Hardtdegen	22.05.2019
19	Development TE Liftoff	AZ 326 MIF @ RT; 90 sec (kräftig bewegen)! stopped in water (overflow rinse) drying with nitrogen gas pistole	Alexander Hardtdegen	22.05.2019
20	TE Evaporation	10 nm Ti + 20 nm Pt	René Borowski	22.05.2019
21	Lifoff	Aceton US Bad St. 5. Trocknen mit N2		22.05.2019
22	Kontrolle	NIKON		22.05.2019

Probe: CPW_HOTO_1

Goals: CPW-Microstructures for ps-pulse measurements by M. von Witzleben, 1" x 1"

MASK: CPW Small v1.3 2018

Layer stack: 5 nm Ta / 25 nm Pt / 3 nm HfO2 / 3 nm TiO2 / 10 nm Ti / 20 nm Pt

Nr.	Process step	Parameters	Comment/Operator	Date
1	Cleaning: thermal oxidized Si substrate	2x Aceton (AC) 5 min; US intensity 1 Isoprpanol (IP) 5 min; US intensity 1 drying with nitrogen gas pistole O2 plasma 30 min 600 W	Alexander Hardtdegen	10.07.19
2	BE metal sputtering	5 nm Ta, 25 nm Pt @ M6 NC	Stephan Aussen	11.07.19
3	Belackung BE Litho	Resist: AZ 5214E Spinner: C-RCP-4 (4000 U/min) Trocken: Heizplatte unten links, 5 min @ 90°C	Alexander Hardtdegen	15.07.19
4	Belichtung BE Litho	Maskaligner Süss MA 6 Constant Power Mode, 350 W Vacuum Contact Mode Exposure Time: 25 s (intensity: 2.2 mW/cm²) MASK: CPW Small B (Ganz rechts)	Alexander Hardtdegen	15.07.19
5	Development BE Litho	AZ 326 MIF @ RT; 90 sec (kräftig bewegen)! stopped in water (overflow rinse) drying with nitrogen gas pistole	Alexander Hardtdegen	15.07.19
6	Control BE Litho	NIKON Microscope	Alexander Hardtdegen	15.07.19
7	RIBE Etching for BE	Ar@-10°: 120 s Ar@-50°:30 s (Fence reduction) Ar @0°: 86 s; Pt etching	René Borowski	15.07.19
8	Resist Removal BE Litho	DMSO @ 80 °C 2h, Wasser abspülen Aceton Swab 2 min Isoprop. Spülen 5 min Kontrolle im NIKON	Alexander Hardtdegen	15.07.19
9	ALD Oxide Deposition	3 nm HfO2 Plasma @ 300 °C Run No. 1348 2.7 nm (XRR, 18.7.19, FC + StA) 3 nm TiO2 Thermal @ 300 °C Run No. 1349 3.4 nm (XRR, 18.7.19, FC+StA) FlexAL @ Nanocluster, Run 1485+1485	Alexander Hardtdegen	17.07.19
10	Belackung Oxidätzung	Resist: AZ 5214E Spinner: C-RCP-4 (4000 U/min) Trocknen: Heizplatte unten links, 5 min @ 90°C	Alexander Hardtdegen / Stephan Außen	17.07.19
11	Belichtung Oxidätzung	Maskaligner Süss MA 6 Constant Power Mode, 350 W Vacuum Contact Mode Exposure Time: 25s (intensity: 2.2 mW/cm²) MASK: CPW Small Ox (Mitte)	Alexander Hardtdegen / Stephan Außen	17.07.19
12	Development Oxidätzun	AZ 326 MIF @ RT; 70 sec (kräftig bewegen)! stopped in water (overflow rinse) drying with nitrogen gas pistole	Alexander Hardtdegen / Stephan Außen	17.07.2019
13	RIBE Oxidätzung		René Borowski	17.07.2019
14	Resist Removal Oxidätzung	DMSO @ 80 °C 2h, Wasser abspülen Aceton Swab 2 min Isoprop. Spülen 5 min Kontrolle im NIKON	Stephan Außen	18.07.2019
15	Belackung TE Liftoff	Resist: AZ 5214E Spinner: C-RCP-4 (4000 U/min) Trocken: Heizplatte unten links, 5 min @ 90°C	Alexander Hardtdegen	18.07.2019
16	Belichtung TE Liftoff	Maskaligner Süss MA 6 Constant Power Mode, 350 W Vacuum Contact Mode Exposure Time: 10 s (intensity: 2.2 mW/cm²) MASK: CPW Small B (Ganz rechts)	Alexander Hardtdegen	18.07.2019
17	Umkehrbacken	60 s @ 120 °C (vorne rechts)	Alexander Hardtdegen	18.07.2019
18	Flutbelichtung	60s, MA/BA 60 (360W), Lamp test mode	Alexander Hardtdegen	18.07.2019
19	Development TE Liftoff	AZ 326 MIF @ RT; 90 sec (kräftig bewegen)! stopped in water (overflow rinse) drying with nitrogen gas pistole	Alexander Hardtdegen	18.07.2019
20	TE Evaporation	10 nm Ti + 20 nm Pt	René Borowski	18.07.2019
21	Lifoff	Aceton US Bad St. 5. Trocknen mit N2		22.07.2019
22	Kontrolle	NIKON	Alexander Hardtdegen: Good alignment row 1-8, bad > 9	22.07.2019

B. LRS values of the SET kinetics

In this section, the distributions of the LRS values are shown, which were measured during the automated SET kinetic measurements in chapter 4.2, in which usually the distribution of the ratio $R_{\mathrm{LRS}}/R_{\mathrm{HRS}}$ was shown instead. The ratio $R_{\mathrm{LRS}}/R_{\mathrm{HRS}}$ does not yield any information on the absolute LRS values, which are, therefore, shown on the following pages.

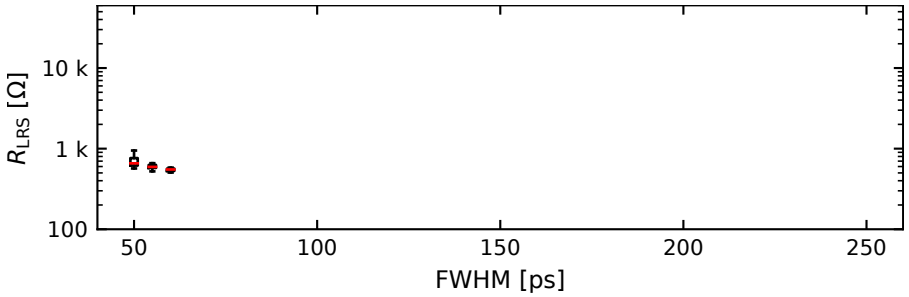

(a) Zr1 device, $V_P = -1.6\,V$.

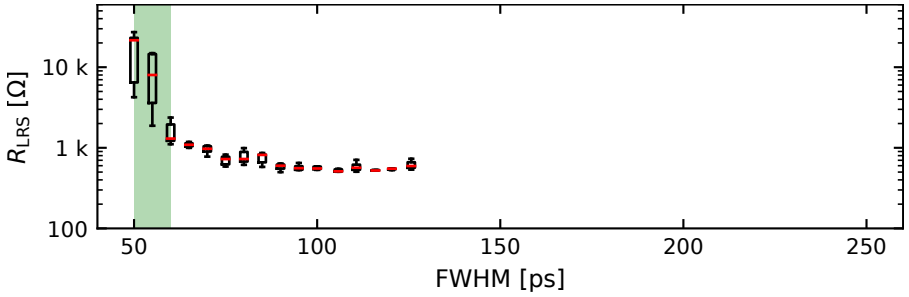

(b) Zr1 device, $V_P = -1.1\,V$.

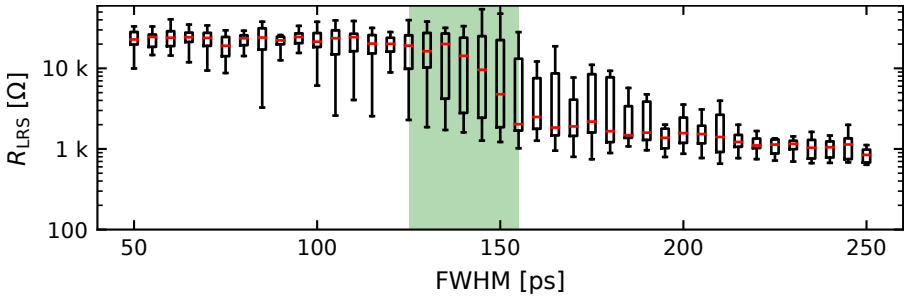

(c) Zr1 device, $V_P = -0.8\,V$.

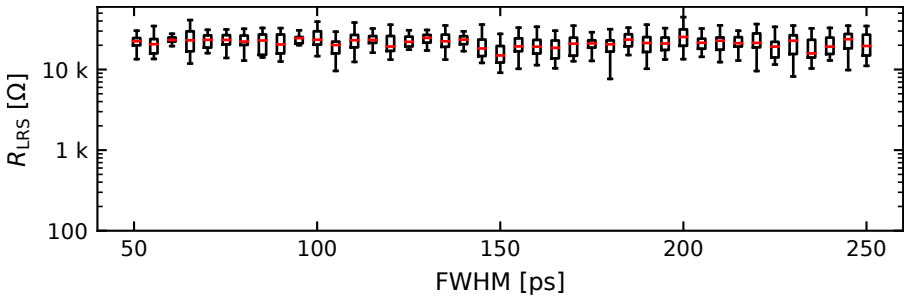

(d) Zr1 device, $V_P = -0.5\,V$.

Figure B.1.: SET kinetics of the Zr1 device (see table 3.1) representing the LRS values. The data set is identical to the one from fig. 4.6. The green shaded areas in (b) and (c) mark the transition time (80 %-20 %). The red bar in the boxplot marks the median. Reprinted from [38], with the permission of AIP Publishing.

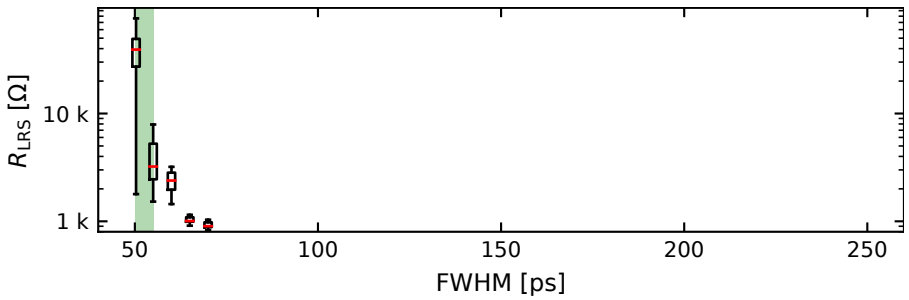

(a) HfA2 device, $V_P = -2.5\,V$.

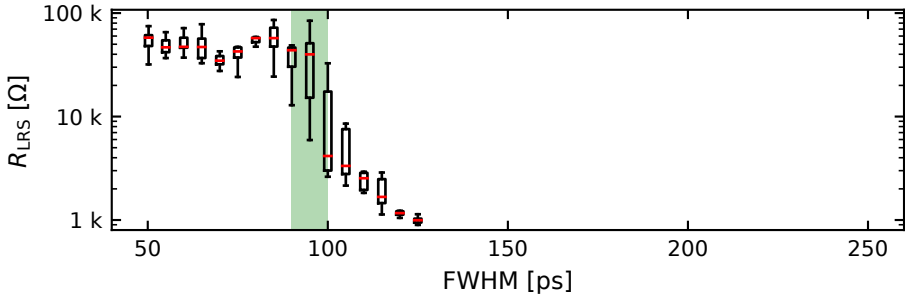

(b) HfA2 device, $V_P = -1.6\,V$.

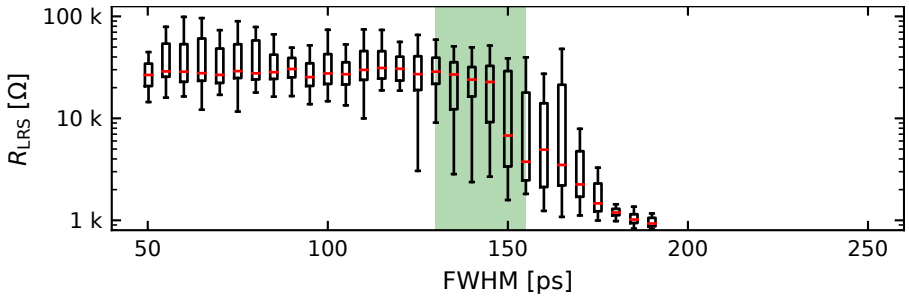

(c) HfA2 device, $V_P = -1.1\,V$.

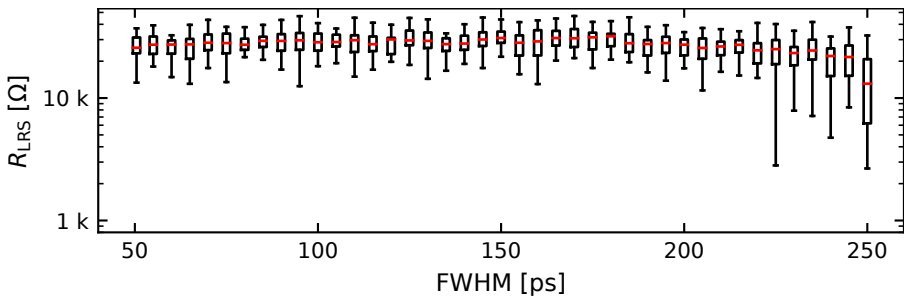

(d) HfA2 device, $V_P = -0.8\,V$.

Figure B.2.: SET kinetics of the HfA2 device (see table 3.1) representing the LRS values. The data set is identical to the one from fig. 4.15. The green shaded areas in (b) and (c) mark the transition time (80 %-20 %). The red bar in the boxplot marks the median.

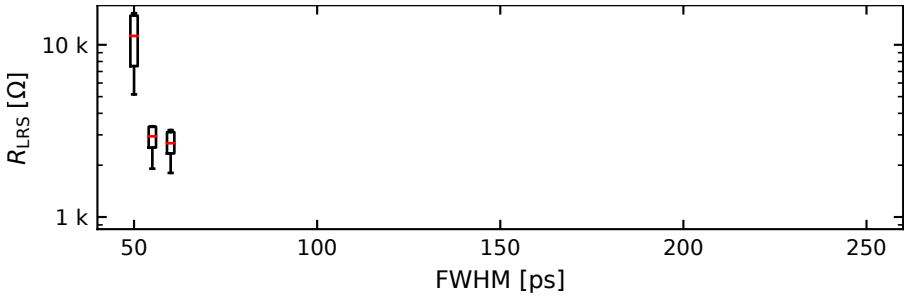

(a) HfB1 device, $V_P = -2.5\,V$.

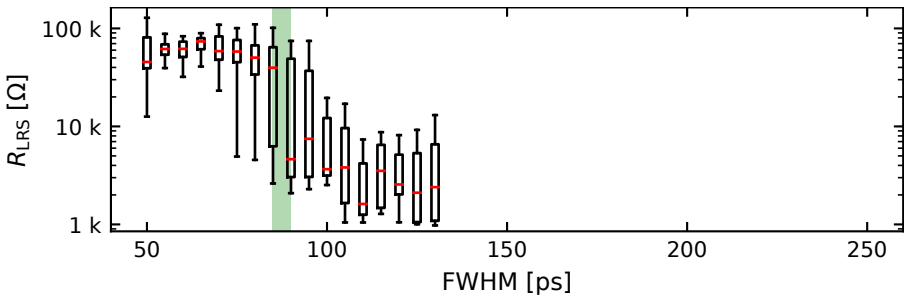

(b) HfB1 device, $V_P = -1.6\,V$.

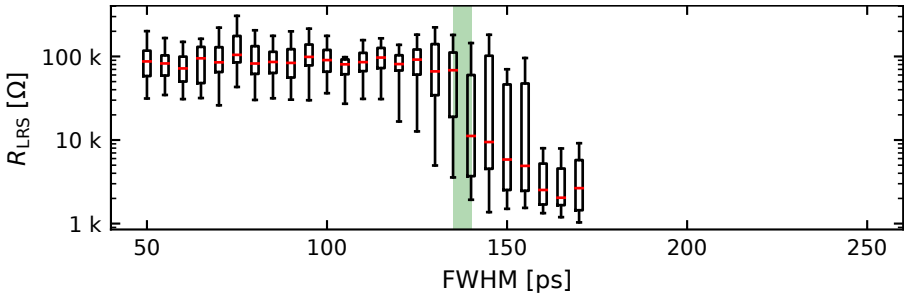

(c) HfB1 device, $V_P = -1.1\,V$.

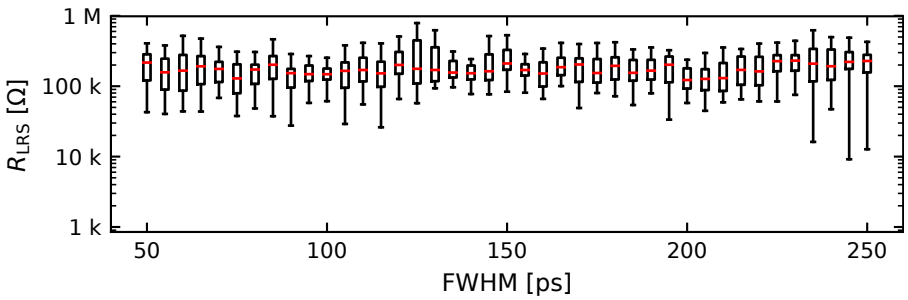

(d) HfB1 device, $V_P = -0.8\,V$.

Figure B.3.: SET kinetics of the HfB1 device (see table 3.1) representing the LRS values. The data set is identical to the one from fig. 4.16. The green shaded areas in (b) and (c) mark the transition time (80 %-20 %). The red bar in the boxplot marks the median.

C. POST values of the RESET kinetics

In this section, the distributions of the POST resistance R_{POST} values are shown, which were measured during the automated RESET kinetic measurements in chapter 5, in which the distribution of the ratio $R_{\mathrm{POST}}/R_{\mathrm{PRE}}$ was shown instead. The PRE resistance value R_{PRE} was read before the application of the pulse and the POST resistance value R_{POST} after its application. The ratio $R_{\mathrm{POST}}/R_{\mathrm{PRE}}$ does not yield any information on the absolute POST resistance values, which are, therefore, shown on the following pages.

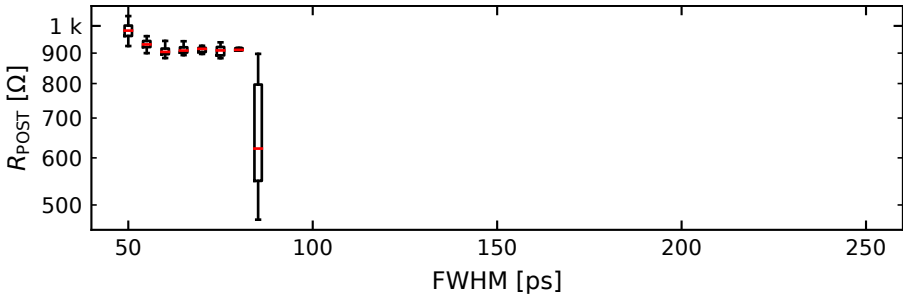

(a) Ta3 device, $V_{\mathrm{P}} = 2.5\,\mathrm{V}$.

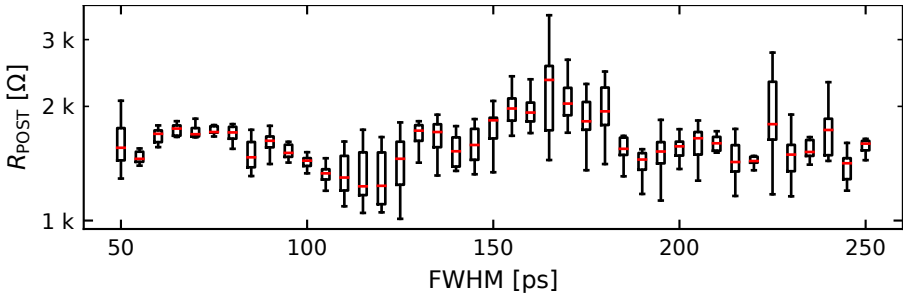

(b) Ta3 device, $V_{\mathrm{P}} = 1.6\,\mathrm{V}$.

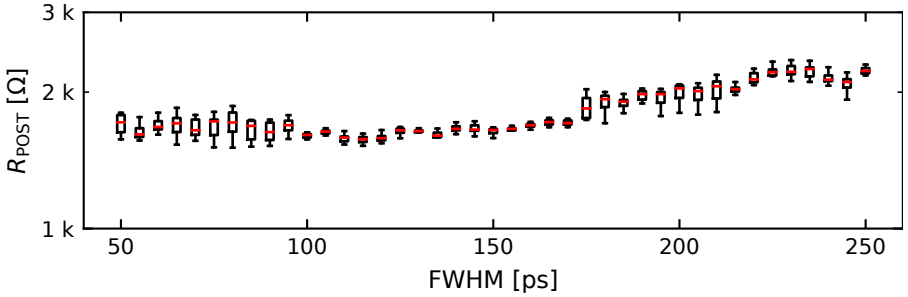

(c) Ta3 device, $V_{\mathrm{P}} = 1.1\,\mathrm{V}$.

Figure C.1.: Regular RESET kinetics of the Ta3 device (see table 3.1), representing the POST resistance values R_{POST}. The data set is identical to the one from fig. 5.6. The red bar in the boxplot marks the median.

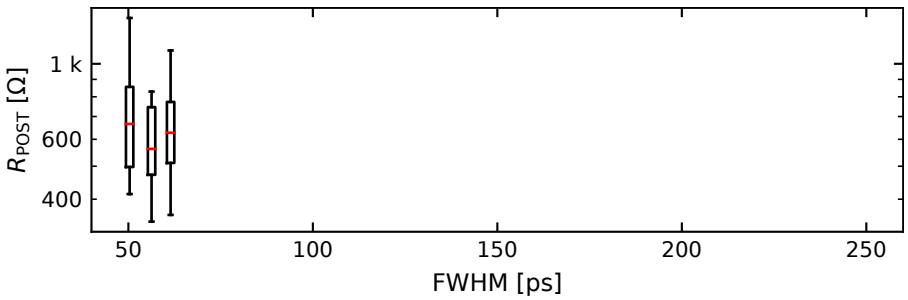

(a) Zr1 device, $V_P = 2.5\,V$.

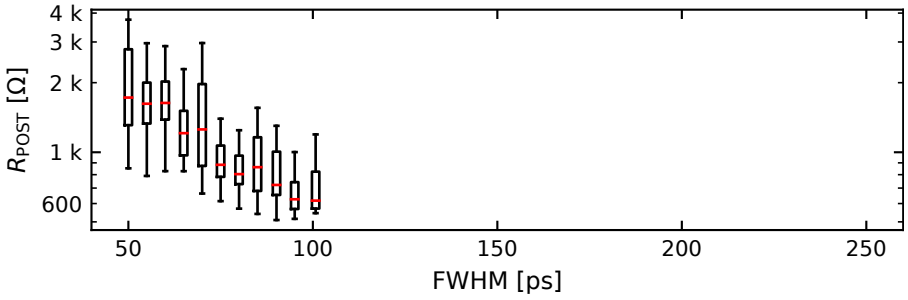

(b) Zr1 device, $V_P = 1.6\,V$.

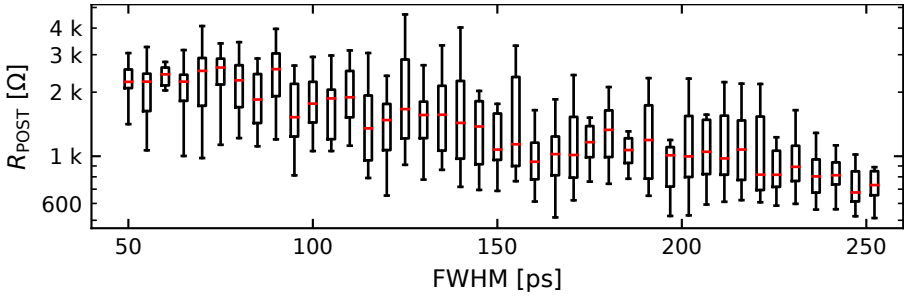

(c) Zr1 device, $V_P = 1.1\,V$.

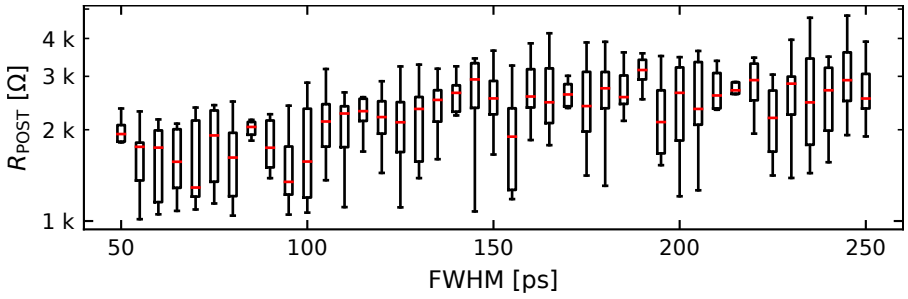

(d) Zr1 device, $V_P = 0.8\,V$.

Figure C.2.: Regular RESET kinetics of the Zr1 device (see table 3.1), representing the POST resistance values R_{POST}. The data set is identical to the one from fig. 5.7. The red bar in the boxplot marks the median.

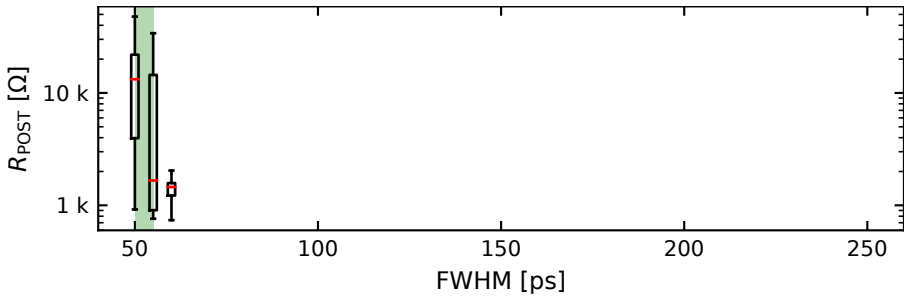

(a) Ta3 device, $V_P = 2.5\,V$.

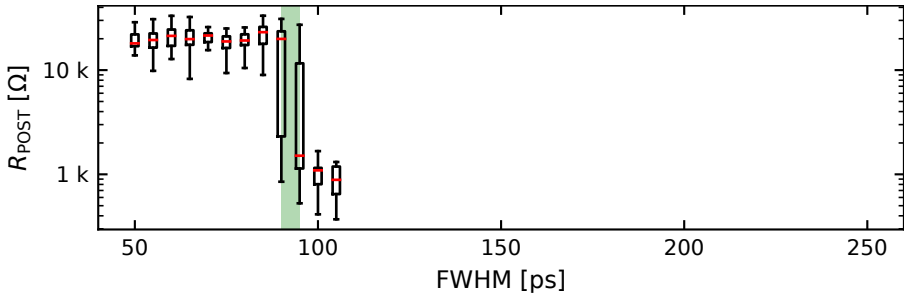

(b) Ta3 device, $V_P = 1.6\,V$.

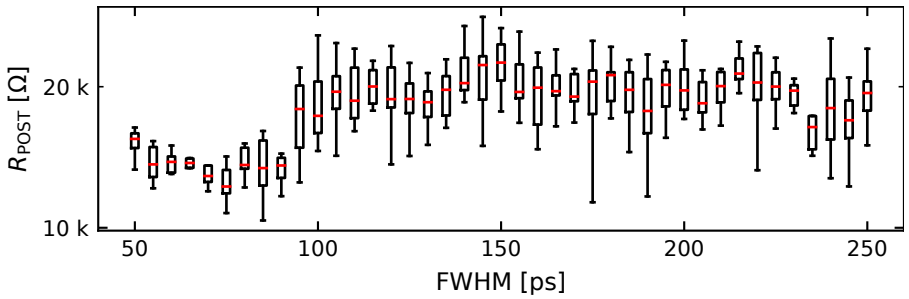

(c) Ta3 device, $V_P = 1.1\,V$.

Figure C.3.: POST resistance values R_{POST} of the Ta3 device's (see table 3.1) unipolar SET kinetics, during which positive voltage pulses were applied to the Pt bottom electrode. The data set is identical to the one from fig. 5.9. The green shaded areas in (a) and (b) mark the transition time (80 %-20 %). The red bar in the boxplot marks the median.

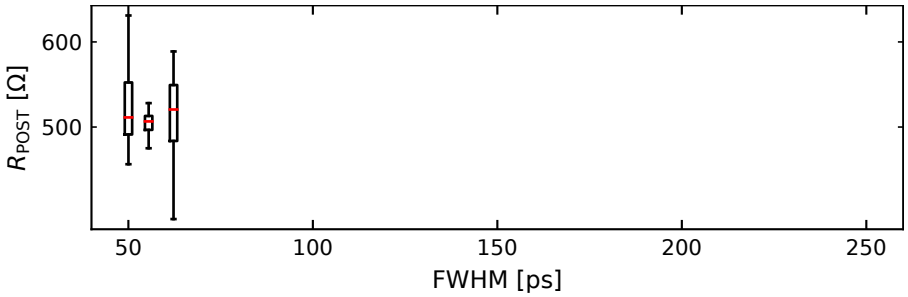

(a) Zr1 device, $V_P = 2.5\,V$.

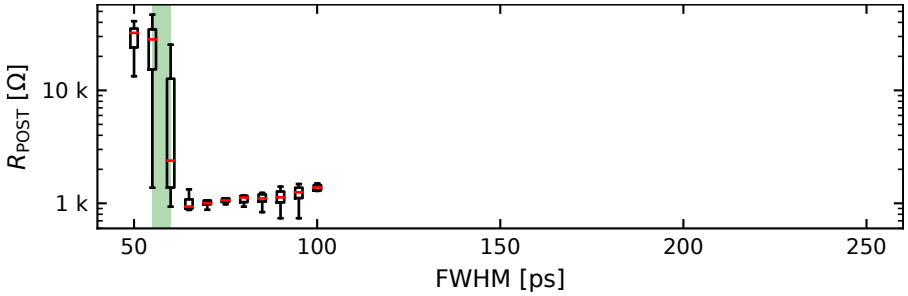

(b) Zr1 device, $V_P = 1.6\,V$.

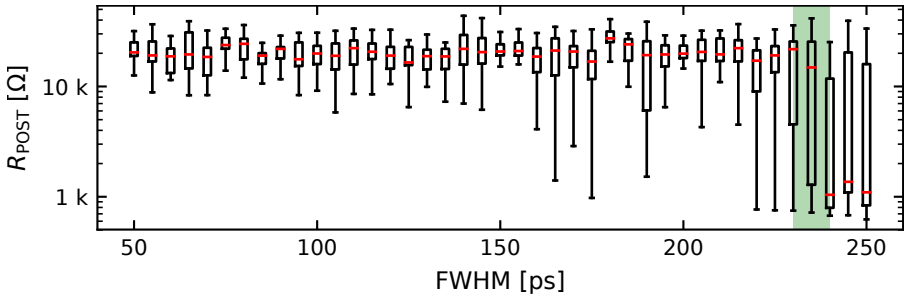

(c) Zr1 device, $V_P = 1.1\,V$.

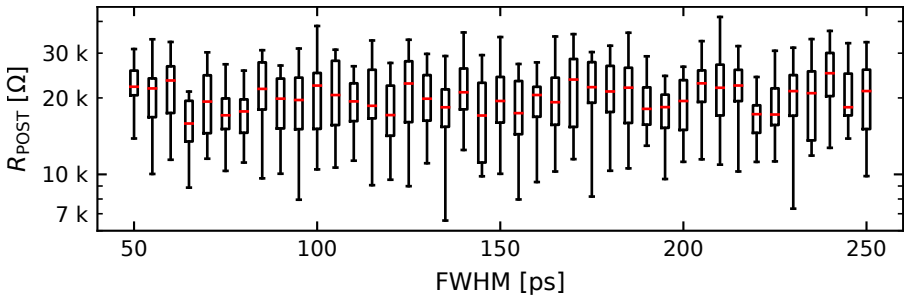

(d) Zr1 device, $V_P = 0.8\,V$.

Figure C.4.: POST resistance values R_{POST} of the Zr1 device's (see table 3.1) unipolar SET kinetics, during which positive voltage pulses were applied to the Pt bottom electrode. The data set is identical to the one from fig. 5.10. The green shaded areas in (b) and (c) mark the transition time (80 %-20 %). The red bar in the boxplot marks the median.

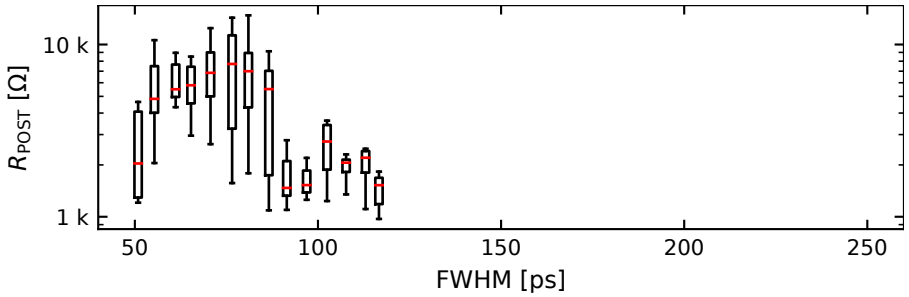

(a) HfA1 device, $V_P = 3.5\,V$.

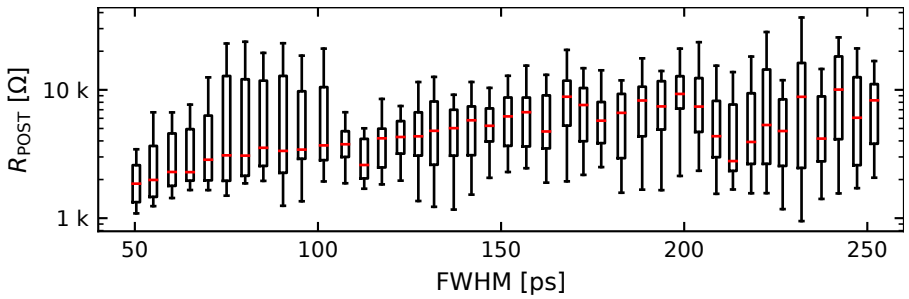

(b) HfA1 device, $V_P = 2.5\,V$.

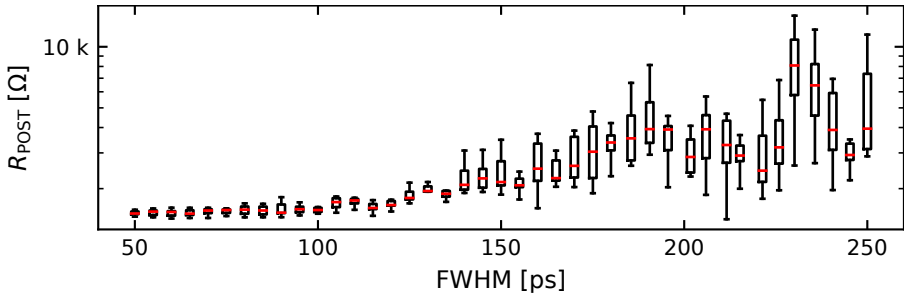

(c) HfA1 device, $V_P = 1.6\,V$.

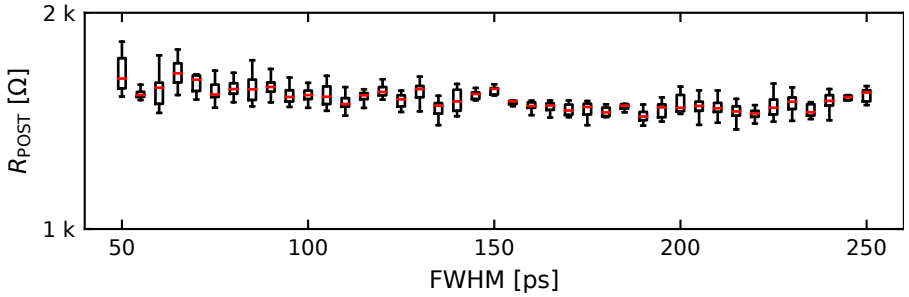

(d) HfA1 device, $V_P = 1.1\,V$.

Figure C.5.: RESET kinetics of the HfA1 device (see table 3.1), representing the POST resistance values R_{POST}. The data set is identical to the one from fig. 5.25. The red bar in the boxplot marks the median.

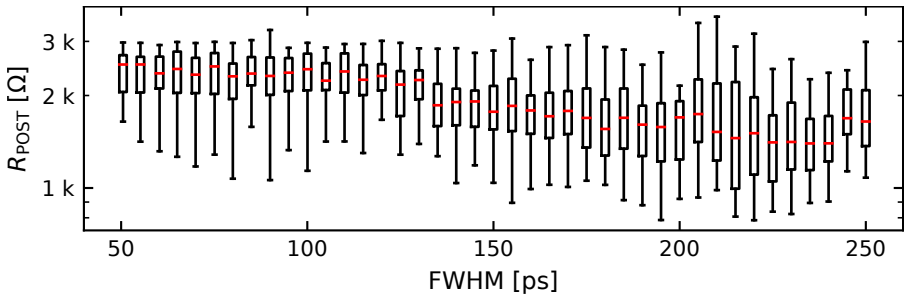

(a) HfA3 device, $V_P = 1.8\,V$.

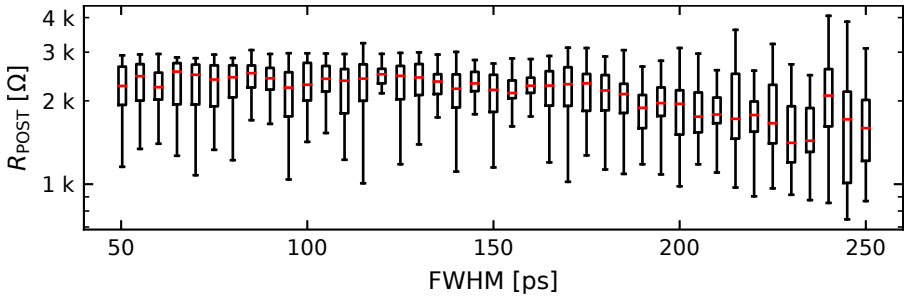

(b) HfA3 device, $V_P = 1.6\,V$.

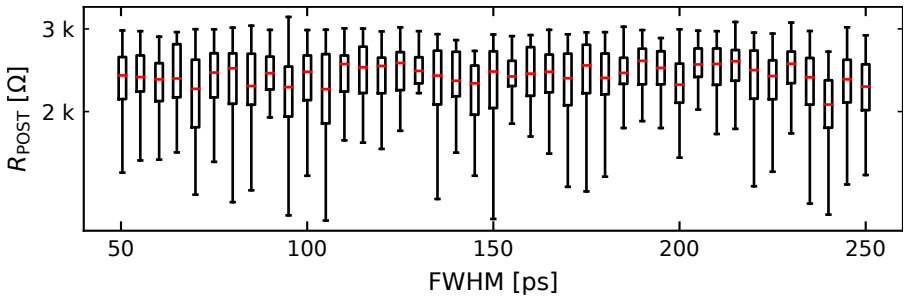

(c) HfA3 device, $V_P = 1.1\,V$.

Figure C.6.: RESET kinetics of the HfA3 device (see table 3.1), representing the POST resistance values R_{POST}. The data set is identical to the one from fig. 5.26. The red bar in the boxplot marks the median.

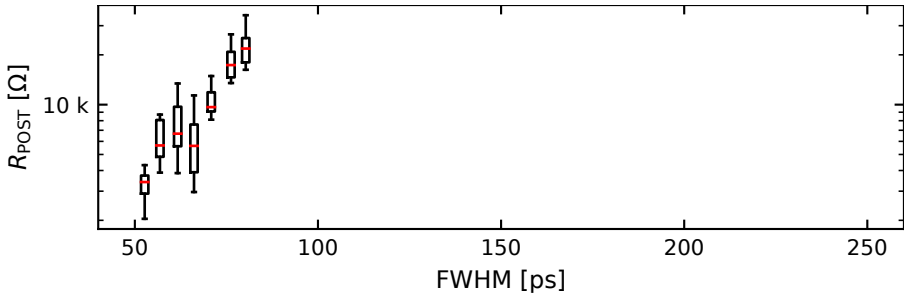

(a) HfB3 device, $V_P = 5.0\,V$.

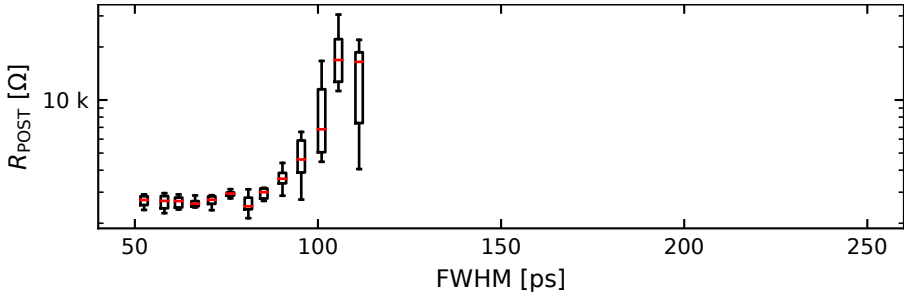

(b) HfB3 device, $V_P = 3.5\,V$.

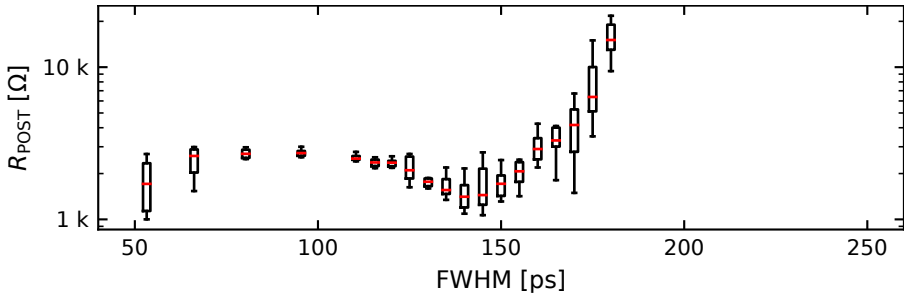

(c) HfB3 device, $V_P = 2.5\,V$.

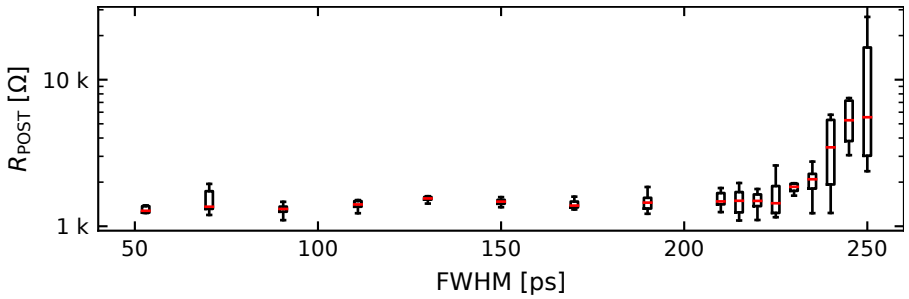

(d) HfB3 device, $V_P = 1.8\,V$.

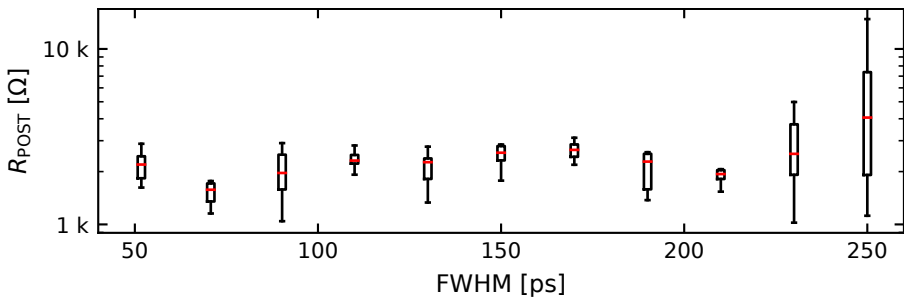

(e) HfB3 device, $V_P = 1.6\,V$.

Figure C.7.: RESET kinetics of the HfB3 device (see table 3.1), representing the POST resistance values R_{POST}. The data set is identical to the one from fig. 5.27. The red bar in the boxplot marks the median.